Title: Reactive high-spin iron(IV)-oxo sites through dioxygen activation in a metal–organic framework

Authors: Kaipeng Hou[1,2]†, Jonas Börgel[l,2]†, Henry Z. H. Jiang[1], Daniel J. SantaLucia[3,4], Hyunchul Kwon[1], Hao Zhuang[5,6], Khetpakorn Chakarawet[7]‡, Rachel C. Rohde[1], Jordan W. Taylor[1], Chaochao Dun[8], Maria V. Paley[1,2], Ari B. Turkiewicz[1], Jesse G. Park[1]§, Haiyan Mao[5], Ziting Zhu[2,6], E. Ercan Alp[9], Jiyong Zhao[9], Michael Y. Hu[9], Barbara Lavina[9,10], Sergey Peredkov[3], Xudong Lv[1], Julia Oktawiec[11], Katie R. Meihaus[1], Dimitrios A. Pantazis[4], Marco Vandone[12], Valentina Colombo[12], Eckhard Bill[3], Jeffrey J. Urban[2,8], R. David Britt[7], Fernande Grandjean[13], Gary J. Long[13], Serena DeBeer[3], Frank Neese[4], Jeffrey A. Reimer[2,5], Jeffrey R. Long[1,2,5]*

Affiliations:

[1]Department of Chemistry, University of California, Berkeley, CA 94720, USA.

[2]Materials Sciences Division, Lawrence Berkeley National Laboratory, Berkeley, CA 94720, USA.

[3]Max Planck Institute for Chemical Energy Conversion, Mülheim an der Ruhr D-45470, Germany.

[4]Max-Planck-Institut für Kohlenforschung, Mülheim an der Ruhr D-45470, Germany.

[5]Department of Chemical and Biomolecular Engineering, University of California, Berkeley, CA 94720, USA.

[6]Department of Materials Science and Engineering, University of California, Berkeley, CA 94720, USA.

[7]Department of Chemistry, University of California, Davis, CA 95616, USA.

[8]The Molecular Foundry, Lawrence Berkeley National Laboratory, Berkeley, CA 94720, USA.

[9]Advanced Photon Source, Argonne National Laboratory, Lemont, IL 60439, USA.

[10]Center for Advanced Radiation Sources, The University of Chicago, Chicago, IL 60637, USA.

[11]Department of Chemistry, Northwestern University, Evanston, IL 60208, USA.

[12]Department of Chemistry, University of Milan, Milan 20133, Italy.

[13]Department of Chemistry, Missouri University of Science and Technology, University of Missouri, Rolla, MO 65409, USA.

* Corresponding author. Email: jrlong@berkeley.edu

† These authors contributed equally to this work.

‡ Present address: Department of Chemistry, Faculty of Science, Mahidol University, Bangkok 10400, Thailand.

§ Present address: Department of Chemistry, Korea Advanced Institute of Science and Technology (KAIST), Daejeon 34141, Republic of Korea.

Abstract: In nature, nonheme iron-containing enzymes use dioxygen to generate high-spin iron(IV)=O species for a variety of oxygenation reactions. Although scientists have long sought to mimic this reactivity, the enzyme-like activation of O_2 to form high-spin iron(IV)=O species remains an unrealized goal in synthetic chemistry. Here, we report a metal–organic framework featuring iron(II) sites with a local structure similar to that in α-ketoglutarate-dependent dioxygenases. The framework reacts with O_2 at low temperatures to form high-spin iron(IV)=O species that are characterized using *in situ* diffuse reflectance infrared Fourier transform, *in situ* and variable-field Mössbauer, Fe Kβ x-ray emission, and nuclear resonance vibrational spectroscopies. In the presence of O_2, the framework is competent for catalytic oxygenation of cyclohexane and the stoichiometric conversion of ethane to ethanol.

One-Sentence Summary: High-spin Fe(IV)=O species competent for hydrocarbon oxidation are generated using O_2 in a synthetic system that mimics α-ketoglutarate-dependent dioxygenases.

The development of catalysts for the selective oxygenation of light hydrocarbons using O_2 remains a formidable but important challenge in the global effort to develop green technologies for the valorization of natural gas components (*1–3*). Nature has developed mononuclear nonheme iron metalloenzymes that utilize O_2 for C–H oxygenation chemistry, such as the ubiquitous α-ketoglutarate-dependent dioxygenases (*4*). One well-studied enzyme in this class is taurine–α-ketoglutarate dioxygenase (TauD), which oxygenates one of the C–H bonds of taurine alpha to the sulfonate group (*5*). Key to the reactivity of TauD and its family of dioxygenases is a high-spin (*S* = 2) Fe(IV)=O intermediate, which is formed following oxidation of iron(II) with O_2 coupled with oxidation and decarboxylation of the α-ketoglutarate co-substrate (Fig. 1A) (*6, 7*). Over the last several decades, significant research effort has been devoted to the design and study of iron(IV)–oxo species in molecular (*8–17*) and iron–zeolite (*18, 19*) model systems in order to better understand and mimic their reactivity in biological systems. However, most examples studied to date feature an intermediate spin ground state (*S* = 1), and only a small number of these are generated using dioxygen in solution (*10–13*). High-spin Fe(IV)=O species have been accessed with oxidants such as trimethylammonium-*N*-oxide, hypervalent iodine reagents, and nitrous oxide (*14, 15, 18*), as well as in the presence of O_2 with light irradiation to cleave the O–O bond (*17*). However, the use of O_2 alone for the generation of high-spin Fe(IV)=O species, in a manner akin to metalloenzyme reactivity, has yet to be achieved in any synthetic system (*16, 19, 20*).

Metal–organic frameworks have received increasing attention in recent years as attractive systems for studying biomimetic chemistry (*21, 22, 23*). These porous, crystalline solids are constructed from metal nodes and organic linkers, and they exhibit chemical and structural tunability that is unmatched in other porous materials (*24, 25*). As such, metal–organic frameworks offer the opportunity to explore O_2 activation in solid–gas reactions, while the immobilization of metal sites in the lattice may serve to prevent the decomposition of reactive species via dimerization or intramolecular ligand oxidation pathways available to molecular compounds (*9, 26, 27*). However, reported mimics of nonheme iron enzymes in metal–organic frameworks are scarce (*28*). In this context, the framework $Fe_{1.5}Zn_{3.5}Cl_4(btdd)_3$ (H_2btdd = bis(1*H*-1,2,3-triazolo [4,5-*b*],[4′,5′-*i*])dibenzo[1,4]dioxin) (*29*) stands out as a suitable biomimetic platform (*22*). This material is synthesized via post-synthetic iron(II) exchange in $Zn_5Cl_4(btdd)_3$ (MFU-4*l*) (*30*) and features pseudo-tetrahedral iron(II) sites with tris(triazolate) coordination reminiscent of the binding of the 2-His-1-carboxylate facial triad in TauD. Herein, we report the frameworks $Fe_xZn_{5-x}(prv)_4(btdd)_3$ (x = 1 or 1.8; Hprv = pyruvic acid) and $FeZn_4(moba)_4(btdd)_3$ (Hmoba = 3,3-dimethyl-2-oxobutanoic acid), which react with O_2 to generate high-spin (S = 2) Fe(IV)=O species that are reactive toward hydrocarbon oxygenation (Figs. 1B and 1C).

Synthesis and characterization of $Fe_xZn_{5-x}(prv)_4(btdd)_3$

The frameworks $Fe_xZn_{5-x}(prv)_4(btdd)_3$ were prepared via post-synthetic cation exchange in $Zn_5Cl_4(btdd)_3$ using ferrous chloride and subsequent ligand exchange with pyruvate (see the supplementary materials (SM)). Energy-dispersive x-ray (EDX) spectroscopy revealed that the iron sites in $Fe_xZn_{5-x}Cl_4(btdd)_3$ are homogeneously distributed within the materials (figs. S1 and S2), and inductively coupled plasma optical emission spectroscopy (ICP-OES) confirmed the extent of iron substitution. Quantitative exchange of chloride for pyruvate in $Fe_xZn_{5-x}(prv)_4(btdd)_3$ is supported by elemental analysis (see section 1.3 of the SM).

Powder x-ray diffraction analysis confirmed that the $Fe_xZn_{5-x}(prv)_4(btdd)_3$ materials are crystalline solids and isostructural to the parent MFU-4l framework (fig. S3), and N_2 adsorption data obtained at 77 K revealed high Brunauer–Emmett–Teller (BET) surface areas of 2130±12 and 2090±15 m^2/g for $x = 1$ and 1.8, respectively (figs. S4 and S5). The 5 K Mössbauer spectrum of desolvated $FeZn_4(prv)_4(btdd)_3$ features a major doublet (area of 84.2(8)%) with an isomer shift (δ) of 1.061(1) mm/s and a quadrupole splitting ($|\Delta E_Q|$) of 2.567(1) mm/s, indicative of high-spin, five-coordinate iron(II) (fig. S18) (*31*). Two minor doublets with slightly different Mössbauer parameters likely correspond to six-coordinate iron(II) sites featuring residual coordinating synthesis solvent (table S6). The magnetic circular dichroism spectrum of $FeZn_4(prv)_4(btdd)_3$ collected at 5 K under a field of 7 T features d-d transitions around 6000 and 14000 cm^{-1}, which are consistent with $S = 2$ iron(II) centers in a five-coordinate ligand field (fig. S8). Continuous-wave parallel mode electron paramagnetic resonance (EPR) spectroscopy and dc magnetic susceptibility data collected for $Fe_xZn_{5-x}(prv)_4(btdd)_3$ further support the assignment of $S = 2$ for the iron(II) sites (figs. S9–S11).

We turned to solid-state ^1H NMR spectroscopy to gain more insight into the possible binding modes of the pyruvate ligands in $FeZn_4(prv)_4(btdd)_3$. The spectrum exhibits broad features owing to the paramagnetic sites, which preclude the extraction of meaningful information (fig. S12). As such, we prepared a crystalline powder sample of $Zn_5(prv)_4(btdd)_3$ featuring pyruvate labeled with ^{13}C at the methyl carbon. The solid-state ^1H NMR spectrum features resonances from the protons of the $btdd^{2-}$ linker and the pyruvate methyl group in approximately a 1:1 ratio, supporting quantitative ligand exchange (fig. S13). We were also able to prepare single crystals of $Zn_5(prv)_4(btdd)_3$ (see sections 1.6 and 1.7 of the SM and figs. S14A and S15A), and analysis via single-crystal x-ray diffraction revealed that pyruvate coordinates to the peripheral zinc(II) centers in a bidentate fashion (figs. S14B and S15B). It was not possible to isolate single crystals of $FeZn_4(prv)_4(btdd)_3$ via single-crystal-to-single-crystal exchange starting from $Zn_5Cl_4(btdd)_3$. However, the powder x-ray diffraction patterns of $Fe_xZn_{5-x}(prv)_4(btdd)_3$ are consistent with the simulated pattern generated for $Zn_5(prv)_4(btdd)_3$ from the single-crystal structure (fig. S3), which may indicate that the coordination mode of the pyruvate ligand is similar in the three frameworks.

In situ DRIFTS analysis of the reactivity of $Fe_{1.8}Zn_{3.2}(prv)_4(btdd)_3$ with O_2

Reactivity between $Fe_xZn_{5-x}(prv)_4(btdd)_3$ and O_2 was examined with variable-temperature *in situ* diffuse reflectance infrared Fourier transform spectroscopy (DRIFTS) (fig. S16). For this purpose, we used $Fe_{1.8}Zn_{3.2}(prv)_4(btdd)_3$ with the goal of maximizing the resulting spectral signal, while $FeZn_4(prv)_4(btdd)_3$ was used for the remaining spectroscopic analyses described below. Following dosing of a sample of desolvated $Fe_{1.8}Zn_{3.2}(prv)_4(btdd)_3$ with O_2 at 100 K, a new absorption band gradually appeared in the DRIFTS spectrum at 2341 cm^{-1}, which we assign as the asymmetric C=O stretch of physisorbed CO_2 formed from decarboxylation of pyruvate (Fig. 2A, solid lines). The intensity of this band increased as the temperature was increased to 150 and 200 K, and above 250 K the band disappeared, consistent with CO_2 desorption from the framework. To verify that the detected CO_2 derived from pyruvate and not from O_2, we carried out an analogous *in situ* experiment using $Fe_{1.8}Zn_{3.2}(1-^{13}C-prv)_4(btdd)_3$ ($1-^{13}C-prv^-$ = pyruvate labeled with ^{13}C on the carboxylate carbon atom) and $^{18}O_2$ (Fig. 2A, dashed lines). Upon dosing with $^{18}O_2$ at 100 K, a new stretch appeared at 2275 cm^{-1}, consistent with formation of the isotopologue $^{13}CO_2$ and not $^{13}C^{18}O_2$, confirming that the oxygen atoms do not originate from dioxygen. The $^{13}CO_2$ stretch grew in intensity with heating to 200 K and disappeared at higher temperatures. A slight deviation of the experimental CO_2 stretching frequencies reported herein from the values associated with gas-phase CO_2 (2349 and 2284 cm^{-1} for CO_2 and $^{13}CO_2$, respectively) can be ascribed to adsorption of

the CO_2 within the pores of the framework at low temperatures. Importantly, *in situ* powder x-ray diffraction data collected for $FeZn_4(prv)_4(btdd)_3$ after dosing with O_2 at 100 K over the course of gradual warming to 298 K revealed that the material remains highly crystalline under these conditions (fig. S24).

An absorption band was observed to grow in at 831 cm^{-1} upon dosing $Fe_{1.8}Zn_{3.2}(prv)_4(btdd)_3$ with O_2 at 100 K, which we assign as an Fe(IV)=O stretch (Fig. 2B, solid lines). This band increased in intensity with heating up to 200 K before diminishing significantly at 250 K and disappearing at 298 K. When the analogous experiment was performed with $^{18}O_2$, the band shifted to 796 cm^{-1}, consistent with a stretching frequency of 794 cm^{-1} calculated for Fe(IV)=^{18}O using a simple harmonic oscillator model (Fig. 2B, dashed lines). For comparison, the Fe(IV)=^{16}O and Fe(IV)=^{18}O stretches in TauD-*J* appear at 821 and 787 cm^{-1}, respectively (*32*). Concomitant with the disappearance of the Fe(IV)=O stretch at 250 K, a new stretch appeared at 3628 cm^{-1} (fig. S17). We attribute this stretch to an Fe(III)–OH species arising from decomposition of the Fe(IV)=O through hydrogen-atom abstraction, possibly from the methyl group of the newly formed acetate ligand (Fig. 2C). At 298 K, a new stretch is apparent at 3678 cm^{-1} (fig. S17), which may correspond to a different coordination environment for the Fe(III)–OH species at higher temperatures. When $^{18}O_2$ was used for dosing, a stretch appeared at 3617 cm^{-1}, in excellent agreement with that calculated for Fe(III)–^{18}OH using a simple harmonic oscillator model (3616 cm^{-1}).

Experimental and computational investigation of the Fe(IV)=O spin state

The species formed upon reaction of $Fe_xZn_{5-x}(prv)_4(btdd)_3$ with dioxygen were further investigated by *in situ* Mössbauer spectroscopy (see section 2.9.1 of the SM). As discussed above, the 5 K Mössbauer spectrum of desolvated $FeZn_4(prv)_4(btdd)_3$ features a major doublet indicative of high-spin, five-coordinate iron(II) (Fig. 3A, table S6). After dosing with 300 mbar of O_2 at 100 K, this doublet persisted and a new doublet was apparent with δ = 0.260(4) mm/s and $|\Delta E_Q|$ = 0.572(8) mm/s (16.7(2)% area), which we assign to an Fe(IV)=O species. These parameters are similar to those determined for the $S = 2$ Fe(IV)=O intermediate of TauD (δ = 0.31 mm/s and ΔE_Q = −0.88 mm/s) (*6*, *7*). A detailed comparison with isomer shift and quadrupole splitting values for other reported iron(IV)–oxos reveals that they are more consistent with an $S = 2$ spin state ($\delta_{S=2}$ = 0.02–0.37 mm/s; $|\Delta E_Q|_{S=2}$ = 0.23–1.27 mm/s) than an $S = 1$ spin state ($\delta_{S=1} < 0.20$ mm/s; $|\Delta E_Q|_{S=1}$ = 0.44–2.09 mm/s) (see fig. S40). Density functional theory (DFT) calculations at the B3LYP/def2-TZVP level of theory predict an isomer shift of 0.25 mm/s for an $S = 2$ six-coordinate Fe(IV)=O moiety featuring acetate coordinated in a κ^2-binding mode, in excellent agreement with the experimental value (tables S6 and S9).

We considered that a slow oxidation rate at 100 K may be a factor limiting the Fe(IV)=O content in O_2-dosed $FeZn_4(prv)_4(btdd)_3$. Indeed, the percent area of the Fe(IV)=O doublet could be increased up to a maximum of 20.0(2)% upon further dosing with of O_2 at 125 and 150 K. (Fig. 3A, table S6). However, subsequent dosing at 163 K did not result in an increase in the percent of the Fe(IV)=O doublet (figs. S19 and S22). At these temperatures, it is possible that a greater quantity of Fe(IV)=O species is generated initially but that some of these sites react with the acetate ligand to generate a hydroxylated product and reform high-spin iron(II) sites. Analogous intramolecular α-C–H hydroxylation is known for α-ketoglutarate dependent dioxygenases (*35*), and we discuss this possibility further below. Finally, spectra were collected at 5 K after heating the sample at 250 and 298 K without additional O_2 dosing. After warming at 250 K, the area of the Fe(IV)=O doublet was only 9.7(3)% and after warming at 298 K, the Fe(IV)=O doublet was

absent, consistent with the decomposition observed in the DRIFTS data (fig. S20). A Mössbauer spectrum collected at 5 K after *ex situ* dosing of $FeZn_4(prv)_4(btdd)_3$ with O_2 at 163 K revealed a slightly higher Fe(IV)=O content of 32.2(6)% relative to that achieved under *in situ* conditions (section 2.9.2 of the SM, fig. S21), which may be due to the different conditions and the nature of the sample used (loose versus compact powder, respectively). The sample remained crystalline after warming to 298 K (fig. S25), and the porosity of the framework did not change significantly (1980 ± 23 m^2/g, fig. S26).

The Mössbauer isomer shift and quadrupole splitting values determined for the Fe(IV)=O species generated in $FeZn_4(prv)_4(btdd)_3$ are more consistent with an $S = 2$ than an $S = 1$ spin state, although these parameters alone do not enable an unambiguous assignment. To experimentally assign the spin state, we turned to applied magnetic field Mössbauer spectroscopy (*6, 17, 36*). We expected that the low concentration of the Fe(IV)=O species accessible upon dosing $FeZn_4(prv)_4(btdd)_3$ with O_2 would limit data resolution. One plausible explanation for the low detected concentration is decomposition of the Fe(IV)=O species via oxygenation of the newly formed acetate ligand (*35*). Such a side reaction would be precluded if pyruvate were replaced with an α-ketocarboxylate lacking α-C–H bonds. Accordingly, we synthesized $FeZn_4(moba)_4(btdd)_3$, which features a 3,3-dimethyl-2-oxobutyrate ligand with a *tert*-butyl group alpha to the carbonyl (see section 1.8 of the SM). This material is isostructural to $Fe_xZn_{5-x}(prv)_4(btdd)_3$ (fig. S27) and exhibits a comparably high BET surface area (fig. S28). *In situ* DRIFTS data collected for $FeZn_4(moba)_4(btdd)_3$ upon dosing with O_2 at 100 K support Fe(IV)=O formation via decarboxylation of 3,3-dimethyl-2-oxobutyrate (see fig. S29; ν(Fe=O) = 828 cm^{-1}, ν(Fe=^{18}O) = 794 cm^{-1}), consistent with data discussed above for $FeZn_4(prv)_4(btdd)_3$.

The zero-field Mössbauer spectrum of $FeZn_4(moba)_4(btdd)_3$ collected at 5 K features a major doublet assigned to high-spin, five-coordinate iron(II) (fig. S31, table S10). Following a sequence of *in situ* dosing with O_2 at 100 K and heating at 200 K, a new quadrupole doublet was apparent in the 5 K Mössbauer spectrum with $\delta = 0.292(1)$ mm/s and $\Delta E_Q = -0.603(1)$ mm/s (61.7(1)% area), assigned to the Fe(IV)=O species (fig. S31; the sign of the quadrupole splitting was determined from variable-field Mössbauer data, see section 2.12 of the SM). This relative area is significantly larger than the maximum relative area of *in situ* O_2-dosed $FeZn_4(prv)_4(btdd)_3$ (21.1(1)%), supporting our hypothesis that intramolecular ligand oxygenation may be limiting the Fe(IV)=O content. Variable-field Mössbauer spectra were subsequently collected for O_2-dosed $FeZn_4(moba)_4(btdd)_3$ at 1.7 K under fields ranging from 0 to 7 T and at temperatures from 1.7 to 40 K under a field of 7 T (Fig. 3B and fig. S33; see section 2.12 of the SM). Spectra were also collected for $FeZn_4(moba)_4(btdd)_3$ at temperatures <5 K and fields ranging from 0 to 7 T (fig. S32) to obtain fixed parameters for modeling the residual iron(II) species for the O_2-dosed material (table S12; see section 2.12.2 of the SM).

Consistent with the zero-field Mössbauer spectrum collected at 5 K, the zero-field spectrum for O_2-dosed $FeZn_4(moba)_4(btdd)_3$ collected at 1.7 K could be fit with three subspectra, corresponding to an $S = 2$ iron(II) component, an iron(III) species, and an Fe(IV)=O component (Fig. 3B). The isomer shift of this Fe(IV)=O species is consistent with reported $S = 2$ iron(IV)–oxo species in the literature (fig. S40), however, both $S = 1$ and $S = 2$ models were considered in fitting the variable-field and variable-temperature data. Initial attempts to simultaneously fit the variable-temperature data collected under a 7 T field using this three subspectra model did not fully account for the total spectral intensity. We found that inclusion of a fourth subspectrum, assigned to an $S = 0$ species, likely arising from antiferromagnetically coupled Fe(IV)=O sites within the same cluster node, affords a good fit to the data (see section 2.12.3 of the SM). While ICP-OES analysis predicts a distribution of one iron site per cluster on average, we cannot exclude

a distribution wherein some clusters feature two iron centers per cluster, some feature a single iron center, and other clusters contain zero iron sites.

Simultaneous modeling of the variable-field and variable-temperature spectra was performed via diagonalization of the spin Hamiltonians for the four subspectra to obtain values of the zero-field splitting (D) and hyperfine coupling parameters (A_{xx}, A_{yy}, A_{zz}) for the uncoupled Fe(IV)=O species when assigned as either $S = 2$ or $S = 1$ (see section 2.12.3 of the SM for details and tables S13–15). While the data could be fit with an $S = 2$ or $S = 1$ model (Fig. 3B and figs. S33–S35), only the results for the $S = 2$ model are chemically reasonable based on a comparison with reported Fe(IV)=O species. The best model for the $S = 2$ Fe(IV)=O species yielded $D = 12.7(6)$ cm^{-1} and $a_{iso} = -16.4(4)$ T (table S13), parameters that are in excellent agreement with those reported for $S = 2$ Fe(IV)=O species ($D_{S=2} = 4$–14 cm^{-1}, $a_{iso(S=2)} = -23$ to -16 T) (*17, 37*). In contrast, the best model for $S = 1$ Fe(IV)=O sites yielded values that are significantly different from those reported previously for $S = 1$ Fe(IV)=O species (table S14) (*37, 38, 39*). Furthermore, the signs and relative magnitudes of the spin-dipole contribution $\vec{A}_{SD}$ to the hyperfine coupling tensor are only consistent with an $S = 2$ spin ground state (see section 2.12.4 of the SM).

Additional experimental support for the $S = 2$ assignment for the Fe(IV)=O species was obtained from Fe Kβ x-ray emission spectroscopy (XES; section 2.13 of the SM). Iron Kβ XES involves the measurement of 3p to 1s emissions, and due to the Fe 3p–3d exchange contributions to the final state, the relative intensities and energies of the Kβ mainline features—the Kβ′ and Kβ$_{1,3}$ peaks—are diagnostic of the local iron spin state (*40–42*). High-spin states typically give rise to more intense Kβ′ features and larger separations between the Kβ′ and Kβ$_{1,3}$ peaks than low-spin states (*41*). The XES spectra for $S = 2$ FeZn$_4$(moba)$_4$(btdd)$_3$ and a sample of the framework dosed *ex situ* with O$_2$ are given in fig. S39, along with a representative spectrum for a reported molecular compound featuring an $S = 1$ Fe(IV)=O (*42*). The spectra for pristine and O$_2$-dosed FeZn$_4$(moba)$_4$(btdd)$_3$ nearly overlay and feature an intense Kβ′ peak, consistent with the dominant presence of $S = 2$ iron sites in both materials. In contrast, there is no clear Kβ′ peak in the $S = 1$ Fe(IV)=O spectrum, and the Kβ$_{1,3}$ peak appears at a lower energy than in the spectrum for O$_2$-dosed FeZn$_4$(moba)$_4$(btdd)$_3$.

Finally, we used DFT to calculate Mössbauer isomer shifts for the model cluster Fe(O)(κ^2-OPiv)Zn$_4$(prv)$_3$(bta)$_6$ (OPiv$^-$ = pivalate formed upon moba$^-$ decarboxylation; bta$^-$ = benzotriazolate) featuring an $S = 2$ or $S = 1$ ground state. Geometry optimizations were performed at the BP86-D3BJ/def2-TZVP level of theory. For the $S = 2$ optimized geometry, $\delta_{calc} = 0.27$ mm/s is in excellent agreement with the experimentally determined isomer shift ($\delta = 0.292(1)$ mm/s), whereas the isomer shift calculated for $S = 1$ deviates significantly from the experimental value ($\delta_{calc} = 0.16$ mm/s) (table S11). Furthermore, CASSCF calculations in combination with *N*-electron valence perturbation theory to second order (NEVPT2) support the assignment of an $S = 2$ ground state, which is predicted to be 25 kcal/mol more stable than the lowest energy $S = 1$ configuration (see section 3 of the SM and fig. S41). Altogether, the Mössbauer, Fe Kβ XES, and computational data clearly support the assignment of an $S = 2$ ground state for the Fe(IV)=O sites formed upon oxidation of FeZn$_4$(moba)$_4$(btdd)$_3$.

Investigation of the local Fe(IV)=O coordination environment using nuclear resonance vibrational spectroscopy

Nuclear resonance vibrational spectroscopy (NRVS) was used to gain further insight into the local structure of the Fe(IV)=O species (see section 2.7 of the SM). This technique selectively yields the complete set of vibrational modes of Mössbauer-active nuclei and can therefore provide structural insights not accessible using other spectroscopic methods. Figures 4A and B,

respectively, show the iron partial vibrational density of states (PVDOS) distributions obtained from data collected at ~100 K for desolvated 95% ^{57}Fe-enriched FeZn$_4$(prv)$_4$(btdd)$_3$ before and after *ex situ* O$_2$-dosing at 163 K. A new peak at 822 cm^{-1} for the O$_2$-dosed sample was assigned to an Fe(IV)=O vibration and is similar in magnitude to NRVS peaks reported for other nonheme Fe(IV)=O species in synthetic systems (*33, 43, 44*). In support of this assignment, when ^{18}O$_2$ was employed for dosing, the vibration appeared instead at 788 cm^{-1} (Fig. 4B, inset; figs. S44 and S47). Consistent results were obtained from PVDOS distributions obtained for ^{57}Fe-enriched FeZn$_4$(moba)$_4$(btdd)$_3$ after dosing with O$_2$ or ^{18}O$_2$ (fig. S50), which feature peaks at 820 and 789 cm^{-1}, respectively. The Fe(IV)=O peak was absent in the PVDOS distribution obtained for both frameworks after warming to 298 K (figs. S43 and S51).

Using the truncated cluster FeZn$_4$(prv)$_4$(bta)$_6$ as a model for FeZn$_4$(prv)$_4$(btdd)$_3$, we performed DFT calculations to simulate the NRVS iron PVDOS for the framework before and after O$_2$ dosing (Figs. 4A and 4B, dark gray curves). The intense stretch at 330 cm^{-1} predicted for the model iron(II) framework corresponds to vibrations associated with bidentate pyruvate binding. Differences in the predicted and experimental intensities likely arise because the cluster model cannot fully describe the phonons of the framework lattice. For the O$_2$-dosed sample, stretches at 282 and 340 cm^{-1} are assigned as Fe–O vibrations resulting from κ^2-binding of the acetate ligand (Fig. 4C). In contrast, Fe–O vibrations associated with κ^1-binding of acetate are predicted to appear at higher wavenumbers (>400 cm^{-1}) (figs. S45 and S46). The calculated Fe(IV)=O stretch is higher than the experimental stretching frequency (919 versus 822 cm^{-1}), likely because of a known systematic overestimation by DFT at these higher energies, which is less pronounced at lower energies (*45*). Finally, simulated NRVS iron PVDOS were also generated for pristine and O$_2$-dosed FeZn$_4$(moba)$_4$(btdd)$_3$ from DFT calculations on the truncated $S = 2$ cluster models Fe(moba)Zn$_4$(prv)$_3$(bta)$_6$ and Fe(O)(κ^2-OPiv)Zn$_4$(prv)$_3$(bta)$_6$, and the results are in good agreement with the experiment (figs. S48 and S49).

Reactivity studies

We evaluated the reactivity of Fe$_x$Zn$_{5-x}$(prv)$_4$(btdd)$_3$ with hydrocarbon substrates in the presence of O$_2$. Desolvated FeZn$_4$(prv)$_4$(btdd)$_3$ was suspended in cyclohexane and exposed to 1 bar of O$_2$ at 21 °C for 24 h. Subsequently, CH$_3$CN-d_3 was added to extract the products, along with CH$_2$Br$_2$ as an internal standard. Analysis of the resulting supernatant using ^{1}H NMR spectroscopy and GC-MS revealed the formation of cyclohexanol (22% NMR yield with respect to the iron sites in the framework) with no detectable cyclohexanone (see section 1.9.1 of the SM and figs. S53 and S54). Mössbauer spectroscopy analysis of the framework isolated following this reaction revealed only iron(II) species (fig. S56). The same stoichiometric reaction was also carried out using FeZn$_4$(moba)$_4$(btdd)$_3$ in the presence of O$_2$ (1 bar, 21 °C), and analysis of the resulting supernatant using ^{1}H NMR spectroscopy and GC-MS revealed the formation of only cyclohexanol (51% NMR yield) (see section 1.11.1 of the SM and figs. S59 and S60). A stoichiometric control reaction between cyclohexane and FeZn$_4$Cl$_4$(btdd)$_3$ in the presence of O$_2$ did not yield any hydrocarbon oxidation products (figs. S57 and S58).

In order to establish the direct role of the Fe(IV)=O species in C–H oxygenation, we sought to perform a stoichiometric reaction using a framework sample in which the Fe(IV)=O species were generated prior to the addition of substrate. A sample of FeZn$_4$(prv)$_4$(btdd)$_3$ was dosed with 200 mbar O$_2$ at 163 K, and after 2 h, the sample headspace was evacuated, refilled with Ar and a mixture of cyclohexane and CD$_2$Cl$_2$ was added. The suspension was then warmed to 195 K and held for 2 h and then allowed to warm to 294 K. Under these conditions, no cyclohexane oxidation

products were detected via ^{1}H NMR spectroscopy. When a similar reaction was performed using FeZn$_4$(moba)$_4$(btdd)$_3$ (see section 1.11.2 of the SM), ^{1}H NMR spectroscopy and GC-MS analysis of the resulting supernatant revealed the formation of cyclohexanone (figs. S61 and S62; 48% NMR yield). The ultimate formation of cyclohexanone in this case—in contrast to cyclohexanol formed in the reaction conducted at 21 °C—is attributed to the lower reaction temperature and slower diffusion of cyclohexanol out of the framework pores, which is then further oxidized to cyclohexanone (see section 1.11 of the SM) (46).

When the cyclohexane oxidation reaction with FeZn$_4$(prv)$_4$(btdd)$_3$ was repeated with the addition of 11 equivalents of pyruvic acid, cyclohexanone and cyclohexanol were obtained in a 2:1 ratio (combined yield of 173%) (see section 1.9.2 of the SM and fig. S64). Powder x-ray diffraction analysis of the solid isolated from this reaction confirmed that the framework remains crystalline (fig. S65). Significantly, this result suggests that FeZn$_4$(prv)$_4$(btdd)$_3$ can act as a catalyst in hydrocarbon oxidation reactions using the free α-keto acid as a co-substrate, presumably via a similar catalytic cycle as proposed for TauD (fig. S71) (6). We found that acetic acid byproduct is formed in this reaction in 288% yield with respect to the iron sites, which suggests 115% of pyruvic acid conversion to unidentified products. Such unproductive turnover at some of the iron sites is consistent with the relatively low yield in the stoichiometric reaction. A number of studies of synthetic and enzymatic systems have established that C–H bond activation by Fe(IV)=O species proceeds via H-atom abstraction, as evidenced by large primary kinetic isotope effects (KIEs) (46, 47). Consistent with these results, we determined an intermolecular competition KIE value of 29.8 ± 1.0 from the reaction of FeZn$_4$(prv)$_4$(btdd)$_3$ with a mixture of cyclohexane and cyclohexane-d_{12} under an atmosphere of O$_2$ (see section 1.10 of the SM and figs. S66 and S67).

The reactivity of Fe$_{1.8}$Zn$_{3.2}$(prv)$_4$(btdd)$_3$ in the presence of O$_2$ was also evaluated using gaseous ethane as a substrate in a high-pressure batch reactor (section 1.12 of the SM). Using a high-pressure mixture of ethane and dioxygen, ethanol and acetaldehyde were obtained in a 3:1 ratio with a high combined yield of 82% (fig. S68). This yield is much higher than that obtained in the stoichiometric cyclohexane oxidation, likely due to the high ethane concentration close to the iron sites under high pressure. Although there are enzymatic systems capable of oxidizing ethane to ethanol with O$_2$ (48), our result is the first synthetic example of ethane oxidation via an unambiguously characterized $S = 2$ Fe(IV)=O intermediate generated by O$_2$.

Outlook

We have developed the frameworks Fe$_x$Zn$_{5-x}$(prv)$_4$(btdd)$_3$ and FeZn$_4$(moba)$_4$(btdd)$_3$ featuring iron(II) sites that activate O$_2$ at 100 K to form high-spin Fe(IV)=O species; reactivity that is reminiscent of O$_2$ activation in TauD. These frameworks are rare non-enzymatic systems capable of catalytic hydrocarbon oxygenation, including the oxidation of ethane to ethanol, via a reactive high-spin Fe(IV)=O intermediate generated from dioxygen. This work establishes a foundation for the development of iron-containing metal–organic frameworks as heterogenous catalysts that closely mimic the reactivity of metalloenzymes.

References and Notes

1. B. G. Hashiguchi, M. M. Konnick, S. M. Bischof, S. J. Gustafson, D. Devarajan, N. Gunsalus, D. H. Ess, R. A. Periana, Main-group compounds selectively oxidize mixtures of methane, ethane, and propane to alcohol esters. *Science* **343**, 1232–1237 (2014).

2. J. Shan, M. Li, L. F. Allard, S. Lee, M. Flytzani-Stephanopoulos, Mild oxidation of methane

to methanol or acetic acid on supported isolated rhodium catalysts. *Nature* **551**, 605–608 (2017).

3.   V. L. Sushkevich, D. Palagin, M. Ranocchiari, J. A. van Bokhoven, Selective anaerobic oxidation of methane enables direct synthesis of methanol. *Science* **356**, 523–527 (2017).

4.   E. G. Kovaleva, J. D. Lipscomb, Versatility of biological non-heme Fe(II) centers in oxygen activation reactions. *Nat. Chem. Biol.* **4**, 186–193 (2008).

5.   C. Krebs, D. G. Fujimori, C. T. Walsh, J. M. Bollinger Jr., Non-heme Fe(IV)–oxo intermediates. *Acc. Chem. Res.* **40**, 484–492 (2007).

6.   J. C. Price, E. W. Barr, B. Tirupati, J. M. Bollinger Jr., C. Krebs, The first direct characterization of a high-valent iron intermediate in the reaction of an α-ketoglutarate-dependent dioxygenase: a high-spin Fe(IV) complex in taurine/α-ketoglutarate dioxygenase (TauD) from Escherichia coli. *Biochemistry*. **42**, 7497–7508 (2003).

7.   S. Sinnecker, N. Svensen, E. W. Barr, S. Ye, J. M. Bollinger Jr., F. Neese, C. Krebs, Spectroscopic and computational evaluation of the structure of the high-spin Fe(IV)-oxo intermediates in taurine: α-ketoglutarate dioxygenase from Escherichia coli and its His99Ala ligand variant. *J. Am. Chem. Soc.* **129**, 6168–6179 (2007).

8.   J. Hohenberger, K. Ray, K. Meyer, The biology and chemistry of high-valent iron–oxo and iron–nitrido complexes. *Nat. Commun.* **3**, 1–13 (2012).

9.   M. P. Mehn, K. Fujisawa, E. L. Hegg, L. Que Jr., Oxygen activation by nonheme iron(II) complexes: α-keto carboxylate versus carboxylate. *J. Am. Chem. Soc.* **125**, 7828–7842 (2003).

10. A. Thibon, J. England, M. Martinho, V. G. Young Jr., J. R. Frisch, R. Guillot, J. J. Girerd, E. Münck, L. Que Jr., F. Banse, Proton- and reductant-assisted dioxygen activation by a nonheme iron(II) complex to form an oxoiron(IV) intermediate. *Angew. Chem. Int. Ed.* **47**, 7064−7067 (2008).

11. F. Li, K. M. Van Heuvelen, K. K. Meier, E. Münck, L. Que Jr., Sc^{3+}-triggered oxoiron(IV) formation from O_2 and its non-heme iron(II) precursor via a Sc^{3+}–peroxo–Fe^{3+} intermediate, *J. Am. Chem. Soc.* **135**, 28, 10198–10201 (2013).

12. D. Kass, T. Corona, K. Warm, B. Braun-Cula, U. Kuhlmann, E. Bill, S. Mebs, M. Swart, H. Dau, M. Haumann, P. Hildebrandt, K. Ray, Stoichiometric formation of an oxoiron(IV) complex by a soluble methane monooxygenase type activation of O_2 at an iron(II)-cyclam center, *J. Am. Chem. Soc.* **142**, 13, 5924–5928 (2020).

13. M. A. Dedushko, M. B. Greiner, A. N. Downing, M. Coggins, J. A. Kovacs, Electronic structure and reactivity of dioxygen-derived aliphatic thiolate-ligated Fe-peroxo and Fe(IV) oxo compounds. *J. Am. Chem. Soc.* **144**, 8515–8528 (2022).

14. J. P. Bigi, W. H. Harman, B. Lassalle-Kaiser, D. M. Robles, T. A. Stich, J. Yano, R. D. Britt, C. J. Chang, A high-spin iron(IV)-oxo complex supported by a trigonal nonheme pyrrolide platform. *J. Am. Chem. Soc.* **134**, 1536–1542 (2012).

15. M. Puri, L. Que Jr., Toward the synthesis of more reactive $S = 2$ non-heme oxoiron(IV) complexes. *Acc. Chem. Res.* **48**, 2443–2452 (2015).

16. C. E. MacBeth, A. P. Golombek, J. Victor G. Young, C. Yang, K. Kuczera, M. P. Hendrich,

A. S. Borovik, O$_2$ activation by nonheme iron complexes: a monomeric Fe(III)-oxo complex derived from O$_2$. *Science* **289**, 938–941 (2000).

17. J. B. Gordon, T. Albert, A. Dey, S. Sabuncu, M. A. Siegler, E. Bill, P. Moënne-Loccoz, D. P. Goldberg, A reactive, photogenerated high-spin (S = 2) Fe^{IV}(O) complex via O$_2$ activation. *J. Am. Chem. Soc.* **143**, 21637–21647 (2021).

18. B. E. R. Snyder, P. Vanelderen, M. L. Bols, S. D. Hallaert, L. H. Böttger, L. Ungur, K. Pierloot, R. A. Schoonheydt, B. F. Sels, E. I. Solomon, The active site of low-temperature methane hydroxylation in iron-containing zeolites. *Nature* **536**, 317–321 (2016).

19. E. Tabor, J. Dedecek, K. Mlekodaj, Z. Sobalik, P. C. Andrikopoulos, S. Sklenak, Dioxygen dissociation over man-made system at room temperature to form the active α-oxygen for methane oxidation. *Sci. Adv.* **6**, eaaz9776 (2020).

20. B. Rungtaweevoranit, A. M. Abdel-Mageed, P. Khemthong, S. Eaimsumang, K. Chakarawet, T. Butburee, B. Kunkel, S. Wohlrab, K. Chainok, J. Phanthasri, S. Wannapaiboon, S. Youngjan, T. Seehamongkol, S. Impeng, K. Faungnawakij, Structural evolution of iron-loaded metal–organic framework catalysts for continuous gas-phase oxidation of methane to methanol. *ACS Appl. Mater. Interfaces* **15**, 26700–26709 (2023).

21. A. M. Wright, Z. Wu, G. Zhang, J. L. Mancuso, R. J. Comito, R. W. Day, C. H. Hendon, J. T. Miller, M. Dincă, A structural mimic of carbonic anhydrase in a metal-organic framework. *Chem.* **4**, 2894–2901 (2018).

22. C. E. Bien, K. K. Chen, S.-C. Chien, B. R. Reiner, L.-C. Lin, C. R. Wade, W. S. W. Ho, Bioinspired metal–organic framework for trace CO$_2$ capture. *J. Am. Chem. Soc.* **140**, 12662–12666 (2018).

23. J. G. Vitillo, C. C. Lu, A. Bhan, L. Gagliardi, Comparing the reaction profiles of single iron catalytic sites in enzymes and in reticular frameworks for methane-to-methanol oxidation. *Cell Rep. Phys. Sci.*, **4**, 101422 (2023).

24. H.-C. Zhou, J. R. Long, O. M. Yaghi, Introduction to metal–organic frameworks. *Chem. Rev.* **112**, 673–674 (2012).

25. H. Furukawa, K. E. Cordova, M. O'Keeffe, O. M. Yaghi, The chemistry and applications of metal–organic frameworks. *Science* **341**, 1230444 (2013).

26. D. J. Xiao, E. D. Bloch, J. A. Mason, W. L. Queen, M. R. Hudson, N. Planas, J. Borycz, A. L. Dzubak, P. Verma, K. Lee, F. Bonino, V. Crocellà, J. Yano, S. Bordiga, D. G. Truhlar, L. Gagliardi, C. M. Brown, J. R. Long, Oxidation of ethane to ethanol by N$_2$O in a metal–organic framework with coordinatively unsaturated iron(II) sites. *Nat. Chem.* **6**, 590–595 (2014).

27. A. Illiescu, J. J. Oppenheim, C. Sun, M. Dincă, Conceptual and practical aspects of metal–organic frameworks for solid–gas reactions. *Chem. Rev.* **123**, 6197–6232 (2023).

28. A. Shaabani, R. Mohammadian, H. Farhid, M. K. Alavijeh, M. M. Amini, Iron-decorated, guanidine functionalized metal–organic framework as a non-heme iron-based enzyme mimic system for catalytic oxidation of organic substrates. *Catal. Lett.* **149**, 1237–1249 (2019).

29. D. Denysenko, J. Jelic, K. Reuter, D. Volkmer, Postsynthetic metal and ligand exchange in MFU-4*l*: a screening approach toward functional metal–organic frameworks comprising

single-site active centers. *Chem. Eur. J.* **21**, 8188–8199 (2015).

30. D. Denysenko, M. Grzywa, M. Tonigold, B. Streppel, I. Krkljus, M. Hirscher, E. Mugnaioli, U. Kolb, J. Hanss, D. Volkmer, Elucidating gating effects for hydrogen sorption in MFU-4-type triazolate-based metal–organic frameworks featuring different pore sizes. *Chem. Eur. J.* **17**, 1837–1848 (2011).

31. P. Gütlich, E. Bill, A. X. Trautwein, *Mössbauer Spectroscopy and Transition Metal Chemistry* (Springer-Verlag, Berlin-Heidelberg, Germany, 2011).

32. D. A. Proshlyakov, T. F. Henshaw, G. R. Monterosso, M. J. Ryle, R. P. Hausinger, Direct detection of oxygen intermediates in the non-heme Fe enzyme taurine/α-ketoglutarate dioxygenase. *J. Am. Chem. Soc.* **126**, 1022–1023 (2004).

33. V. F. Oswald, J. L. Lee, S. Biswas, A. C. Weitz, K. Mittra, R. Fan, J. Li, J. Zhao, M. Y. Hu, E. E. Alp, E. L. Bominaar, Y. Guo, M. T. Green, M. P. Hendrich, A. S. Borovik, Effects of noncovalent interactions on high-spin Fe(IV)−oxido complexes. *J. Am. Chem. Soc.* **142**, 11804–11817 (2020).

34. K. Warm, A. Paskin, U. Kuhlmann, E. Bill, M. Swart, M. Haumann, H. Dau, P. Hildebrandt, K. Ray, A pseudotetrahedral terminal oxoiron(IV) complex: mechanistic promiscuity in C–H Bond oxidation reactions. *Angew. Chem. Int. Ed.* **60**, 6752–6756 (2021).

35. M. G. Thompson, J. M. Blake-Hedges, J. H. Pereira, J. A. Hangasky, M. S. Belcher, W. M. Moore, J. F. Barajas, P. Cruz-Morales, L. J. Washington, R. W. Haushalter, C. B. Eiben, Y. Liu, W. Skyrud, V. T. Benites, T. P. Barnum, E. E. K. Baidoo, H. V. Scheller, M. A. Marletta, P. M. Shih, P. D. Adams, J. D. Keasling, An iron (II) dependent oxygenase performs the last missing step of plant lysine catabolism. *Nat. Commun.* **11**, 2931 (2020).

36. V. Ksenofontov, H. Spiering, S. Reiman, Y. Garcia, A. B. Gaspar, J. A. Real, P. Gütlich, Determination of spin state in dinuclear iron(II) coordination compounds using applied field Mössbauer spectroscopy. *Hyperfine Interact.* **141**, 47–52 (2002).

37. A. R. McDonald, L. Que Jr., High-valent nonheme iron-oxo complexes: synthesis, structure, and spectroscopy. *Coord. Chem. Rev.* **257**, 414–428 (2013).

38. T. A. Jackson, J.-U. Rohde, M. S. Seo, C. V. Sastri, R. DeHont, A. Stubna, T. Ohta, T. Kitagawa, E. Münck, W. Nam, L. Que Jr., Axial ligand effects on the geometric and electronic structures of nonheme oxoiron(IV) complexes. *J. Am. Chem. Soc.* **130**, 12394–12407 (2008).

39. J. England, M. Martinho, E. R .Farquhar, J. R. Frisch, E. L. Bominaar, E. Münck, L. Que Jr., A synthetic high-spin oxoiron(IV) complex: generation, spectroscopic characterization, and reactivity. *Angew. Chem., Int. Ed.* **48**, 3622−3626 (2009).

40. N. Lee, T. Petrenko, U. Bergmann, F. Neese, S. DeBeer, Probing valence orbital composition with iron Kβ x-ray emission spectroscopy. *J. Am. Chem. Soc.* **132**, 9715–9727 (2010).

41. C. J. Pollock, M. U. Delgado-Jaime, M. Atanasov, F. Neese, S. DeBeer, Kβ mainline x-ray emission spectroscopy as an experimental probe of metal−ligand covalency. *J. Am. Chem. Soc.* **136**, 9453–9463 (2014).

42. G. E. Cutsail III, R. Banerjee, D. B. Rice, O. McCubbin Stepanic, J. D. Lipscomb, S. DeBeer, Determination of the iron(IV) local spin states of the Q intermediate of soluble

methane monooxygenase by Kβ x-ray emission spectroscopy. *J. Biol. Inorg. Chem.* **27**, 573–582 (2022).

43. C. B. Bell, S. D. Wong, Y. Xiao, E. J. Klinker, A. L. Tenderholt, M. C. Smith, J.-U. Rohde, L. Que Jr., S. P. Cramer, E. I. Solomon, A combined NRVS and DFT study of Fe^{IV}-O model complexes: a diagnostic method for the elucidation of non-heme iron enzyme intermediates. *Angew. Chem. Int. Ed.* **47**, 9071–9074 (2008).

44. A. C. Weitz, E. A. Hill, V. F. Oswald, E. L. Bominaar, A. S. Borovik, M. P. Hendrich, Y. Guo, Probing hydrogen bonding interactions to iron-oxido/hydroxido units by ^{57}Fe nuclear resonance vibrational spectroscopy. *Angew. Chem. Int. Ed.* **57**, 16010–16014 (2018).

45. B. E. R. Snyder, L. H. Böttger, M. L. Bols, J. J. Yan, H. M. Rhoda, A. B. Jacobs, M. Y. Hu, J. Zhao, E. E. Alp, B. Hedman, K. O. Hodgson, R. A. Schoonheydt, B. F. Sels, E. I. Solomon, Structural characterization of a non-heme iron active site in zeolites that hydroxylates methane. *Proc. Natl. Acad. Sci. U. S. A.* **115**, 4565−4570 (2018).

46. A. N. Biswas, M. Puri, K. K. Meier, W. N. Oloo, G. T. Rohde, E. L. Bominaar, E. Münck, L. Que Jr., Modeling TauD-*J*: A high-spin nonheme oxoiron(IV) complex with high reactivity toward C–H bonds. *J. Am. Chem. Soc.* **137**, 2428–2431 (2015).

47. J. C. Price, E. W. Barr, T. E. Glass, C. Krebs, J. M. Bollinger Jr., Evidence for hydrogen abstraction from C1 of taurine by the high-spin Fe(IV) intermediate detected during oxygen activation by taurine:α-ketoglutarate dioxygenase (TauD). *J. Am. Chem. Soc.* **125**, 13008–13009 (2003).

48. P. Meinhold, M. W. Peters, M. M. Y. Chen, K. Takahashi, F. H. Arnold, Direct conversion of ethane to ethanol by engineered cytochrome P450 BM3. *ChemBioChem* **6**, 1765–1768 (2005).

49. S. O. Nwaukwa, P. M. Keehn, The oxidation of alcohols and ethers using calcium hypochlorite [Ca(OCl)$_2$], *Tetrahedron Lett*, **23**, 35 (1982).

50. G. M. Sheldrick, SHELXT – Integrated space-group and crystal-structure determination. *Acta Crystallogr. A,* **71**, 3–8 (2015).

51. G. M. Sheldrick, SHELXT and SHELXL, University of Göttingen, Germany (2015).

52. O. V. Dolomanov, L. J. Bourhis, R. J. Gildea, J. A. K. Howard, H. Puschmann, OLEX2: a complete structure solution, refinement and analysis program. *J. Appl. Crystallogr.* **42**, 339–341 (2009).

53. A. L. Spek, PLATON SQUEEZE: a tool for the calculation of the disordered solvent contribution to the calculated structure factors. *Acta Crystallogr. C,* **71**, 9 (2015).

54. S. Stoll, A. Schweiger, EasySpin, a comprehensive software package for spectral simulation and analysis in EPR. *J. Magn. Reson.* **178** , 42–55 (2006).

55. W. Sturhahn, CONUSS and PHOENIX: Evaluation of nuclear resonant scattering data. *Hyperfine Interact.* **125**,149–172 (2000).

56. W. Sturhahn, T. S. Toellner, E. E. Alp, X. Zhang, M. Ando, Y. Yoda, S. Kikuta, M. Seto, C. W. Kimball, B. Dabrowski, Phonon density of states measured by inelastic nuclear resonant scattering. *Phys. Rev. Lett.* **74**, 3832–3835 (1995).

57. Gnuplot 5.2, An Interactive Plotting Program, Thomas Williams & Colin Kelley, (2019).

58.   C. K. Brozek, A. Ozarowski, S. A. Stoian, M. Dincă, Dynamic structural flexibility of Fe-MOF-5 rvidenced by ^{57}Fe Mössbauer spectroscopy. *Inorg. Chem. Front.* **4**, 782–788 (2017).

59.   C. Gallenkamp, U. Kramm, J. Proppe, V. Krewald, Calibration of computational Mössbauer spectroscopy to unravel active sites in FeNC catalysts for the oxygen reduction reaction. *Int. J. Quantum Chem.* **121**, e26394 (2021).

60.   E. Koch, Exchange Mechanisms. *in* Correlated electrons: From models to materials, Forschungszentrum Jülich GmbH Institute for Advanced Simulation (2012).

61.   J. B. Goodenough, Theory of the role of covalence in the perovskite-type manganites [La, *M*(II)]MnO₃. *Phys. Rev.* **100**, 564–573 (1955).

62.   J. B. Goodenough, An interpretation of the magnetic properties of the perovskite-type mixed crystals La1−xSrxCoO3−λ. J. *Phys. Chem. Solids* **6**, 287–297 (1958).

63.   J. Kanamori, Superexchange interaction and symmetry properties of electron orbitals. *J. Phys. Chem. Solids* **10**, 87–98 (1959).

64.   F. Lloret, M. Julve, J. Cano, G. De Munno, Topology and spin polarization in sheetlike metal(II) polymers: ML₂X₂ (M = Mn, Fe, Co or Ni, L = pyrimidine or pyrazine and X = NCS or NCO). *Mol. Cryst. Liquid Cryst. Science Tech. A* **334**, 569–585 (1999).

65.   F. Biaso, C. Duboc, B. Barbara, G. Serratrice, F. Thomas, D. Charapoff; C. Béguin, High-field EPR study of frozen aqueous solutions of iron(III) citrate complexes. *Eur. J. Inorg. Chem.*, 467–478 (2005).

66.   J. Telser, EPR interactions – zero-field splittings. *eMagRes* **6**, 207–234 (2017).

67.   C. E. Schulz, R. Rutter, J. T. Sage, P. G. Debrunner, Mössbauer and electron paramagnetic resonance studies of horseradish peroxidase and its catalytic iintermediates. *Biochemistry* **23**, 4743–4754 (1984).

68.   G. A. Grapperhaus, B. Mienert, E. Bill, T. Weyhermüller, K. Wieghardt, Mononuclear (nitrido)iron(V) and (oxo)iron(IV) complexes via photolysis of [(cyclam-acetato)Fe^{III}(N₃)]$^{+}$ and ozonolysis of [(cyclam-acetato)Fe^{III}(O₃SCF₃)]+ in water/acetone mixtures. *Inorg. Chem.* **39**, 5306–5317 (2000).

69.   J. F. Berry, E. Bill, E. Bothe, F. Neese, K. Wieghardt, Octahedral non-heme oxo and non-oxo Fe(IV) complexes: an experimental/theoretical comparison. *J. Am. Chem. Soc.* **128**, 13515–13528 (2006).

70.   M. Bennati, "EPR Interactions – Hyperfine Couplings." in *EPR Spectroscopy: Fundamentals and Methods*, D. Goldfarb, S. Stoll, Eds. (John Wiley & Sons, 2018), pp. 81–94.

71.   N. M. Atherton, "The anisotropic hyperfine interaction." in *Principles of Electron Spin Resonance*, (Ellis Horwood, 1993), pp. 169–223.

72.   G. Hölzer, M. Fritsch, M. Deutsch, J. Härtwig, E. Förster, Kα₁,₂ and Kβ₁,₃ x-ray emission lines of the 3d transition metals. *Phys. Rev. A* **56**, 4554–4568 (1997).

73.   F. Neese, The ORCA program system. Wiley Interdiscip. *Rev. Comput. Mol. Sci.* **2**, 73–78 (2012).

74. A. D. Becke, Density-functional thermochemistry. III. The role of exact exchange, *J. Chem. Phys.* **98**, 5648–5652(1993).

75. C. Lee, W. Yang, R. G. Parr, Development of the Colle-Salvetti correlation-energy formula into a functional of the electron density. *Phys. Rev. B* **37**, 785–789 (1988).

76. F. Weigend, R. Ahlrichs, Balanced basis sets of split valence, triple zeta valence and quadruple zeta valence quality for H to Rn: design and assessment of accuracy, *Phys. Chem. Chem. Phys.* **7**, 3297–3305 (2005).

77. A. D. Becke, Density-functional exchange-energy approximation with correct asymptotic behavior. *Phys. Rev. A* **38**, 3098–3100 (1988).

78. S. Grimme, S. Ehrlich, L. Goerigk, Effect of the damping function in dispersion corrected density functional theory. *J. Comput. Chem.* **32**, 1456–1465 (2011).

79. F. Neese, Prediction and interpretation of the ^{57}Fe isomer shift in Mössbauer spectra by density functional theory. *Inorg. Chim. Acta* **337**, 181-192 (2002).

80. M. Römelt, S. Ye, F. Neese, Calibration of modern density functional theory methods for the prediction of ^{57}Fe Mössbauer isomer shifts: meta-GGA and double-hybrid functionals. *Inorg. Chem.* **48**, 784–785 (2009).

81. P.-Å. Malmqvist, B. O. Roos, The CASSCF state interaction method. *Chem. Phys. Lett.* **155**, 189–194 (1989).

82. C. Angeli, R. Cimiraglia, J.-P. Malrieu, N-electron valence state perturbation theory: A spinless formulation and an efficient implementation of the strongly contracted and of the partially contracted variants. *J. Chem. Phys.* **117**, 9138–9153 (2002).

83. F. Neese, Definition of corresponding orbitals and the diradical character in broken symmetry DFT calculations on spin coupled systems. *J. Phys. Chem. Solids* **65**, 781–785 (2004).

84. G. A. Zhurko, Chemcraft - graphical program for visualization of quantum chemistry computations. https://chemcraftprog.com.

85. Diamond-Crystal and Molecular Structure Visualization, Crystal Impact. https://www.crystalimpact.de/diamond.

86. G. Le Caër, J. M. Dubois, Evaluation of hyperfine parameter distributions from overlapped Mössbauer spectra of amorphous alloys. *J. Phys. E: Sci. Instrum.* **12**, 1083–1090 (1979).

87. J.-U. Rohde, J.-H. In, M. H. Lim, W. W. Brennessel, .M R. Bukowski, A. Stubna, E. Münck, W. Nam, L. Que Jr., Crystallographic and spectroscopic evidence for a nonheme Fe(IV)=O complex. *Science* **299**, 1037−1039 (2003).

88. J. Kaizer, E. J. Klinker, N. Y. Oh, J.-U. Rohde, W. J. Song, A. Stubna, J. Kim, E. Münck, W. Nam, L. Que Jr., Nonheme Fe^{IV}O complexes that can oxidize the C–H bonds of cyclohexane at Room Temperature. *J. Am. Chem. Soc.* **126**, 472−473 (2004).

89. O. Pestovsky, S. Stoian, E. L. Bominaar, X. Shan, E. Münck, L. Que Jr.; A. Bakac, Aqueous Fe^{IV}=O: spectroscopic identification and oxo group exchange. *Angew. Chem. Int. Ed.* **44**, 6871−6874 (2005).

90.   J. England, Y. Guo, K. M. Van Heuvelen, M. A. Cranswick, G. T. Rohde, E. L .Bominaar, E. Münck, L. Que Jr., A more reactive trigonal bipyramidal high-spin oxoiron(IV) complex with a cis-labile site. *J. Am. Chem. Soc.* **133**, 11880−11883 (2011).

91.   D. C. Lacy, R. Gupta, K. L. Stone, J. Greaves, J. W. Ziller, M. P. Hendrich, A. S. Borovik, Formation, structure, and EPR detection of a high spin Fe^{IV}–oxo species derived from either an Fe^{III}–Oxo or Fe^{III}–OH Complex. *J. Am. Chem. Soc.* **132**, 12188−12190 (2010).

92.   G. Xue, A. T. Fiedler, M. Martinho, E. Münck, L. Que Jr., Insights into the P-to-Q conversion in the catalytic cycle of methane monooxygenase from a synthetic model system. *Proc. Natl. Acad. Sci. U. S. A.* **105**, 20615−20620 (2008).

93.   G. Xue, D. Wang, R. De Hont, A. T. Fiedler, X. Shan, E. Münck, L. Que Jr., A synthetic precedent for the $[Fe^{IV}_2(\mu\text{-O})_2]$ diamond core proposed for methane monooxygenase intermediate Q. *Proc. Natl. Acad. Sci. U. S. A.* **104**, 20713−20718 (2007).

94.   G. Xue, R. F. De Hont, E. Münck, L. Que Jr., Million-fold activation of the $[Fe_2(\mu\text{-O})_2]$ diamond core for C−H bond cleavage. *Nat. Chem.* **2**, 400−405 (2010).

95.   R. F. De Hont, G. Xue, M. P. Hendrich, L. Que Jr.; E. L. Bominaar, E. Münck, Mö ssbauer, electron paramagnetic resonance, and density functional theory studies of synthetic $S = 1/2$ Fe^{III}−O−Fe^{IV}=O complexes. Superexchange-mediated spin transition at the Fe^{IV}=O Site. *Inorg. Chem.* **49**, 8310−8322 (2010).

96.   H. Zheng, Y. Zang, Y. Dong, V. G. Young Jr., L. Que Jr., Complexes with $Fe^{III}_2(\mu\text{-O})(\mu\text{-OH})$, $Fe^{III}_2(\mu\text{-O})_2$, and $[Fe^{III}_3(\mu_2\text{-O})_3]$ cores: structures, spectroscopy, and core interconversions. *J. Am. Chem. Soc.* **121**, 2226–2235 (1999).

97.   Y. Dong, L. Que Jr.; K. Kauffmann, E. Münck, An exchange coupled complex with localized high-spin Fe^{IV} and Fe^{III} sites of relevance to cluster X of escherichia coli ribonucleotide reductase. *J. Am. Chem. Soc*. **117**, 11377−11378 (1995).

98.   M. H. Lim, J.-U. Rohde, A. Stubna, M. R. Bukowski, M. Costas, R. Y. N. Ho, E. Münck, W. Nam, L. Que Jr., An Fe^{IV}=O complex of a tetradentate tripodal nonheme ligand. *Proc. Natl. Acad. Sci. U. S. A.***100**, 3665−3670 (2003).

99.   T. K. Paine, M. Costas, J. Kaizer, L. Que Jr., Oxoiron(IV) complexes of the tris(2-pyridylmethyl)amine ligand family: effect of pyridine α-substituents. *J. Biol. Inorg. Chem.* **11**, 272−276 (2006).

100. M. S. Seo, N. H. Kim, K.-B. Cho, J. E. So, S. K. Park, M. Clemancey, R. Garcia-Serres, J.-M. Latour, S. Shaik, W. A. Nam, A mononuclear non-heme iron(IV)-oxo complex which is more reactive than cytochrome P450 model compound I. *Chem. Sci.* **2**, 1039−1045 (2011).

101. L. M. Hoffart, E. W. Barr, R. B. Guyer, J. M. Bollinger Jr., C. Krebs, Direct spectroscopic detection of a C–H-cleaving high-spin Fe(IV) complex in a prolyl-4-hydroxylase. *Proc. Natl. Acad. Sci. U. S. A*. **103**, 14738−14743 (2006).

102. D. P. Galonic, E. W. Barr, C. T. Walsh, J. M. Bollinger Jr., C. Krebs, Two interconverting Fe(IV) intermediates in aliphatic chlorination by the halogenase CytC3. *Nat. Chem. Biol.* **3**, 113−116 (2007).

103. M. L. Matthews, C. M. Krest, E. W. Barr, F. H. Vaillancourt, C. T. Walsh, M. T. Green, C. Krebs, J. M. Bollinger Jr. Substrate triggered formation and remarkable stability of the C−H bond cleaving chloroferryl intermediate in the aliphatic halogenase, SyrB2. *Biochemistry* **48**, 4331−4343 (2009).

104. B. E. Eser, E. W. Barr, P. A. Frantom, L. Saleh, J. M. Bollinger Jr., C. Krebs, P. F. Fitzpatrick, Direct spectroscopic evidence for a high-spin Fe(IV) intermediate in tyrosine hydroxylase. *J. Am. Chem. Soc.* **129**, 11334−11335 (2007).

105. E. A. Hill, A. C. Weitz, E. Onderko, A. Romero-Rivera, Y. Guo, M. Swart, E. L. Bominaar, M. T. Green, M. P. Hendrich, D. C. Lacy, A. S. Borovik, Reactivity of an Fe^{IV}–oxo complex with protons and oxidants. *J. Am. Chem. Soc.* **138**, 13143–13146 (2016).

Author contributions: K.H., J.B., and J.R.L. formulated the project. K.H. and J.B. synthesized the materials. J.B. and K.H. collected and analyzed reactivity study data. K.H. and J.B. collected and analyzed the gas adsorption data. H.K., J.W.T., and A.B.T. collected and analyzed the single-crystal x-ray diffraction data. H.Z., H.M., X.L., and J.A.R. collected and analyzed the solid-state

NMR spectra. D.J.S collected the applied-field Mössbauer data. D.J.S., K.H., J.B., K.R.M., F.G., G.J.L. and F.N. analyzed the data. D.J.S. and E.B. collected and analyzed the MCD data. K.C. and R.D.B. collected and analyzed EPR data. C.D. and J.J.U. collected and analyzed the EDX data. Z.Z. collected and analyzed the thermogravimetric analysis data. J.G.P. collected and analyzed the magnetic susceptibility data. H.Z.H.J., K.H., and J.B. collected and analyzed the IR spectra. M.V.P., H.Z.H.J., K.H., J.B., J.O., M.V., and V.C. collected and analyzed the PXRD data. J.B., K.H., E.E.A., J.Z., M.Y.H., and B.L. collected and analyzed the NRVS data. K.H., J.B., R.C.R., F.G., and G.J.L. collected and analyzed the Mössbauer spectroscopy data. J.B., K.H., D.A.P., and F.N. performed the electronic structure calculations and analyzed the results. S.P. and S.D. collected and analyzed the Fe Kβ XES data. K.H., J.B., K.R.M. and J.R.L. wrote the manuscript, and all authors contributed to revising the manuscript.

Competing interests: The University of California, Berkeley has applied for a patent (International application no. PCT/US23/70362) on the synthesis of the iron containing metal–organic frameworks and their reactivity with hydrocarbon substrates in the presence of dioxygen, on which J.B., K.H., and J.R.L. are listed as coinventors.

Data and materials availability: The supplementary materials contain complete experimental and spectral details for all new compounds reported herein. Single-crystal x-ray diffraction data have been made available free of charge from the Cambridge Crystallographic Data Centre under reference numbers CCDC 2166411 and 2166412. Powder x-ray diffraction and iron Kβ x-ray emission spectroscopy data are deposited in Dryad (https://doi.org/10.5061/dryad.wh70rxwtp).
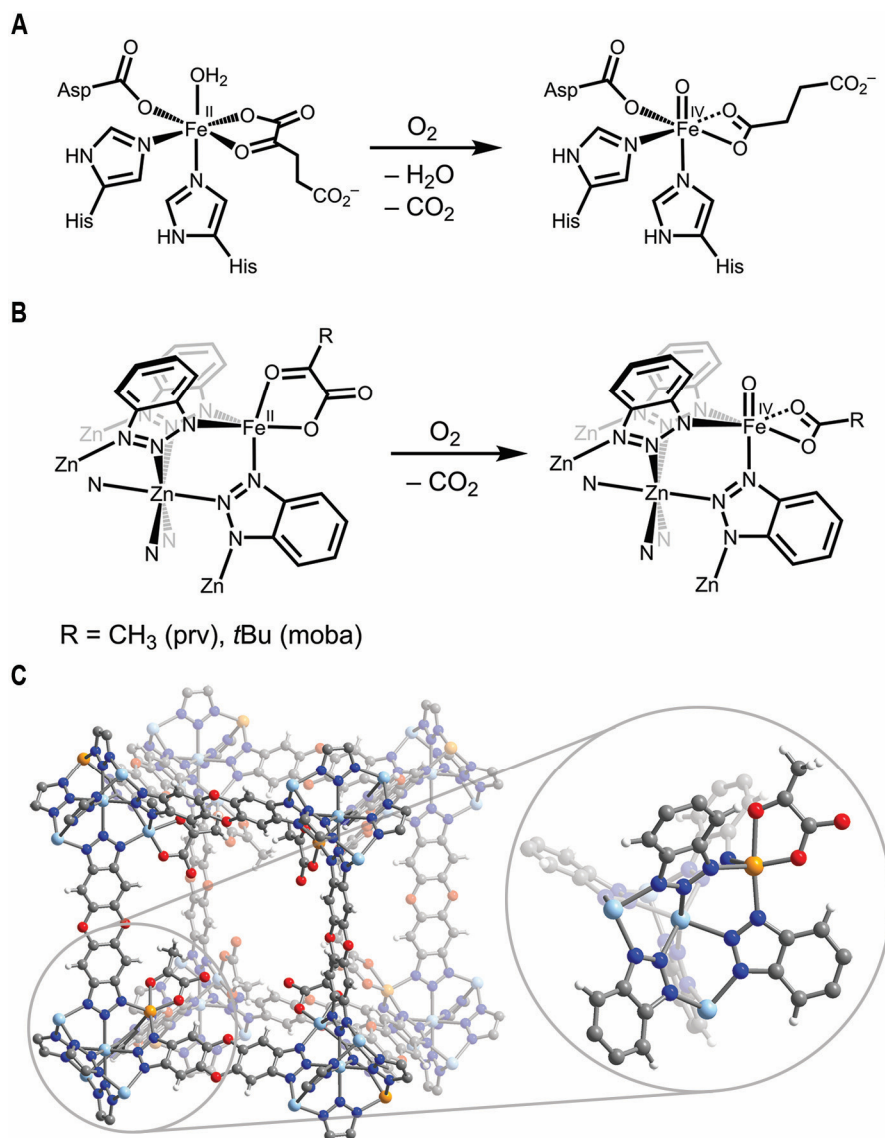
Supplementary Materials

Materials and Methods

Supplementary Text

Figs. S1 to S71

Tables S1 to S17

References (*49–105*)

Data S1 and S2 (.cif)

Fig. 1. Design of a metal–organic framework mimic of taurine–α-ketoglutarate dioxygenase (TauD). (**A**) Illustration of the local structure of the mononuclear nonheme iron(II) sites in TauD and generation of the reactive high-spin Fe(IV)=O species (TauD-***J***) via oxidation with O_2 coupled with decarboxylation of the α-ketoglutarate co-substrate. (**B**) Illustration of the local coordination environment of the iron(II) sites in $FeZn_4(prv)_4(btdd)_3$ (R = CH_3) or $FeZn_4(moba)_4(btdd)_3$ (R = *t*Bu) and observed reactivity with O_2 at low temperatures to form an Fe(IV)=O species coordinated by acetate or pivalate formed via the decarboxylation of pyruvate (prv) or 3,3-dimethyl-2-oxobutyrate (moba), respectively. (**C**) (Left) Illustration of a cubic pore within $FeZn_4(prv)_4(btdd)_3$ derived using single-crystal x-ray diffraction data obtained for $Zn_5(prv)_4(btdd)_3$ (fig. S15B) and (right) expanded view of the truncated structure of a cluster node of the framework showing the nature of the pyruvate coordination, as supported by Mössbauer, magnetic circular dichroism, and nuclear resonance vibrational spectroscopies. Light blue, orange, red, blue, gray, and white spheres represent Zn, Fe, O, N, C, and H atoms, respectively.
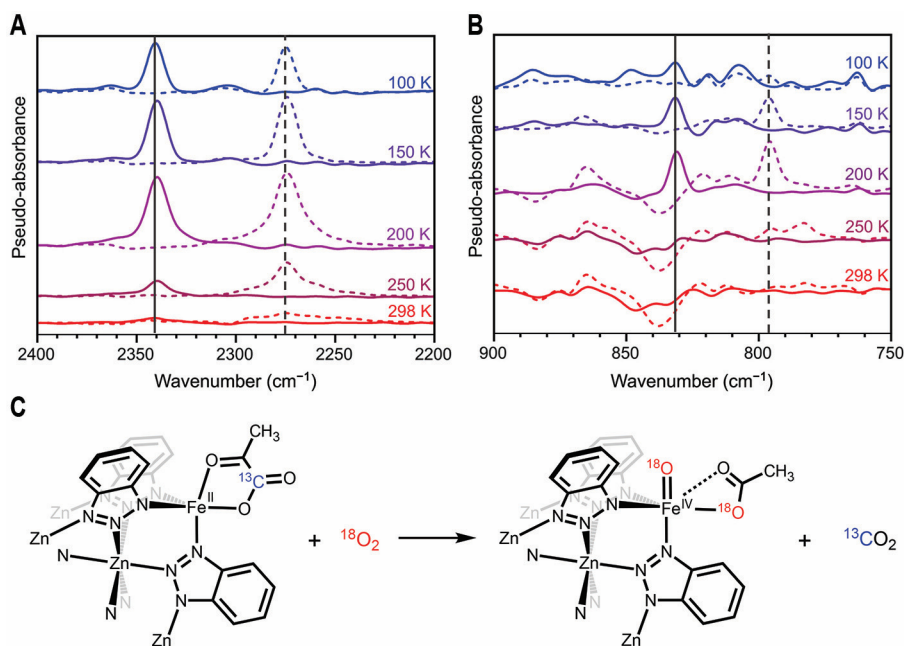
Fig. 2. Investigation of reactivity between Fe$_{1.8}$Zn$_{3.2}$(prv)$_4$(btdd)$_3$ and O$_2$ using variable-temperature *in situ* DRIFTS. (**A**) Spectra obtained after dosing Fe$_{1.8}$Zn$_{3.2}$(prv)$_4$(btdd)$_3$ with 20 mbar of O$_2$ at 100 K and gradually warming to 298 K (solid lines). The peak at 2341 cm^{-1} corresponds to CO$_2$ formed from the decarboxylation of pyruvate. This peak shifts to approximately 2275 cm^{-1} when Fe$_{1.8}$Zn$_{3.2}$(1-^{13}C-prv)$_4$(btdd)$_3$ is dosed with ^{18}O$_2$ under the same conditions (dashed lines), consistent with formation of the isotopologue ^{13}CO$_2$. (**B**) Spectra obtained as described in **A** showing the signature peaks for the iron(IV)=O species formed from the reaction between Fe$_{1.8}$Zn$_{3.2}$(prv)$_4$(btdd)$_3$ and O$_2$ (831 cm^{-1}) and Fe$_{1.8}$Zn$_{3.2}$(1-^{13}C-prv)$_4$(btdd)$_3$ and ^{18}O$_2$ (796 cm^{-1}). All data shown correspond to difference spectra obtained using the desolvated iron(II) frameworks as the background. Minor differences in the intensities of the absorption bands for the natural abundance and heavier isotopologue samples are likely due to differences in powder sample mass, sample distribution in the background matrix, and slight positioning differences in the infrared beam. (**C**) The reaction probed by DRIFTS, wherein for simplicity FeZn$_4$(1-^{13}C-prv)$_4$(btdd)$_3$ is shown to react with ^{18}O$_2$.
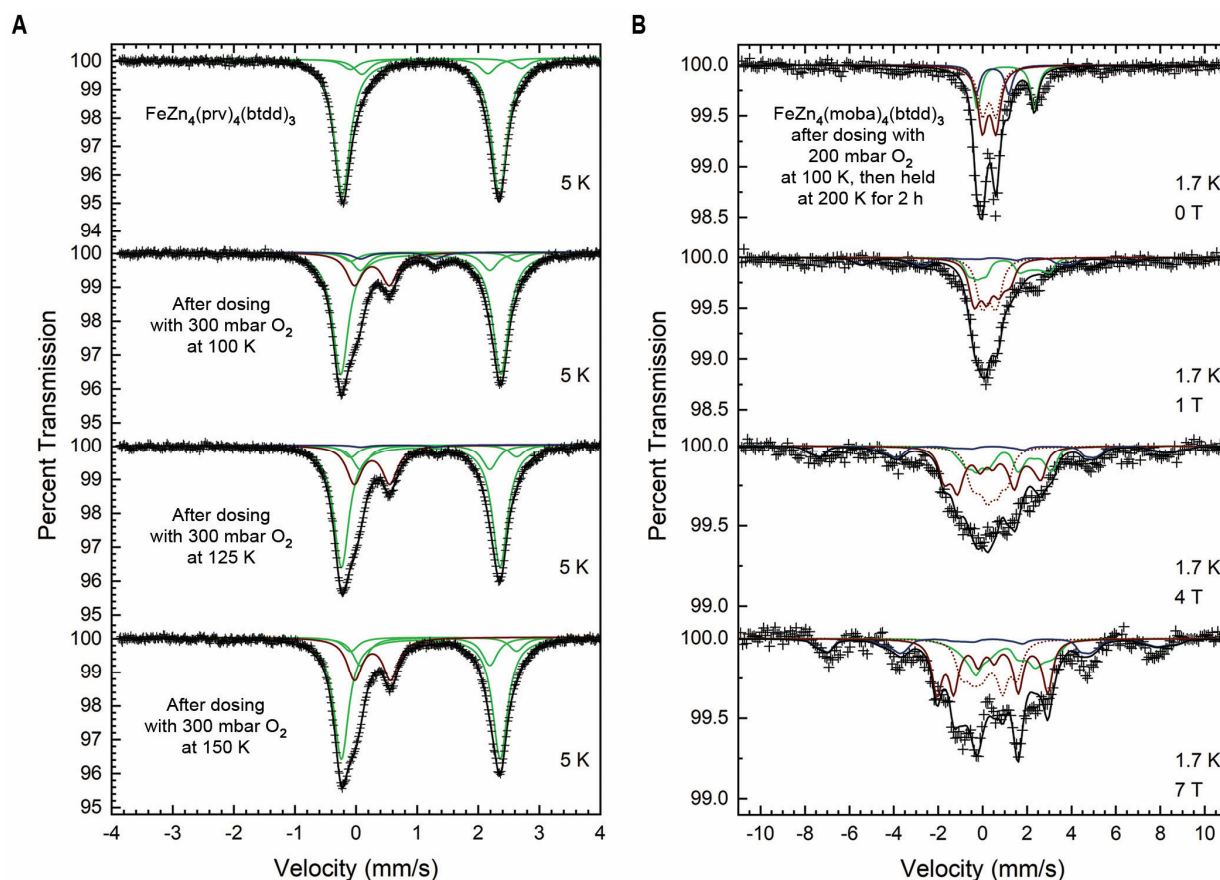
Fig. 3. *In situ* **and variable-field Mössbauer spectra.** (**A**) *In* situ Mössbauer spectra collected at 5 K for desolvated $FeZn_4(prv)_4(btdd)_3$ before and after dosing with 300 mbar of O_2 at 100, 125, and 150 K. All spectra were fit with a minimum number of symmetric quadrupole doublets, all of which have the same linewidth for a given spectrum (see fig. S22 for a timeline of the *in situ* dosing experiment). Green, blue, and dark red subspectra, respectively, are consistent with iron(II), iron(III), and iron(IV) species. (**B**) Variable magnetic field Mössbauer spectra collected at 1.7 K and the indicated fields for a sample of $FeZn_4(moba)_4(btdd)_3$ that had been dosed with 100 mbar of O_2 at 100 K, held for 2 h at 200 K and subsequently dosed with 200 mbar of O_2 at 100 K and then warmed again at 200 K for 2 h. Green, blue, dark red solid, and dark red dotted subspectra, respectively, were modeled as $S = 2$ iron(II), $S = {}^5/_2$ iron(III), isolated $S = 2$ Fe(IV)=O species, and $S = 0$ species arising from antiferromagnetic coupling between Fe(IV)=O species within the same node. The spectra were modeled as described in the main text to extract $D = 12.7(6)$ cm^{-1} and A_{iso} $= -16.4(4)$ T for the uncoupled Fe(IV)=O species (see table S13). Note, the width of the spectral splitting for the red trace at 7 T is smaller than has been observed for other $S = 2$ Fe(IV)=O species in the literature (~5 versus ~8 mm/s, respectively) (*6, 17, 33*). However, as demonstrated for another $S = 2$ Fe(IV)=O complex (*34*), a spectral splitting of about 5 mm/s can be observed if the hyperfine parameters are smaller than the isotropic Fermi-contact contribution of ~−21 T, as it is the case for $FeZn_4(moba)_4(btdd)_3$ (see also fig. S36).
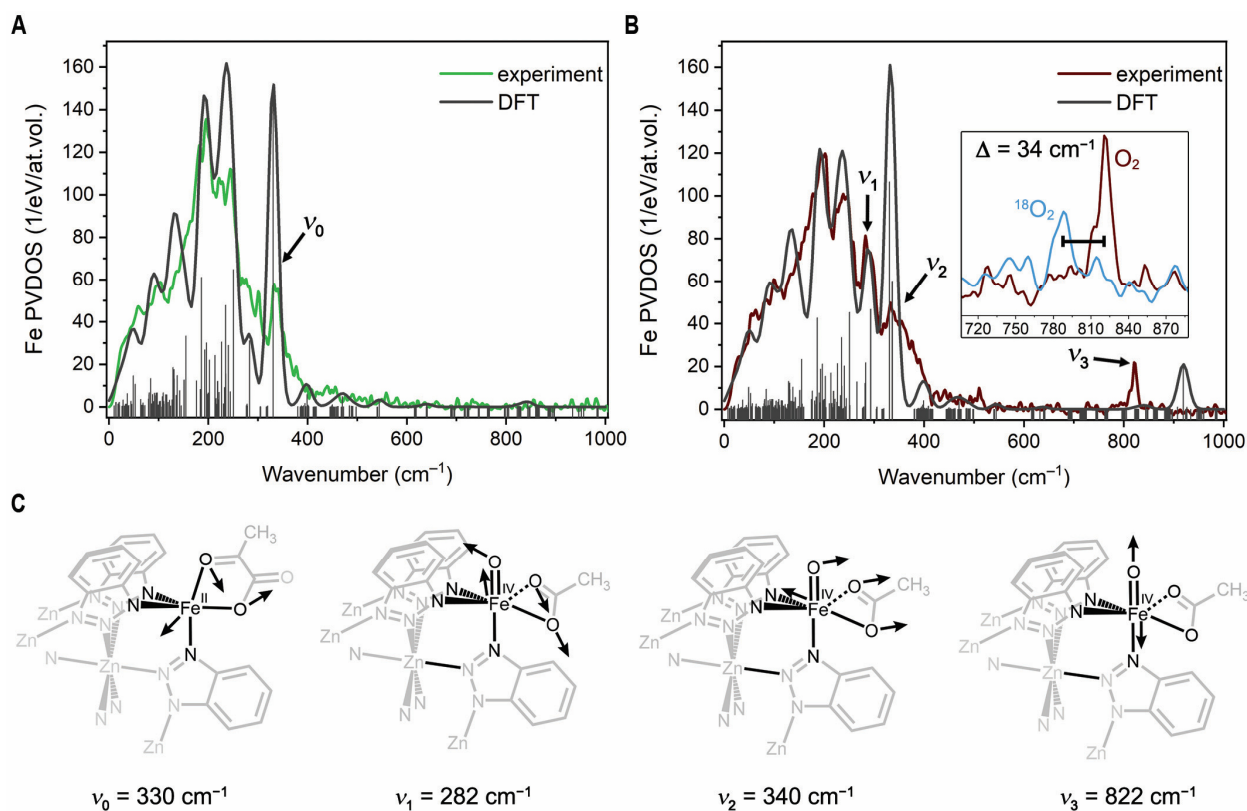
Fig. 4. Nuclear resonance vibrational spectroscopy (NRVS). (**A**) Iron partial vibrational density of states (PVDOS) distribution of ^{57}Fe-enriched, desolvated $FeZn_4(prv)_4(btdd)_3$ from NRVS data collected at ~100 K (green) and DFT computed Fe PVDOS for $FeZn_4(prv)_4(bta)_6$ (dark gray). (**B**) Iron PVDOS distribution of ^{57}Fe-enriched, desolvated $FeZn_4(prv)_4(btdd)_3$ obtained from NRVS data collected at ~100 K after dosing with 200 mbar of O_2 at 163 K (dark red) and DFT computed PVDOS distribution for ~70% $FeZn_4(prv)_4(bta)_6$ and ~30% of $Fe(O)(\kappa^2\text{-OAc})Zn_4(prv)_3(bta)_6$ (dark gray). The inset shows a shift of the Fe(IV)=O vibration to lower wavenumbers (Δ = 34 cm^{-1}) when $^{18}O_2$ is used (light blue, see also fig. S46). Vertical lines indicate the individual vibrational transitions. (**C**) Assigned vibrational modes of $FeZn_4(prv)_4(btdd)_3$ and the O_2-dosed framework.

Science

AAAS

Supplementary Materials for

Reactive high-spin iron(IV)-oxo sites through dioxygen activation in a metal–organic framework

Authors: Kaipeng Hou[1,2]†, Jonas Börgel[1,2]†, Henry Z. H. Jiang[1], Daniel J. SantaLucia[3,4], Hyunchul Kwon[1], Hao Zhuang[5,6], Khetpakorn Chakarawet[7]‡, Rachel C. Rohde[1], Jordan W. Taylor[1], Chaochao Dun[8], Maria V. Paley[1,2], Ari B. Turkiewicz[1], Jesse G. Park[1]§, Haiyan Mao[5], Ziting Zhu[2,6], E. Ercan Alp[9], Jiyong Zhao[9], Michael Y. Hu[9], Barbara Lavina[9,10], Sergey Peredkov[3], Xudong Lv[1], Julia Oktawiec[11], Katie R. Meihaus[1], Dimitrios A. Pantazis[4], Marco Vandone[12], Valentina Colombo[12], Eckhard Bill[3], Jeffrey J. Urban[2,8], R. David Britt[7], Fernande Grandjean[13], Gary J. Long[13], Serena DeBeer[3], Frank Neese[4], Jeffrey A. Reimer[2,5], Jeffrey R. Long[1,2,5]*

*Correspondence to: jrlong@berkeley.edu

This PDF file includes:

Materials and Methods
Figs. S1 to S71
Tables S1 to S17
Captions for Data S1 and S2

Other Supplementary Materials for this manuscript include the following:

Data S1 and S2 (.cif)

1. Materials, synthesis methods, and reactivity studies

1.1 General procedures. All syntheses of iron containing metal–organic frameworks were performed in a N_2-filled VAC Atmospheres or Ar-filled MBraun gloveboxes. Methanol was purchased from EMD Millipore Corporation as DriSolv grade, sparged with Ar, and dried over 3 Å molecular sieves before use. Other solvents were dried using a commercial solvent purification system designed by JC Meyer Solvent Systems. Pyruvic acid was purchased from Sigma-Aldrich, distilled, and degassed before use. Anhydrous triethylamine was purchased from Sigma-Aldrich and sparged with Ar before use. Cyclohexanone-d_{10}, used as a standard for gas chromatography, was synthesized according to a known procedure (*49*). All other reagents were obtained from commercial vendors and used without further purification. Proton NMR spectra collected for liquid samples were recorded at 25 °C with a Bruker Avance NEO 500 MHz or a Bruker Avance 600 MHz spectrometer. All chemical shifts are reported in ppm with the respective solvent residual peak as the reference. The linker H_2btdd and the framework $Zn_5Cl_4(btdd)_3$ (MFU-4*l*) were synthesized according to previously reported procedures (*29, 30*). Samples analysis with gas chromatography (GC) was performed with an Agilent Technologies 7890B GC System equipped with an Agilent 19091S-433 GC column, a flame-ionization detector (FID), and a mass selective detector (Agilent Technologies 5977A MSD). Calibration curves for quantification of reaction products with GC-FID were recorded using standard samples of cyclohexanol, cyclohexanone, cyclohexanol-d_{12}, and cyclohexanone-d_{10} dissolved in ethyl acetate. All samples were analyzed using the following GC method: the oven temperature was held at 50 °C for 3.0 min. The temperature was ramped to 150 °C with a ramp rate of 10 °C/min. The temperature was held at 150 °C for 1.5 min, resulting in a total time of 14.5 min per run.

1.2 Synthesis of $Fe_xZn_{5-x}Cl_4(btdd)_3$ (x = 1 or 1.8). To $Zn_5Cl_4(btdd)_3$ (MFU-4*l*) (0.120 g, 0.0951 mmol, 1.00 equiv) and $FeCl_2$ (50.0 mg, 0.395 mmol, 4.14 equiv for x = 1) or $FeCl_2$ (0.300 g, 2.37 mmol, 24.9 equiv for x = 1.8) in a 20 mL scintillation vial were added 20 mL *N,N*-dimethylformamide (DMF). The suspension was heated at 50 °C for 20 h. The supernatant was decanted, and the solid residue was soaked with 20 mL DMF for 12 h. This process was repeated twice with DMF, six times with CH_3OH, three times with CH_3CN, and three times with CH_2Cl_2 and the total washing time was 180 h. The supernatant was removed, and the residue was heated under dynamic vacuum at 120 °C for 6–12 h to afford the desolvated frameworks $FeZn_4Cl_4(btdd)_3$ and $Fe_{1.8}Zn_{3.2}Cl_4(btdd)_3$ as yellow solids in quantitative yield.

1.3 Synthesis of $Fe_xZn_{5-x}(prv)_4(btdd)_3$ (x = 1 or 1.8). A sample of $FeZn_4Cl_4(btdd)_3$ (0.120 g, 0.0959 mmol, 1.00 equiv) or $Fe_{1.8}Zn_{3.2}Cl_4(btdd)_3$ (0.120 g, 0.0964 mmol, 1.00 equiv) was suspended in CH_2Cl_2 (2 mL) in a 20 mL scintillation vial. To another 20 mL scintillation vial, pyruvic acid (846 mg, 9.61 mmol, 100 equiv) was added into CH_3CN (18 mL) and triethylamine (1.34 mL, 973 mg, 9.61 mmol, 100 equiv) was added. The mixture was then transferred to the 20 mL vial containing the framework suspension. After 24 h, the supernatant was decanted, and the solid residue was soaked with 20 mL CH_3CN. This process was repeated four times with CH_3CN and three times with CH_2Cl_2 and the total washing time was 36 h. The supernatant was removed, and the residue was heated under dynamic vacuum at 120 °C for 6–12 h to afford the desolvated framework $FeZn_4(prv)_4(btdd)_3$ (0.110 g, 79%) or $Fe_{1.8}Zn_{3.2}(prv)_4(btdd)_3$ (0.105 g, 75%) as light yellow powders. Analysis for $C_{48}H_{24}N_{18}O_{18}FeZn_4$: calculated: C, 39.54; H, 1.66; N, 17.29; found: C, 41.04; H, 2.23; N, 17.05. Analysis for $C_{48}H_{24}N_{18}O_{18}Fe_{1.8}Zn_{3.2}$: calculated: C, 39.75; H, 1.67; N, 17.38; found: C, 39.46; H, 2.22; N, 16.62.

1.4 Synthesis of Fe$_{1.8}$Zn$_{3.2}$(1-^{13}C-prv)$_4$(btdd)$_3$ (^{13}C-label on carboxy group). A sample of Fe$_{1.8}$Zn$_{3.2}$Cl$_4$(btdd)$_3$ (60.0 mg, 0.0482 mmol, 1.00 equiv) was suspended in CH$_2$Cl$_2$ (2 mL) in a 20 mL vial. Pyruvic-1-^{13}C acid (85.0 mg, 0.955 mmol, 19.8 equiv) was added to another 20 mL vial containing CH$_3$CN (18.0 mL), followed by addition of triethylamine (0.134 mL, 97.3 mg, 0.962 mmol, 20.0 equiv). The resulting mixture was added to the 20 mL vial containing the suspended framework. After 24 h, the supernatant was decanted, and the solid residue was soaked with 20 mL CH$_3$CN. This process was repeated four times with CH$_3$CN and three times with CH$_2$Cl$_2$ and the total washing time was 36 h. The supernatant was removed, and the residue was heated under dynamic vacuum at 120 °C for 6–12 h to afford the desolvated framework Fe$_{1.8}$Zn$_{3.2}$(1-^{13}C-prv)$_4$(btdd)$_3$ (50.0 mg, 71%) as a light yellow powder.

1.5 Synthesis of Zn$_5$(3-^{13}C-prv)$_4$(btdd)$_3$ (^{13}C-label on methyl group). Zn$_5$Cl$_4$(btdd)$_3$ (MFU-4*l*) (60.0 mg, 0.0476 mmol, 1.00 equiv) was suspended in CH$_2$Cl$_2$ (2 mL) in a 20 mL vial. Pyruvic-3-^{13}C acid (85.0 mg, 0.955 mmol, 20.1 equiv) was added to another 20 mL vial containing CH$_3$CN (18 mL), followed by addition of triethylamine (0.134 mL, 97.3 mg, 0.962 mmol, 20.0 equiv). The resulting mixture was added to the 20 mL vial containing the suspended framework. After 24 h, the supernatant was decanted, and the solid residue was soaked with 20 mL CH$_3$CN. This process was repeated four times with CH$_3$CN and three times with CH$_2$Cl$_2$ and the total washing time was 36 h. The supernatant was removed, and the residue was heated under dynamic vacuum at 120 °C for 6–12 h to afford the desolvated framework Zn$_5$(3-^{13}C-prv)$_4$(btdd)$_3$ (51.0 mg, 73%) as a light yellow powder.

1.6 Synthesis of single crystals of Zn$_5$Cl$_4$(btdd)$_3$ (MFU-4*l*). Solid H$_2$btdd (0.100 g, 0.376 mmol, 1.00 equiv) was added to a 15 mL pressure vessel with a stir bar, followed by addition of DMF (4 mL). A solution of [HDMF]$^+$[OTf]$^-$ (0.640 g, 2.87 mmol, 7.63 equiv) in DMF (1 mL) was added into the pressure vessel, and the mixture was heated to 120 °C until all solids were dissolved. The solution was then cooled to about 25 °C and anhydrous ZnCl$_2$ (0.100 mg, 0.734 mmol, 1.95 equiv) was added. The mixture was again stirred until a homogenous solution was obtained, and the stir bar was removed from the vessel. The pressure vessel was placed into a 600 mL beaker that was filled three-quarters full of copper shot, and the beaker was placed in an oven preheated to 120 °C. After 12 days at 120 °C, brown cubic crystals were obtained. The pressure vessel was taken out of the oven and placed onto a hot plate preheated to 120 °C. The crystals were transferred to a 4 mL vial preheated to 120 °C. The supernatant was decanted, and the crystals were soaked in DMF (2 mL) for 30 min. This process was repeated nine times with hot DMF. The hot plate was then set to 60 °C and the contents allowed to cool to that temperature gradually. The supernatant was decanted and the crystals were soaked in hot CH$_3$OH (2 mL). This process was repeated nine times with hot CH$_3$OH. Following these washes, the hot plate was then turned off and the crystals allowed to gradually cool to 25 °C.

1.7 Synthesis of single crystals of Zn$_5$(prv)$_4$(btdd)$_3$. Crystals of Zn$_5$Cl$_4$(btdd)$_3$ (MFU-4*l*) (approximately 2 mg) were added to CH$_3$CN (2 mL) in a 20 mL vial. Pyruvic acid (88.0 mg, 1.00 mmol) was added into CH$_3$CN (2 mL) in a 4 mL vial and triethylamine (0.139 mL, 101 mg, 1.00 mmol) was added. The resulting mixture was transferred to the 20 mL vial containing the MFU-4*l* single crystals. After a week, the supernatant was decanted, and the solid residue was soaked with 20 mL DMF for 12 h. This process was repeated two times with DMF, six times with methanol, three times with acetonitrile, three times with CH$_2$Cl$_2$, three times with benzene, and the total washing time was 216 h. The supernatant was decanted, the vial was cooled down to 195 K, and the trace benzene left in the vial was frozen. The vial was slowly warmed to ambient

3

temperature while dynamic vacuum was applied overnight to afford the desolvated single crystals of $Zn_5(prv)_4(btdd)_3$ suitable for structure elucidation by single-crystal x-ray diffraction (for detailed data collection methods, see section 2.2).

1.8 Synthesis of FeZn₄(moba)₄(btdd)₃. A sample of $FeZn_4Cl_4(btdd)_3$ (0.120 g, 0.0959 mmol, 1.00 equiv) was suspended in CH_2Cl_2 (2 mL) in a 20 mL scintillation vial. To another 20 mL scintillation vial, 3,3-dimethyl-2-oxobutanoic acid (1.25 g, 9.61 mmol, 100 equiv) was dissolved in CH_3CN (18 mL) and triethylamine (1.34 mL, 973 mg, 9.61 mmol, 100 equiv) was added. The mixture was then transferred to the 20 mL vial containing the framework suspension. After 24 h, the supernatant was decanted, and the solid residue was soaked with 20 mL CH_3CN. This process was repeated four times with CH_3CN and three times with CH_2Cl_2 and the total washing time was 36 h. The supernatant was removed, and the residue was heated under dynamic vacuum at 120 °C for 6–12 h to afford the desolvated framework $FeZn_4(moba)_4(btdd)_3$ (0.127 g, 81%) as a tan powder. Analysis for $C_{60}H_{48}N_{18}O_{18}FeZn_4$: calculated: C, 44.31; H, 2.97; N, 15.50; found: C, 43.21; H, 2.84; N, 15.75.

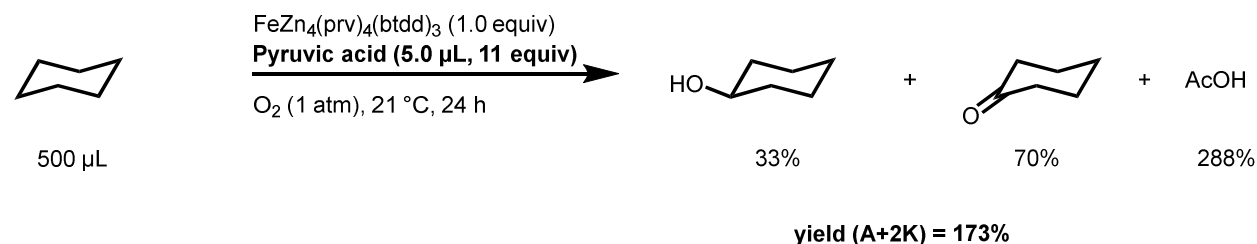**1.9 Reactivity studies of FeZn₄(prv)₄(btdd)₃ with O₂ and cyclohexane.**

1.9.1 Stoichiometric reaction
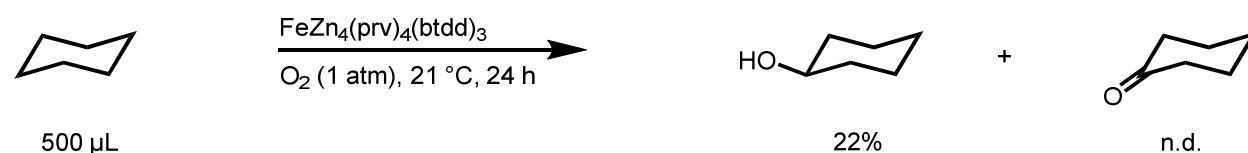
FeZn₄(prv)₄(btdd)₃

O₂ (1 atm), 21 °C, 24 h

500 µL   HO~~~   +   O~~~

                22%   n.d.
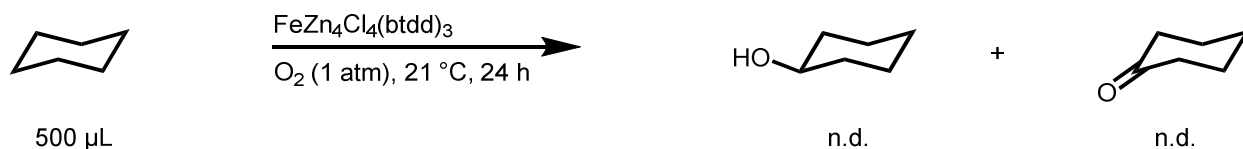
In an Ar-filled glovebox, a 20 mL scintillation vial was charged with $FeZn_4(prv)_4(btdd)_3$ (40 mg, 27 µmol, 1.0 equiv) and a magnetic stir bar. The solid was suspended in cyclohexane (0.500 mL, 4.63 mmol, 172 equiv). The vial was capped with a rubber septum, taken out of the glovebox, and cooled in a liquid N_2 bath. The headspace was then evacuated and refilled with O_2 (1 atm). The septum was replaced with a Teflon-lined cap. The mixture was allowed to warm to 21 °C and stirred for 24 h. Subsequently, CD_3CN (0.7 mL) and CH_2Br_2 (2.0 µL, 5.0 mg, 29 µmol, 5.0 equiv) were added. The mixture was allowed to stir vigorously for 10 min before it was filtered over a glass fiber filter. The filtrate was analyzed by ^1H NMR spectroscopy (d_1 = 10 s), and the yield of cyclohexanol (22%) was determined by integrating the ^1H-resonance of the proton alpha to the hydroxy group (δ = 3.47 ppm) relative to the ^1H-resonances of the internal standard CH_2Br_2 (δ = 5.09 ppm). Cyclohexanone was not detected (fig. S53). The identity of the product cyclohexanol was further confirmed by GC-MS (R_T = 7.2 min; m/z = 100, 82, 57; see fig. S54) Powder x-ray diffraction analysis of the solid isolated after the reaction confirmed that the framework remained crystalline (fig. S55). The solid material was further studied by Mössbauer spectroscopy (see section 2.9.3).

1.9.2 Catalytic reaction

FeZn₄(prv)₄(btdd)₃ (1.0 equiv)
Pyruvic acid (5.0 µL, 11 equiv)

O₂ (1 atm), 21 °C, 24 h

500 µL   HO~~~   +   O~~~   +   AcOH

                33%   70%   288%

yield (A+2K) = 173%

4

In an Ar-filled glovebox, a 20 mL scintillation vial was charged with $FeZn_4(prv)_4(btdd)_3$ (9.6 mg, 6.6 µmol, 1.0 equiv) and a magnetic stir bar. The solid was suspended in cyclohexane (0.500 mL, 4.63 mmol, 702 equiv). The vial was capped with a rubber septum and taken out of the glovebox. Under a stream of Ar, pyruvic acid (5.0 µL, 6.3 mg, 72 µmol, 11 equiv) was added and the mixture was cooled using liquid N_2. The headspace was then evacuated and refilled with O_2 (1 atm). The septum was replaced with a Teflon-lined cap. The mixture was allowed to warm to 23 °C and stirred for 24 h. Subsequently, CD_3CN (0.7 mL) and CH_2Br_2 (2.0 µL, 5.0 mg, 29 µmol, 4.4 equiv) were added. The mixture was allowed to stir vigorously for 10 min before it was filtered over a glass fiber filter. The filtrate was analyzed by ^1H NMR spectroscopy (d_1 = 10 s), and the yield of cyclohexanol (A) (33%) was determined by integrating the ^1H-resonance of the proton alpha to the hydroxy group (δ = 3.47 ppm) relative to the ^1H-resonances of the internal standard CH_2Br_2 (δ = 5.09 ppm). The yield of cyclohexanone (K) (70%) was determined by integrating the ^1H-resonance of the protons alpha to the ketone (δ = 2.28 ppm) relative to the ^1H-resonances of the internal standard CH_2Br_2 (δ = 5.09 ppm). The overall yield (A + 2K) is 173% with a ratio A:K = 2.1:1.0. The yield of acetic acid (288%) was determined by integrating the ^1H-resonance of the protons of the methyl group (δ = 1.96 ppm) relative to the ^1H-resonances of the internal standard CH_2Br_2 (δ = 5.09 ppm) (fig. S64). Powder x-ray diffraction analysis of the solid isolated after the reaction confirmed that the framework remained crystalline (fig. S65).

1.9.3 Control experiment with $FeZn_4Cl_4(btdd)_3$

In an Ar-filled glovebox, a 20 mL scintillation vial was charged with $FeZn_4Cl_4(btdd)_3$ (10 mg, 8.0 µmol, 1.0 equiv) and a magnetic stir bar. The solid was suspended in cyclohexane (0.500 mL, 4.63 mmol, 798 equiv). The vial was capped with a rubber septum, taken out of the glovebox, and cooled in a liquid N_2 bath. The headspace was then evacuated and refilled with O_2 (1 atm). The septum was replaced with a Teflon-lined cap. The mixture was allowed to warm to 21 °C and stirred for 24 h. Subsequently, CD_3CN (0.7 mL) and CH_2Br_2 (2.0 µL, 5.0 mg, 29 µmol, 5.0 equiv) were added. The mixture was allowed to stir vigorously for 10 min before it was filtered over a glass fiber filter. The filtrate was analyzed by ^1H NMR spectroscopy (d_1 = 10 s) and GC-MS. The expected products, cyclohexanol and cyclohexanone, were not observed (figs. S57 and S58).

1.10 Kinetic isotope effect study with cyclohexane. In an Ar-filled glovebox, a 20 mL scintillation vial was charged with $FeZn_4(prv)_4(btdd)_3$ (14.7 mg, 10.1 µmol, 1.00 equiv) and a magnetic stir bar. Cyclohexane (0.200 mL, 1.92 mmol, 190 equiv) and cyclohexane-d_{12} (0.200 mL, 1.92 mmol, 190 equiv) were added, and the vial was closed with a rubber septum. The vial was taken out of the glovebox and frozen in liquid N_2. Under a stream of Ar, 0.5 mL of dry, degassed CD_3CN were added to the vial. The headspace was evacuated and refilled with O_2 (1 bar) at −196 °C. The septum was replaced by a Teflon-lined cap and the vial was transferred to an ice/NaCl bath (T = −5 to −10 °C). The mixture was stirred for 2 h. Subsequently, while the mixture was still cold, CH_2Br_2 (2.0 µL, 5.0 mg, 29 µmol, 2.9 equiv) was added, and the reaction mixture was filtered over celite in air. Analysis by ^1H NMR spectroscopy confirmed the formation of cyclohexanol and cyclohexanone (fig. S67). Ethyl acetate (1 mL) was added, the mixture was filtered over silica, and analyzed by GC-FID. The competition kinetic isotope effect was

determined using equation (1), for which the compound concentrations were calculated from the respective peak areas and the calibration curves for each product (fig. S66).

$$\text{KIE}(i) = \frac{k_H}{k_D} = \frac{c_{cyclohexanol} + c_{cyclohexanone}}{c_{cyclohexanol-d_{12}} + c_{cyclohexanone-d_{10}}} \tag{1}$$

The kinetic isotope effect experiment was run in triplicate. KIE(1) = 28.7; KIE(2) = 31.8; KIE(3) = 28.8. Final KIE and standard error: KIE = 29.8 ± 1.04.
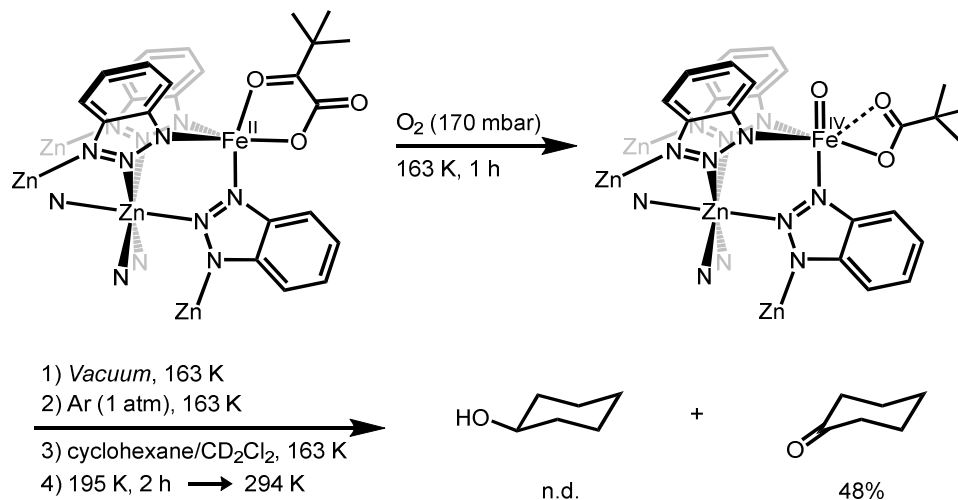
1.11 Reactivity studies of FeZn$_4$(moba)$_4$(btdd)$_3$ with O$_2$ and cyclohexane.

1.11.1 Stoichiometric reaction

500 µL   51%   n.d.
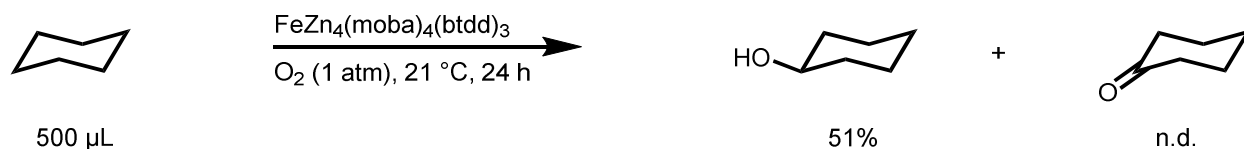
In an Ar-filled glovebox, a 20 mL scintillation vial was charged with FeZn$_4$(moba)$_4$(btdd)$_3$ (11 mg, 6.7 µmol, 1.0 equiv) and a magnetic stir bar. The solid was suspended in cyclohexane (0.500 mL, 4.63 mmol, 691 equiv). The vial was capped with a rubber septum, taken out of the glovebox, and cooled in a liquid N$_2$ bath. The headspace was then evacuated and refilled with O$_2$ (1 atm). The septum was replaced with a Teflon-lined cap. The mixture was allowed to warm to 21 °C and stirred for 20 h. Subsequently, CD$_2$Cl$_2$ (0.7 mL) and CH$_2$Br$_2$ (2.0 µL, 5.0 mg, 29 µmol, 4.3 equiv) were added. The suspension was allowed to stir vigorously for 10 min before it was filtered over a glass fiber filter. The filtrate was analyzed by ^{1}H NMR spectroscopy (d_1 = 10 s), and the yield of cyclohexanol (51%) was determined by integrating the ^{1}H-resonance of the proton alpha to the hydroxy group (δ = 3.62 ppm) relative to the ^{1}H-resonances of the internal standard CH$_2$Br$_2$ (δ = 4.97 ppm). Cyclohexanone was not detected (fig. S59). The identity of the product cyclohexanol was further confirmed by GC-MS (R_T = 7.2 min; m/z = 100, 82, 57) alongside the identity of the by-product pivalic acid (R_T = 5.8 min; m/z = 102, 87, 69, 57). (fig. S60). Powder x-ray diffraction analysis of the solid isolated after the reaction confirmed that the framework remained crystalline (fig. S63).

1.11.2 Sequential reaction with O$_2$ and cyclohexane.

1) *Vacuum*, 163 K
2) Ar (1 atm), 163 K

3) cyclohexane/CD$_2$Cl$_2$, 163 K
4) 195 K, 2 h → 294 K

HO   +

n.d.   48%

In an Ar-filled glovebox, a flame-dried 25 mL Schlenk-tube was charged with $FeZn_4(moba)_4(btdd)_3$ (25 mg, 15 µmol, 1.0 equiv). The reaction vessel was capped with a Teflon screw cap, taken out of the glovebox, and cooled to 163 K. The Schlenk-tube was evacuated and subsequently dosed with O_2 (170 mbar) for 1 h at 163 K using a custom-made Swagelok gas dosing manifold (fig. S30). The headspace was evacuated at 163 K, and the Schlenk-tube was refilled with Ar (1 atm). A mixture of dry and degassed cyclohexane (0.30 mL, 2.8 mmol, 187 equiv) in dry and degassed CD_2Cl_2 (0.7 mL) was added under Ar, and the flask was allowed to warm up to 195 K for 1 h. In a period of 19 h, the reaction was allowed to warm up to 294 K. Under Ar, CH_2Br_2 (2.0 µL, 5.0 mg, 29 µmol, 1.9 equiv) was added. The tube was shaken, and the suspension was filtered over a glass fiber filter into an NMR sample tube under Ar. The filtrate was analyzed by ^{1}H NMR spectroscopy (d_1 = 10 s), and the yield of cyclohexanone (48%) was determined by integrating the ^{1}H-resonance of the protons alpha to the carbonyl group (δ = 2.33 ppm) relative to the ^{1}H-resonances of the internal standard CH_2Br_2 (δ = 4.97 ppm). Cyclohexanol was not detected. (fig. S61) The identity of the product cyclohexanone was further confirmed by GC-MS (R_T = 7.4 min; m/z = 98, 69, 55) (fig. S62). Powder x-ray diffraction analysis of the solid isolated after the reaction confirmed that the framework remained crystalline (fig. S63).

1.12 Reactivity studies of $Fe_{1.8}Zn_{3.2}(prv)_4(btdd)_3$ with O_2 and C_2H_6.
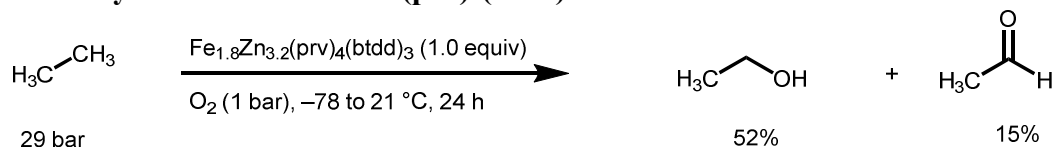
yield (ethanol + 2 × acetaldehyde) = 82%

In a batch reactor experiment, desolvated $Fe_{1.8}Zn_{3.2}(prv)_4(btdd)_3$ (10.0 mg, 12.4 µmol, 1.00 equiv) was loaded into a 25 mL Parr bomb reactor in an Ar-filled glovebox. The reactor was then removed from the glovebox and connected to a custom-made Swagelok dosing manifold (fig. S30). Dynamic vacuum was applied, and the reactor was cooled with a dry ice/acetone bath for 10 min. Subsequently, 1 bar O_2 and 29 bar C_2H_6 were pre-mixed in the manifold and dosed into the reactor. After 12 hours, the products extracted with CD_3CN and CH_2Br_2 (2.0 µL, 5.0 mg, 29 µmol, 2.3 equiv) was added as internal standard. The resulting mixture was filtered over glass fiber. The filtrate was analyzed by ^{1}H NMR spectroscopy, and the yield of ethanol (52%) was determined by integrating the ^{1}H-resonance of the proton alpha to the hydroxy group (δ = 3.54 ppm) relative to the ^{1}H-resonances of the internal standard CH_2Br_2 (δ = 5.09 ppm). The yield of acetaldehyde (15%) was determined by integrating the ^{1}H-resonance of the aldehyde proton (δ = 9.69 ppm) relative to the ^{1}H-resonances of the internal standard CH_2Br_2 (δ = 5.09 ppm). The overall yield (ethanol + 2 × acetaldehyde) was 82% with a ratio ethanol:acetaldehyde = 3.5:1.0 (fig. S68). Powder x-ray diffraction analysis of the solid isolated after the reaction confirmed that the framework remained crystalline (fig. S70). As a control, a sample of the same batch of $Fe_{1.8}Zn_{3.2}(prv)_4(btdd)_3$ was exposed to air, extracted with CD_3CN, and treated as described above. No ethanol or acetaldehyde were detected by ^{1}H NMR spectroscopy (fig. S69).

2. Experimental analysis

2.1 Gas-adsorption measurements. Gas adsorption isotherms were measured by a volumetric method using a Micromeritics ASAP2420 instrument. In an Ar-filled glovebox, a typical sample of about 50 mg was transferred to a pre-weighed analysis tube, which was capped with a transeal

and evacuated by heating at 120 °C under dynamic vacuum (<1.3 μbar) for about 6–12 h. The evacuated analysis tube containing the degassed sample was then transferred to an electronic balance and weighed again to determine the mass of sample. The tube was then transferred back to the analysis port of the gas adsorption instrument. For all isotherms, warm and cold free space correction measurements were performed using ultra-high purity He gas (UHP grade 5.0, 99.999% purity); N_2 isotherms at 77 K were measured in liquid N_2 with UHP-grade gas sources.

2.2 Single-crystal x-ray diffraction analysis. Single-crystal x-ray diffraction data were collected as follows: data collection was performed on a single crystal coated with Paratone-N oil and mounted on a Kapton loop. During measurements, the crystal was frozen at 100 K under a stream of N_2. Data were collected using a Rigaku XtaLAB P200 instrument equipped with a MicroMax-007 HF microfocus rotating anode and a Pilatus 200K hybrid pixel array detector using monochromated Cu Kα radiation (λ = 1.54184 Å). CrysAlisPro was used for the data collection and data processing, including a multi-scan absorption correction applied using the SCALE3 ABSPACK scaling algorithm within CrysAlisPro. Initial structure solutions were found via Intrinsic Phasing by SHELXT (*50*), and the resulting structures were refined through least-square refinement against F_2 by SHELXL (*51*), as implemented in OLEX2 crystallographic software (*52*). Solvent mask, as implemented in OLEX2 (analogous to SQUEEZE), was used to remove residual electron density in the pore (*53*). The structures have been deposited to the Cambridge Crystallographic Data Centre (CCDC), with deposition numbers 2166411 and 2166412 for $Zn_5Cl_4(btdd)_3$ and $Zn_5(prv)_4(btdd)_3$, respectively.

The cubic metal–organic framework $Zn_5Cl_4(btdd)_3$ crystallizes in the $Fm\bar{3}m$ space group (no. 225) with the unit cell parameters $a = b = c = 30.9085(3)$ Å, $V = 29528.0(5)$ Å^3 (table S1). The pentanuclear zinc nodes are bridged by btdd^{2-} ligands, and one chloride ligand binds to each peripheral Zn center (see fig. S15). In the asymmetric unit, there are two types of Zn (Zn1 and Zn2), two types of N (N1 and N2), three types of C (C1, C2, and C3), one O (O1), and one H (H2) on sp^2 C2 atom from the framework and one type of chloride. In the structure, all non-hydrogen atoms were refined anisotropically. The hydrogen atom on C2 was manually placed with DFIX restraints (DFIX 0.95 C2 H2, DFIX 2.1 H2 C3). No alert A or B was found in the checkcif file.

The cubic metal–organic framework $Zn_5(prv)_4(btdd)_3$ crystallizes in the $Fm\bar{3}m$ space group with the unit cell parameters $a = b = c = 30.7107(2)$ Å, $V = 28964.7(8)$ Å^3 (table S2). The pentanuclear zinc nodes are bridged by btdd^{2-} ligands, and one pyruvate binds to each peripheral Zn center (see fig. S15). The asymmetric unit shows a similar composition of atoms than the $Zn_5Cl_4(btdd)_3$ framework except that the chloride ligand is replaced by pyruvate. For the pyruvate ligand, there are three types of C (C4, C5, and C6), three types of O (O2, O3, and O4), and two types of H (H6A and H6B), which are bound to the sp^3-hybridized C6 atom. In the structure, all non-hydrogen atoms were refined anisotropically. Due to severe disorder of the pyruvate ligand, several restraints are applied for the oxygen and carbon atoms (DFIX 1.5 C6 C5, DFIX 1.23 C5 O3, DFIX 1.21 O4 C4, DFIX 1.28 C4 O2, DANG 2.41 C6 O3, DANG 2.63 C6 C4, DELU C6 C4 O2 O4, SIMU O4 C4 C6 O2). The hydrogen atoms on C6 and C2 atoms were manually placed with DFIX and DANG restraints (DFIX 0.95 C2 H2, DFIX 0.96 C6 H6B, DFIX 0.96 C4 H4A, DFIX 0.96 C6 H6A, DANG 1.95 H6B C5, DANG 1.95 H6A C5). In the checkcif file, two B alerts (PLAT242_ALERT_2_B and PLAT242_ALERT_2_B) were found because the structure is largely disordered.

2.3 Solid-state magic angle spinning (MAS) NMR spectroscopy. Desolvated $Zn_5(3\text{-}^{13}C\text{-prv})_4(btdd)_3$ was loaded into rotors in an Ar-filled glovebox. The ^{1}H solid-state NMR experiment

was performed at 16.4 T using a Bruker 3.2 mm probe with a MAS rate of 25 kHz. ^{13}C and ^{1}H → ^{13}C HETCOR experiments were acquired at 11.7 T using a Bruker 4 mm probe, and with TPPM ^{1}H decoupling scheme at 66 kHz and 83 kHz RF field strength, respectively, and a MAS rate of 10 kHz. The contact time in the ^{1}H → ^{13}C HETCOR experiment was 100 μs. The ^{1}H and ^{13}C chemical shifts were referenced to 1.8 ppm (adamantane) and 38.5 ppm (adamantane tertiary carbon, left-hand resonance), respectively.

2.4 Dc magnetic susceptibility measurements. Samples were prepared by adding microcrystalline powder to a 5-mm i.d. 7-mm o.d. quartz tube containing a raised quartz platform. These samples include desolvated $Fe_{1.8}Zn_{3.2}Cl_4(btdd)_3$ (23.2 mg, 0.0186 mmol) and $Fe_{1.8}Zn_{3.2}(prv)_4(btdd)_3$ (27.1 mg, 0.0187 mmol) powders. The sample powders were restrained with a plug of compacted glass wool to prevent crystallite torquing during measurements. The quartz tubes were transferred to a Schlenk line and evacuated until the internal pressure reached 30 mTorr. The tubes were then cooled in liquid N_2 and flame-sealed under static vacuum. All magnetic measurements were performed using a Quantum Design MPMS2 SQUID magnetometer from 3 to 300 K using a dc magnetic field of 1 T. Diamagnetic corrections were applied to the data using Pascal's constants to give $\chi_D = -0.000622095$ emu/mol for $Fe_{1.8}Zn_{3.2}Cl_4(btdd)_3$ sample and $\chi_D = -0.000725295$ emu/mol for $Fe_{1.8}Zn_{3.2}(prv)_4(btdd)_3$ sample. Variable-temperature dc magnetic susceptibility data were collected between 3–300 K under a dc field of 1 T and plotted as molar susceptibility times temperature ($\chi_M T$) versus temperature (fig. S11). At 300 K, $Fe_{1.8}Zn_{3.2}Cl_4(btdd)_3$ exhibits a $\chi_M T$ value of 6.36 emu·K/mol, which is in reasonable agreement with the expected value (5.4 emu·K/mol) for 1.8 equivalents of magnetically noninteracting high-spin ($S = 2$) Fe^{II} with $g = 2$. In contrast, the predicted $\chi_M T$ value for isolated low-spin ($S = 0$) Fe^{II}, low-spin ($S = 1/2$) Fe^{III}, and high-spin ($S = 5/2$) Fe^{III} centers are 0, 0.675, and 7.875 emu·K/mol, respectively. Below 150 K, the decrease in $\chi_M T$ value with decreasing temperature may be attributed to antiferromagnetic interactions between Fe^{II} ions. Upon ligand exchange, $Fe_{1.8}Zn_{3.2}(prv)_4(btdd)_3$ exhibits a $\chi_M T$ value of 4.94 emu·K/mol at 300 K, suggesting that the Fe centers remain in the high-spin ($S = 2$) Fe^{II} electronic configuration. Similarly, $\chi_M T$ decreases gradually with temperature followed by a sharp downturn below 50 K, indicating antiferromagnetic interactions between Fe^{II} ions at low temperatures.

2.5 EPR spectroscopy. Microcrystalline $Fe_xZn_{5-x}(prv)_4(btdd)_3$ ($x = 1.0$ or 1.8) and $FeZn_4(moba)_4(btdd)_3$ were loaded into 4 mm EPR tubes capped with J-Young adapters. Continuous-wave X-band EPR spectra were collected on the Bruker Biospin EleXsys E500 spectrometer with a dual mode cavity (ER4116DM) in parallel mode. Cryogenic temperatures were achieved and controlled using an ESR900 liquid helium cryostat in conjunction with a temperature controller (Oxford Instruments ITC503) and gas flow controller. Measurement conditions for $Fe_{1.8}Zn_{3.2}(prv)_4(btdd)_3$: temperature, 5 K; microwave frequency, 9.403 GHz; microwave power, 5.0 mW; modulation frequency, 100 kHz; modulation amplitude, 0.9 mT. Measurement conditions for $FeZn_4(prv)_4(btdd)_3$: temperature, 5 K; microwave frequency, 9.399 GHz; microwave power, 2.0 mW; modulation frequency, 100 kHz; modulation amplitude, 0.3 mT. Simulations of all EPR spectra were generated using the Easyspin 6.0.0 toolbox in the Matlab R2021b software suite (Mathworks Inc., Natick, MA) (*54*). Measurement conditions for $FeZn_4(moba)_4(btdd)_3$: temperature, 5 K; microwave frequency, 9.399 GHz; microwave power, 2.0 mW; modulation frequency, 100 kHz; modulation amplitude, 0.3 mT. After initial measurement, the sample was cooled down to 163 K, evacuated, dosed with 200 mbar of O_2 for 30 min, and measured at 5, 10, 20, and 30 K (fig S41).

2.6 *In situ* diffuse reflectance infrared spectroscopy. *In situ* diffuse reflectance infrared Fourier transform spectroscopy (DRIFTS) data were collected using a Bruker Vertex 70 spectrometer equipped with a glowbar source, KBr beamsplitter, and a liquid N_2 cooled mercury-cadmium-telluride detector. A custom-built diffuse reflectance system with an IR-accessible gas dosing cell was used for all measurements. The atmosphere over the sample was controlled by an ASAP 2020 PLUS and the temperature was controlled by an Oxford Instruments OptistatDry cryostat. In a typical gas dosing experiment, desolvated framework was dispersed in dry diamond powder in an Ar-filled glovebox, cooled down to 100 K, and evacuated at 100 K overnight. Spectra were collected *in situ* under O_2 gas and $^{18}O_2$ gas (~20 mbar for each experiment) at 4 cm^{-1} resolution at 100 K and additional spectra were collected at various intervals with increasing temperature up to 298 K as discussed in the main text. Spectra of the pristine iron(II) frameworks were subtracted as backgrounds.

2.7 Nuclear resonance vibrational spectroscopy (NRVS). Samples of desolvated 95% ^{57}Fe enriched $FeZn_4(prv)_4(btdd)_3$ (~10 mg) and $FeZn_4(moba)_4(btdd)_3$ (~10 mg) were loaded into custom-made screw-top high-density polyethylene NRVS cells in an Ar-filled glovebox. The iron(II) reference samples were sealed, put in 20 mL vials, removed from the glovebox, and shipped to the beamline. For the preparation of O_2-dosed samples, NRVS cells were loaded in the glovebox in the same way as described above, left partially open, placed into a gas-tight drying chamber, and removed from the glovebox. The drying chamber was connected to a customized Swagelok gas dosing manifold (fig. S30). Vacuum was applied, and the vacuum chamber cooled with a liquid N_2/ethanol bath to 163 K. Subsequently, for $FeZn_4(prv)_4(btdd)_3$, the sample was dosed with 200 mbar O_2 (or $^{18}O_2$), and the temperature was held at 163 K for 2 h, and for $FeZn_4(moba)_4(btdd)_3$, the sample was dosed with 60 mbar O_2 (or $^{18}O_2$), and the temperature was held at 163 K for 1 h. Excess O_2 was then removed, and the vacuum chamber was filled with Ar. The cell was quickly removed from the Ar chamber in air, and the screw-top of the cell was tightened. The cell was quickly transferred into a liquid N_2-cooled dry shipper and shipped to the beamline overnight. Spectra were collected at the Advanced Photon Source (APS) at Argonne National Laboratory at beamline 3-ID-B. The samples were mounted cold from a liquid N_2 bath directly into the sample cryostat, which was held at 10–15 K, resulting in sample temperatures of approximately 100 K. NRVS data for each sample was acquired in 9–22 scans with 3 s/point at 36 min per scan with a scan range between −50 meV to 130 meV around the resonance peak. For the O_2-dosed sample, the sample cell was removed from the cryostat, warmed to 298 K, and re-inserted into the cryostat for further data collection. The Phoenix 3.0.4 software package was used to add the scans, correct for background counts, subtract the resolution function, and generate the iron partial vibrational density of states (PVDOS) distribution plots (*55*, *56*).

2.8 Powder x-ray diffraction studies.

2.8.1. *General*. Standard diffraction patterns were collected with 0.01° steps using a Bruker AXS D8 Advance diffractometer equipped with Cu−Kα radiation (λ = 1.5418 Å), a Göbel mirror, a Lynxeye linear position-sensitive detector, and the following optics: fixed divergence slit (0.6 mm), receiving slit (3 mm), and secondary beam Soller slits (2.5°). The generator was set at 40 kV and 40 mA. Samples were loaded on zero background sample holders.

High-resolution powder x-ray diffraction patterns were collected at Beamline 17-BM-B at the Advanced Photon Source (APS) at Argonne National Laboratory. The diffraction patterns were collected between 100 and 298 K with wavelengths of 0.45191 Å or 0.45213 Å. Scattered intensity

was recorded by a Varex 4343CT a-Si Flat Panel detector. Owing to the large number of data collected, all diffraction patterns were rebinned to a step size of 0.005° in 2θ.

2.8.2 *In situ* O_2 dosing at APS. Approximately 3 mg desolvated framework was loaded into a borosilicate glass capillary of 1.0 mm diameter under a N_2 atmosphere and cooled to 100 K under vacuum. A diffraction pattern was taken at this temperature as a reference. The sample was then dosed with 80 mbar of O_2 at 100 K and diffraction patterns were collected at set temperature intervals as the sample was heated to 298 K (ramp rate of 6 K per min) (figs. S24 and S27).

2.9 Mössbauer spectroscopy.

2.9.1 *In situ* spectroscopy. In place of the typical He connection, a custom-made Swagelok dosing manifold (fig. S30) was connected to an O_2 cylinder, He cylinder, a vacuum pump, and the Mössbauer instrument. About 50 mg desolvated $FeZn_4(prv)_4(btdd)_3$ was placed in between two stacked nylon washers and sealed between three layers of commercially available Scotch tape in an Ar-filled glovebox. The sample thus prepared was transferred into the Mössbauer chamber, in which approximately 150 mbar of He was dosed at 100 K. The sample was then cooled down to 5 K. A spectrum was collected for the desolvated sample at 5 K with a constant acceleration spectrometer, which utilized a rhodium matrix ^{57}Co-source. The absorber contained approximately 50 mg/cm^2 of powder. After data collection on the parent framework, the temperature was raised to 100 K, gaseous He was removed under vacuum, and subsequently 300 mbar O_2 was dosed into the chamber, and the sample was held at this temperature for 16 h. After this period, unreacted O_2 was removed from the sample headspace by applying dynamic vacuum, 150 mbar He was dosed at 100 K, and the sample was then cooled to 5 K for data collection. This process of dosing with O_2 and data collection at 5 K was repeated for a dosing temperature of 125 K at 300 mbar O_2, 150 K and 300 mbar O_2, 150 K and 600 mbar O_2, and 163 K and 300 mbar O_2. The sample was then warmed to 250 K, held for 2 h, and then cooled to 5 K for data collection. This process was repeated with warming to 298 K. A detailed timeline of the experiment is shown in fig. S22. All isomer shifts are reported relative to 27 μm α–iron foil at 295 K. Fits were generated with gnuplot 5.2, which calculates statistical uncertainties from the variance-covariance matrix after the final iteration (*57*).

2.9.2 *Ex situ* spectroscopy. In an Ar-filled glovebox, about 50 mg desolvated $FeZn_4(prv)_4(btdd)_3$ was filled into a plastic Mössbauer cell, which was placed in a 20 mL vial. The 20 mL vial was placed into a gas-tight drying chamber and removed from the glovebox. The drying chamber was connected to a customized Swagelok gas dosing manifold (fig. S30). Vacuum was applied, and the vacuum chamber cooled with a liquid N_2/ethanol bath to 163 K. Subsequently, the sample was dosed with 200 mbar O_2, and the temperature was held at 163 K for 2 h. Excess O_2 was removed, and the vacuum chamber was filled with Ar. The cell was closed with a plastic cap and quickly transferred into a liquid N_2 bath. The sample was loaded directly from the liquid N_2 bath into the pre-cooled Mössbauer sample chamber ($T < 100$ K), which was then evacuated, dosed with 150 mbar He, and cooled down to 5 K for data collection. All isomer shifts are reported relative to 27 μm α–iron foil at 295 K. Fits were generated with gnuplot 5.2, which calculates statistical uncertainties from the variance-covariance matrix after the final iteration (*57*).

2.9.3 Post cyclohexane oxidation material. The procedure of catalytic cyclohexane oxidation (see 1.8.1) with $FeZn_4(prv)_4(btdd)_3$ (40 mg, 27 μmol, 1.0 equiv) was followed. The reaction yield of cyclohexane (22%) was determined by ^{1}H NMR spectroscopy (fig. S53), and the product identity was confirmed by GC-MS (fig. S54). After the filtration step, the solid material was dried

under dynamic vacuum at 120 °C for 12 h. The sample was transferred to an Ar-filled glovebox, placed in between two stacked nylon washers, and sealed between three layers of commercially available Scotch tape. The sample was transferred to the Mössbauer chamber at 298 K, dosed with approximately 150 mbar of He, and cooled down to 5 K for data collection (fig. S56, table S16).

2.10 Magnetic circular dichroism spectroscopy. At the MPI CEC in the Joint Workspace of the MPI KoFo, magnetic circular dichroism (MCD) spectra for $FeZn_4(prv)_4(btdd)_3$ were measured with an in-house MCD setup at MPI CEC, Mülheim an der Ruhr, Germany, which includes an OLIS DSM17 UV-Vis-NIR CD spectrophotometer and Cryogenic Ltd high field cryogen free measurement system with a superconducting magnet capable of reaching fields of ±11 T, in conjunction with a Cryomech PT415 pulse tube cryocooler and a Janis SHI model 350 temperature controller. The measured sample was prepared as a mull in polydimethylsiloxane in a dry, Ar-atmosphere glovebox. Two detectors were used depending on the energy of the light being detected: an InGaAs detector in the range of 2150–900 nm and a photomultiplier tube detector in the range of 1100–300 nm. The measurement was conducted at 5 K with external applied fields of ±7 T. The spectra resulting from both wavelength ranges were spliced together using the in-house software mcd.specView.SL (written by Eckhard Bill and available by email to daniel.santalucia@cec.mpg.de).

2.11 Thermogravimetric analysis. Thermogravimetric analysis data were collected using a TA Instruments Discovery TGA. Masses are uncorrected for buoyancy effects. Thermogravimetric decomposition experiments were collected under 100% N_2 with a temperature ramp rate of 2 °C/min from 30 to 600 °C for $Fe_{1.8}Zn_{3.2}(prv)_4(btdd)_3$ and $FeZn_4(prv)_4(btdd)_3$ (figs. S6 and S7).

2.12 Applied-field Mössbauer spectroscopy.

2.12.1 Sample preparation. At UC Berkeley, analogous to the sample preparation described in section 2.9.1, about 50 mg desolvated $FeZn_4(moba)_4(btdd)_3$ was placed in between two stacked nylon washers and sealed between three layers of commercially available Scotch tape in an Ar-filled glovebox. The sample was transferred into the Mössbauer chamber, in which approximately 150 mbar of He was dosed at 100 K. The sample was then cooled down to 5 K. After data collection on the parent framework, the temperature was raised to 100 K, gaseous He was removed under vacuum, and subsequently 100 mbar O_2 was dosed into the chamber. The temperature was then increased to 200 K and the sample was held at this temperature for 2 h. After this period, unreacted O_2 was removed from the sample headspace by applying dynamic vacuum, 150 mbar He was dosed at 100 K, and the sample was then cooled to 5 K for data collection. The sample was then warmed to 100 K, the gaseous He removed under vacuum, and the process of O_2 dosing and data collection at 5 K was repeated for a dosing pressure of 200 mbar (see fig. S31, table S10). After data collection, the sample was taken out of the Mössbauer spectrometer and kept cold in liquid N_2. The sample was quickly transferred into a liquid N_2-cooled dry shipper and shipped to the MPI CEC, Mülheim an der Ruhr, Germany, for applied-field Mössbauer measurements.

2.12.2 General measurement details. At the MPI CEC in the Joint Workspace of the MPI KoFo, zero field Mössbauer spectra at 80 K were measured with a conventional Mössbauer spectrometer employing a constant acceleration Doppler drive (in-house construction) to which the γ-ray source was attached. The radioactive source is $^{57}Co/Rh$ (1.8 GBq), which was kept at room temperature. The sample temperature was maintained at 80 K with an Oxford Instruments Variox cryostat using liquid N_2 as well as a Lakeshore model 350 temperature controller. Sample temperatures from 80–

300 K are achievable. The γ-ray detector is a Si drift diode (150 mm^2 SDD CUBE) from the AXAS-M1 system with 512 channels, available from Ketek GmbH.

Applied magnetic field Mössbauer spectra were measured with a conventional Mössbauer spectrometer employing a constant acceleration Doppler drive (in-house construction) to which the γ-ray source was attached. The radioactive source is ^{57}Co/Rh (1.8 GBq), which was kept at room temperature and positioned inside the gap of the magnet via a re-entrant bore tube. The source was adjusted to a zero-field position approximately 9 cm away from the sample. The sample was kept at a constant temperature with a cryogen-free closed-cycle cryostat from Cryogenic Ltd. The instrument includes a top-loading variable-temperature insert that, in conjunction with the cryostat, allows for temperatures in the range of 1.6–80 K to be achieved. The instrument also features a split-pair superconducting magnet, capable of achieving fields in the range of 0–7 T; the magnetic coils are oriented vertically such that the field is perpendicular to the γ-rays, the standard configuration. The γ-ray detector is a Si drift diode (150 mm^2 SDD CUBE) from the AXAS-M1 system with 512 channels, available from Ketek GmbH. The detector is mounted to the tip of a 200 mm hermetically-sealed stainless-steel finger. The finger is positioned horizontally in the magnet gap into the cryostat such that it approaches the sample where the γ-beam aperture is wider.

The spectra were collected in the velocity range of ±11 mm/s, and were calibrated to 12.5 μm α-Fe foil at 298 K. The minimum experimental linewidth (full width at half maximum) was 0.27 mm/s based on the minimum linewidth observed in the α-Fe foil calibration spectra. The spectra were simulated via diagonalization of the spin Hamiltonians for multiple subspectra (corresponding to different Fe species) using the in-house software mx.1.84.SL (written by Eckhard Bill and available by email to daniel.santalucia@cec.mpg.de). The spin Hamiltonian is given by:

$$\hat{H} = \mu_B \vec{S}\,\overleftrightarrow{g}\,\vec{H} + \vec{S}\,\overleftrightarrow{D}\,\vec{S} + \vec{S}\,\overleftrightarrow{A}\,\vec{I} - g_N \mu_N \vec{I}\cdot\vec{H} + \vec{I}\,\overleftrightarrow{Q}\,\vec{I}$$

$$= g_{avg}\mu_B \vec{S}\cdot\vec{H} + D\left[\vec{S_z}^2 - \frac{1}{3}\vec{S}(\vec{S}+1)\right] + E\left[\vec{S_x}^2 - \vec{S_y}^2\right]$$

$$-g_N\mu_N\left(\frac{-\langle\vec{S}\rangle_i\,\overleftrightarrow{A}}{g_N\mu_N} + \vec{H}\right)\cdot\vec{I} + \frac{eQV_{zz}}{4\vec{I}(2\vec{I}-1)}\left[3\vec{I_z}^2 - \vec{I}(\vec{I}+1) + \eta\left(\vec{I_x}^2 - \vec{I_y}^2\right)\right]$$

where μ_B is the Bohr magneton, $\vec{S}$ is the (effective) spin vector (which can be split into x-, y-, and z-components), $\overleftrightarrow{g}$ is the electron g-tensor (here modeled isotropically with $g_{avg} = 2.00$, close to the free electron value of 2.002319), $\vec{H}$ is the external magnetic field, $\overleftrightarrow{D}$ is the zero-field splitting (ZFS) tensor (here modeled axially with the axial ZFS parameter D or, alternatively, rhombically with the addition of the rhombic ZFS parameter E such that the rhombicity parameter $E/D \neq 0$), $\overleftrightarrow{A}$ is the electron-nuclear hyperfine coupling tensor (which is herein modeled axially with $A_{xx} = A_{yy} \neq A_{zz}$ or, alternatively, rhombically with $A_{xx} \neq A_{yy} \neq A_{zz}$), g_N is the nuclear g-factor, μ_N is the nuclear magneton, $\vec{I}$ is the nuclear spin vector, $\overleftrightarrow{Q}$ is the quadrupole interaction tensor, $\frac{-\langle\vec{S}\rangle_i\,\overleftrightarrow{A}}{g_N\mu_N}$ is the internal field at the nucleus (which incorporates the spin-expectation values $\langle\vec{S}\rangle_i$ for each eigenstate of the electron spin vector (for $i = 1, \ldots, 2S+1$) to decouple the electronic and nuclear parts of the Hamiltonian), e is the elementary charge of a proton, Q is the nuclear quadrupole moment, V_{zz} is the main/z-component of the electric-field gradient, and η is the asymmetry parameter (which is given by $\eta = \frac{V_{xx}-V_{yy}}{V_{zz}}$, where V_{xx} and V_{yy} are the x- and y-components of the electric-field gradient,

respectively; $0 \leq \eta \leq 1$). The isomer shift is not included in the Hamiltonian because it is merely an additive effect (*31*). Uncertainties were estimated based on the observed variability of the fits.

2.12.3 Discussion of Variable-Temperature, Variable-Field (VTVH) Mössbauer spectra and modeling approach. Zero-field Mössbauer data were collected for $FeZn_4(moba)_4(btdd)_3$ at 1.7 K (see fig. S33). The zero-field spectrum was fit with a single quadrupole doublet, yielding δ and $|\Delta E_Q|$ parameters (1.050(11) and 2.57(8) mm/s, respectively) consistent with high-spin iron(II) ($S = 2$). The linewidth was chosen as a reasonable value of 0.40 mm/s. This linewidth is slightly broader than a typical linewidth observed in Mössbauer spectroscopy (ca. 0.3 mm/s), and plausibly results from multiple unresolved coordination geometries present in the framework (*58*). While fitting the linewidths for zero-field Mössbauer spectra is appropriate, often when fitting VTVH Mössbauer data (as described below), subspectra tend to become artificially broadened due to unresolved hyperfine splittings. As such, the zero-field linewidth was used as a fixed parameter when modeling variable-field data collected for this material (see below).

Variable-field Mössbauer data were also collected for $FeZn_4(moba)_4(btdd)_3$ at 1.7 K and fields of 1, 4, and 7 T (fig. S32) to correspond with the fields used for collecting the VTVH Mössbauer spectra for O_2-dosed $FeZn_4(moba)_4(btdd)_3$ as discussed below. The zero- and variable-field data were modeled simultaneously using a single subspectrum; the isomer shift, quadrupole splitting, and linewidth were taken as fixed parameters based on the fit to the zero-field spectrum. The sign of the quadrupole splitting was determined to be positive based on the variable-field data. The spin Hamiltonian parameters derived from simultaneously fitting the zero- and variable-field data are reported in table S12. It should be noted that the spin Hamiltonian parameters for this subspectrum should not be taken to be the true spin Hamiltonian parameters for a given iron(II) site in the framework. It is plausible that more than one site is present (e.g., with different coordination geometries), and these sites would have slightly different spin Hamiltonian parameters. Indeed, in fitting the VTVH data for the O_2-dosed framework (see below), it is clear that this single subspectrum does not perfectly capture the signal associated with the iron(II) species in the framework: this is apparent, for example, in the data collected at 1.7 K and 1 T (see Fig. 3B in the main text and fig. S33), where the feature at ~2.5 mm/s is not modeled by the single subspectrum. However, ultimately these parameters should reasonably approximate the electronic structure of a given iron(II) site. Thus, these parameters were used as fixed values for a single iron(II) subspectrum used in the model for the VTVH Mössbauer data for O_2-dosed $FeZn_4(moba)_4(btdd)_3$; this approach avoided overparameterization.

The zero-field Mössbauer spectrum for O_2-dosed $FeZn_4(moba)_4(btdd)_3$ collected at 1.7 K is displayed in Fig. 3B in the main text. In addition to the subspectrum corresponding to the high-spin iron(II) nodes in the parent framework, two other subspectra were needed to model the spectrum. The linewidths for all subspectra were again fixed at reasonable values of either 0.40 mm/s or 0.50 mm/s, such that, when later modeling the VTVH data, unresolved hyperfine splittings could be accounted for without the subspectra becoming unreasonably broad (again, the relatively large linewidths plausibly arise as a result of multiple unresolved coordination geometries associated with each site, as previously observed in Mössbauer spectra for another Fe-containing framework (*58*). One of the zero-field subspectra has δ and $|\Delta E_Q|$ parameters of 0.440(4) and 1.47(4) mm/s, respectively, consistent with a high-spin ($S = 5/2$) iron(III) species. The other subspectrum has δ and $|\Delta E_Q|$ parameters of 0.300(3) and 0.610(18) mm/s, respectively, consistent with an Fe(IV)=O species. Based on the range of isomer shifts and quadrupole splittings reported for $S = 1$ and $S = 2$ Fe(IV)=O species in the literature (see fig. S40), these values do not allow a

14

definitive assignment of the Fe(IV)=O spin state in O_2 dosed $FeZn_4(moba)_4(btdd)_3$ (*31, 59*). From VTVH Mössbauer spectroscopy data, we can extract additional parameters for these sites, namely the zero-field splitting and electron-nuclear hyperfine coupling tensors, in order to make a more definitive assignment of the spin state for the Fe(IV)=O species. Our detailed approach is described below.

Variable-field Mössbauer data were collected for the same O_2-dosed sample of $FeZn_4(moba)_4(btdd)_3$ at 1.7 K at fields of 1, 4, and 7 T, and are plotted with the 1.7 K, 0 T data in Fig. 3B in the main text. It is apparent from these data that the three subspectra used for the zero-field fit cannot model the data. For example, the observed splittings in the range of −2 to +3 mm/s in the 7 T spectrum cannot be accounted for by a single subspectrum corresponding to the Fe(IV)=O species, and thus at least one additional subspectrum is needed. Based on the isomer shift, quadrupole splitting, and relative intensity of the peaks in this region under applied fields, the most chemically reasonable possibility for including any additional subspectra is that they also correspond to Fe(IV)=O species. Initially, it was hypothesized that there was a mixture of two types of Fe(IV)=O nodes in the MOF, some with intermediate spin states ($S = 1$) and others with high-spin states ($S = 2$). Two possibilities could give rise to this situation: field-induced spin-state mixing or spin-crossover. In the former scenario, varying the field would lead to changes in the signal intensities for the $S = 1$ and $S = 2$ Fe(IV)=O subspectra in each of the different variable-field spectra. However, fitting these spectra individually showed that there was no significant variation in the areas of these subspectra. Alternatively, if spin-crossover was operative, then adding thermal energy to the system would alter the relative signal intensities of the $S = 1$ and $S = 2$ Fe(IV)=O subspectra and adding enough thermal energy should cause the complete disappearance of one signal. Variable-temperature Mössbauer spectra were collected at 40, 15, 5, and 1.7 K under an applied field of 7 T to examine the relevance of this hypothesis (see fig. S33). It is apparent from this dataset that both subspectra are still present at all temperatures, and fits to the data showed again little-to-no variability in the signal intensities over the entire temperature range. Thus, there was no evidence found for field-induced mixing or spin-crossover.

These analyses led us to hypothesize that a second subspectrum corresponding to the Fe(IV)=O species arises from a fraction of nodes in the framework featuring two Fe(IV)=O species that are antiferromagnetically coupled ($S_{tot} = 0$). The other subspectrum corresponding to the Fe(IV)=O species arises from the fraction of the nodes that feature an isolated Fe(IV)=O site. In this case, antiferromagnetic coupling presumably occurs via a superexchange mechanism, according to the Goodenough-Kanamori rules, considering that the nearest metal–metal distances between Fe(IV)=O sites within a node rules out direct exchange (*60–63*). Spin polarization mechanisms with conjugated ligands leading to superexchange between metal centers in polymeric structures have been investigated previously (*64*). Note, the zero-field Mössbauer spectrum could be adequately modeled using only a single subspectrum for the Fe(IV)=O sites, given that any effect of antiferromagnetic superexchange is not visible under zero-field. In the variable-field spectra, the isomer shift and quadrupole splitting values for the $S_{tot} = 0$ antiferromagnetically coupled Fe(IV)=O sites were assigned to be the same as those of the uncoupled Fe(IV)=O sites, because the antiferromagnetic exchange is expected to be a relatively weak effect that only slightly perturbs the energies of the electronic states and leaves the nuclear energy levels relatively unperturbed (any perturbations are likely outside of the experimental resolution). Changes in the isomer shift and quadrupole splitting require much stronger effects, namely changes in iron–ligand bond-lengths and changes in coordination number/environment, respectively) (*31*).

Having identified the four relevant subspectra, we set out to model the applied field data to extract zero-field splitting and electron-nuclear hyperfine coupling tensors for the uncoupled Fe(IV)=O sites in order to fully support an assignment of the spin state. To this end, two series of models were considered, one in which the uncoupled Fe(IV)=O sites in the framework are $S = 1$, and the other series where the uncoupled Fe(IV)=O sites are $S = 2$. For both series of models, the isomer shifts (δ), quadrupole splittings ($|\Delta E_Q|$), and linewidths (Γ) for the iron(II), iron(III), and iron(IV) subspectra determined at zero field were taken as fixed parameters; the signs of the quadrupole splittings for the subspectra corresponding to the iron(III) and iron(II) species were determined from fitting the VTVH data, whereas both possibilities for the sign of ΔE_Q were considered when modeling the Fe(IV)=O species. Unlike the subspectrum corresponding to the iron(II) nodes (fig. S32, table S12), no asymmetry parameter was found to be necessary for the other three subspectra; therefore, their asymmetry parameters were fixed at 0. The ZFS parameters (D and E) were fixed for the $S = 2$ iron(II) sites from the previously discussed fits of the VTVH data for FeZn$_4$(moba)$_4$(btdd)$_3$; D and E were fixed at 0 cm^{-1} for the $S_{tot} = 0$ subspectrum and for the $S = 5/2$ iron(III) species with the rationale that the electronic symmetry resulting from the single-occupation of each of the d orbitals leads to a very small ZFS (outside the resolution of the model to this set of experiments) (65, 66). Because the subspectrum corresponding to the iron(III) species has peaks that do not overlap with others in the experimental data, the spin Hamiltonian parameters for this subspectrum were also first fit separately, before any parameters for the other subspectra were fit. This yielded the sign of the quadrupole splitting and a set of hyperfine parameters (A_{xx} and A_{yy} were allowed to refine freely); these parameters were then used as fixed parameters for the other models discussed below.

Within each series of models, multiple scenarios were considered for modeling the Fe(IV)=O species. Models that were axial ($E/D = 0$ and $A_{xx} = A_{yy}$) or that incorporated rhombicity ($E/D \neq 0$ and $A_{xx} \neq A_{yy}$) were investigated to account for deviations from axial symmetry; changing the sign of V_{zz} (i.e., the sign of the quadrupole splitting) was also investigated because it was not immediately obvious what the sign should be from examining the data. The effect of including or excluding A_{zz} was also investigated. This led to a total of 16 possible models for the Mössbauer data that were investigated, eight models for each series.

Before the individual fits within each series of models (i.e., the $S = 1$ and $S = 2$ cases) were conducted, the areas for each subspectrum were optimized. From preliminary fits, it was apparent that the model that best captures the data has a negative quadrupole splitting, is axial ($E/D = 0$ and $A_{xx} = A_{yy}$), and includes A_{zz} (for example, c.f. Fig. 3B and fig. S37, which feature fits with and without A_{zz} for the $S = 2$ case). Thus, the areas for each subspectrum were optimized within these bounds and then used for the 16 models investigated. Areas were optimized separately for the $S = 1$ and $S = 2$ series of models so that there was no inherent bias towards either spin state. The optimization of areas was done iteratively using the following two sequential steps: first the spin Hamiltonian parameters for each subspectrum were fit to minimize the residual between the fit and the data while the areas for each subspectrum were fixed; second, the spin Hamiltonian parameters were then fixed, while the areas were optimized. These steps were repeated until neither the areas nor the spin Hamiltonian parameters changed significantly, and the residual sum of squares (RSS) was minimized, meaning that a global minimum had been found. For the $S = 1$ series of models, it was found that the areas of the four subspectra were as follows: 21.5(4)% for the $S = 2$ iron(II) sites; 14.8(3)% for the $S = 5/2$ iron(III) sites; 24.1(5)% for the $S_{tot} = 0$ antiferromagnetically coupled Fe(IV)=O species; and 39.6(8)% for the $S = 1$ Fe(IV)=O sites.

16

Similarly, for the $S = 2$ series of models, it was found that the areas of the four subspectra were as follows: 21.2(4)% for the iron(II) sites; 14.0(3)% for the iron(III) sites; 27.9(6)% for the $S_{tot} = 0$ antiferromagnetically coupled Fe(IV)=O species; and 36.9(7)% for the uncoupled $S = 2$ Fe(IV)=O species. It was found that the areas of the subspectra do not vary much upon changing from one specific type of fit to another, but that they do display some variability upon changing the spin state of the subspectrum corresponding to the uncoupled Fe(IV)=O sites; as such, the optimized areas for the $S = 1$ case were used for all other $S = 1$ models, while the optimized areas for the $S = 2$ case were used for all other $S = 2$ models. Regardless of the series of models considered, the combined area of the coupled and uncoupled Fe(IV)=O sites shows that the O_2-dosed framework contains ~64–65% Fe(IV)=O, ~21% iron(II) sites, and ~14–15% iron(III) species. (See table S13 and table S14 for the optimized areas for the $S = 1$ and $S = 2$ series of models, respectively).

The final $S = 2$ and $S = 1$ models were ultimately arrived at by simultaneous fitting of the different datasets (including the zero-field Mössbauer spectrum), carefully checking how varying the fit parameters changed the overall quality of the fit (measured by the RSS) and taking care to avoid local minima (see table S15). The spin Hamiltonian parameters for the chosen optimal axial ($E/D = 0$ and $A_{xx} = A_{yy}$) $S = 2$ and $S = 1$ models are reported in tables S13 and S14, respectively; both have negative ΔE_Q and include A_{zz}.

We briefly discuss the impact of the model parameters on the quality of the fits. Changing the sign of the quadrupole splitting shows in general that, regardless of the spin state of the Fe(IV)=O species ($S = 1$ or 2), whether the subspectrum is modeled as axial or not, and whether A_{zz} is included or excluded, fits with negative ΔE_Q values led to better quality fits (apparent by the smaller associated RSS values. For a magnetically split spectrum, changing the sign of the quadrupole splitting has the effect of shifting the inner four lines of the six-line spectrum relative to the outer two. Positive values of the quadrupole splitting led to models where the peak at approximately -1.2 mm/s in the 1.7 K, 7 T data was left unmodeled. Additionally, inclusion of A_{zz} led to better quality fits. While the inclusion of rhombicity also improved the fits slightly, the simpler axial models were sufficient to describe the electronic structure. Thus, the rhombic models do not necessarily describe the electronic structure any more accurately and were considered overparameterized. Examples of how altering these parameters affect the quality of the fits are shown in fig. S37. Thus, models with positive ΔE_Q, no A_{zz} parameter, or inclusion of E were eliminated, leaving two remaining models, 5 ($S = 1$) and 13 ($S = 2$) (see table S15).

From a purely statistical perspective (comparing RSS values), the data were slightly better modeled with the $S = 1$ model (model 5) than the $S = 2$ model (model 13). However, the difference in the RSS values is small, and inspection of the overall models shows that they are of similar quality to one another (see Fig. 3B and figs. S34–36). However, as discussed in the main text, the optimal $S = 1$ model afforded chemically unreasonable parameters: a D value (15.6(8) cm^{-1}) that is smaller than most D values for $S = 1$ Fe(IV)=O complexes reported in the literature (typically ≥ 20 cm^{-1}; in fact, all the $S = 1$ models herein have a D value smaller than 20 cm^{-1}) (*38, 67–69*). Additionally, the electron-nuclear hyperfine coupling parameters converge to values about two times larger than those reported for $S = 1$ Fe(IV)=O complexes (*39*). In contrast, the D (12.7(6) cm^{-1}) and hyperfine coupling parameters for the optimal $S = 2$ model are in excellent agreement with reported $S = 2$ Fe(IV)=O species in the literature (*17, 37*).

2.12.4 Analysis of the spin-dipole contribution to the hyperfine coupling tensor for the uncoupled $S = 2$ Fe(IV)=O sites. The hyperfine tensor modeled for the uncoupled $S = 2$ Fe(IV)=O

17

subspectrum was: $[A_{xx}/(g_N\mu_N), A_{yy}/(g_N\mu_N), A_{zz}/(g_N\mu_N)] = [-14.0, -14.0, -21.2]$ T, implying an isotropic hyperfine coupling constant of $a_{iso} = -16.4$ T. The hyperfine tensor has three contributions: these are the Fermi contact contribution, the spin-dipole contribution, and the orbital contribution, the first of which is isotropic and the latter two of which are anisotropic. The hyperfine tensor is therefore given by:

$$\overleftrightarrow{A} = a_{iso} + \overleftrightarrow{T} = a_{iso} + \overleftrightarrow{A}_{SD} + \overleftrightarrow{A}_{orbit}$$

Assuming a negligible orbital contribution, the entirety of the anisotropic component of the hyperfine coupling tensor originates from the spin-dipole contribution. Therefore, for the uncoupled $S = 2$ Fe(IV)=O subspectrum $\overleftrightarrow{A}_{SD} = [+2.4, +2.4, -4.8]$ T. The signs of and relative magnitudes (i.e. $A_{zz}/(g_N\mu_N) = -2\,A_{xx}/(g_N\mu_N) = -2\,A_{yy}/(g_N\mu_N)$) give information about the d-orbital occupation as will be explained briefly below:

The matrix elements of $\overleftrightarrow{A}_{SD}$ are given by:

$$A_{\mu\nu} = \frac{\mu_0}{4\pi} g_e \mu_B g_N \mu_N \left\langle \psi_0 \left| \frac{3r_\mu r_\nu - r^2 \delta_{\mu\nu}}{r^5} \right| \psi_0 \right\rangle$$

where μ_0 is the vacuum magnetic permeability, g_e is the free-electron g-factor, μ_B is the Bohr magneton, g_N is the nuclear g-factor for the ^{57}Fe nucleus, μ_N is the nuclear magneton, ψ_0 is the wavefunction for a given electron orbital, and r is the distance between the two interacting dipoles (in this case the nuclear spin and the electron spin) defined such that the origin is at the nucleus (70). The off-diagonal matrix elements are 0 (when the spin-dipole tensor is aligned with the orbital coordinate system). Solving the integrals for the rest of the elements gives the following spin-dipole matrices for the d-orbitals (71):

$$A_{SD}^{d_{xy}} = \frac{\mu_0}{4\pi} g_e \mu_B g_N \mu_N \cdot \frac{2}{7} \begin{vmatrix} +1 & & \\ & +1 & \\ & & -2 \end{vmatrix} \langle r^{-3} \rangle$$

$$A_{SD}^{d_{xz}} = \frac{\mu_0}{4\pi} g_e \mu_B g_N \mu_N \cdot \frac{2}{7} \begin{vmatrix} +1 & & \\ & -2 & \\ & & +1 \end{vmatrix} \langle r^{-3} \rangle$$

$$A_{SD}^{d_{yz}} = \frac{\mu_0}{4\pi} g_e \mu_B g_N \mu_N \cdot \frac{2}{7} \begin{vmatrix} -2 & & \\ & +1 & \\ & & +1 \end{vmatrix} \langle r^{-3} \rangle$$

$$A_{SD}^{d_{x^2-y^2}} = \frac{\mu_0}{4\pi} g_e \mu_B g_N \mu_N \cdot \frac{2}{7} \begin{vmatrix} +1 & & \\ & +1 & \\ & & -2 \end{vmatrix} \langle r^{-3} \rangle$$

$$A_{SD}^{d_{z^2}} = \frac{\mu_0}{4\pi} g_e \mu_B g_N \mu_N \cdot \frac{2}{7} \begin{vmatrix} -1 & & \\ & -1 & \\ & & +2 \end{vmatrix} \langle r^{-3} \rangle$$

The matrices corresponding to singly-occupied d-orbitals can be summed up to give a total spin-dipole hyperfine coupling matrix. We consider the cases for an $S = 1$ and an $S = 2$ Fe(IV)=O species. An $S = 1$ Fe(IV)=O species has a d-orbital occupation of $(d_{xy})^2(d_{xz})^1(d_{yz})^1$, and thus the summed spin-dipole hyperfine coupling matrix is given by:

$$A_{SD}^{S=1} = \frac{\mu_0}{4\pi} g_e \mu_B g_N \mu_N \cdot \frac{2}{7} \begin{vmatrix} -1 & & \\ & -1 & \\ & & +2 \end{vmatrix} \langle r^{-3} \rangle$$

On the other hand, an $S = 2$ Fe(IV)=O has a d-orbital occupation of $(d_{xy})^1(d_{xz})^1(d_{yz})^1(d_{x2-y2})^1$; the summed spin-dipole hyperfine coupling matrix is given by:

$$A_{SD}^{S=2} = \frac{\mu_0}{4\pi} g_e \mu_B g_N \mu_N \cdot \frac{2}{7} \begin{vmatrix} +1 & & \\ & +1 & \\ & & -2 \end{vmatrix} \langle r^{-3} \rangle$$

It is therefore apparent that the predicted signs of the spin-dipole hyperfine coupling matrix for the $S = 1$ case are opposite those of the $S = 2$ case. The anisotropic hyperfine coupling tensor for the subspectrum corresponding to the uncoupled Fe(IV)=O sites in the framework is therefore consistent only with a spin ground state of $S = 2$, further supporting the assignment of the Fe(IV)=O sites as high-spin.

2.13 Iron Kβ x-ray emission spectroscopy (XES)

2.13.1 Sample preparation. In an Ar-filled glovebox, samples of FeZn$_4$(moba)$_4$(btdd)$_3$ (~5 mg) were loaded into custom-made aluminum sample holders that were closed on one side with commercially available Kapton tape. The iron(II) reference sample was sealed on the other side with Kapton tape, and placed inside of a 100 mL glass jar. The capped jar was removed from the glovebox, wax sealed, and shipped to the BESSY II lightsource at the Helmholtz-Zentrum Berlin. For the preparation of the O$_2$-dosed sample, the filled sample holder was closed on the second side with Kapton tape except for one small opening, placed into a gas-tight drying chamber, and removed from the glovebox. The drying chamber was connected to a customized Swagelok gas dosing manifold (fig. S30). Vacuum was applied, and the vacuum chamber cooled with a liquid N$_2$/ethanol bath to 163 K. Subsequently, the sample was dosed with 70 mbar O$_2$, and the temperature was held at 163 K for 1 h. Excess O$_2$ was then removed, and the vacuum chamber was filled with Ar. The sample holder was transferred from the Ar chamber in air at 77 K to a pre-cooled snap-cap plastic tube at 77 K. The snap-cap plastic tube was closed and was quickly transferred into a liquid N$_2$-cooled dry shipper and shipped to the the BESSY II lightsource at the Helmholtz-Zentrum Berlin.

2.13.2 Measurement Details. Iron Kβ X-ray emission spectroscopy (XES) data were collected at the PINK tender x-ray beamline at BESSY II. The beam size was 30 × 500 μm FWHM (V×H). The excitation energy was 8000 eV and the incoming photon flux was ~10^{13} ph/s. The spectra were recorded by the use of a dispersive von Hamos spectrometer equipped with Si(110) cylindrically bent crystal (bending radius R = 250 mm) and an Eiger2 R 500K (75 μm × 75 μm pixel size, 512 × 1030 pixels) detector. The analyzer was set up in a vertical dispersion direction, taking advantage of the small vertical beam size to improve the energy resolution. The Si(440)

reflection was utilized at Bragg angles from 65° to 67°. Under these conditions the spectrometer resolution was about 0.6–0.8 eV.

The samples were placed in a cryogenic chamber at $T = 30$ K. A helium exchange gas under pressure of 8 mbar was used for sample cooling. The entrance window of the cryostat is made from 1 μm graphenic carbon and for the exit windows, a cold window of 8 μm Kapton and a window to the spectrometer of 13 μm Kapton were used. The samples were continuously scanned over the x-ray beam in order to reduce and evenly distribute the absorbed dose. Samples were scanned at a rate of 100 μm/s.

Calibration of the energy scale was done by measuring emission lines of Co (Kα_1, Kα_2) and Fe (K$\beta_{1,3}$) foils. The energy points used for the energy calibration were Co Kα_1: 6930.38 eV, Co K$\alpha2$: 6915.54 eV, and Fe Kβ: 7058.18 eV (*72*). To define the peak positions, these lines were fitted with a split Voigt function. Energies were translated into Bragg angles, and a fit with a tangential function was applied. The accuracy of the energy calibration between measurements was determined to be ±30meV. All spectra were normalized to the maximum of the Kβ line (see fig. S39).

3. Computational Details

3.1 Methods. Unrestricted Kohn-Sham Density Functional Theory (UKS-DFT) calculations were performed on the computing cluster (Tiger) of the Molecular Graphics and Computation Facility (MGCF) at UC Berkeley using the ORCA 5.0 program package (*73*). Calculations were performed using a model of the pentanuclear cluster node, in which the btdd^{2-} linkers were truncated to benzotriazolate ligands (bta$^-$). Initial coordinates for geometry optimizations were taken from the crystal structure of $Zn_5(prv)_4(btdd)_3$, and one peripheral Zn^{2+} center was replaced by an Fe^{2+} center to generate the model cluster representative for the clusters of $FeZn_4(prv)_4(btdd)_3$. The initial structure of the six-coordinate Fe(IV)=O site was generated from the Fe^{2+}-containing cluster model. Geometry optimizations were performed in the gas phase at the B3LYP/def2-TZVP level of theory on the quintet potential energy surface (*74–76*). The five-coordinate Fe(IV)=O site was generated from the optimized structure of the six-coordinate Fe(IV)=O site and was optimized at the B3LYP/def2-TZVP level of theory. For $Fe(O)(\kappa^2\text{-}OAc)Zn_4(prv)_3(bta)_6$ (OAc$^-$ = acetate), an additional geometry optimization was performed in the gas phase at the B3LYP/def2-TZVP level of theory on the triplet surface. For the $FeZn_4(moba)_4(btdd)_3$ derived model clusters, initial coordinates were generated for $Fe(moba)Zn_4(prv)_3(bta)_6$ and $Fe(O)(\kappa^2\text{-}OPiv)Zn_4(prv)_3(bta)_6$ (OPiv$^-$ = pivalate), respectively, by replacing prv$^-$ with moba$^-$ as the Fe ligand in the optimized structure of $FeZn_4(prv)_4(bta)_6$, and by replacing OAc$^-$ with OPiv$^-$ in the optimized structure of $Fe(O)(\kappa^2\text{-}OAc)Zn_4(prv)_3(bta)_6$. To minimize computational costs, prv$^-$ was retained as the ligand on the Zn sites in each case. Geometry optimizations were performed at the BP86-D3BJ/def2-TZVP level (*77, 78*) on the triplet and quintet surfaces. Optimized structures and cartesian coordinates for the model structures $FeZn_4(prv)_4(bta)_6$, $S = 2$ $Fe(O)(\kappa^2\text{-}OAc)Zn_4(prv)_3(bta)_6$, $S = 2$ $Fe(O)(\kappa^1\text{-}OAc)Zn_4(prv)_3(bta)_6$, $Fe(moba)Zn_4(prv)_3(bta)_6$, $S = 2$ $Fe(O)(\kappa^2\text{-}OPiv)Zn_4(prv)_3(bta)_6$, and $S = 1$ $Fe(O)(\kappa^2\text{-}OPiv)Zn_4(prv)_3(bta)_6$ are given below in table S17.

Single point calculations for determining Mössbauer parameters for the optimized structures were performed using the B3LYP exchange-correlation functional for $FeZn_4(prv)_4(bta)_6$, $S = 2$ $Fe(O)(\kappa^2\text{-}OAc)Zn_4(prv)_3(bta)_6$, and $S = 2$ $Fe(O)(\kappa^1\text{-}OAc)Zn_4(prv)_3(bta)_6$, and BP86-D3BJ on $S = 2$ $Fe(O)(\kappa^2\text{-}OPiv)Zn_4(prv)_3(bta)_6$, and $S = 1$ $Fe(O)(\kappa^2\text{-}OPiv)Zn_4(prv)_3(bta)_6$ with the CP(PPP) basis set on Fe (*79*), and the def2-TZVP basis set on all other atoms. Mössbauer isomer shifts were

calculated from the electron density on Fe using reported linear fit parameters (table S9 and table S11) (80). Numerical frequency calculations for simulating the NRVS iron PVDOS were obtained at the same level of theory as the geometry optimizations for each model cluster, respectively. For all frequency calculations, the masses of the artificial capping H atoms on the bta$^-$ ligands were set to $m = 16$, the mass of oxygen. The NRVS iron PVDOS distribution plots were generated using the *orca_vib* and *orca_mapspc* programs. The individual NRVS transitions were plotted as vertical lines. For $S = 2$ Fe(O)(κ^2-OAc)Zn$_4$(prv)$_3$(bta)$_6$ and Fe(O)(κ^1-OAc)Zn$_4$(prv)$_3$(bta)$_6$, the overall simulated iron PVDOS are constructed from 70% of the simulated iron PVDOS of FeZn$_4$(prv)$_4$(bta)$_6$ and 30% of the simulated iron PVDOS of Fe(O)(OAc)Zn$_4$(prv)$_3$(bta)$_6$. For $S = 2$ Fe(O)(κ^2-OPiv)Zn$_4$(prv)$_3$(bta)$_6$, the overall simulated iron PVDOS are constructed from 50% of the simulated iron PVDOS of FeZn$_4$(moba)(prv)$_3$(bta)$_6$ and 50% of the simulated iron PVDOS of Fe(O)(κ^2-OPiv)Zn$_4$(prv)$_3$(bta)$_6$, applying a frequency scale factor of 0.95.

Complete Active Space Self Consistent Field (CASSCF) combined with *N*-Electron Valence Pertubation Theory to second order (NEVPT2) was performed on the optimized geometry for $S = 2$ Fe(O)(κ^2-OPiv)Zn$_4$(prv)$_3$(bta)$_6$ using the basis set def2-TZVP with the auxiliary basis set def2/JK (*81, 82*). An active space with 10 electrons in 8 orbitals (CAS(10,8)) was used. The initial orbitals were selected from quasi-restricted orbitals, which were obtained by unitary transformations of the respective Kohn-Sham orbitals and comprise the molecular orbitals with the largest Fe 3d orbital contributions (*83*). A total of 5 triplet and 5 quintet states were computed. For NEVPT2 calculations, 2 triplet and 2 quintet states were calculated. The $S = 2$ configuration was found to be more stable than the $S = 1$ configuration by 25.1 kcal/mol (see fig. S41).

All output files were analyzed using Chemcraft 1.8 (*84*), and images of optimized structures were generated using Diamond 4.6.6 (*85*).

4. Supplementary figures
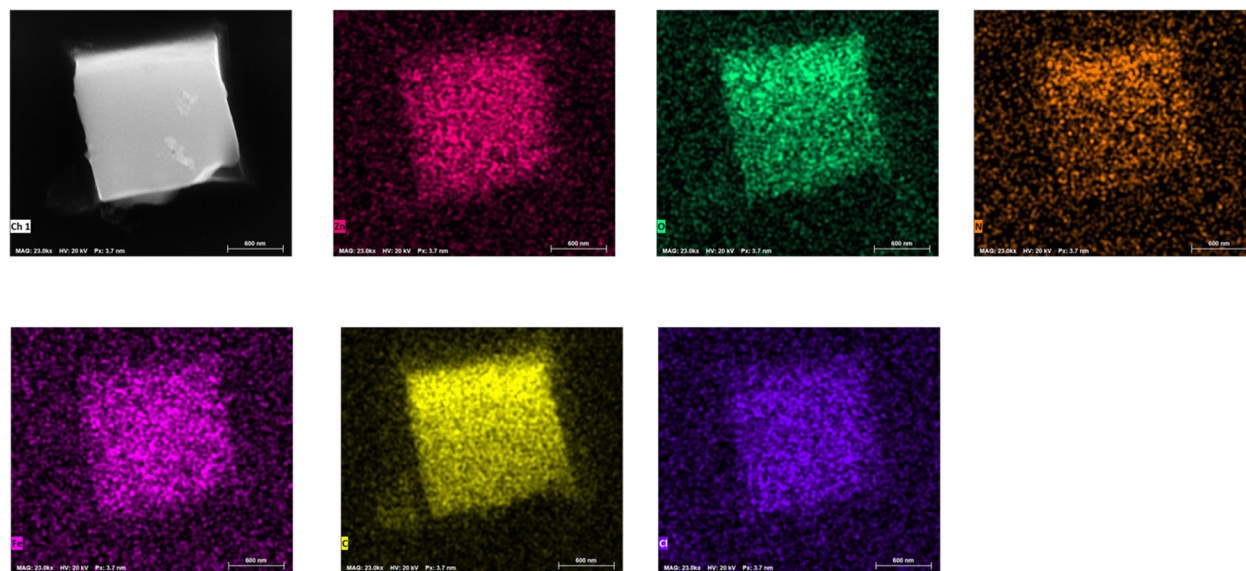
Fig. S1. Top left: Scanning electron microscopy image of a single particle sample of FeZn$_4$Cl$_4$(btdd)$_3$ analyzed using energy-dispersive x-ray spectroscopy. Elemental maps are shown

at the right and bottom; color code: Zn = dark pink, O = green, N = orange, Fe = magenta, C = yellow, Cl = purple.
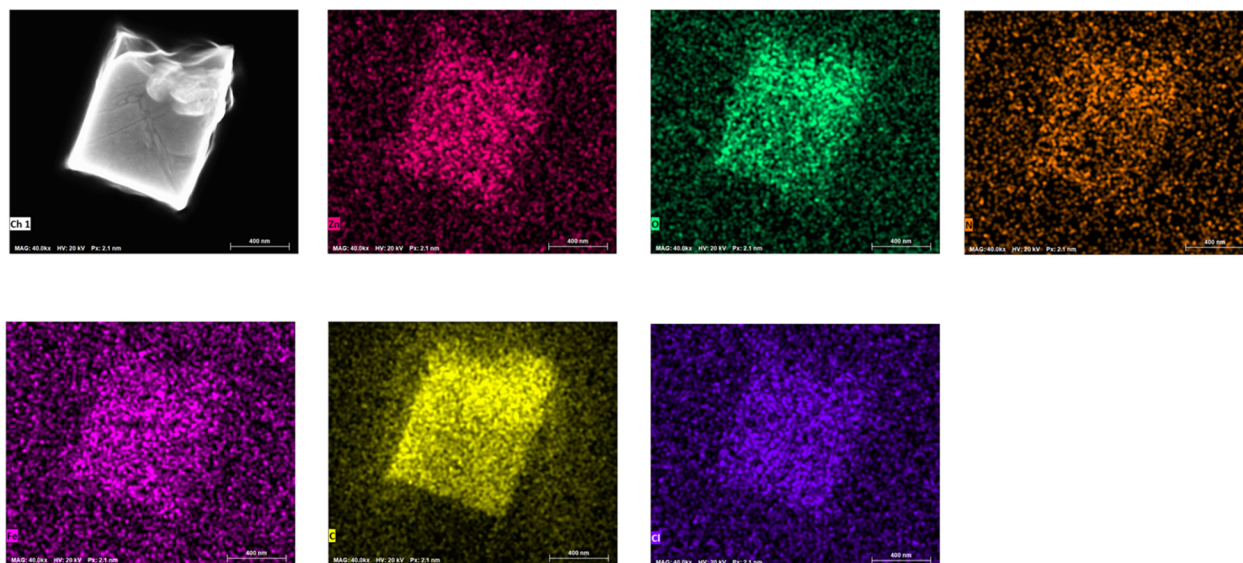
Fig. S2. Top left: Scanning electron microscopy image of a single particle sample of $Fe_{1.8}Zn_{3.2}Cl_4(btdd)_3$ analyzed using energy-dispersive x-ray spectroscopy. Elemental maps are shown at the right and bottom; color code: Zn = dark pink, O = green, N = orange, Fe = magenta, C = yellow, Cl = purple.
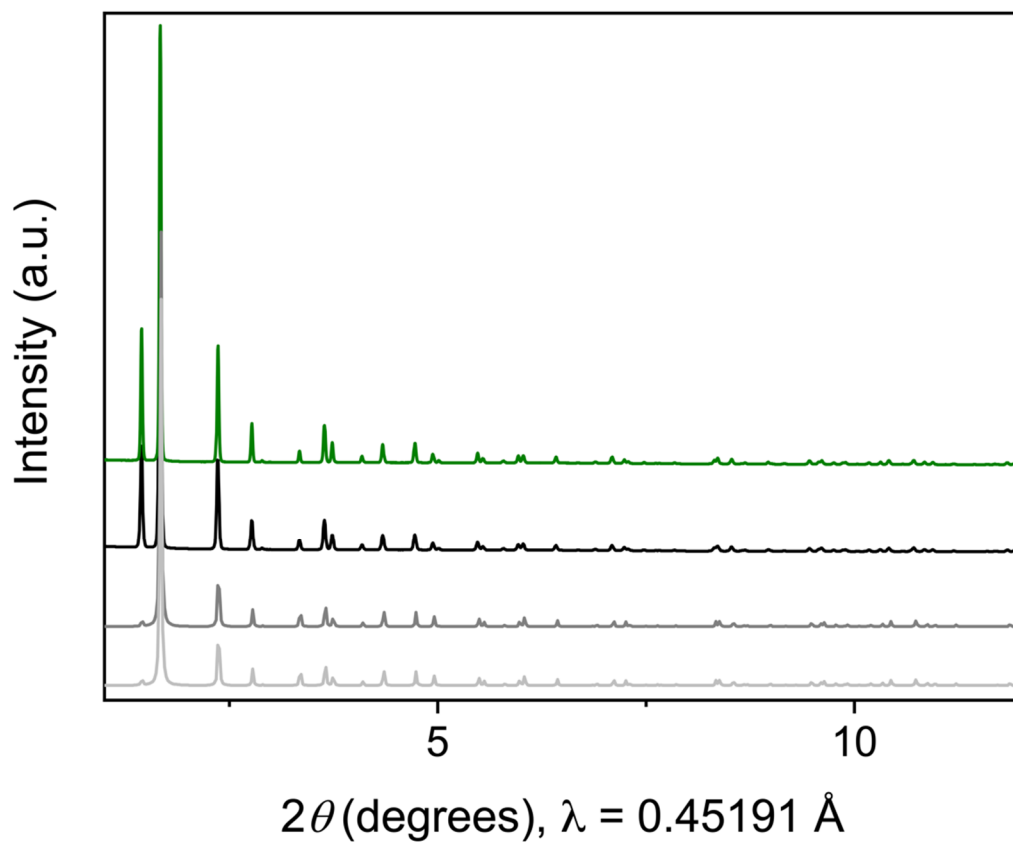
Fig. S3. Experimental powder x-ray diffraction patterns for FeZn$_4$(prv)$_4$(btdd)$_3$ (green) and Fe$_{1.8}$Zn$_{3.2}$(prv)$_4$(btdd)$_3$ (black). The simulated powder pattern from the single-crystal x-ray diffraction structure of Zn$_5$(prv)$_4$(btdd)$_3$ and Zn$_5$Cl$_4$(btdd)$_3$ are shown in dark gray and light gray, respectively.
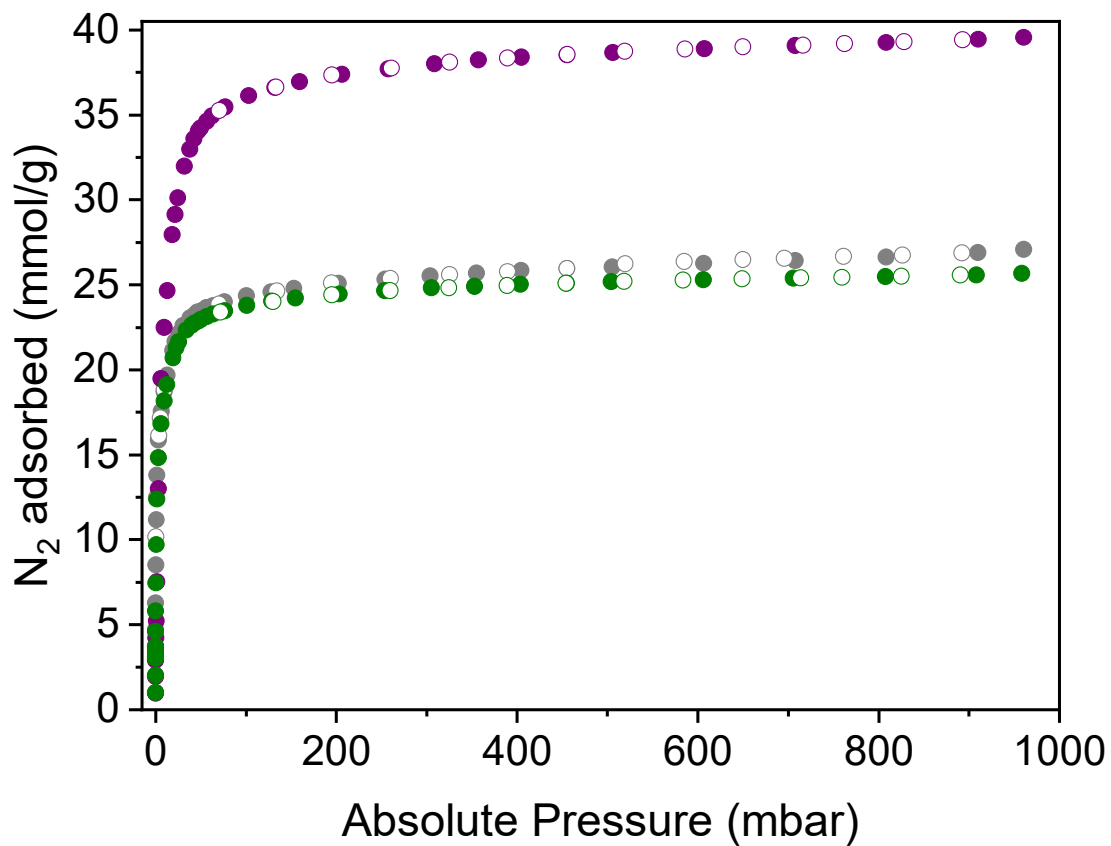
Fig. S4. Nitrogen adsorption (filled symbols) and desorption (open symbols) isotherms collected at 77 K for $FeZn_4Cl_4(btdd)_3$ (purple), $FeZn_4(prv)_4(btdd)_3$ (green), and $Zn_5(prv)_4(btdd)_3$ (gray).
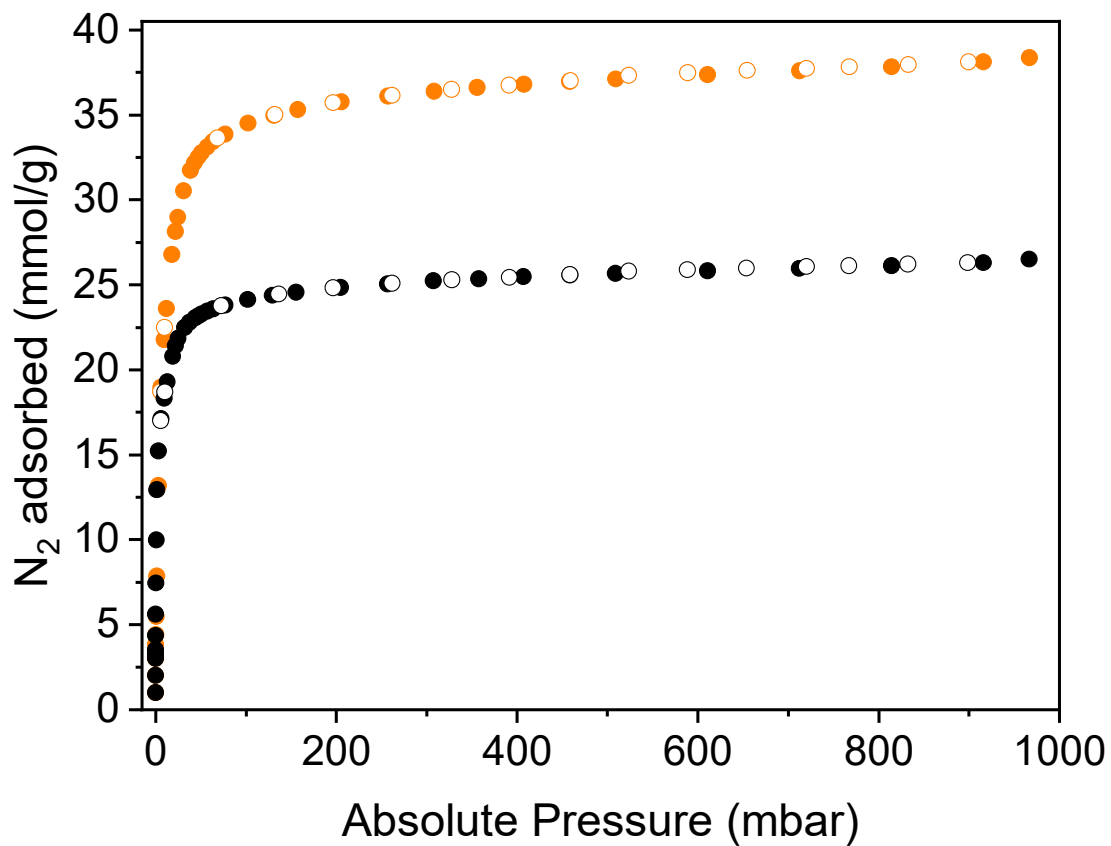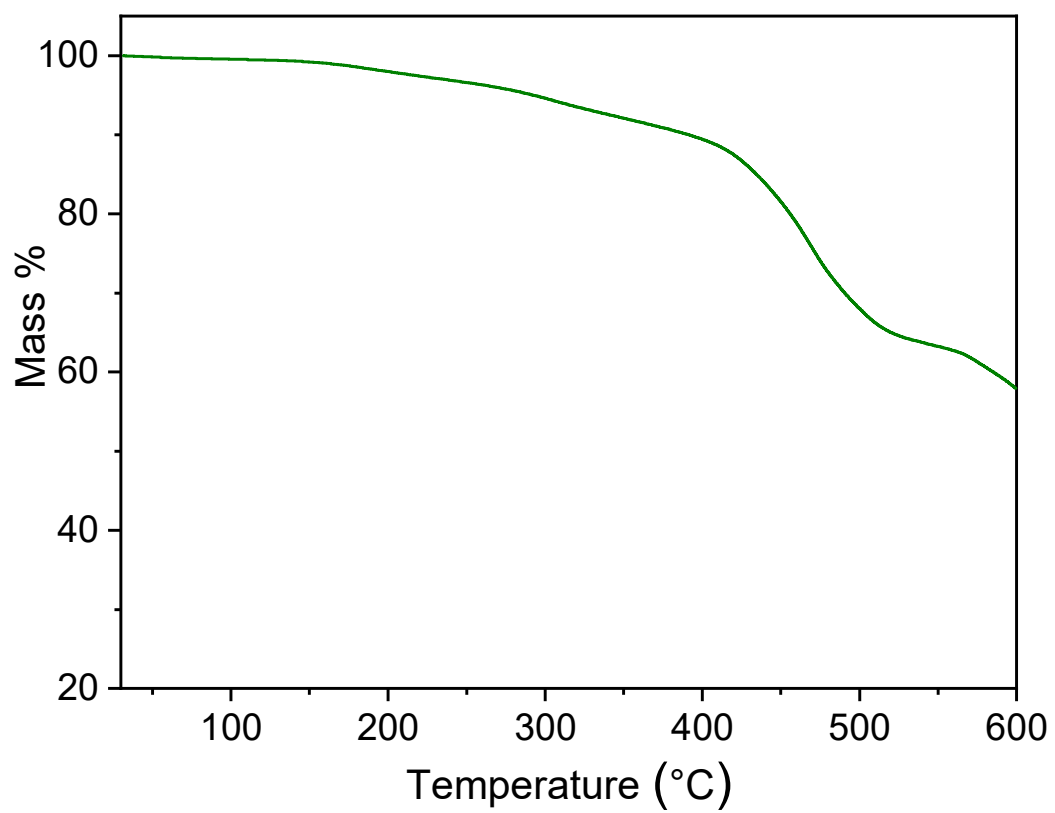
Fig. S5. Nitrogen adsorption (filled symbols) and desorption (open symbols) isotherms collected at 77 K for $Fe_{1.8}Zn_{3.2}Cl_4(btdd)_3$ (orange) and $Fe_{1.8}Zn_{3.2}(prv)_4(btdd)_3$ (black).
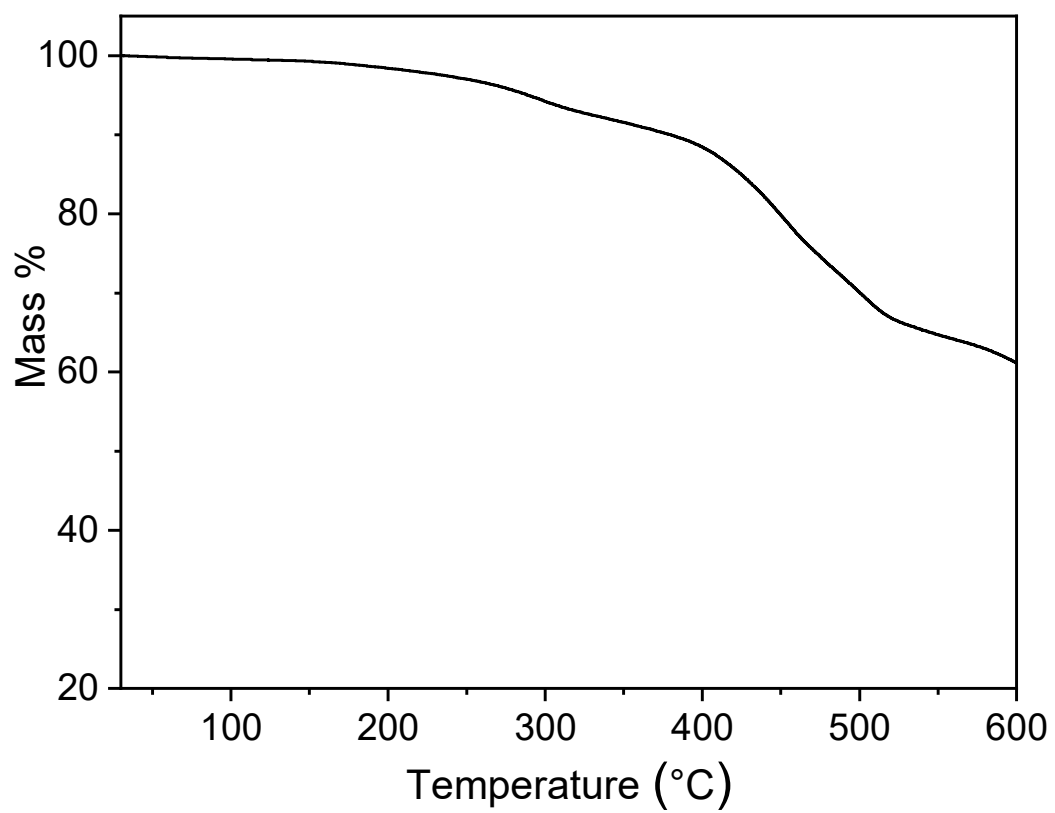
Fig. S6. Thermogravimetric analysis data for $Fe_{1.8}Zn_{3.2}(prv)_4(btdd)_3$.

Fig. S7. Thermogravimetric analysis data for FeZn$_4$(prv)$_4$(btdd)$_3$.
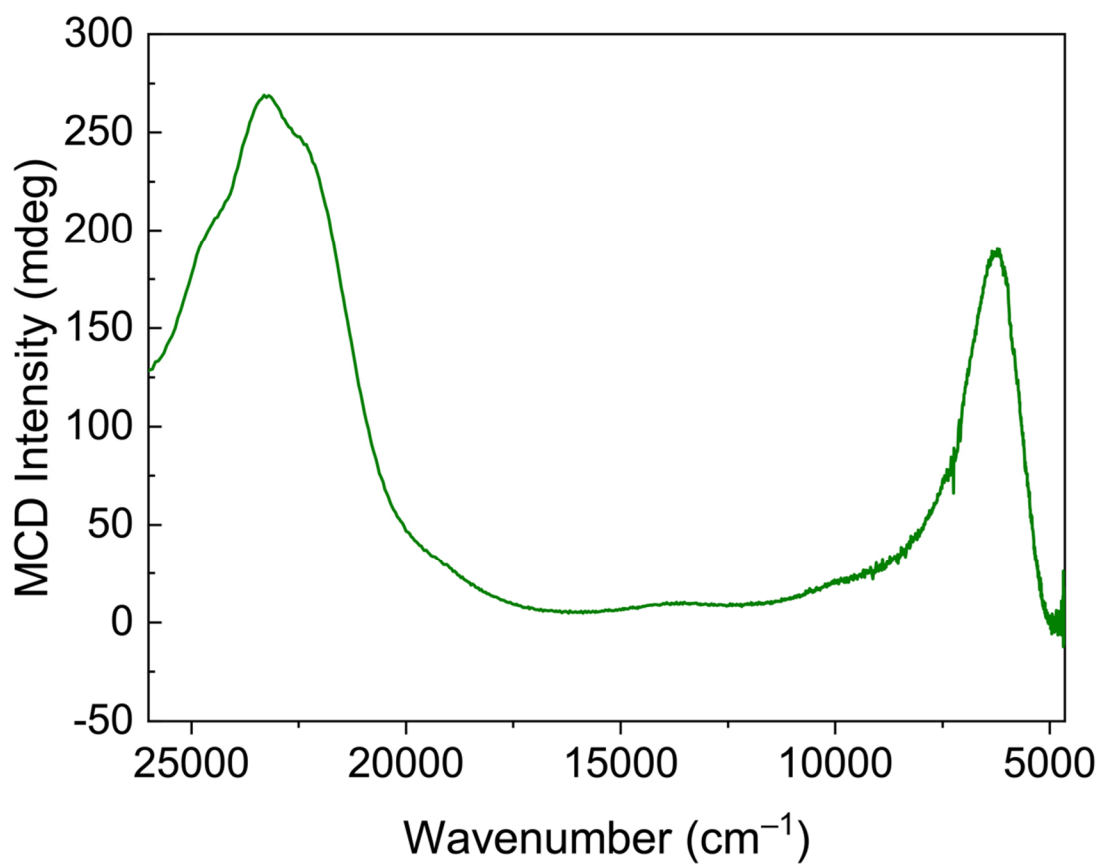
Fig. S8. A representative magnetic circular dichroism spectrum for $FeZn_4(prv)_4(btdd)_3$ collected at 5 K in a magnetic field of 7 T.
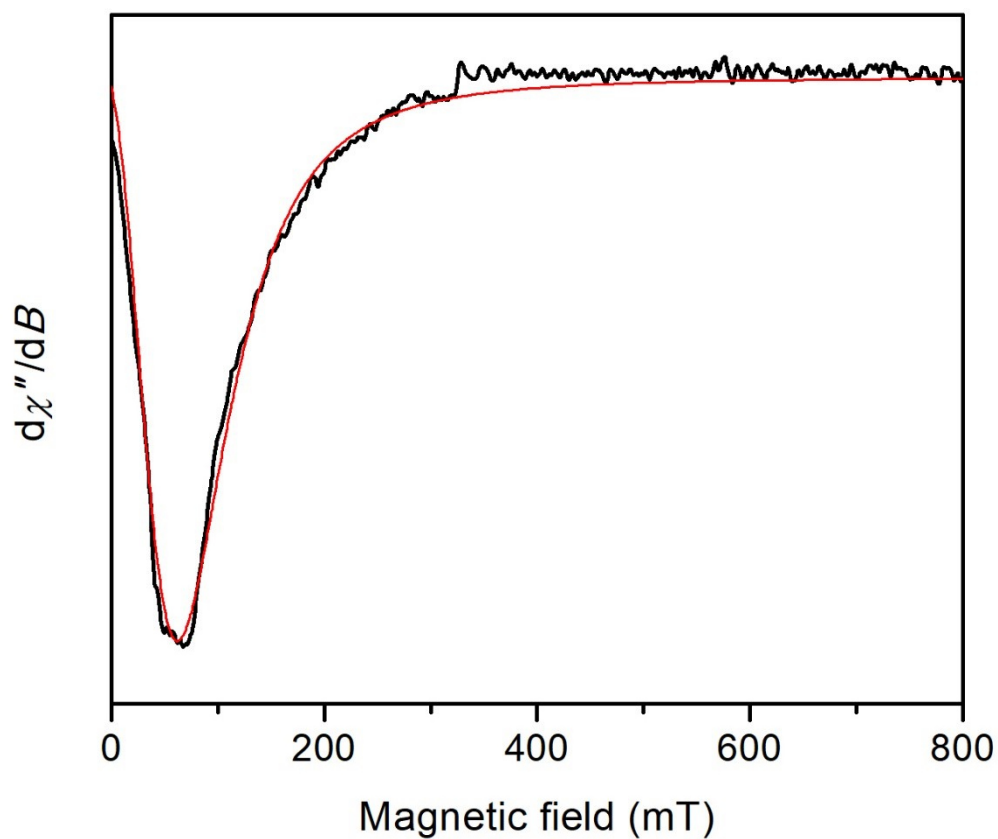
Fig. S9. Continuous-wave parallel mode EPR spectrum for FeZn$_4$(prv)$_4$(btdd)$_3$ (black line) and the corresponding simulation (red line). Simulation parameter: $S = 2$, $|D| = 2.50$ cm^{-1}, $E/D = 0.2071$, linewidth for isotopic broadening (lwpp) = [40 75] mT.
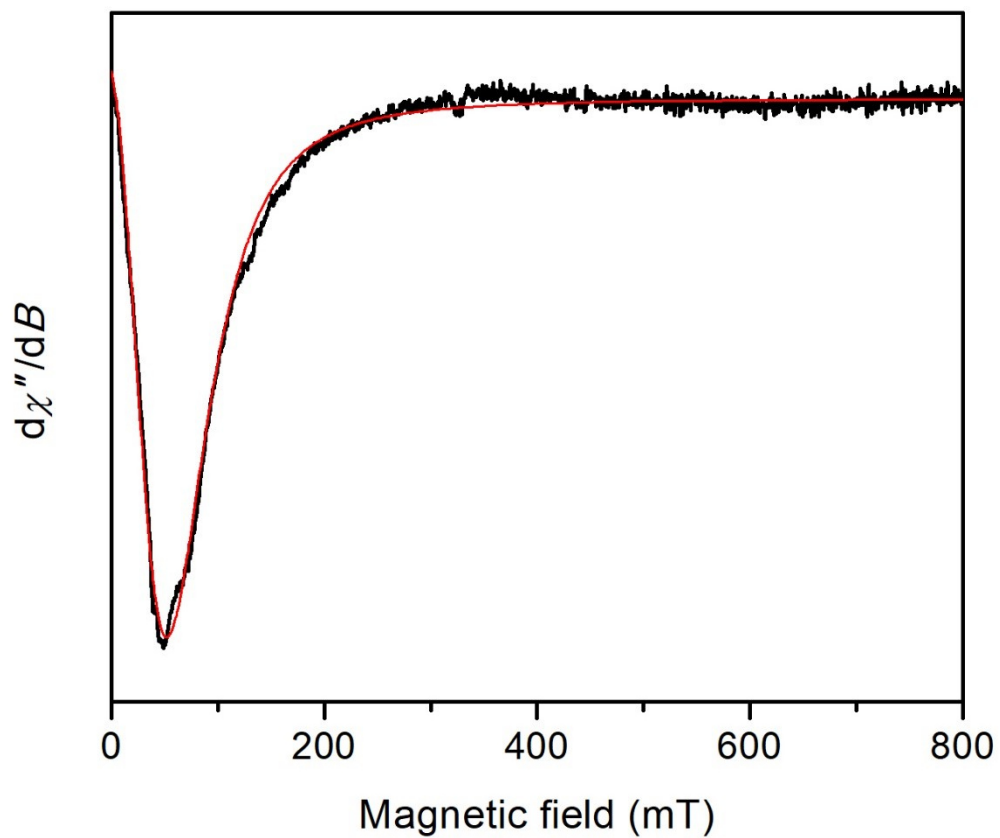
Fig. S10. Continuous-wave parallel mode EPR spectrum for $Fe_{1.8}Zn_{3.2}(prv)_4(btdd)_3$ (black line) and the corresponding simulation (red line). Simulation parameter: $S = 2$, $|D| = 2.50$ cm^{-1}, $E/D = 0.2071$, linewidth for isotopic broadening (lwpp) = [35 55] mT.
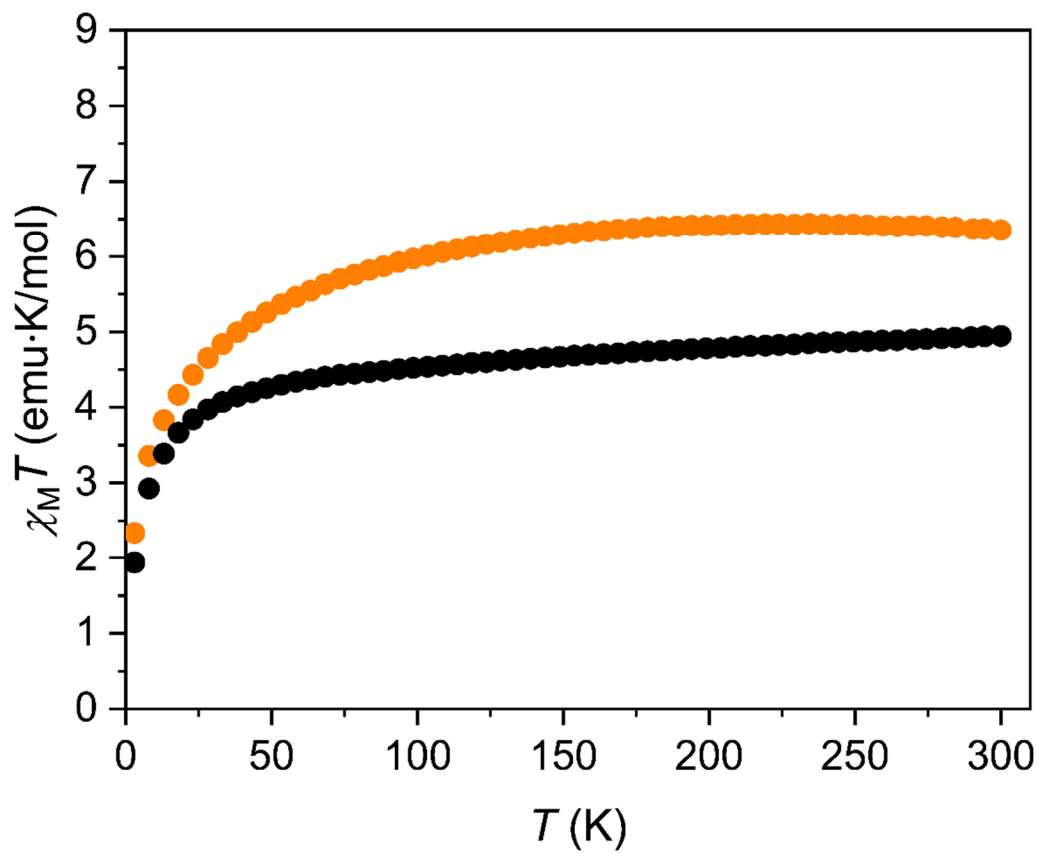
Fig. S11. Dc magnetic susceptibility data for Fe$_{1.8}$Zn$_{3.2}$Cl$_4$(btdd)$_3$ (orange) and Fe$_{1.8}$Zn$_{3.2}$(prv)$_4$(btdd)$_3$ (black).
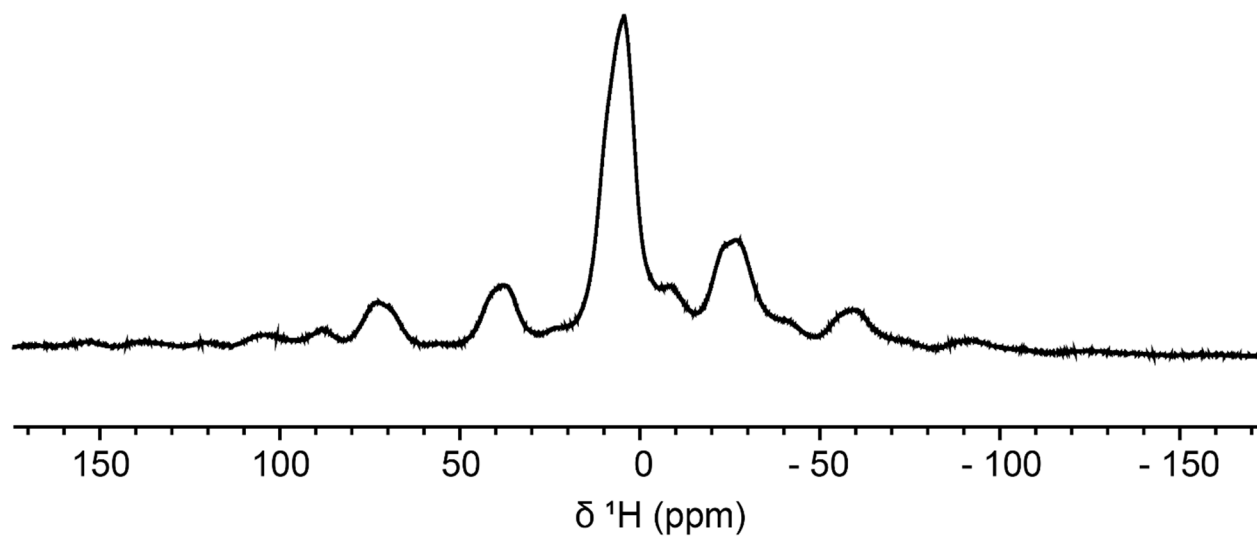
Fig. S12. Solid-state ^{1}H NMR spectrum of FeZn$_4$(prv)$_4$(btdd)$_3$.
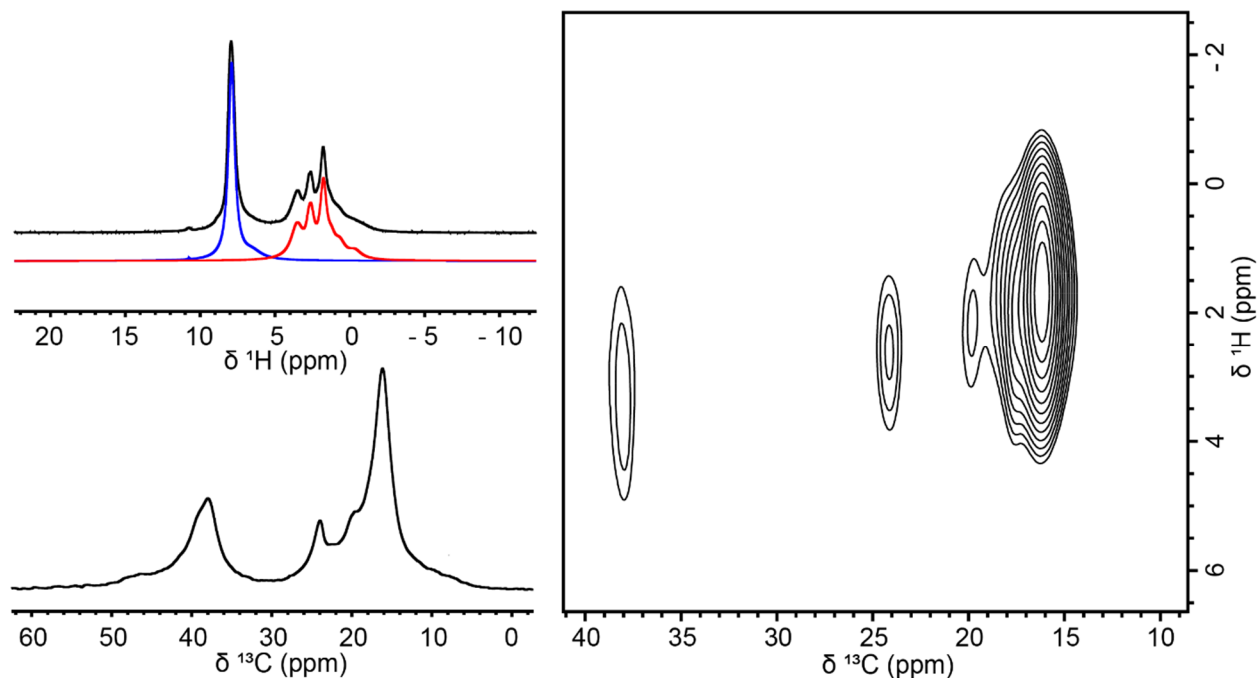
Fig. S13. (Upper left) Solid-state ^1H NMR spectrum for $Zn_5(prv)_4(btdd)_3$ (black) and simulated peaks for the protons of the btdd^{2-} linker (blue) and pyruvate (red). The peak at 7.8 ppm is assigned to protons of the btdd^{2-} linker. The peaks at 3.5, 2.7, and 1.7 ppm are assigned to the protons of pyruvate. (Lower left) Solid-state ^{13}C NMR spectrum for $Zn_5(3\text{-}^{13}C\text{-}prv)_4(btdd)_3$ (3-^{13}C-prv = pyruvate labeled with ^{13}C on the methyl group carbon atom). All peaks (16.2, 19.6, 24.0, and ~38.2 ppm) were assigned to carbons of the pyruvate methyl group. Several carbon and hydrogen resonances assigned to pyruvate are observed in the spectra, possibly due to slightly different orientations of the ligand. (Right) Solid-state ^1H-^{13}C hetero-nuclear correlation spectrum for $Zn_5(3\text{-}^{13}C\text{-}prv)_4(btdd)_3$ (contact time 100 μs). The short contact time allows the detection of protons close to the ^{13}C nucleus of the pyruvate methyl group, confirming all the correlations are from protons of the methyl group. The ^{13}C and ^1H chemical shifts in the correlation spectrum match with the one-dimensional ^{13}C and ^1H NMR spectra.
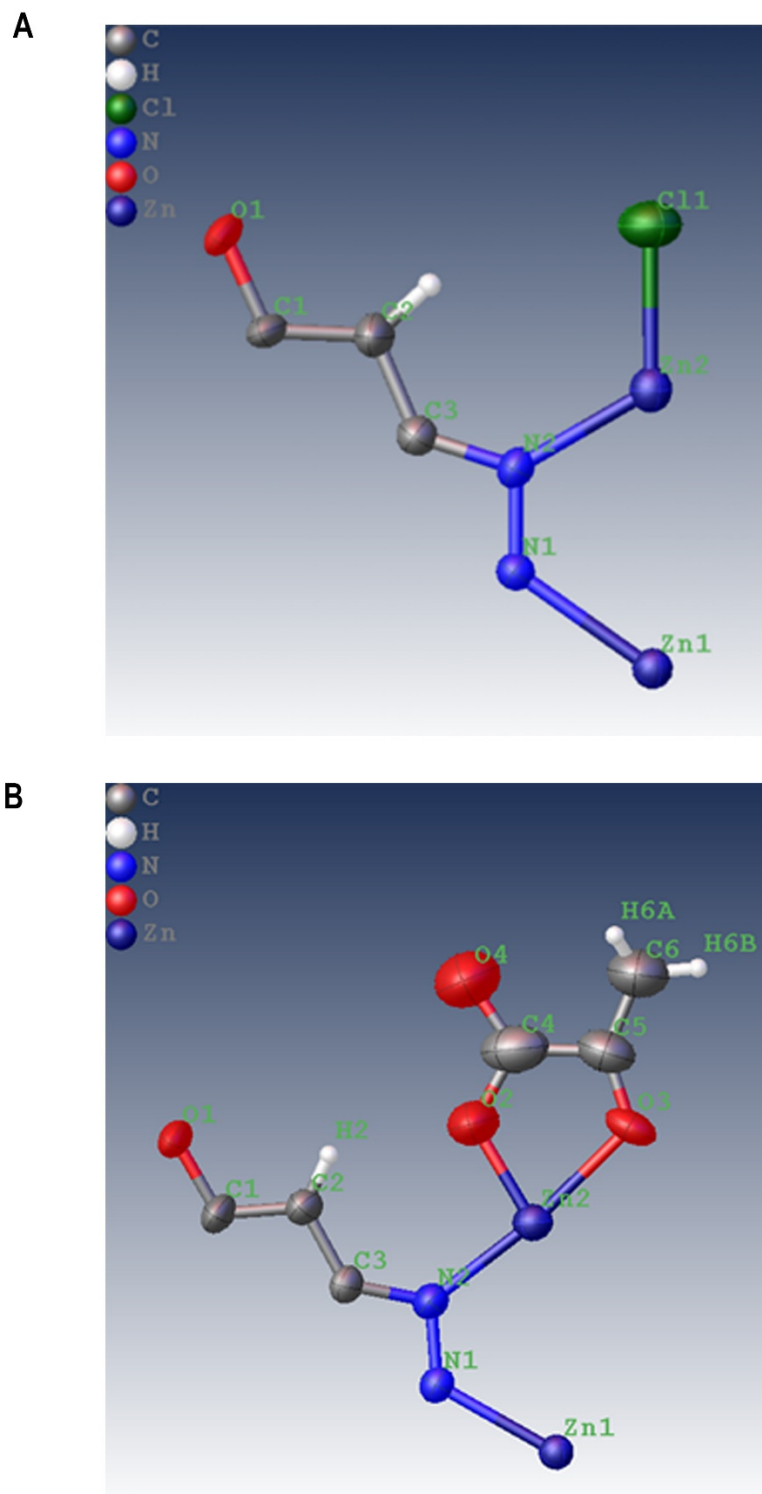
Fig. S14. Asymmetric units of the $Zn_5Cl_4(btdd)_3$ (**A**) and $Zn_5(prv)_4(btdd)_3$ (**B**) structures refined in the space group $Fm\bar{3}m$.
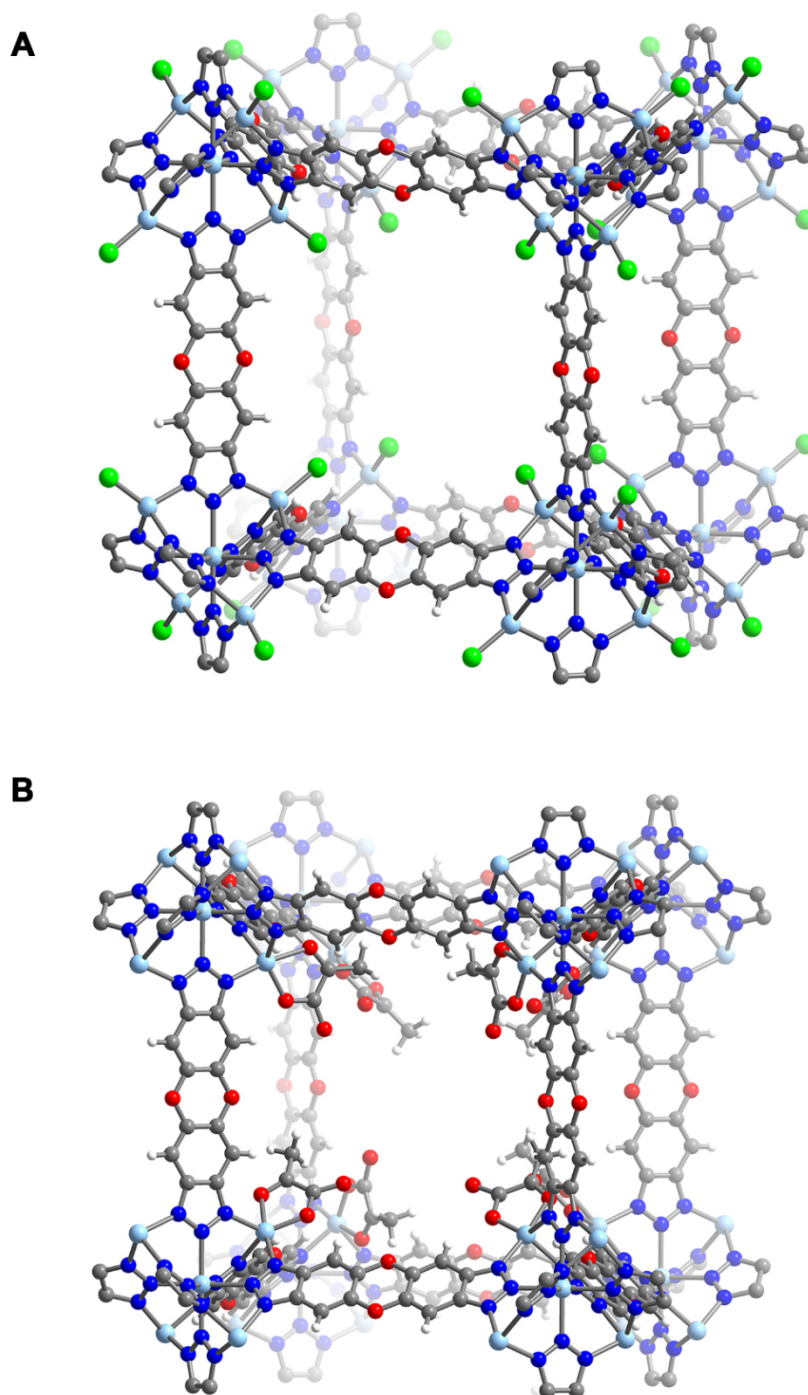
Fig. S15. Structures of $Zn_5Cl_4(btdd)_3$ (**A**) and $Zn_5(prv)_4(btdd)_3$ (**B**) obtained from single-crystal x-ray diffraction. Average positions of the linker atoms are shown because of disorder. Light blue, lime green, gray, red, blue, and white spheres represent Zn, Cl, C, O, N, and H atoms, respectively.
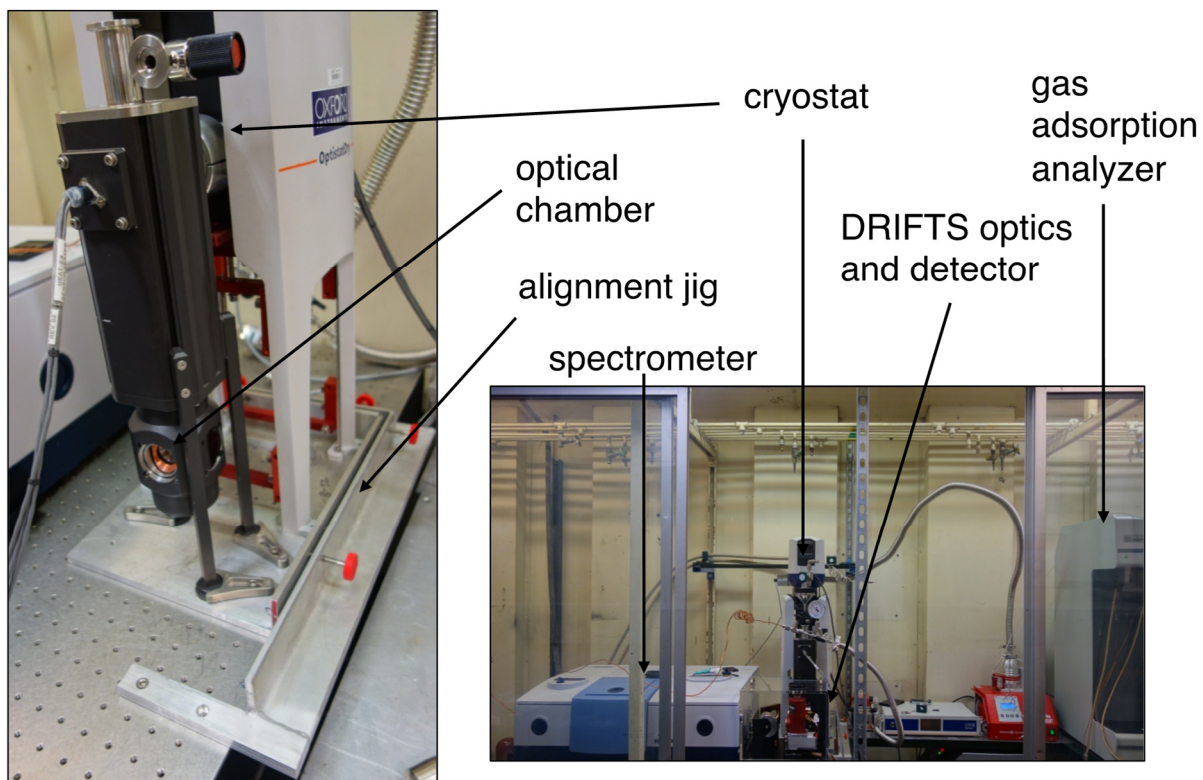
Fig. S16. Custom-made *in situ* DRIFTS apparatus.
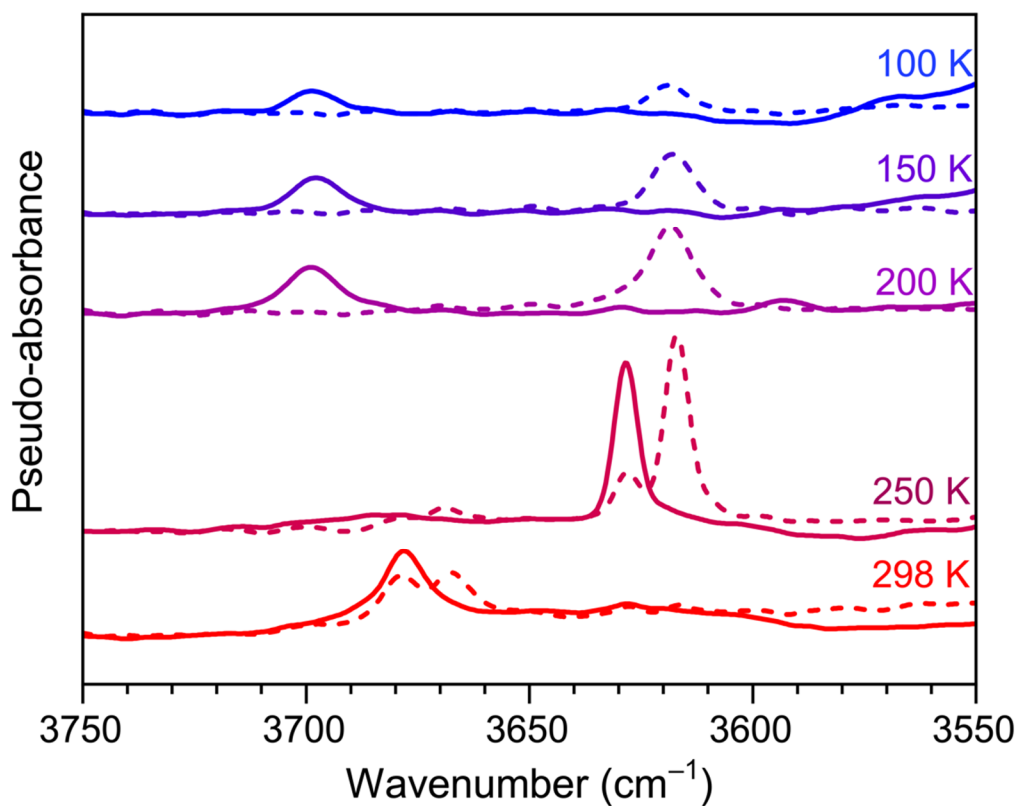
Fig. S17. *In situ* O_2 dosing DRIFTS experiments. For the standard reaction (solid lines), desolvated $FeZn_4(prv)_4(btdd)_3$ was dosed with 20 mbar O_2 at 100 K and slowly heated to 298 K. For the isotopic labelling experiment (dotted lines), the framework sample was labeled with ^{13}C at the carboxylic acid carbon of pyruvate and $^{18}O_2$ was used for dosing. The two peaks observed in the data obtained from the labelling experiment at higher temperatures suggest there may be scrambling of the oxygen atom from the proposed Fe(III)–^{18}OH and ^{16}O-atom of the formed acetate ligand.
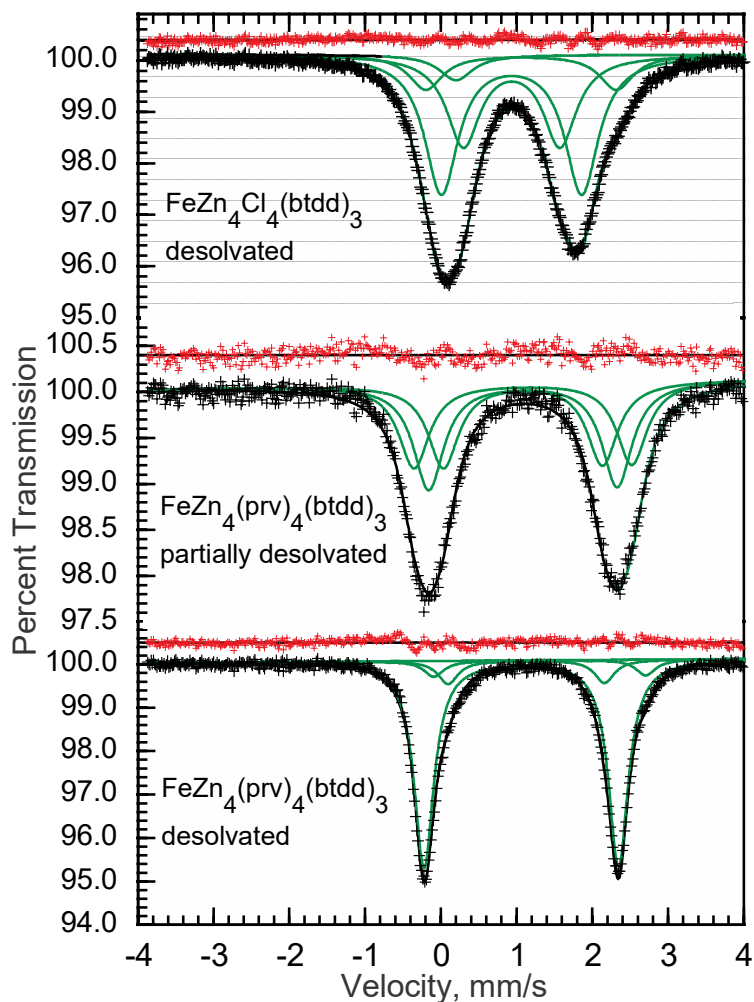
Fig. S18. Mössbauer spectra obtained at 5 K for $FeZn_4Cl_4(btdd)_3$ (upper), partially-solvated $FeZn_4(prv)_4(btdd)_3$ (middle), and desolvated $FeZn_4(prv)_4(btdd)_3$ (lower). The fit residuals are shown in red above the spectra. Details about the data fits are listed in table S5.
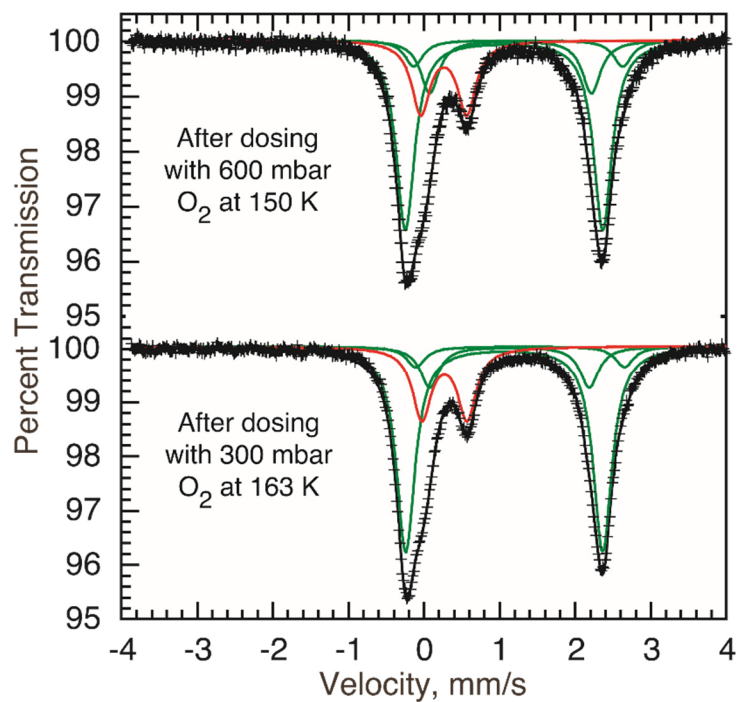
Fig. S19. Mössbauer spectra obtained at 5 K for FeZn$_4$(prv)$_4$(btdd)$_3$ after dosing *in situ* with 600 mbar O$_2$ at 150 K (upper) and 300 mbar O$_2$ at 163 K (lower) as indicated in timeline plot fig. S22. Details about the data fits are listed in table S7.
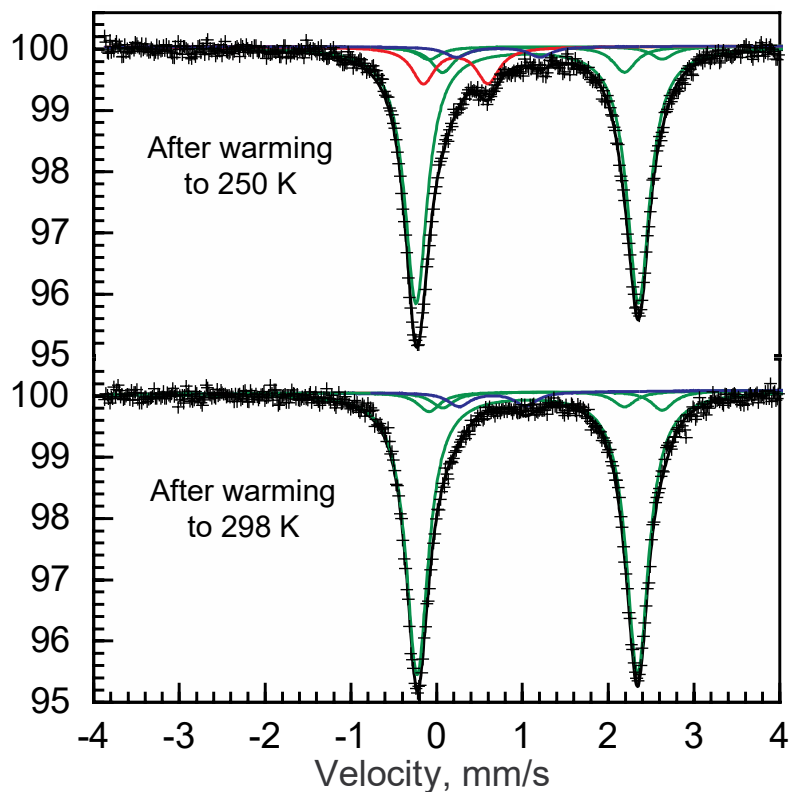
Fig. S20. Mössbauer spectra obtained at 5 K for *in situ* O_2-dosed $FeZn_4(prv)_4(btdd)_3$ after heating at 250 K for 2 h (upper) and subsequent heating at 298 K (lower) as indicated in timeline plot fig. S22. Fit details are given in table S6.
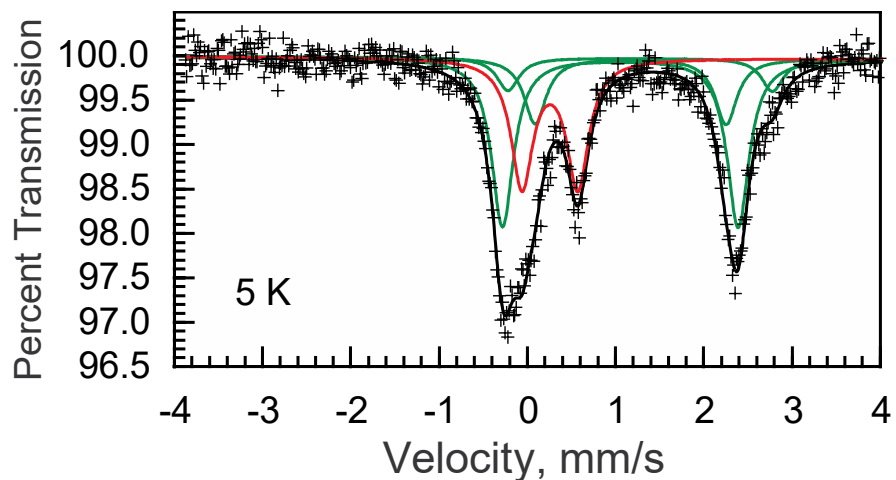
Fig. S21. Mössbauer spectrum of $FeZn_4(prv)_4(btdd)_3$ dosed *ex situ* with 200 mbar O_2 at 163 K. Details about the data fits are listed in table S8.
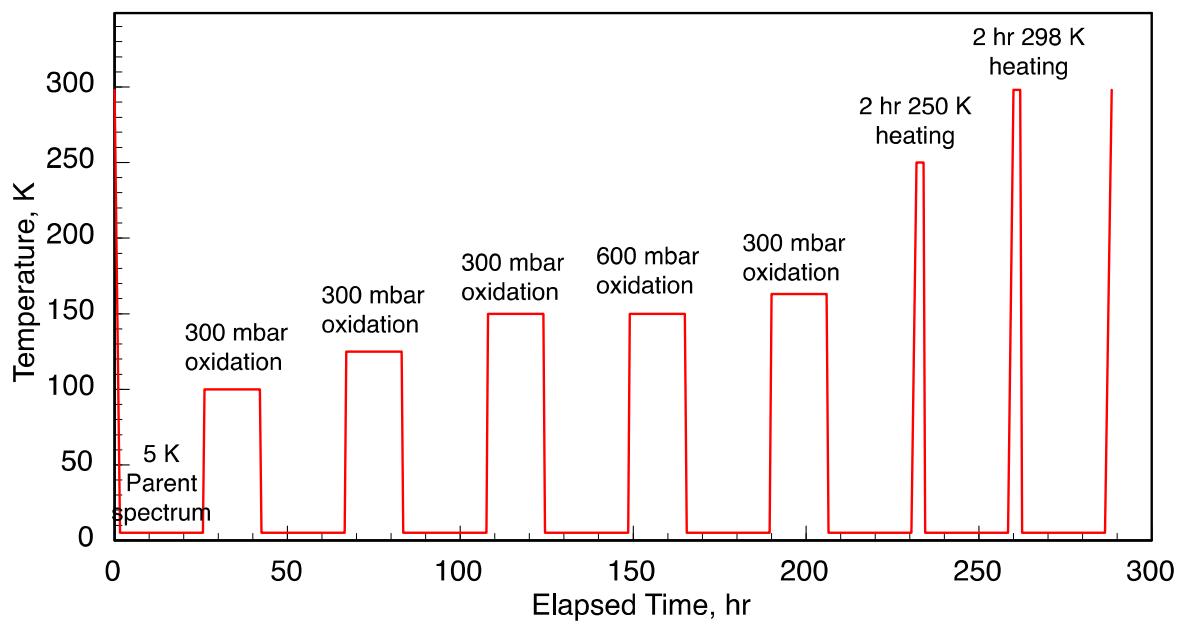
Fig. S22. Timeline and corresponding dosing conditions for the 5 K *in situ* Mössbauer spectroscopy experiment performed with FeZn$_4$(prv)$_4$(btdd)$_3$.
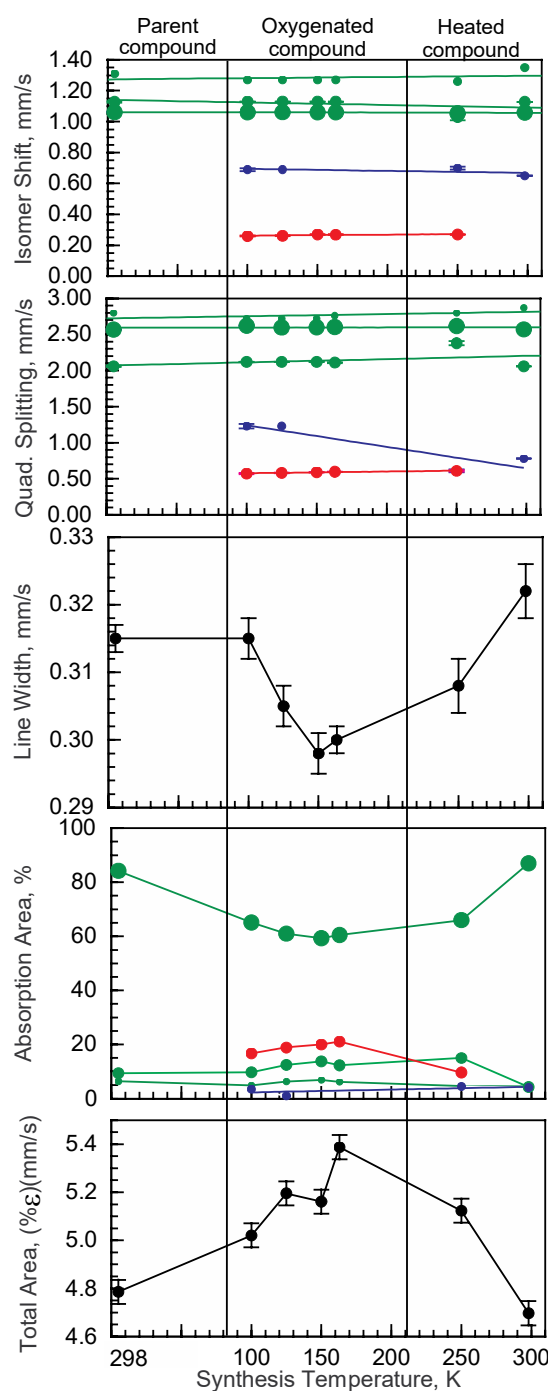
Fig. S23. Mössbauer spectral fit parameters obtained at 5 K for desolvated FeZn$_4$(prv)$_4$(btdd)$_3$ before (left) and after dosing with O$_2$ at the indicated temperatures and waiting for a period of 16 h, (middle) and after heating to 250 and 298 K (right) with no further oxidation. Green, red, and blue correspond to iron(II), iron(IV), and iron(III) components, respectively (table S6). Note that all the spectra were collected at 5 K and fit with a minimum number of symmetric quadrupole doublet components, all of which have the same linewidth in a given spectrum. When no uncertainty is shown it is less than the size of the data points.

44
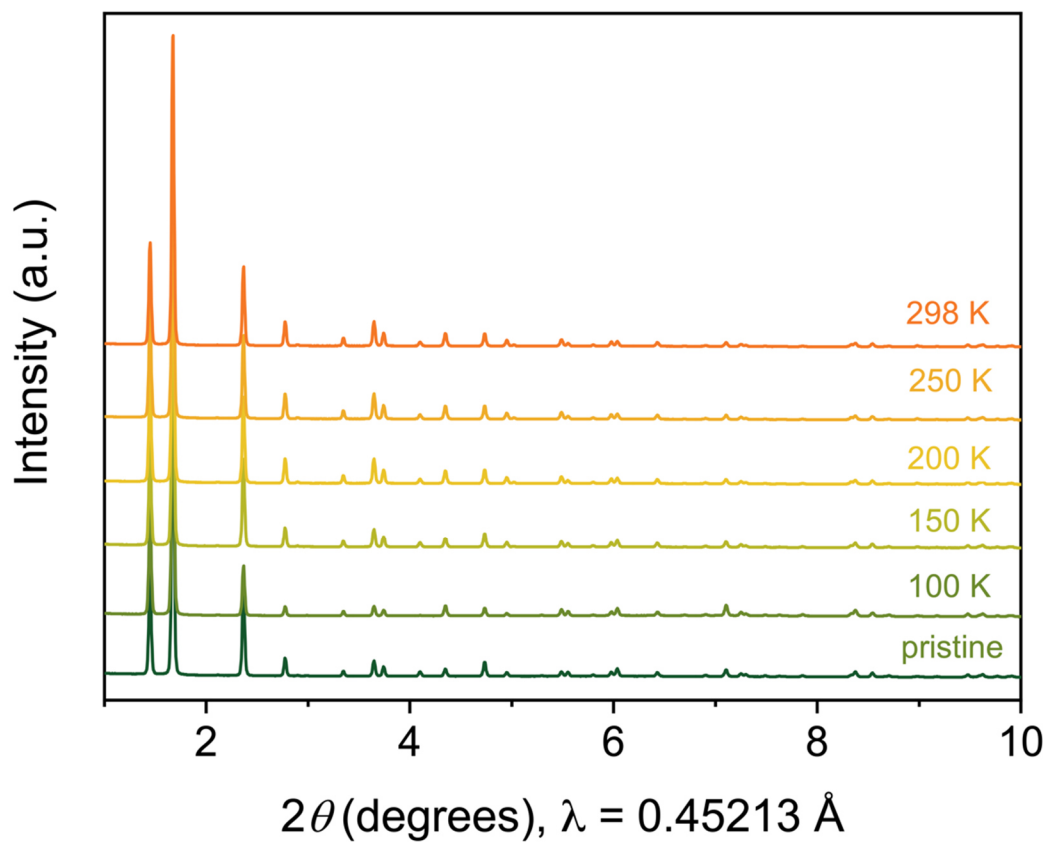
Fig. S24. Powder x-ray diffraction patterns collected for pristine, desolvated $FeZn_4(prv)_4(btdd)_3$ under vacuum (dark green) and after *in situ* dosing with 80 mbar of O_2 at 100 K and gradual warming to 298 K (light green to orange).
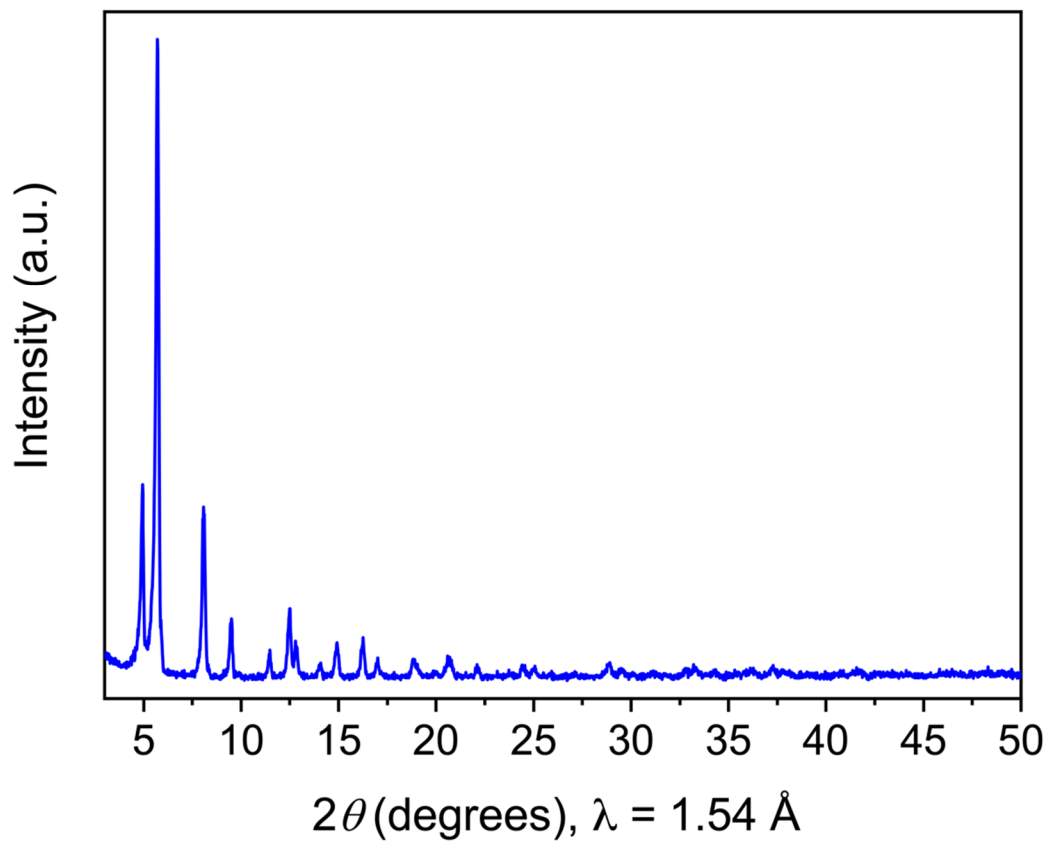
Fig. S25. Powder x-ray diffraction pattern obtained for a sample of $FeZn_4(prv)_4(btdd)_3$ following *ex situ* dosing with 200 mbar O_2 at 163 K and warming to 298 K.
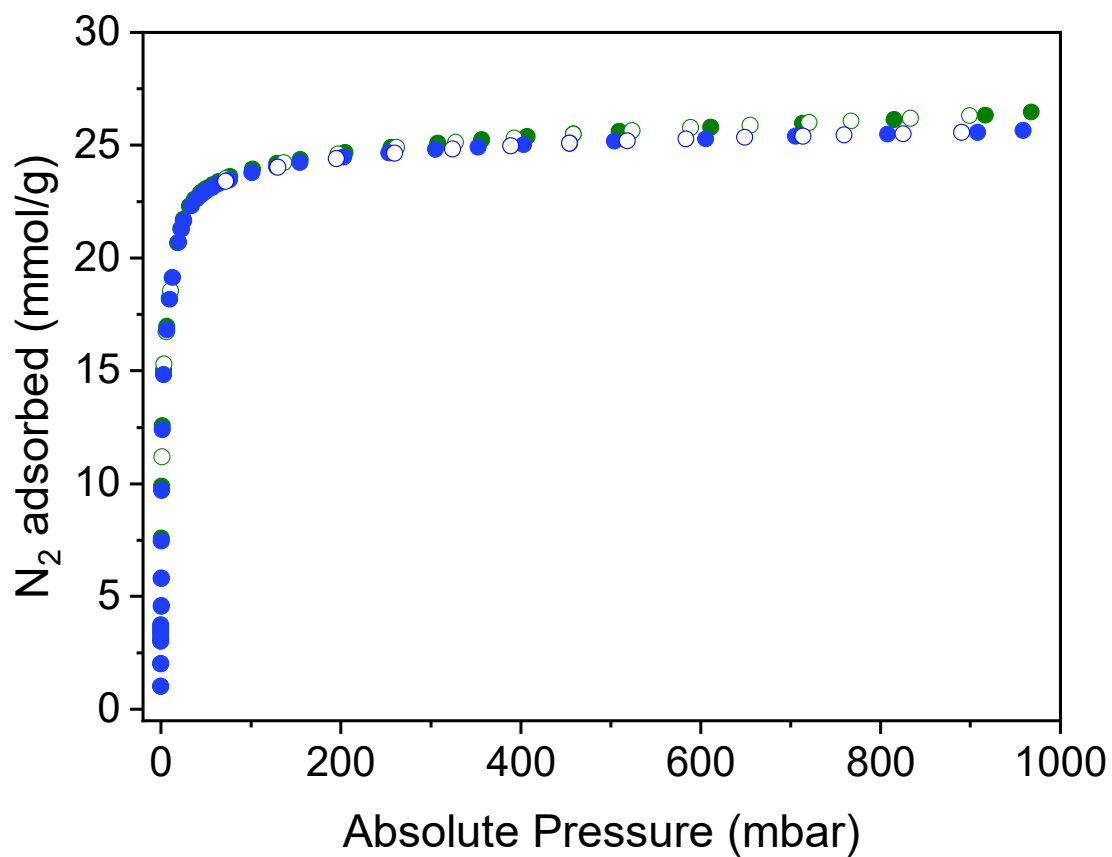
Fig. S26. Nitrogen adsorption (open symbols) and desorption (closed symbols) data collected at 77 K for a sample of $FeZn_4(prv)_4(btdd)_3$ before (green) and after dosing with 200 mbar O_2 at 163 K followed by warming to 298 K (blue).
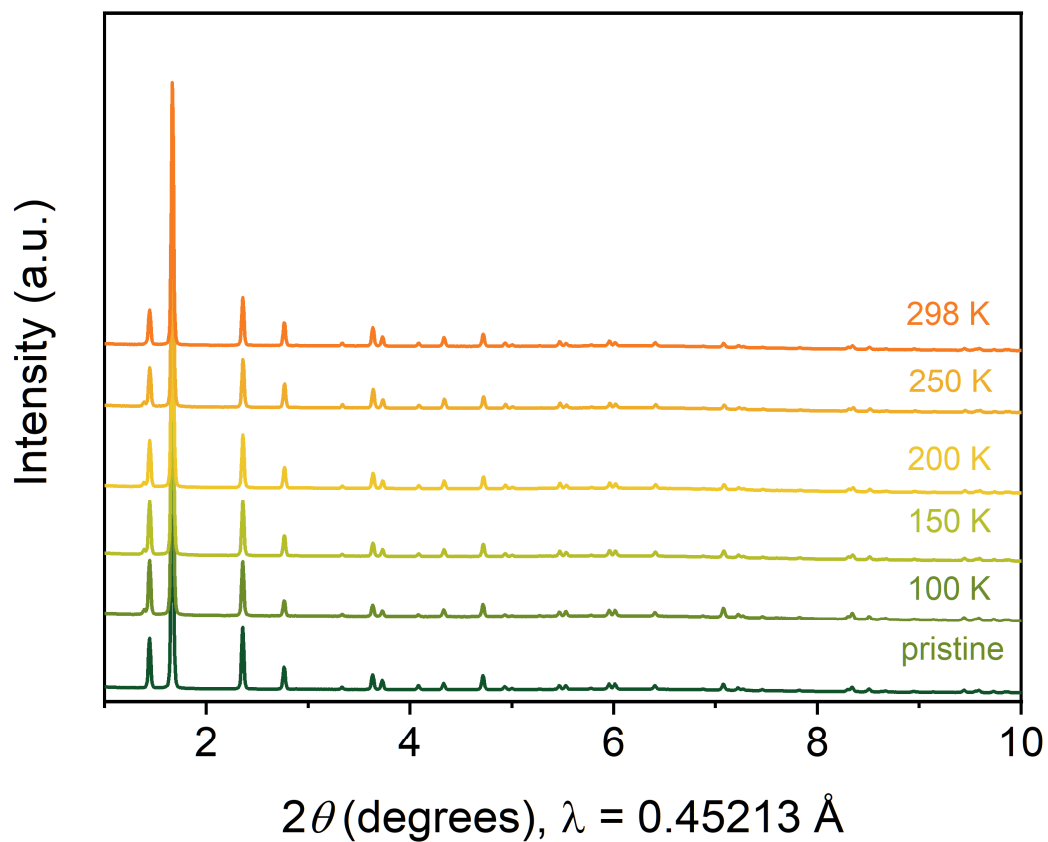
Fig. S27. Powder x-ray diffraction patterns collected for pristine, desolvated $FeZn_4(moba)_4(btdd)_3$ under vacuum (dark green) and after *in situ* dosing with 80 mbar of O_2 at 100 K and gradual warming to 298 K (light green to orange).
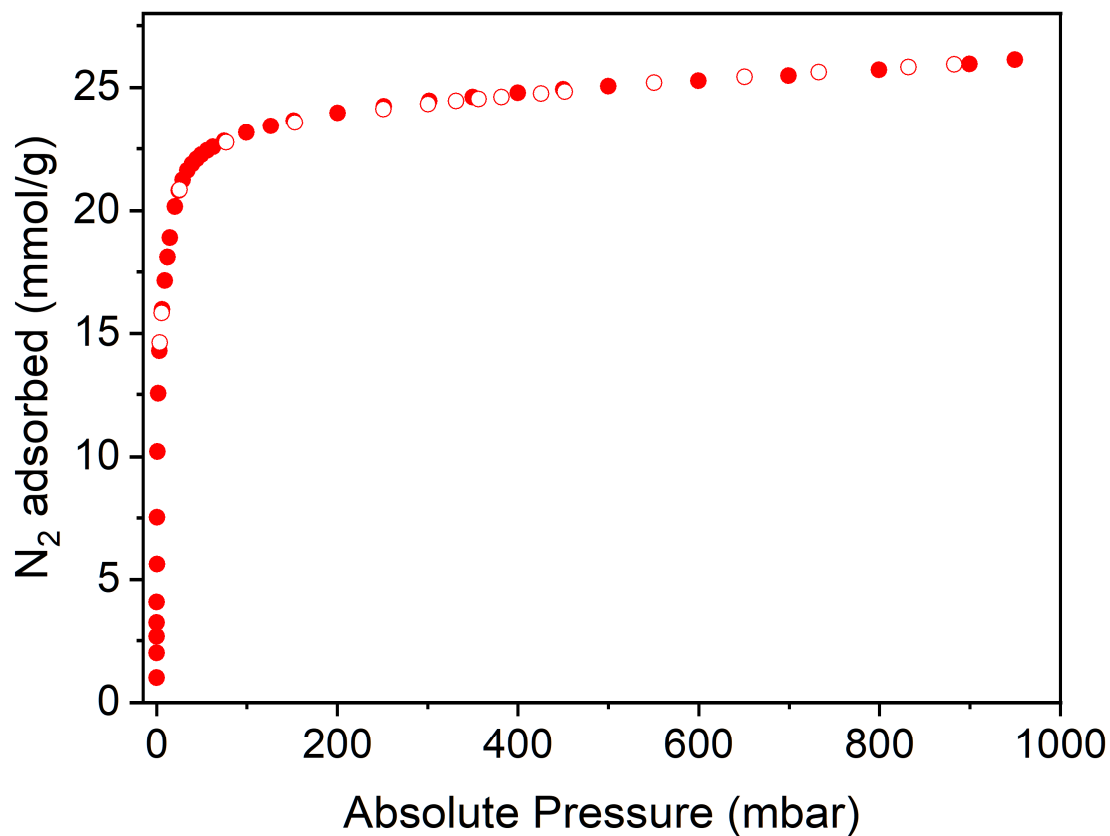
Fig. S28. Nitrogen adsorption (filled symbols) and desorption (open symbols) data collected at 77 K for FeZn$_4$(moba)$_4$(btdd)$_3$. The BET surface area is 2180±11 m^2/g.
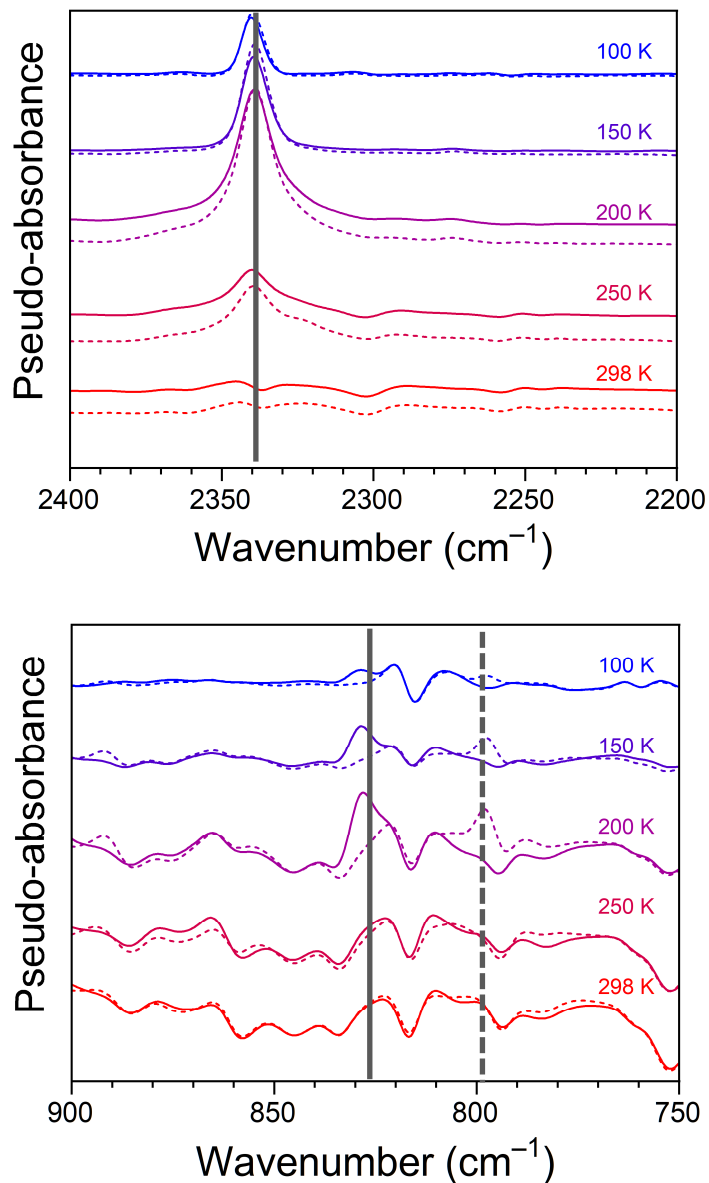
Fig. S29. Variable-temperature diffuse reflectance Fourier transform spectra for $FeZn_4(moba)_4(btdd)_3$ dosed with 20 mbar O_2 at 100 K. The band at $v = 2340$ cm^{-1} is consistent with CO_2 formation, adsorption at low temperatures, and desorption at higher temperatures (top). The band at $v = 828$ cm^{-1} is assigned as the Fe(IV)=O species and the band at $v = 794$ cm^{-1} as Fe(IV)=^{18}O. The disappearance of the bands above 200 K is consistent with decomposition of the Fe(IV)=O species. The observed bathochromic shift is in excellent agreement with the prediction by a simple harmonic oscillator calculation ($v = 792$ cm^{-1}).
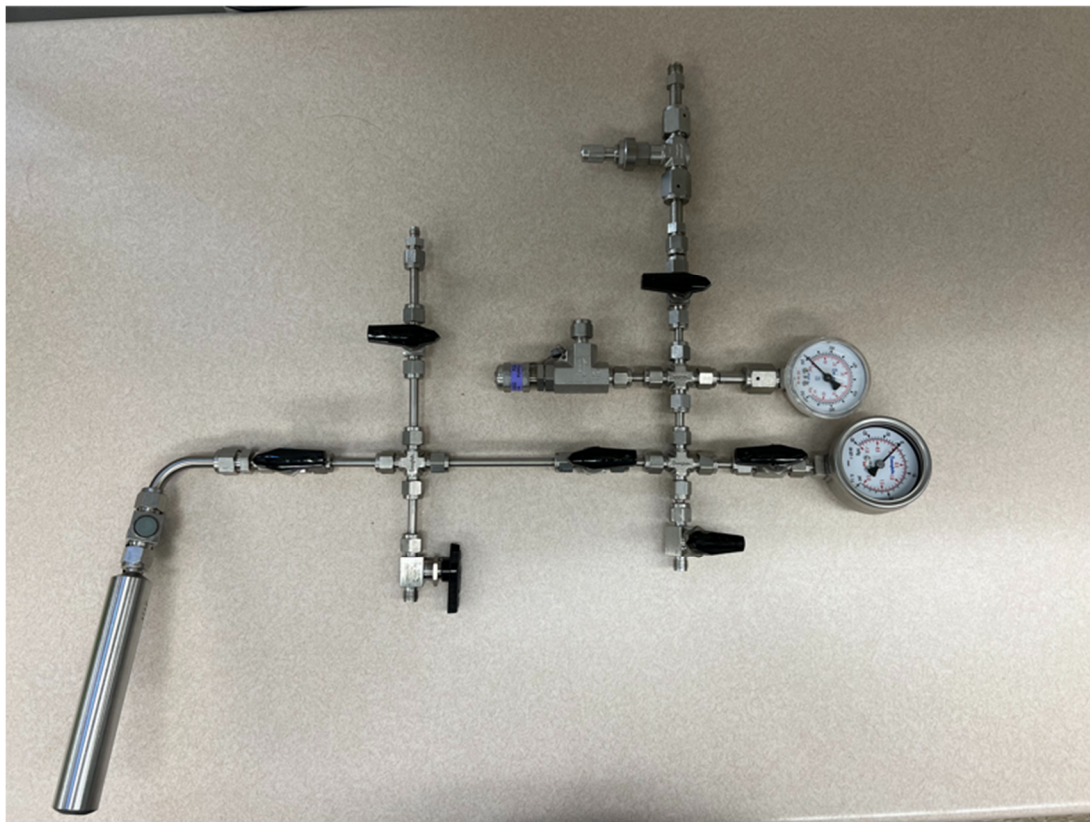
Fig. S30. Custom-made gas dosing manifold used in nuclear resonance vibrational spectroscopy, Mössbauer spectroscopy, and reactivity studies.
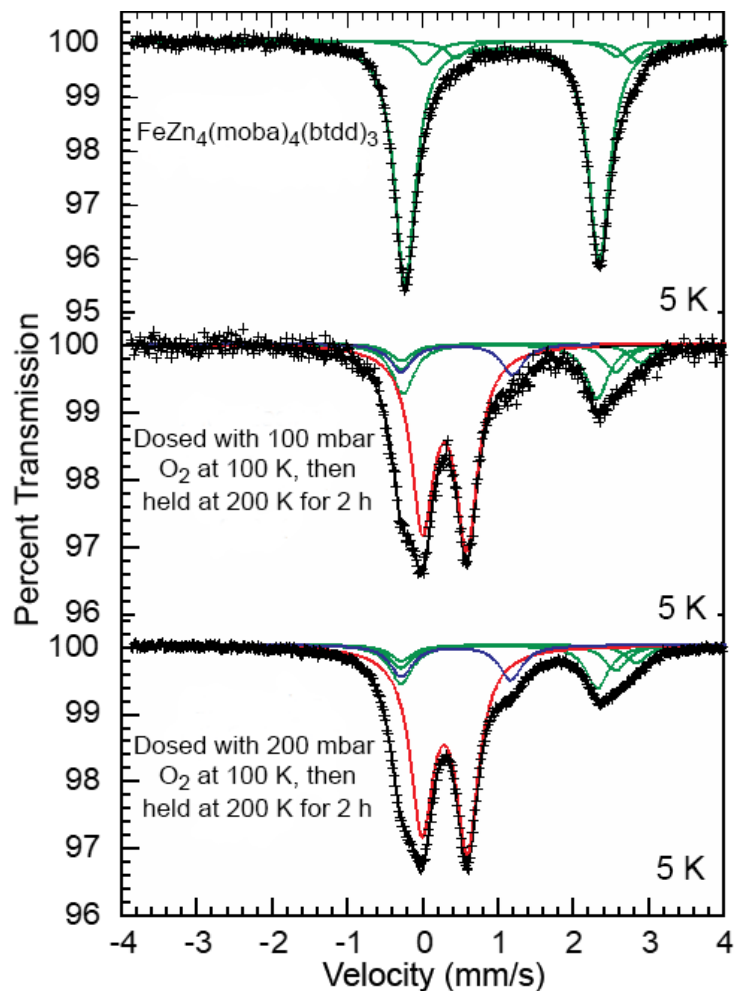
Fig S31. Mössbauer spectra collected at 5 K for FeZn$_4$(moba)$_4$(btdd)$_3$ before (upper) and after (middle, lower) *in situ* dosing with O$_2$ under the indicated conditions (see Section 2.12.1). Green, red, and blue lines correspond to fits assigned to iron(II), iron(IV), and iron(III), respectively. Details about the fits are given in table S10.
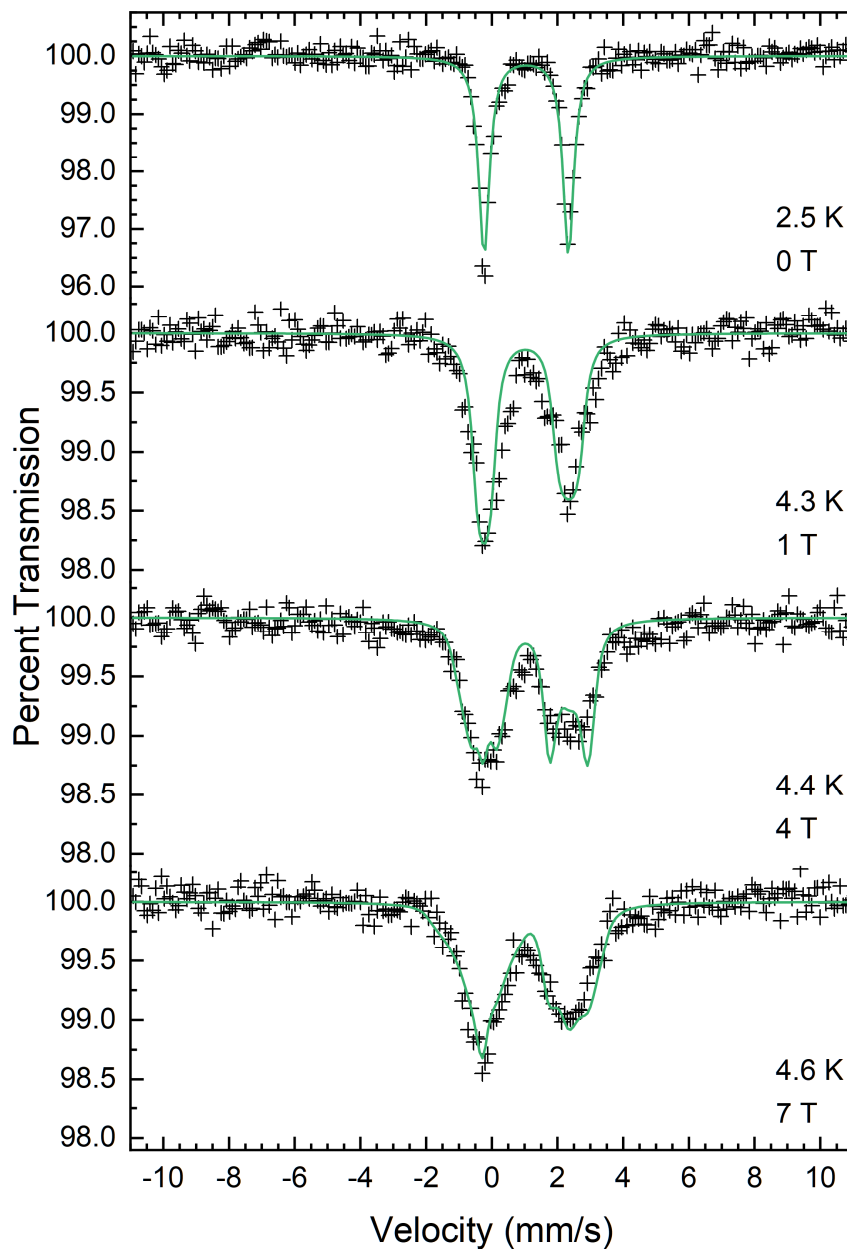
Fig. S32. Mössbauer data collected at low temperatures and 0, 1, 4, and 7 T (top to bottom) for the framework $FeZn_4(moba)_4(btdd)_3$. The data were modeled with a single subspectrum (green trace) with spin Hamiltonian parameters reported in table S12. In order to avoid overparameterization, this single site model was deemed adequate to capture the behavior of the residual iron(II) species in all other applied field Mössbauer spectra for O_2-dosed $FeZn_4(moba)_4(btdd)_3$.
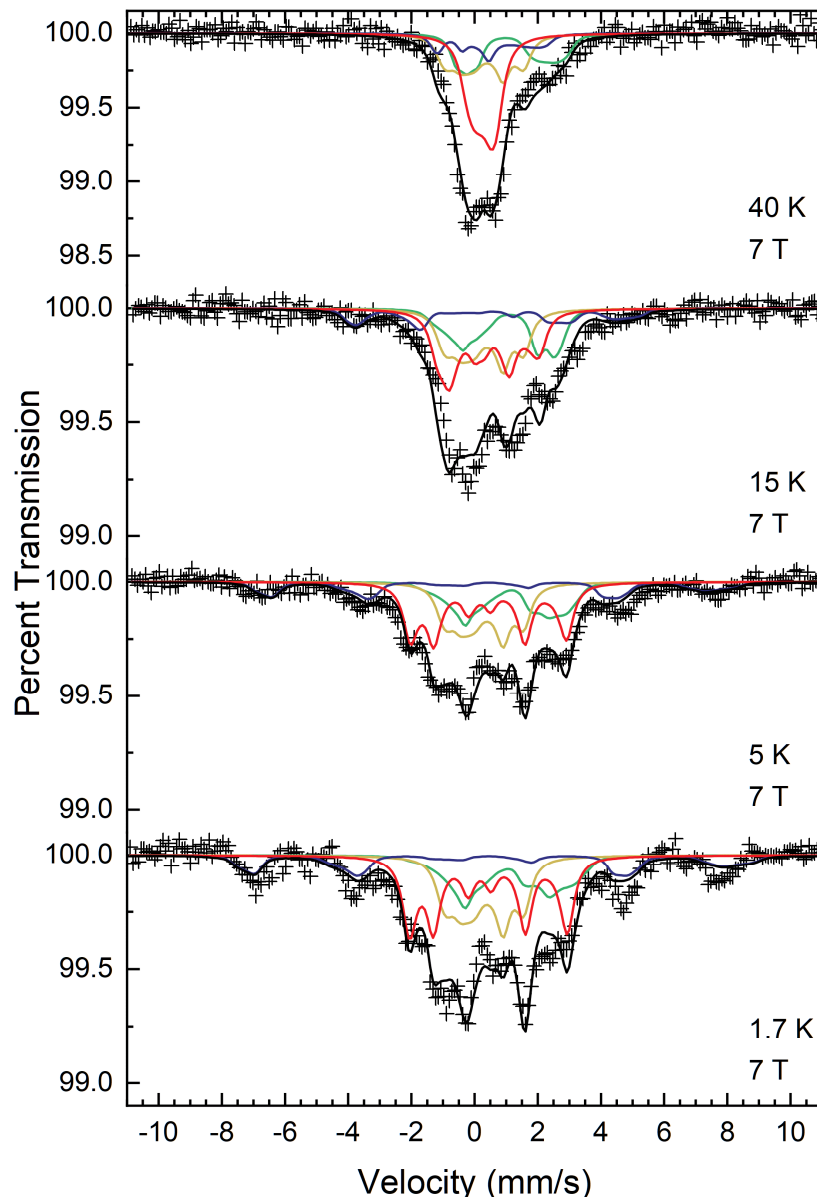
Fig. S33. Mössbauer data collected for O_2-dosed $FeZn_4(moba)_4(btdd)_3$ under a 7 T magnetic field at 40, 15, 5, and 1.7 K (plus symbols) plotted together with the optimized model for a system featuring $S = 2$ Fe(IV)=O species, as discussed in Section 2.12.3. The overall model is shown as a black solid line, and the four subspectra (modeled with the spin Hamiltonian parameters reported in table S13) correspond to the following species in the framework: $S = 2$ Fe(II) species (green); $S = 5/2$ Fe(III) species (blue); $S = 2$ Fe(IV)=O species (red); and $S_{tot} = 0$ species formed from antiferromagnetic coupling between neighboring $S = 2$ Fe(IV)=O sites in one cluster node (dark yellow). The combined areas of the dark yellow and red subspectra show that the sample is comprised of ~65% Fe(IV)=O, ~21% unoxidized Fe(II) starting-material, and ~14% Fe(III) species. Of the ~65% Fe(IV)=O species, ~43% (corresponding to approximately 28% of the total spectral area) are engaged in antiferromagnetic coupling, while ~57% (corresponding to approximately 37% of the total spectral area) are not.

54
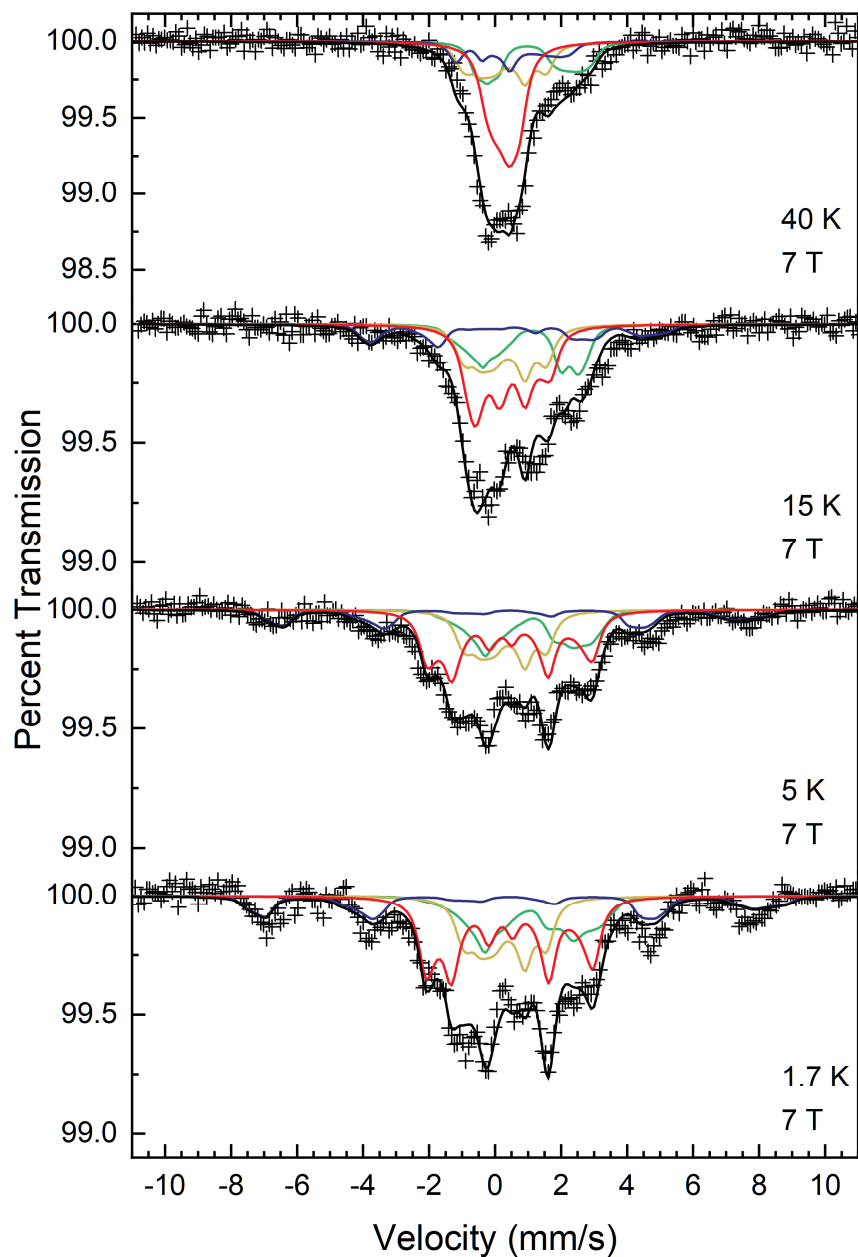
Fig. S34. Mössbauer data collected for O_2-dosed $FeZn_4(moba)_4(btdd)_3$ at 40, 15, 5, and 1.7 K and 7 T (plus symbols) plotted together with the optimized model for a system featuring $S = 1$ Fe(IV)=O species, as discussed in Section 2.12.3 (solid black line). The four subspectra (modeled with the spin Hamiltonian parameters reported in table S14) correspond to the following species in the framework: $S = 2$ Fe(II) species (green); $S = 5/2$ Fe(III) species (blue); $S = 1$ Fe(IV)=O species (red); $S_{tot} = 0$ species formed from antiferromagnetic coupling between neighboring $S = 1$ Fe(IV)=O sites in one cluster node (dark yellow).

55
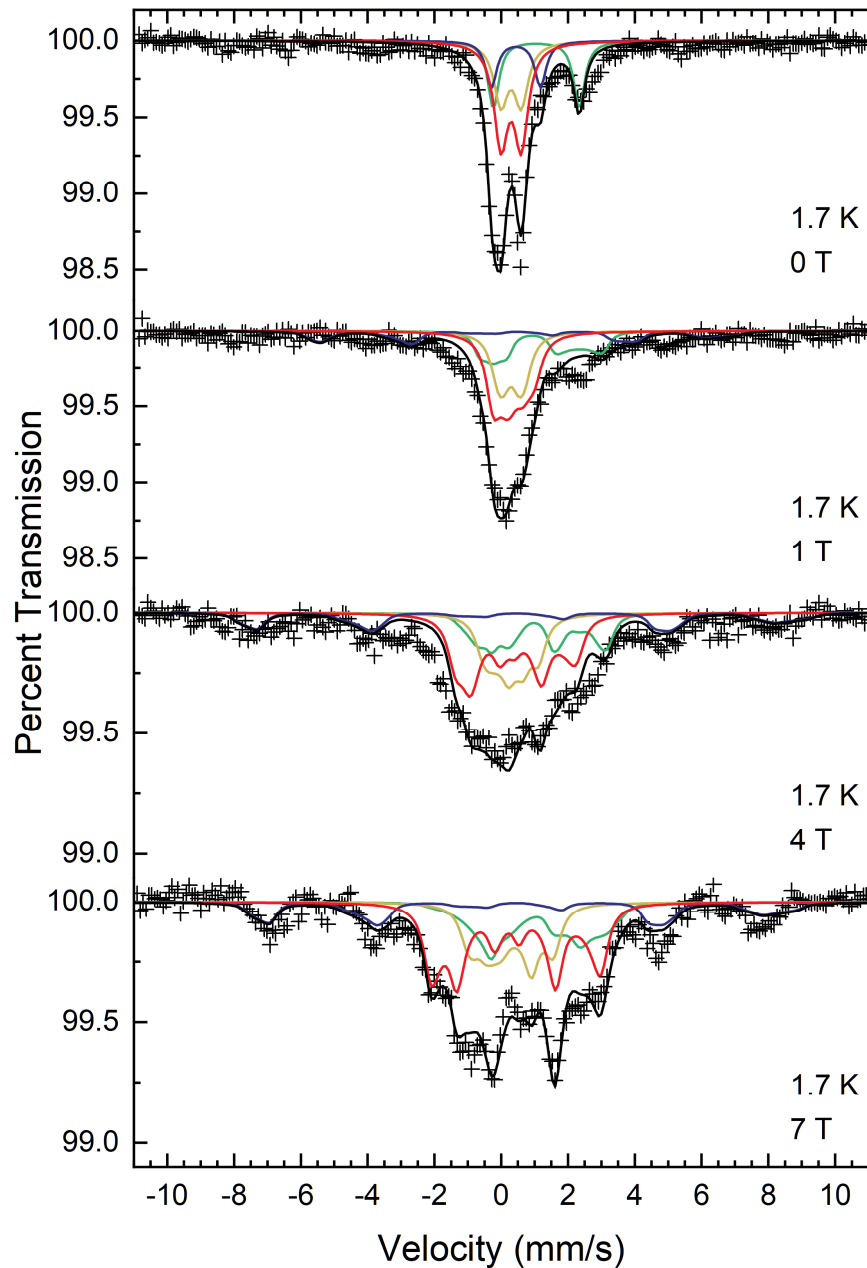
Fig. S35. Mössbauer data collected for O_2-dosed $FeZn_4(moba)_4(btdd)_3$ at 0, 1, 4, and 7 T and 1.7 K (plus symbols) plotted together with the optimized model for a system featuring $S = 1$ Fe(IV)=O species, as discussed in Section 2.12.3 (solid black line). The four subspectra (modeled with the spin Hamiltonian parameters reported in table S14) correspond to the following species in the framework: $S = 2$ Fe(II) species (green); blue: $S = 5/2$ Fe(III) species (blue); $S = 1$ Fe(IV)=O species (red); $S_{tot} = 0$ species formed from antiferromagnetic coupling between neighboring $S = 1$ Fe(IV)=O sites in one cluster node (dark yellow).

56
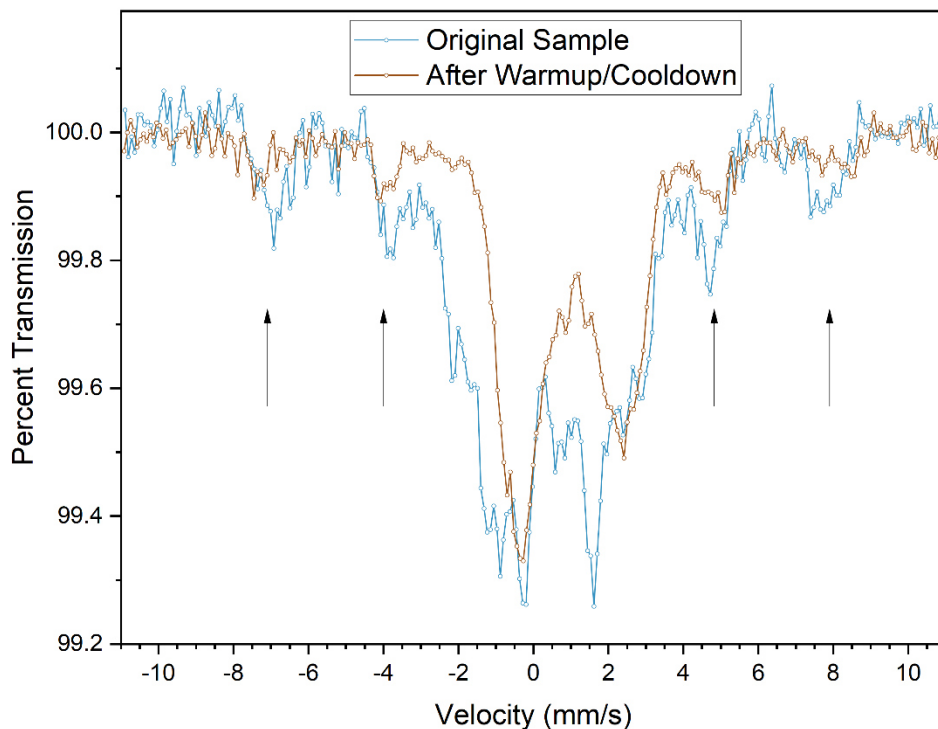
Fig. S36. Overlay of the Mössbauer data collected for O$_2$-dosed FeZn$_4$(moba)$_4$(btdd)$_3$ at 1.7 K and 7 T (blue trace) and the same sample after warming to 300 K for 2 h, followed by cooling to 1.7 K and data collection at 1.7 K and 7 T (brown trace). As discussed in the main text, the features near ±4 mm/s in the initial (blue) spectrum are similar to features that have been associated with S = 2 Fe(IV)=O complexes in the literature (*6, 17, 31*). However, it is clear that these features persist in the brown spectrum, which was collected after warming the sample to 300 K (and corresponding Fe(IV)=O decomposition). As such, these features are not associated with the subspectrum corresponding to the Fe(IV)=O species of interest, but rather result from the Fe(III) species present.
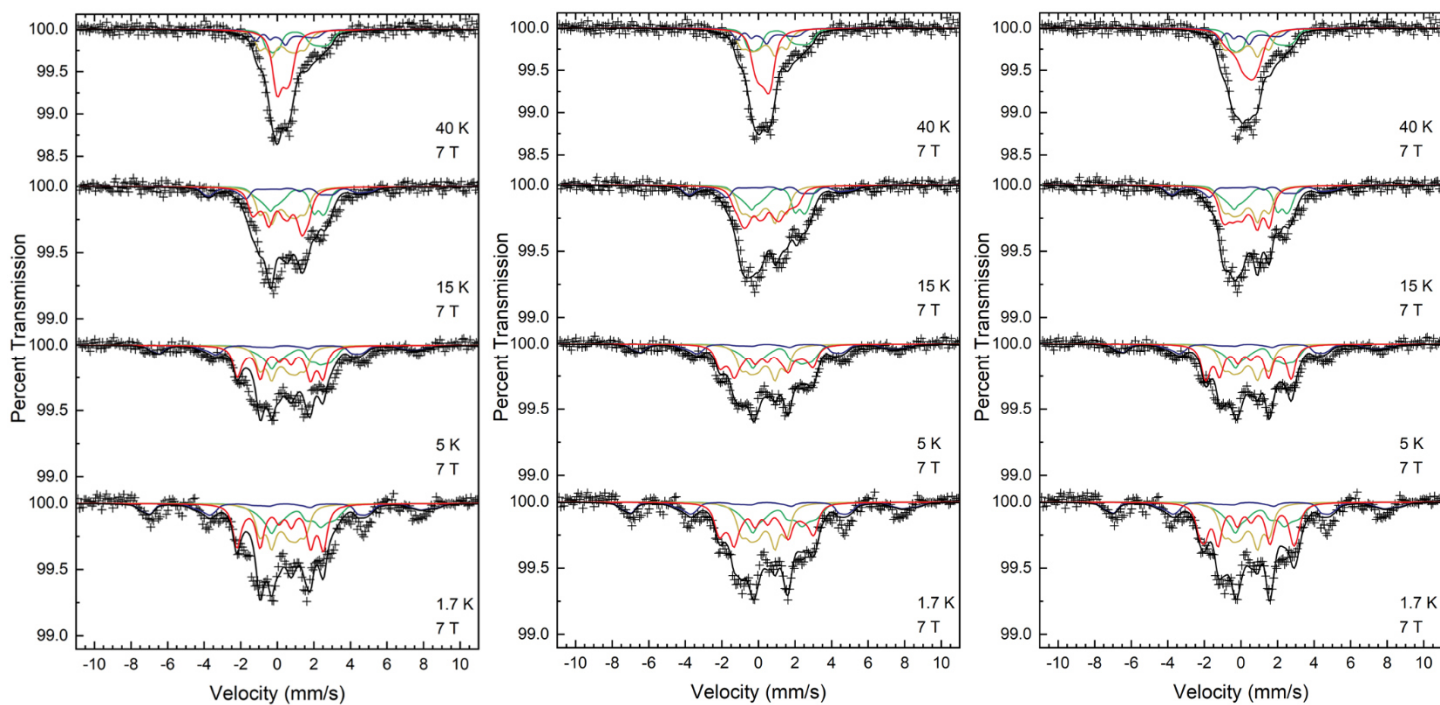
Fig. S37. Mössbauer data collected at 40, 15, 5, and 1.7 K at 7 T for O_2-dosed $FeZn_4(moba)_4(btdd)_3$ (plus symbols) plotted with alternative models for the $S = 2$ Fe(IV)=O subspectrum featuring a positive quadrupole splitting (left), including rhombicity (middle), and excluding A_{zz} (right). These correspond to models 9, 15, and 14, respectively, in table S15.
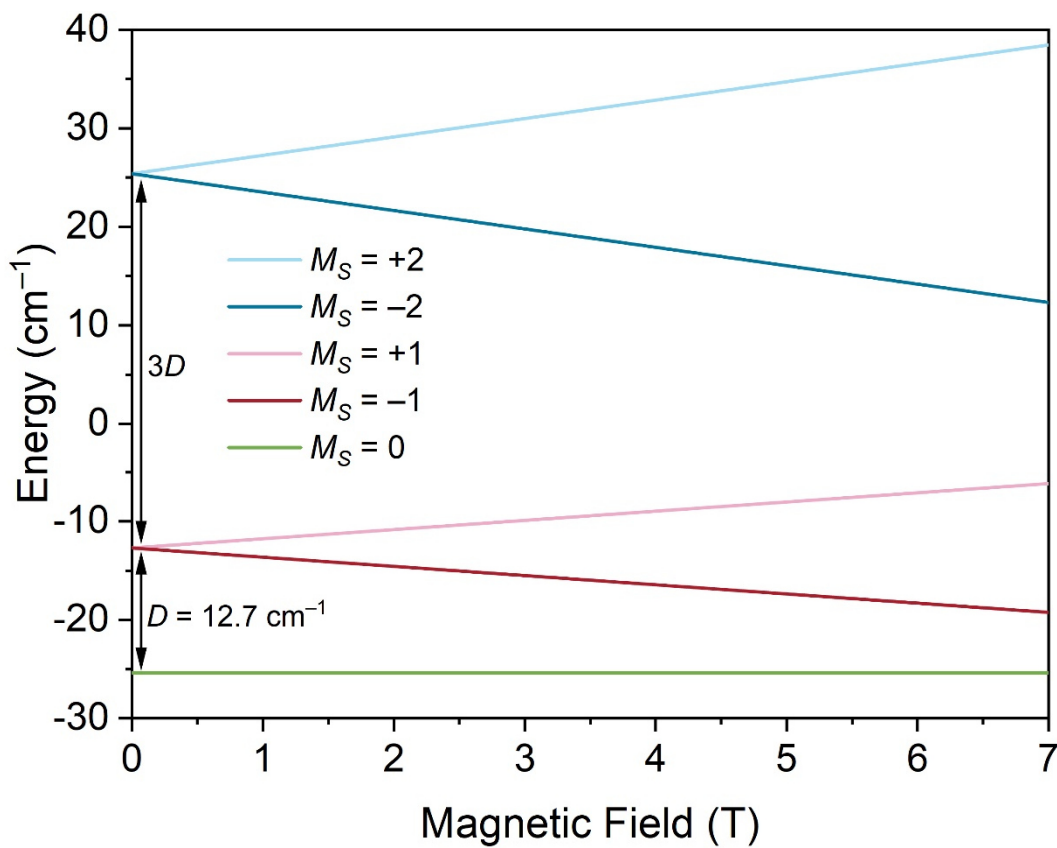
Fig. S38. Zero-field splitting diagram at 1.7 K based on the final model chosen for $S = 2$ Fe(IV)=O species in FeZn$_4$(moba)$_4$(btdd)$_3$ ($D = 12.7$ cm^{-1}; see table S15, model 13). The diagram was generated by simulating the expectation values when applying the external field in the z-direction for each of the M_S levels according to the following spin Hamiltonian: $\widehat{H} = \mu_B gHS + D\left[S_z^2 - \frac{1}{3}S(S+1)\right]$, where $g = 2.0$, close to the free electron value $g_e = 2.002319$. The different M_S components are projections of the spin onto the z-axis. The energies were generated using the program spex.SL (written by Eckhard Bill and available by email to daniel.santalucia@cec.mpg.de).
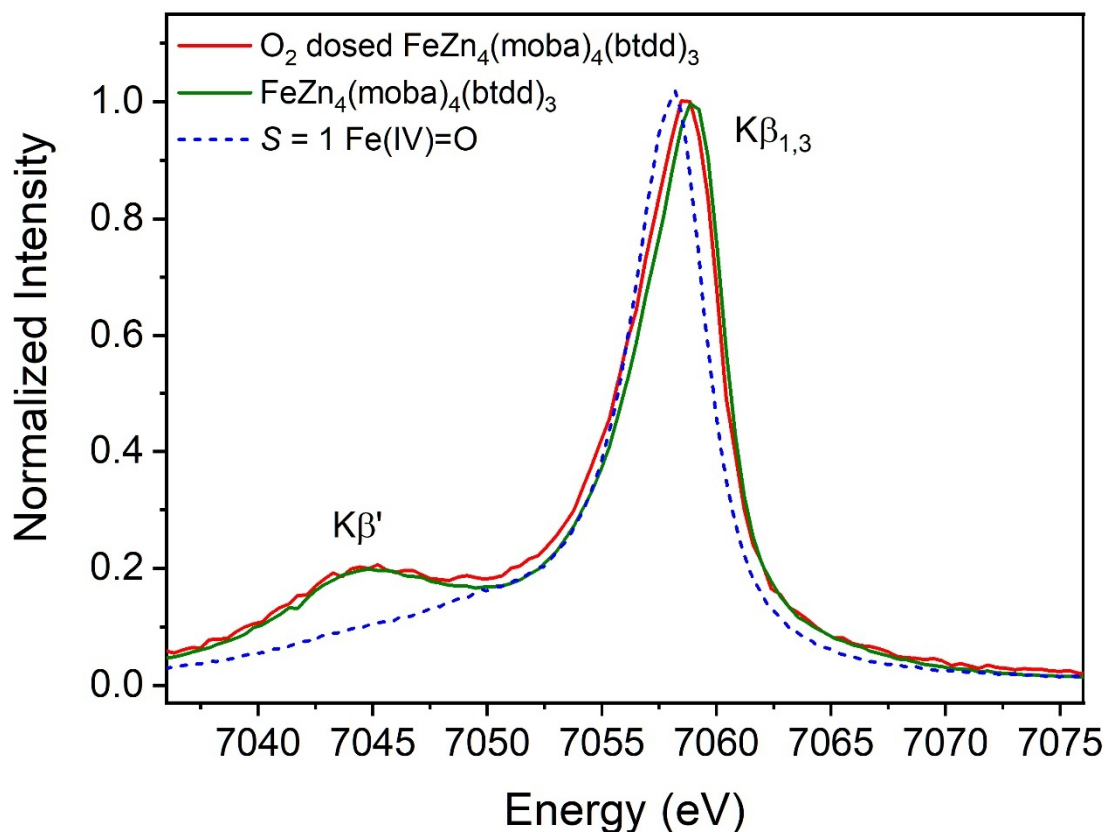
Fig. S39. Comparison of the Fe Kβ x-ray emission spectra of FeZn4(moba)4(btdd)3 (solid green line) and the O2-dosed sample (solid red line), both collected at 30 K, with the Fe Kβ x-ray emission spectrum for an $S = 1$ Fe(IV)-oxo complex ([Fe^{IV}(O)(2PyN2Q)](PF6)2; 2PyN2Q = 1,1-di(pyridin-2-yl)-*N,N*-bis(quinolin-2-ylmethyl)methanamine) collected at 20 K (dashed blue line) as reported in reference *42*. The data for the $S = 1$ Fe(IV)-oxo complex was reproduced with permission under a Creative Commons Attribution 4.0 International license (http://creativecommons.org/licenses/by/4.0/). Note, the Kβ$_{1,3}$ feature for the O2-dosed sample is ~0.3 eV lower in energy than the Kβ$_{1,3}$ peak for FeZn4(moba)4(btdd)3, which is consistent with higher covalency in the Fe(IV)–ligand interactions relative to the Fe(II)–ligand interactions.
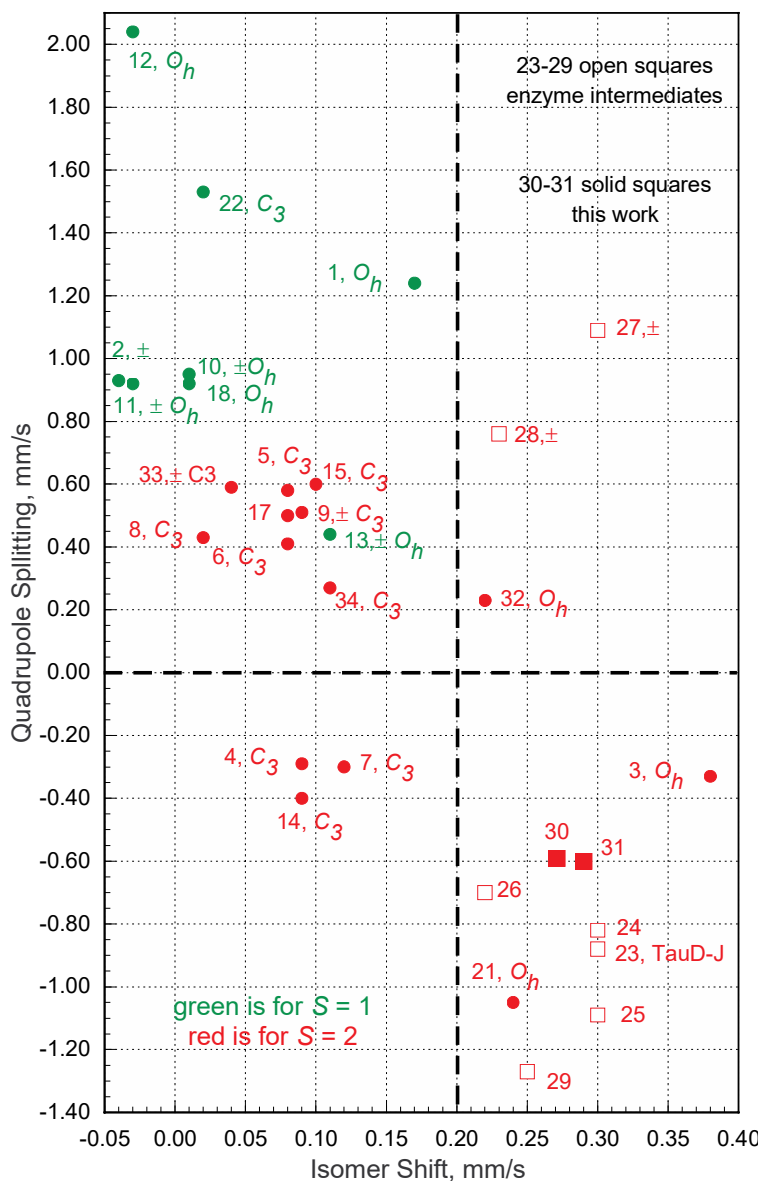
Fig. S40. Correlation between the quadrupole splitting, $\varDelta E_Q$, and the isomer shift, δ, determined for iron(IV)=O sites in the compounds indexed in table S3, a list that is derived from Table 1 in reference *15*. Green and red symbols denote assignments made for $S = 1$ and $S = 2$ Fe(IV)=O species, respectively. For data points accompanied by "±", the sign of $\varDelta E_Q$ is unknown, and the reported value represents the magnitude only. When known, the approximate iron(IV) local coordination environments are also given. The solid square symbols represent the results for FeZn$_4$(prv)$_4$(btdd)$_3$ (**30**) and FeZn$_4$(moba)$_4$(btdd)$_3$ (**31**) and the open square symbols are the results for Fe(IV)=O enzyme intermediates. These data indicates that an isomer shift of 0.20 mm/s is an upper bound for an $S = 1$ five or six-coordinate Fe(IV)=O species, whereas the five or six-coordinate $S = 2$ Fe(IV)=O species exhibit isomer shifts between 0.02 and 0.37 mm/s. The absolute quadrupole splitting values for the $S = 2$ six-coordinate Fe(IV)=O species are between 0.23 and 1.27 mm/s. The parameters determined for the Fe(IV)=O component of O$_2$-dosed FeZn$_4$(prv)$_4$(btdd)$_3$ and FeZn$_4$(moba)$_4$(btdd)$_3$ are consistent with an $S = 2$ spin state assignment.

61
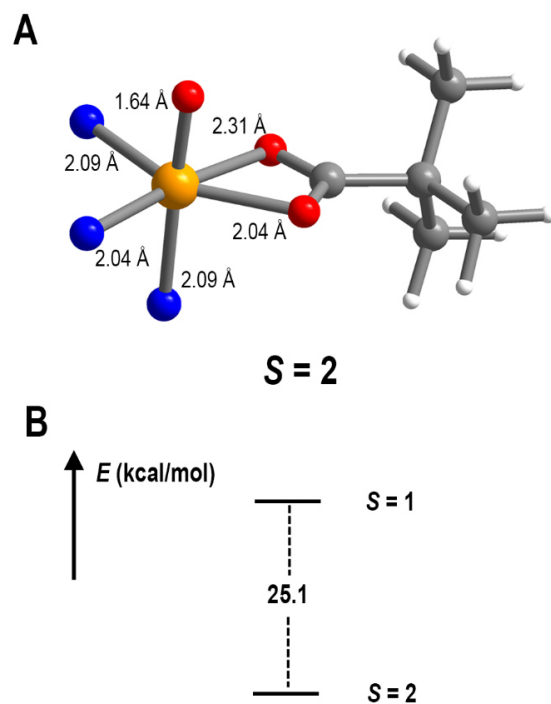
Fig. S41. (**A**) Iron–ligand bond lengths for the DFT-optimized $S = 2$ geometry of Fe(O)(κ^2-OPiv)Zn$_4$(prv)$_3$(bta)$_6$. (**B**) Energy difference between the $S = 2$ ground state and lowest $S = 1$ excited state obtained from CASSCF/NEVPT2 calculations using the DFT-optimized geometry for an $S = 2$ ground state.
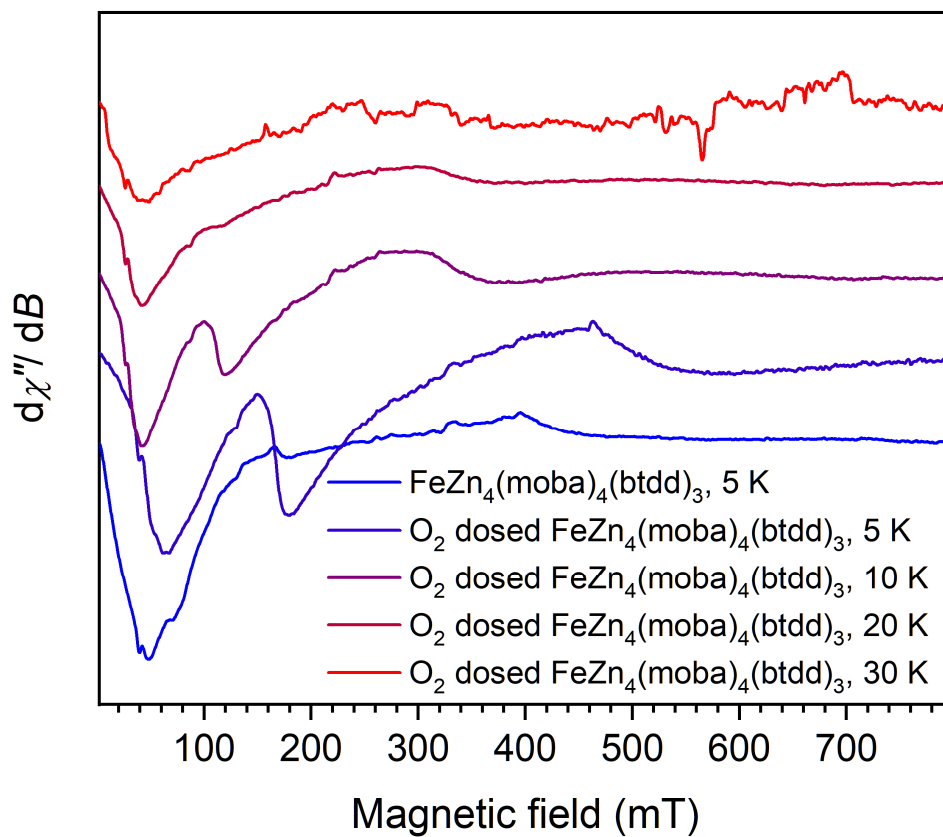
Fig. S42. Continuous-wave parallel mode EPR spectra obtained for FeZn4(moba)4(btdd)3 at 5 K (light blue trace) and samples of FeZn4(moba)4(btdd)3 dosed with O2 at various temperatures from 5 to 30 K (dark blue to red). The spectra are very broad and could not be simulated with a unique set of parameters.
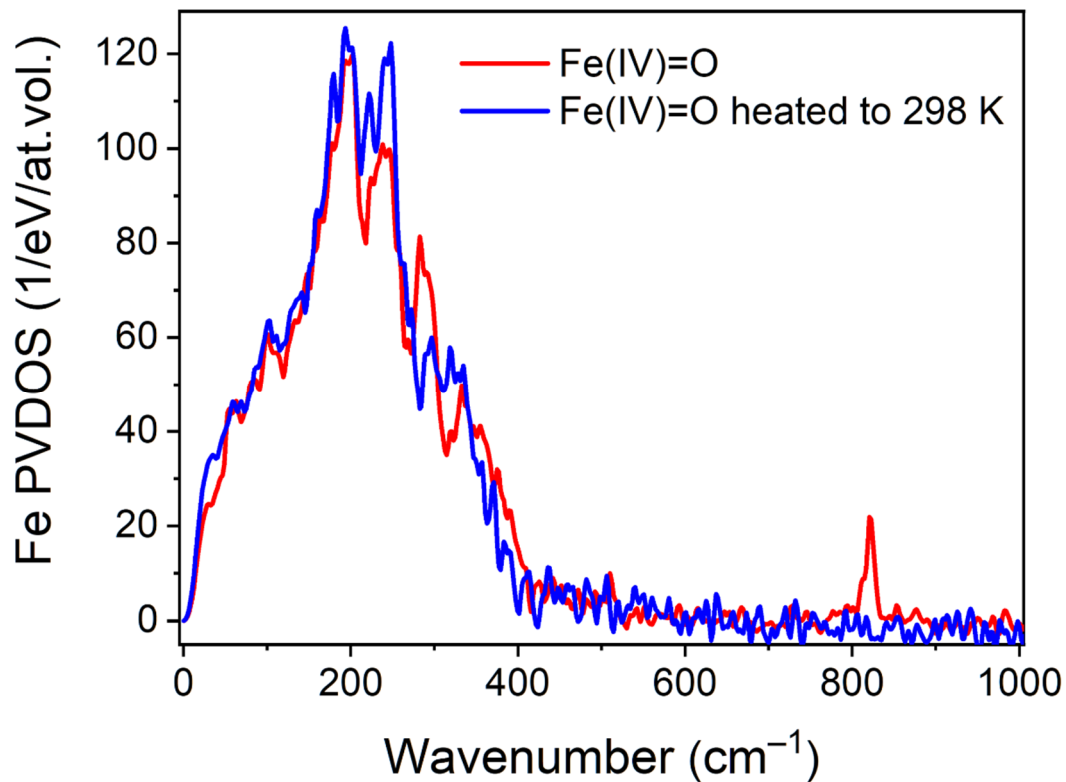
Fig. S43. NRVS iron PVDOS distribution plots of a sample of ^{57}Fe enriched, desolvated FeZn$_4$(prv)$_4$(btdd)$_3$ after *ex situ* dosing with 200 mbar O$_2$ at 163 K (red) and subsequent warming up to ambient temperature (blue).
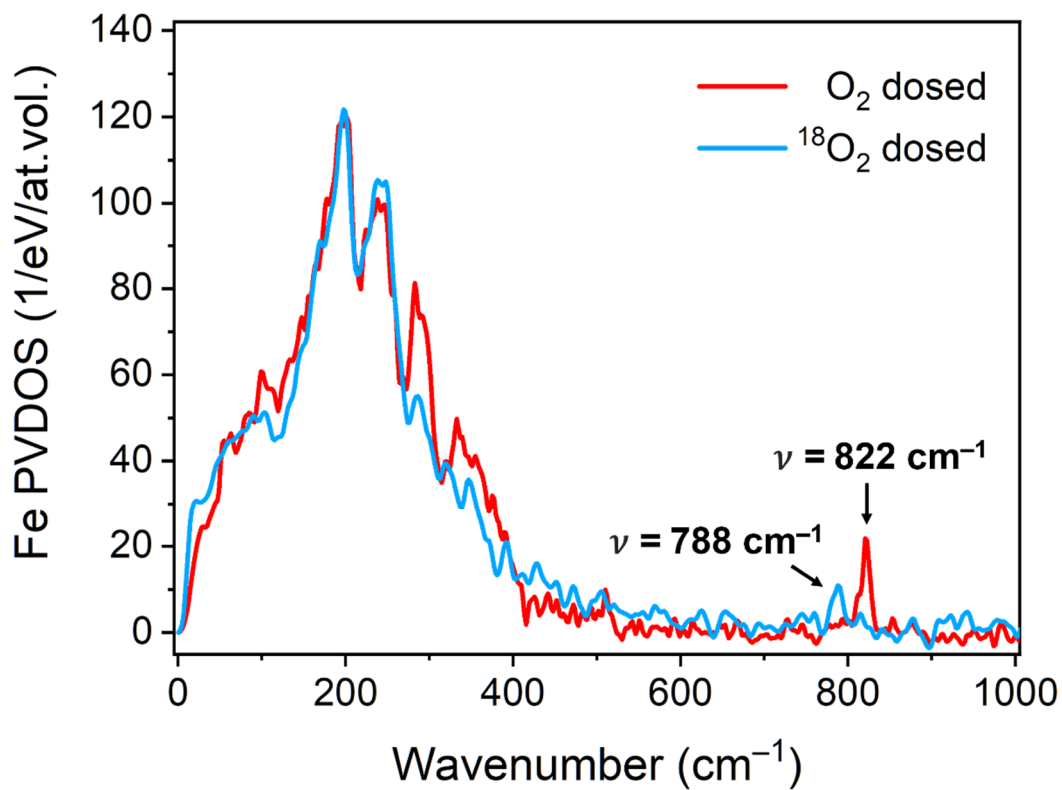
Fig. S44. NRVS iron PVDOS distribution plots of samples of ^{57}Fe enriched, desolvated FeZn$_4$(prv)$_4$(btdd)$_3$ after *ex situ* dosing at 163 K with 200 mbar O$_2$ (red) or ^{18}O$_2$ (light blue).
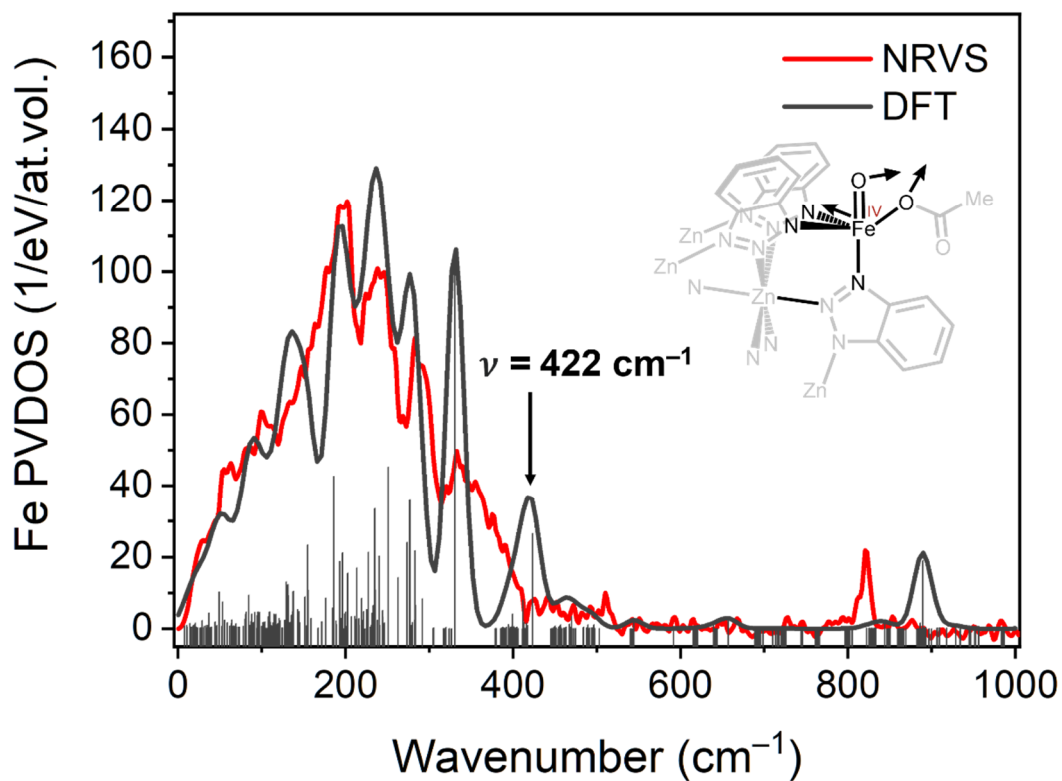
Fig. S45. NRVS iron PVDOS distribution plot for ^{57}Fe enriched, desolvated FeZn$_4$(prv)$_4$(btdd)$_3$ after *ex situ* dosing at 163 K with 200 mbar O$_2$ (red) and DFT computed NRVS iron PVDOS distribution for ~70% FeZn$_4$(prv)$_4$(bta)$_6$ and ~30% of Fe(O)(κ^1-OAc)Zn$_4$(prv)$_3$(bta)$_6$ (dark gray). Vertical lines indicate the individual vibrational transitions. The mode at 422 cm^{-1} in the computed spectrum is inconsistent with a κ^1-binding mode of the acetate ligand as discussed in the main text.
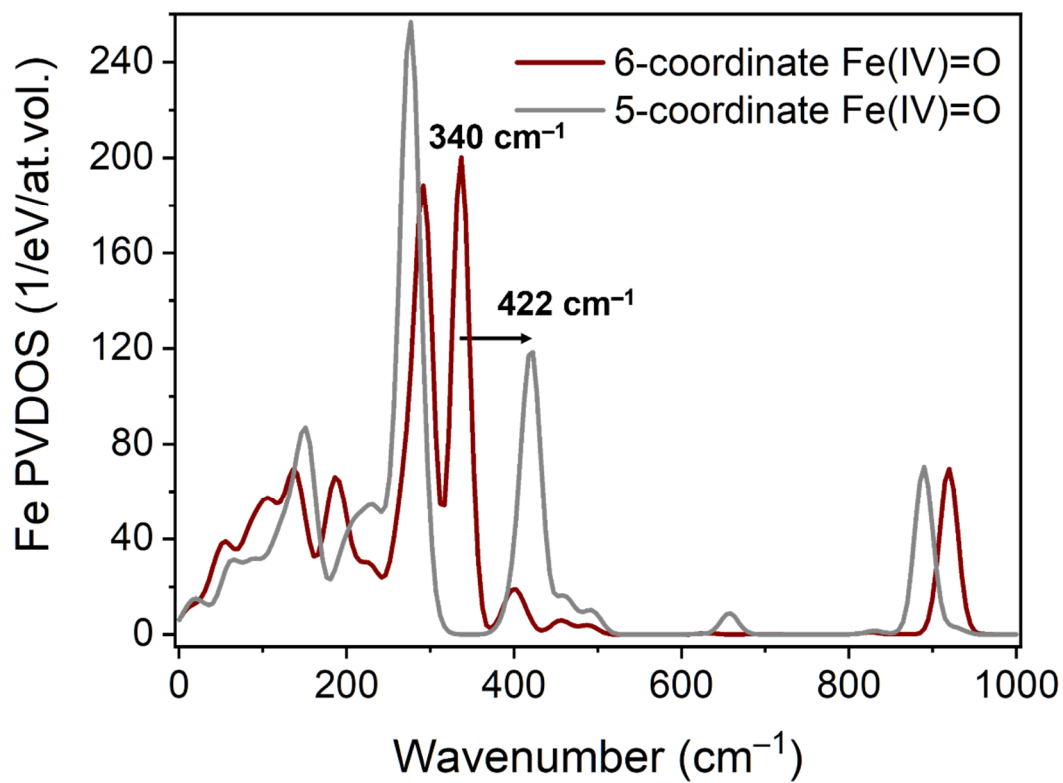
Fig. S46. Density functional theory-computed NRVS iron PVDOS distributions for $Fe(O)(\kappa^1\text{-}OAc)Zn_4(prv)_3(bta)_6$ (gray) and $Fe(O)(\kappa^2\text{-}OAc)Zn_4(prv)_3(bta)_6$ (dark red).
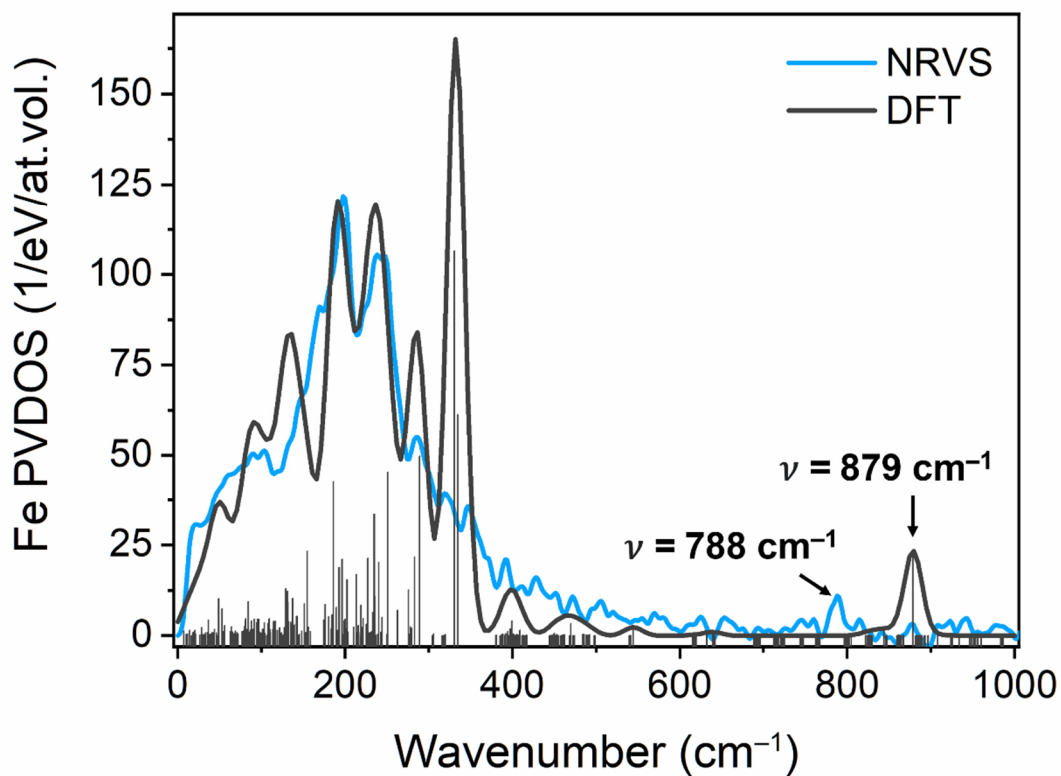
Fig. S47. Iron PVDOS distribution plot for a sample of ^{57}Fe enriched, desolvated FeZn$_4$(prv)$_4$(btdd)$_3$ after *ex situ* dosing with 200 mbar ^{18}O$_2$ at 163 K (light blue) and computed NRVS iron PVDOS for ~70% FeZn$_4$(prv)$_4$(bta)$_6$ and ~30% Fe(^{18}O)(κ^2-OAc)Zn$_4$(prv)$_3$(bta)$_6$ (dark gray). The vertical lines indicate the individual vibrational transitions.
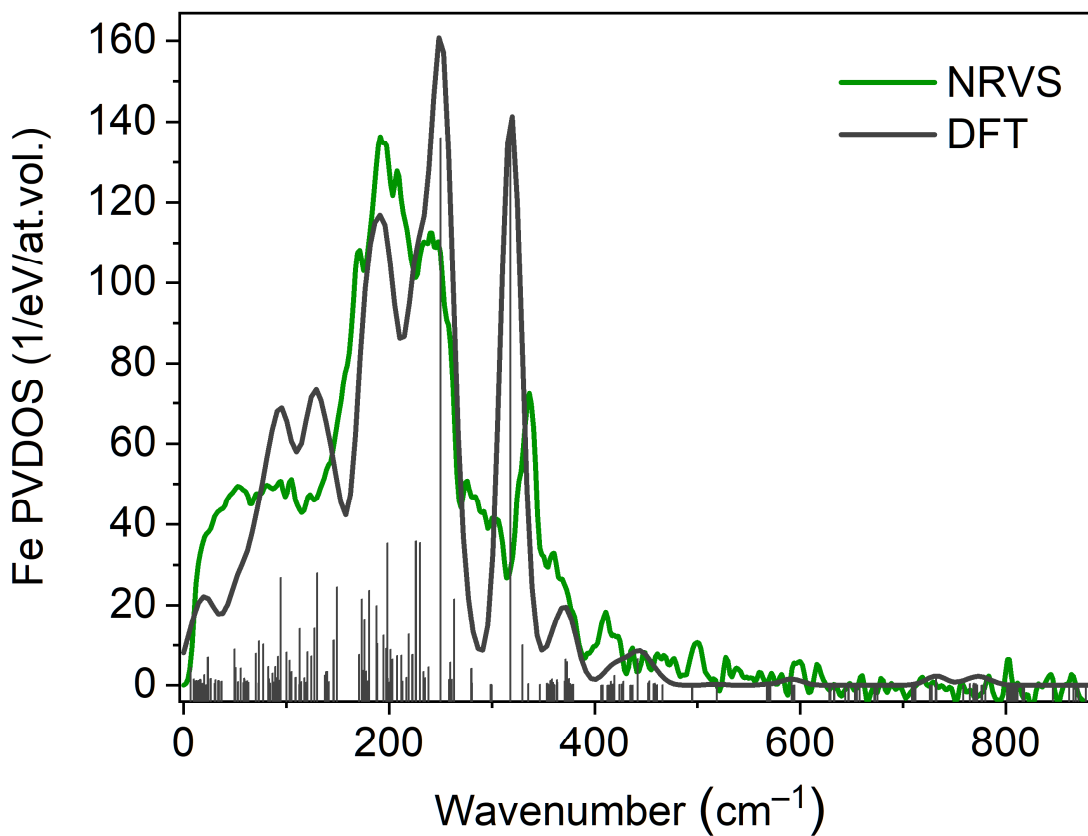
Fig. S48. NRVS iron PVDOS distribution plots of samples of ^{57}Fe enriched, desolvated FeZn$_4$(moba)$_4$(btdd)$_3$ (green) and computed NRVS iron PVDOS for Fe(moba)Zn$_4$(prv)$_3$(bta)$_6$ (dark gray). The vertical lines indicate the individual vibrational transitions.
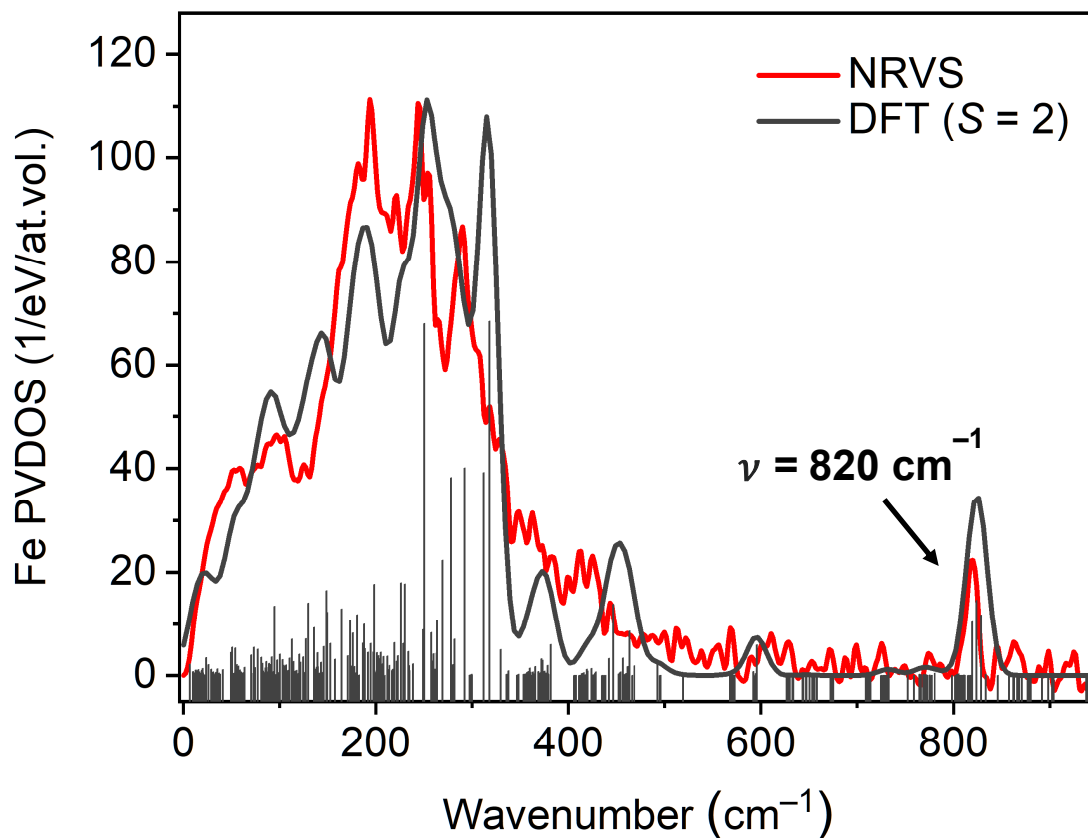
Fig. S49. NRVS iron PVDOS distribution plot for a sample of ^{57}Fe enriched, desolvated FeZn$_4$(moba)$_4$(btdd)$_3$ after *ex situ* dosing with 60 mbar O$_2$ at 163 K (red) and computed NRVS iron PVDOS for ~50% Fe(moba)Zn$_4$(prv)$_3$(bta)$_6$ and ~50% $S = 2$ Fe(O)(κ^2-OPiv)Zn$_4$(prv)$_3$(bta)$_6$ (dark gray). The vertical lines indicate the individual vibrational transitions. Relative to the data collected for O$_2$-dosed FeZn$_4$(prv)$_4$(btdd)$_3$ (see Fig. 4B in the main text), there is better agreement between simulation and experiment for the high energy vibration at 820 cm^{-1}. We attribute this to our use of distinct exchange-correlation functionals in calculating the optimized geometry for the corresponding calculated structures.
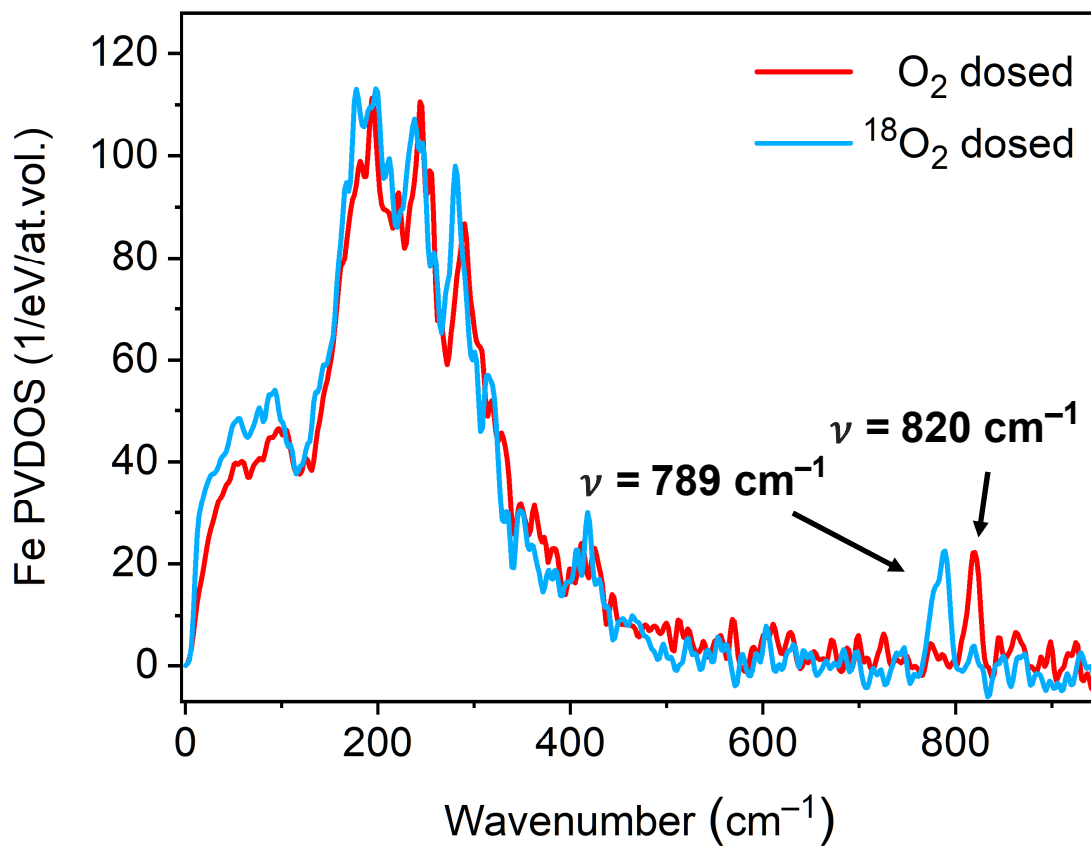
Fig. S50. NRVS iron PVDOS distribution plot for a sample of ^{57}Fe enriched, desolvated FeZn$_4$(moba)$_4$(btdd)$_3$ after *ex situ* dosing with 60 mbar O$_2$ at 163 K (red) and after *ex situ* dosing with 60 mbar ^{18}O$_2$ at 163 K (light blue).
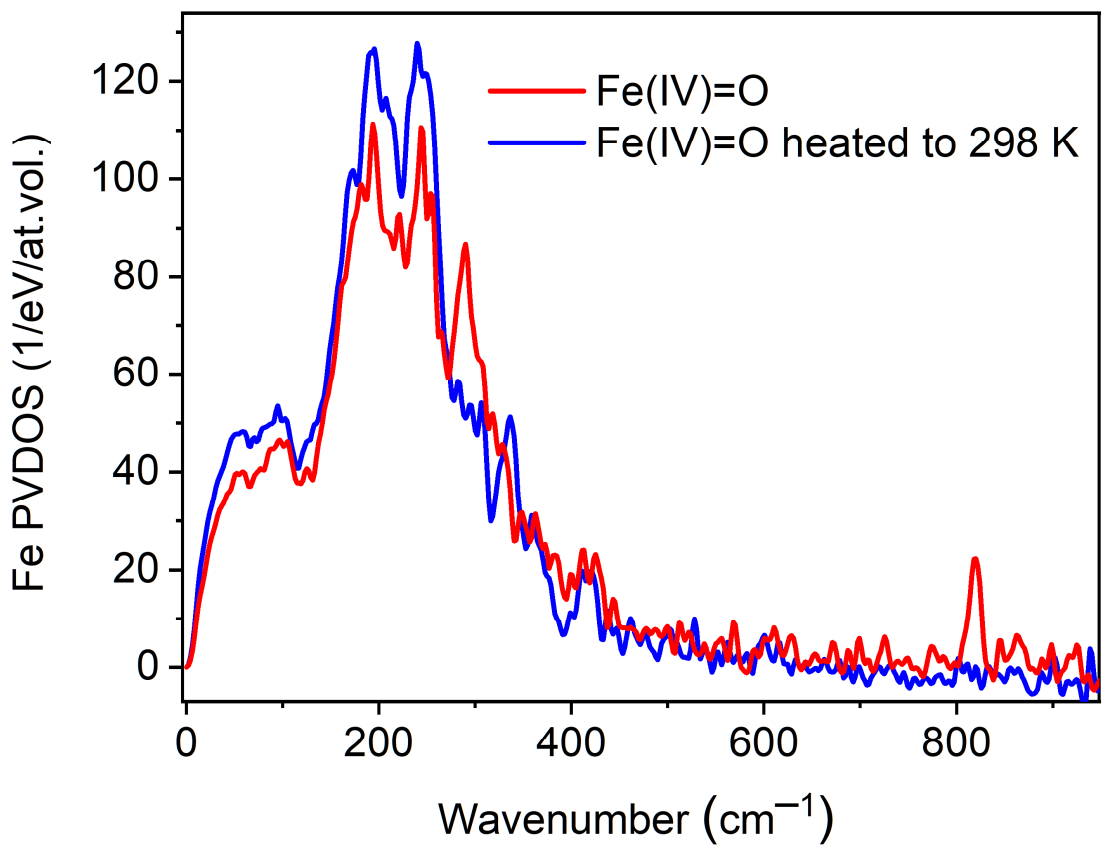
Fig. S51. NRVS iron PVDOS distribution plots of a sample of ^{57}Fe enriched, desolvated FeZn$_4$(moba)$_4$(btdd)$_3$ after *ex situ* dosing with 60 mbar O$_2$ at 163 K (red) and subsequent warming up to ambient temperature (blue).
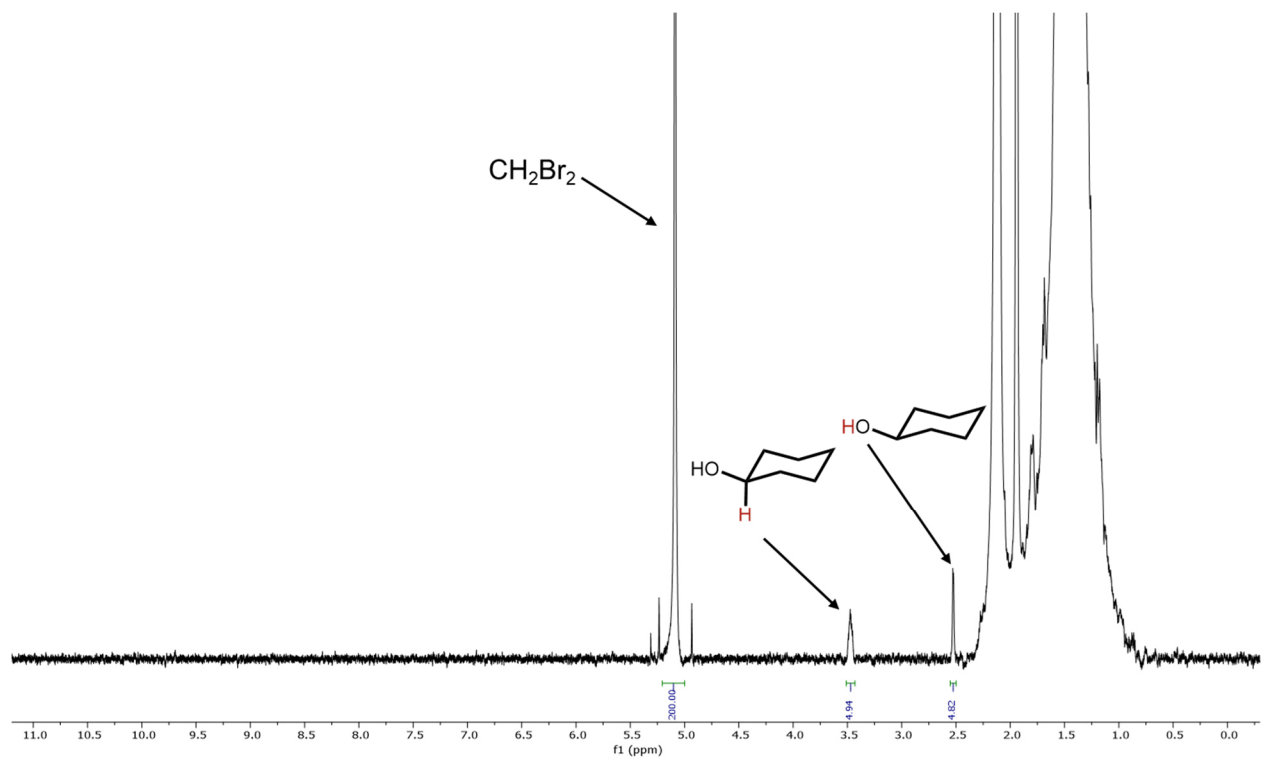
Fig. S52. Proton NMR spectrum (600 MHz, CD$_3$CN, 25 °C) of the solution resulting from the stoichiometric reaction of FeZn$_4$(prv)$_4$(btdd)$_3$ with O$_2$ and cyclohexane. The yield determined for cyclohexanol is 24%.
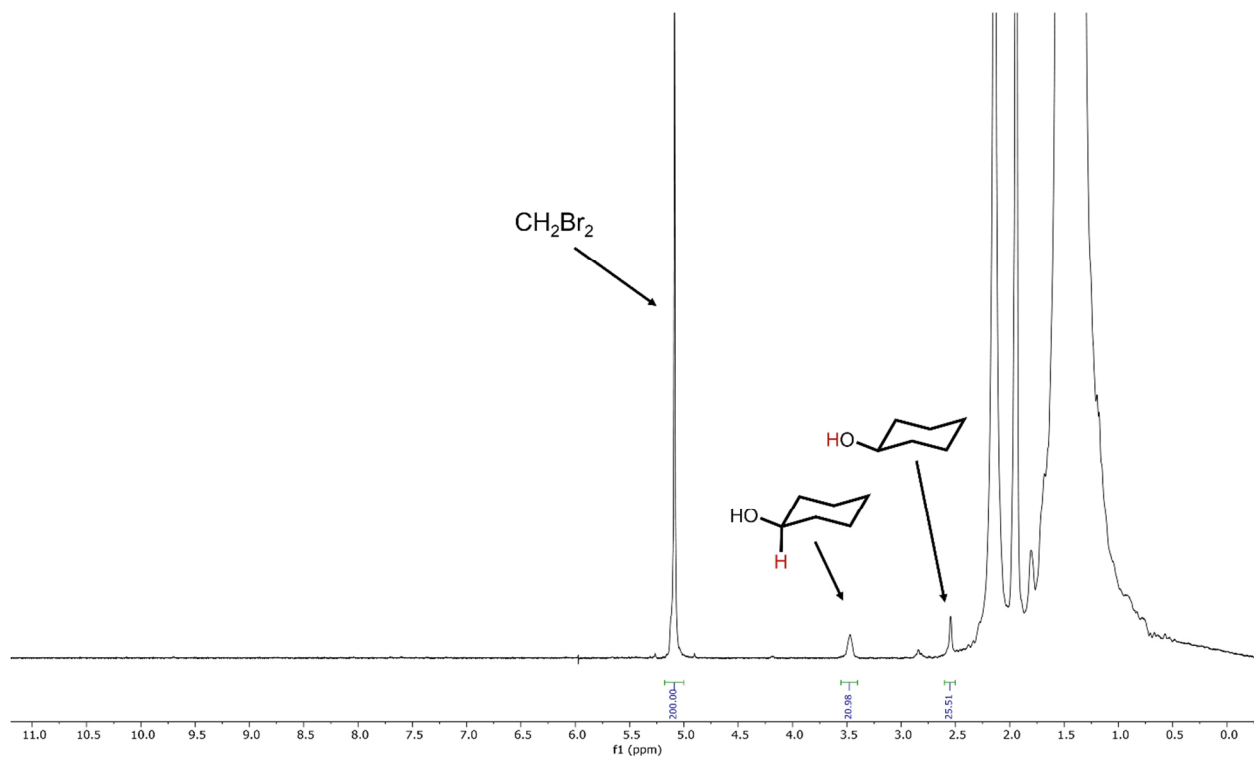
Fig. S53. Proton NMR spectrum (500 MHz, CD₃CN, 25 °C) of the solution resulting from the stoichiometric reaction of FeZn₄(prv)₄(btdd)₃ with O₂ and cyclohexane (duplicate experiment). The cyclohexanol yield determined from this reaction was 22%, consistent with the 24% yield from the first experiment (see fig. S52). The framework isolated following this reaction was analyzed by Mössbauer spectroscopy (see fig. S56).
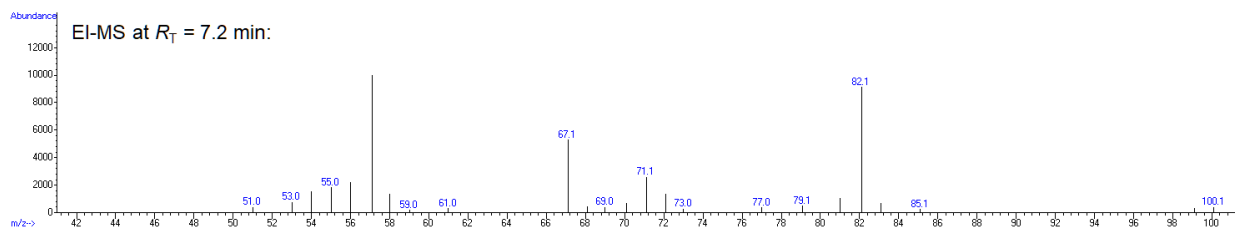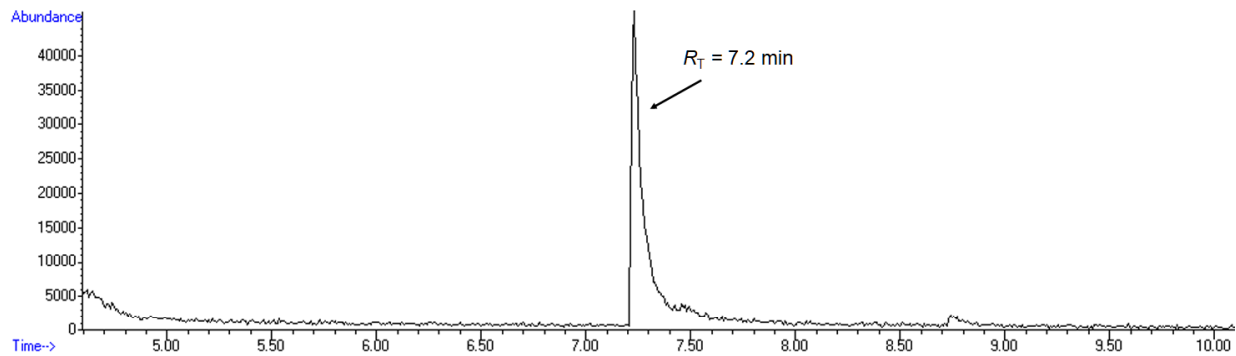
Fig. S54. (Upper) Gas chromatogram obtained for the supernatant resulting from the stoichiometric reaction of cyclohexane with $FeZn_4(prv)_4(btdd)_3$ in the presence of O_2, as described in the main text. (Lower) EI-MS trace for the peak at $R_T = 7.2$ min, corresponding to cyclohexanol. The framework isolated following this reaction was analyzed by Mössbauer spectroscopy (see fig. S56).
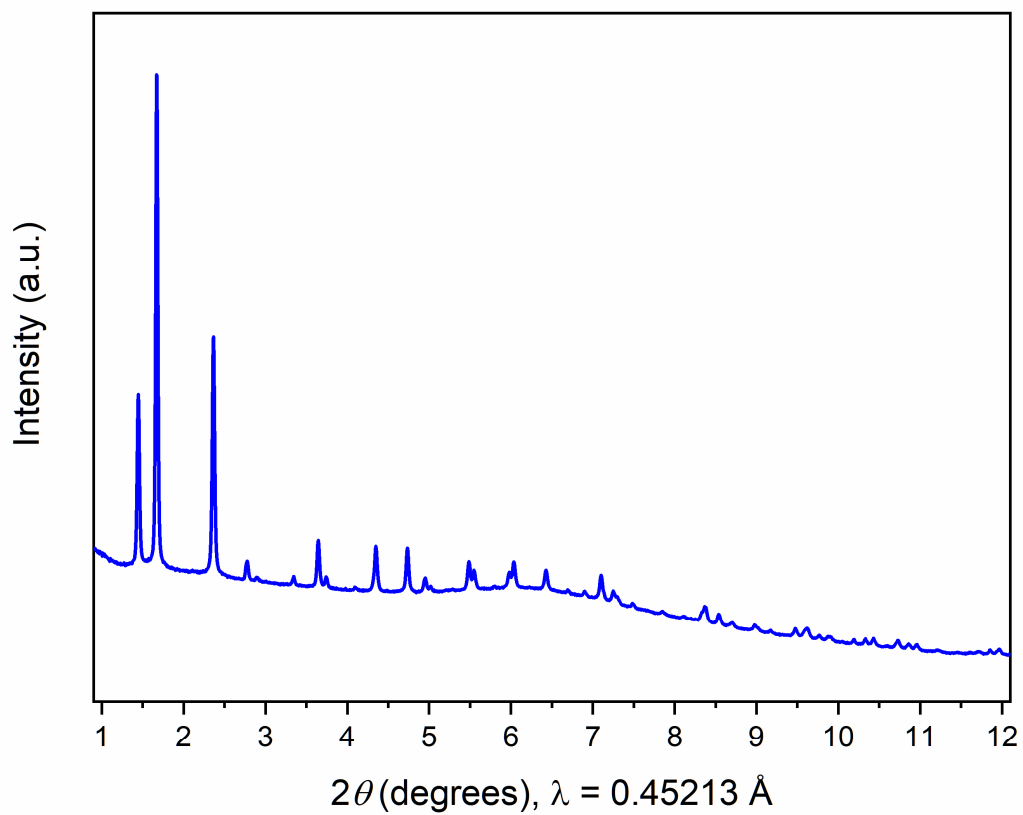
Fig. S55. Powder x-ray diffraction pattern obtained for FeZn$_4$(prv)$_4$(btdd)$_3$ after stoichiometric cyclohexane oxidation.
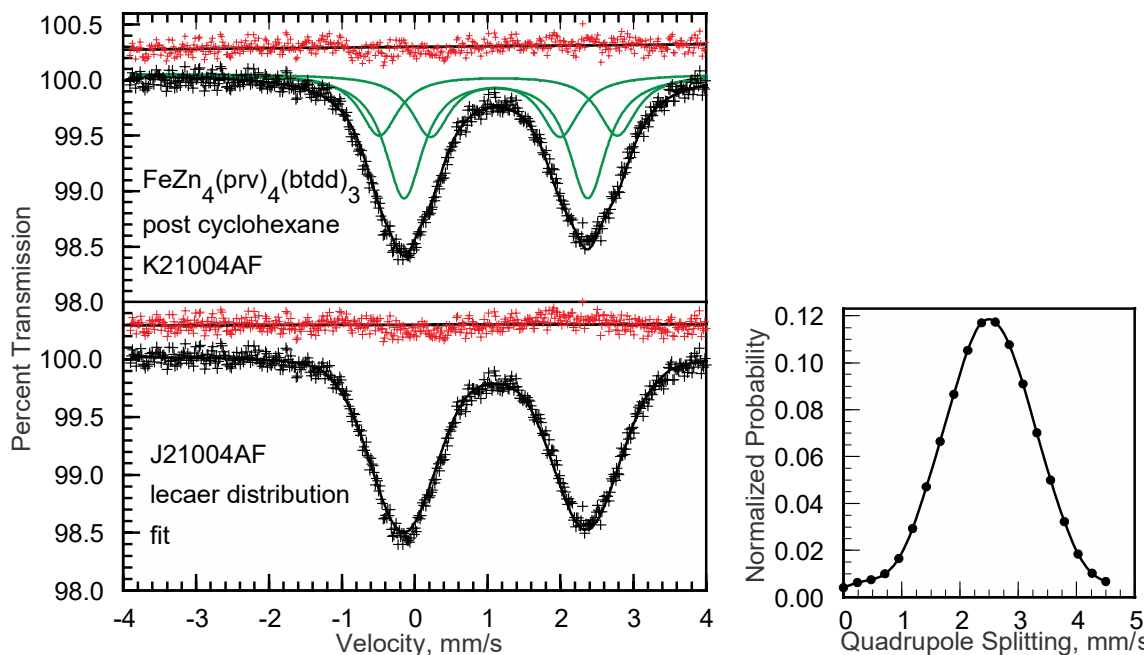
Fig. S56. (Left) Mössbauer spectrum collected at 5 K for a sample of $FeZn_4(prv)_4(btdd)_3$ following a reaction with cyclohexane and O_2 at 21°C for 24 h, as described in the main text. In the upper plot, the data are fit with three symmetric doublets, while in the lower plot, the data are fit with a quadrupole splitting distribution using the Le Caër and Dubois method. (Right) The corresponding normalized probability distribution of the quadrupole splitting for the 20 component fit (*86*). The isomer shifts determined from both fits indicate the presence of predominately high-spin iron(II). Details about the data fits are given in table S16.
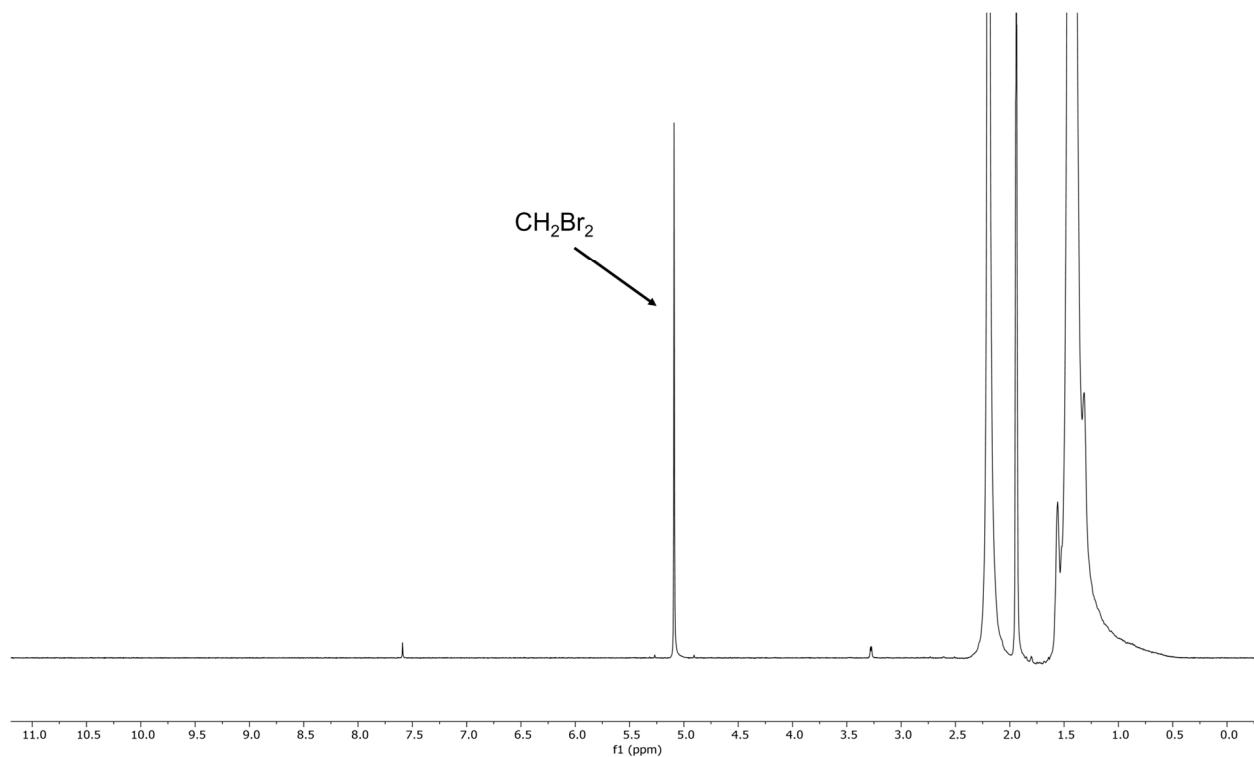
Fig. S57. Proton NMR spectrum (500 MHz, CD$_3$CN, 25 °C) of the supernatant resulting from the stoichiometric control reaction between FeZn$_4$Cl$_4$(btdd)$_3$ dosed *in situ* with O$_2$ and cyclohexane. No cyclohexanol or cyclohexanone was detected.
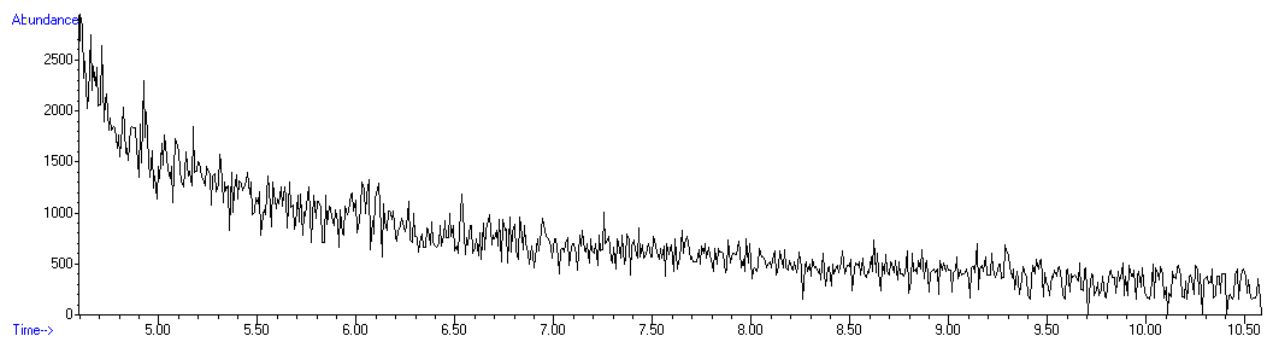
Fig. S58. Gas chromatogram resulting from treatment of FeZn$_4$Cl$_4$(btdd)$_3$ with O$_2$ and cyclohexane. No cyclohexanol or cyclohexanone is detected.
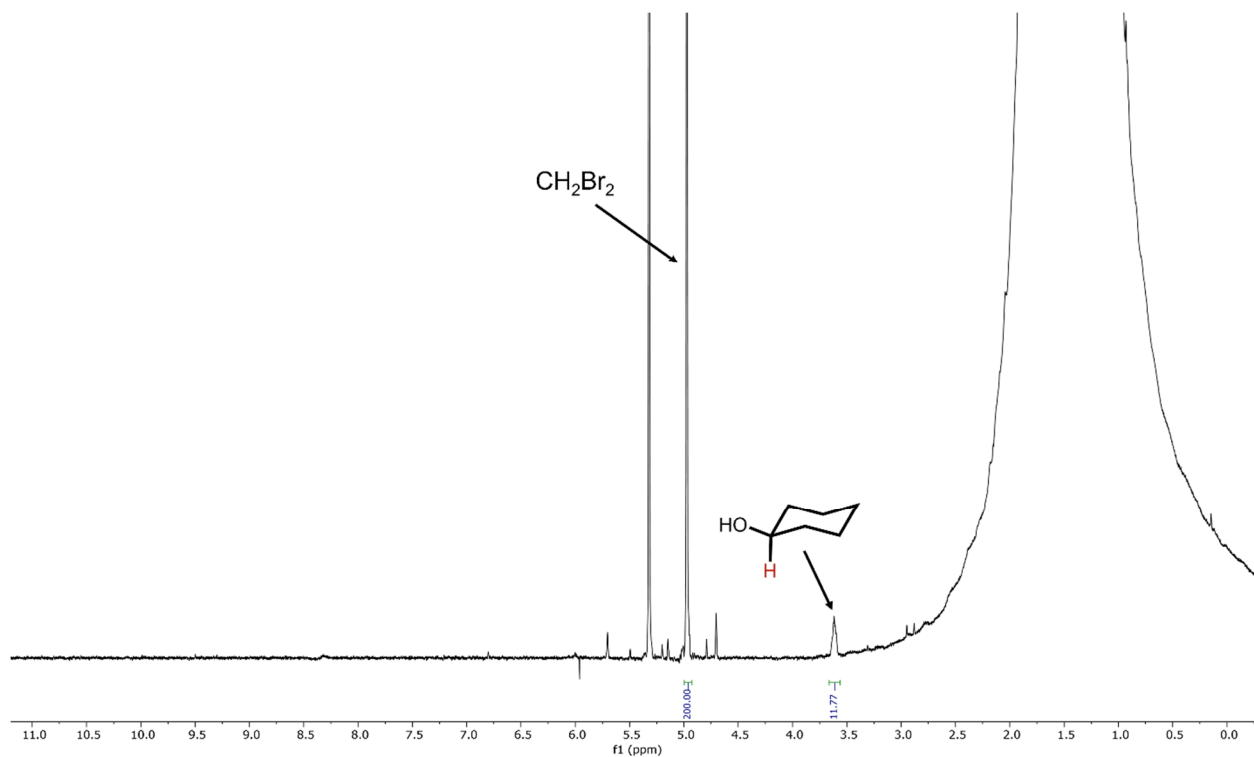
Fig. S59. Proton NMR spectrum (500 MHz, CD$_2$Cl$_2$, 25 °C) of the solution resulting from the stoichiometric reaction of FeZn$_4$(moba)$_4$(btdd)$_3$ with O$_2$ and cyclohexane. The yield of cyclohexanol determined from this reaction was 51% (see section 1.11.1).
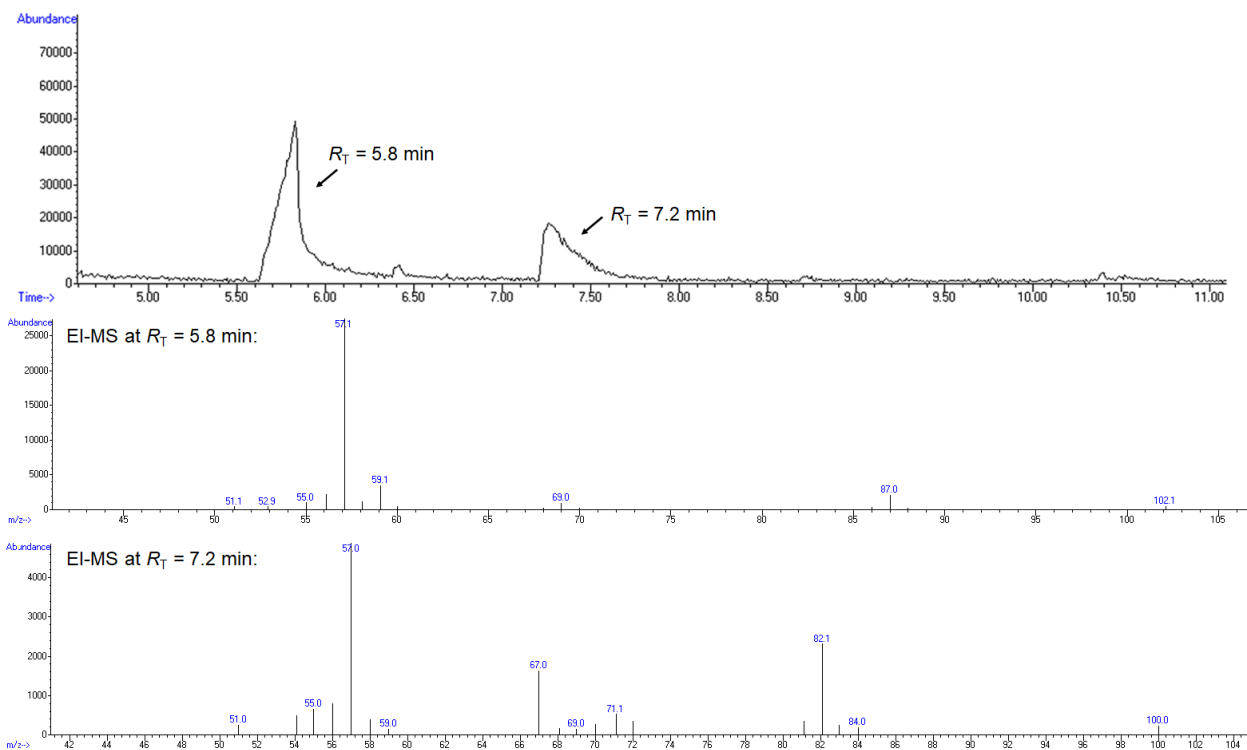
Fig. S60. (Upper) Gas chromatogram of the supernatant resulting from the stoichiometric oxygenation of cyclohexane with $FeZn_4(moba)_4(btdd)_3$ in the presence of O_2. (Middle) EI-MS trace for the peak at $R_T = 5.8$ min in the GC. (Lower) EI-MS trace for the peak at $R_T = 7.2$ min in the GC. The EI-MS spectrum at $R_T = 5.8$ min is consistent with the formation of pivalic acid, and the spectrum at $R_T = 7.2$ min is consistent with the formation of cyclohexanol.
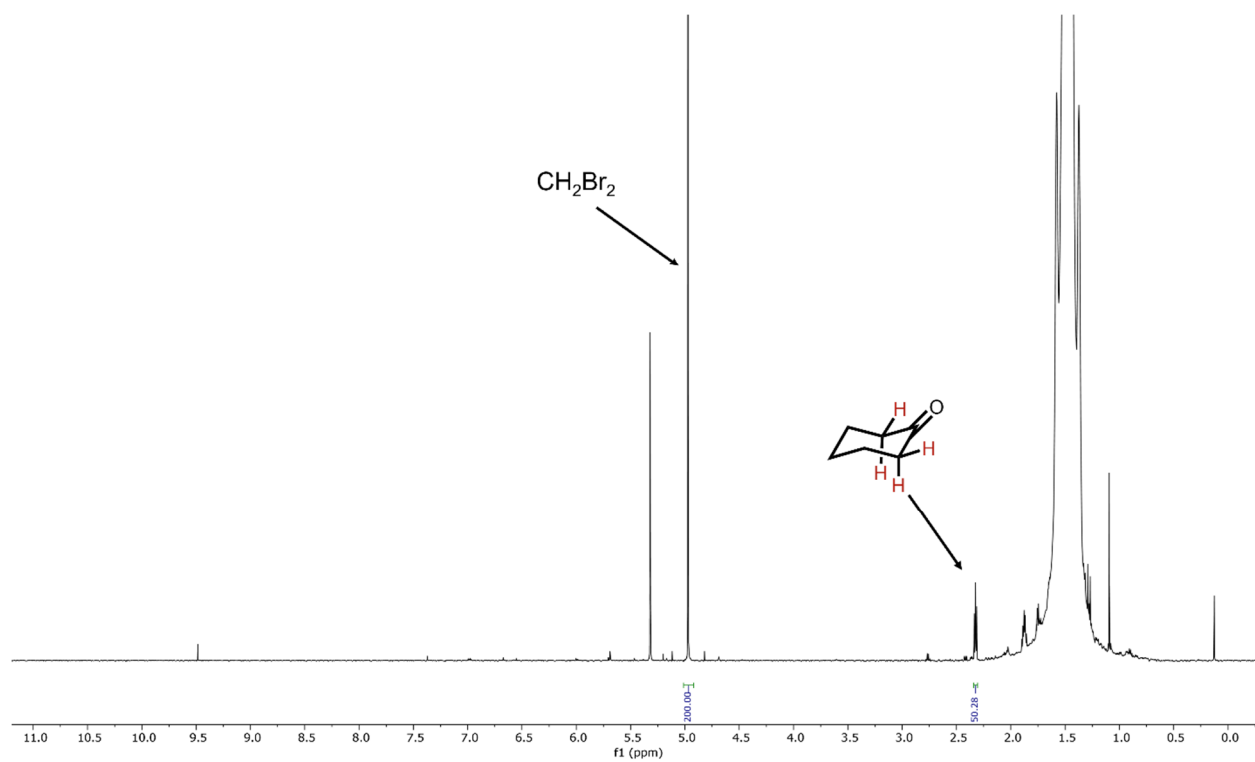
Fig. S61. Proton NMR spectrum (600 MHz, CD$_2$Cl$_2$, 25 °C) of the solution resulting from the stoichiometric reaction (in CD$_2$Cl$_2$) between cyclohexane and a sample of FeZn$_4$(moba)$_4$(btdd)$_3$ previously dosed *ex situ* with 170 mbar O$_2$ at 163 K.
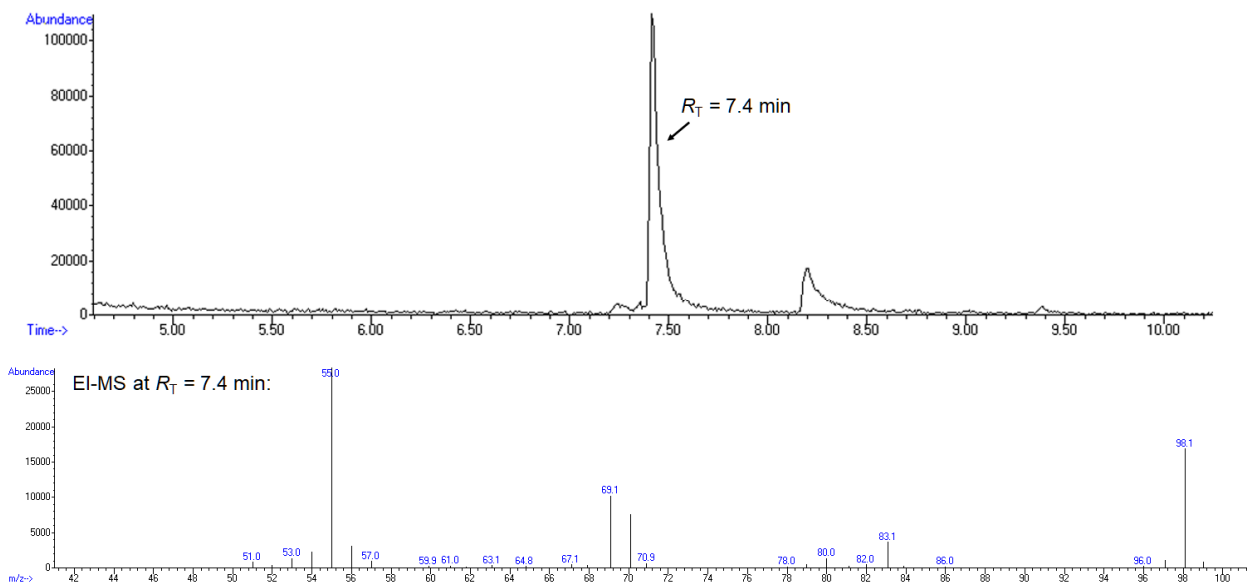
Fig. S62. (Upper) Gas chromatogram obtained for the supernatant resulting from the stoichiometric reaction (in CD_2Cl_2) between cyclohexane and a sample of $FeZn_4(moba)_4(btdd)_3$ dosed *ex situ* with O_2. (Lower) EI-MS trace for the peak at R_T = 7.4 min, corresponding to cyclohexanone.
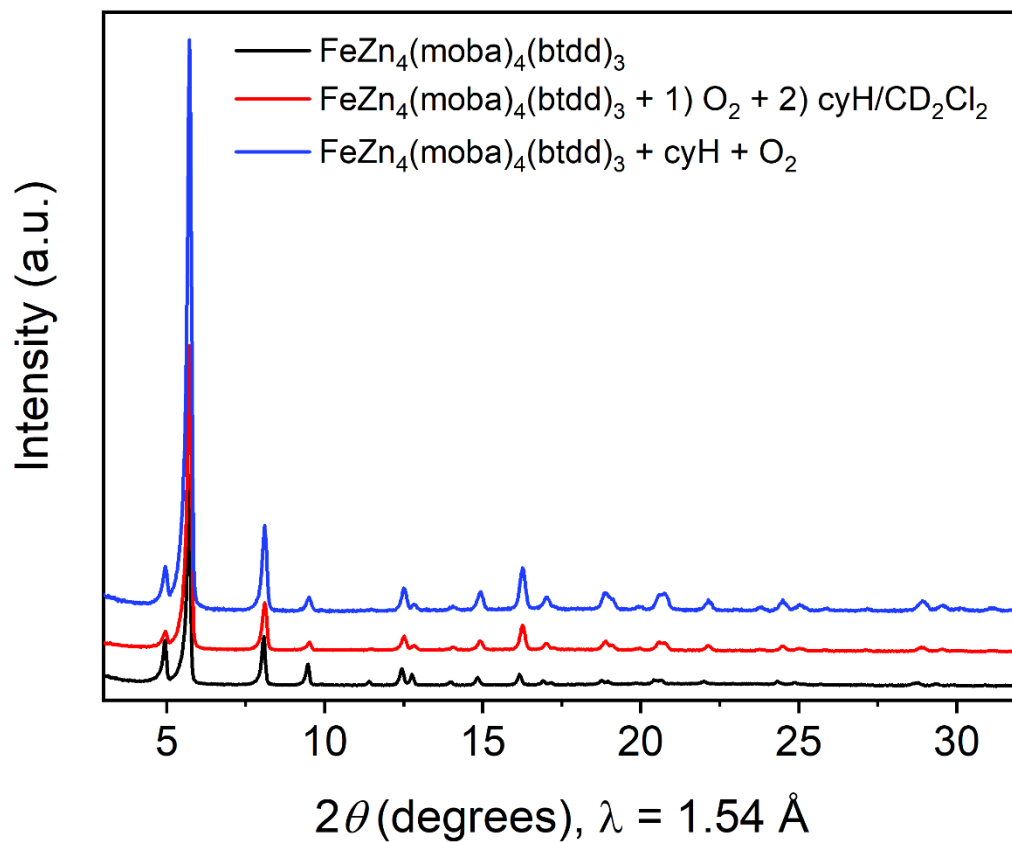
Fig. S63. Powder x-ray diffraction patterns for pristine FeZn4(moba)4(btdd)3 (black trace) and the material after stoichiometric reactions with O_2 and cyclohexane as described in sections 1.11.2 and 1.11.1 (red and blue traces, respectively).
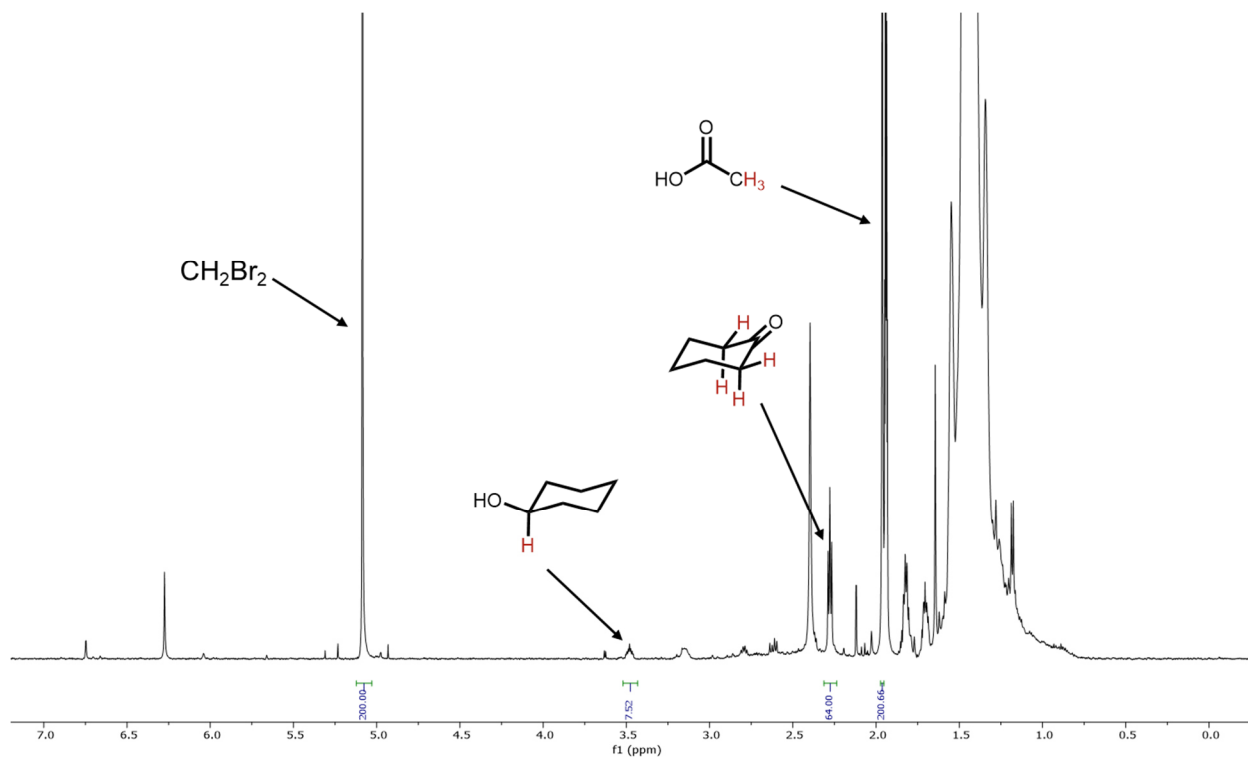
Fig. S64. Proton NMR spectrum (600 MHz, CD$_3$CN, 25 °C) of the solution resulting from the catalytic reaction of FeZn$_4$(prv)$_4$(btdd)$_3$ with O$_2$ and cyclohexane.
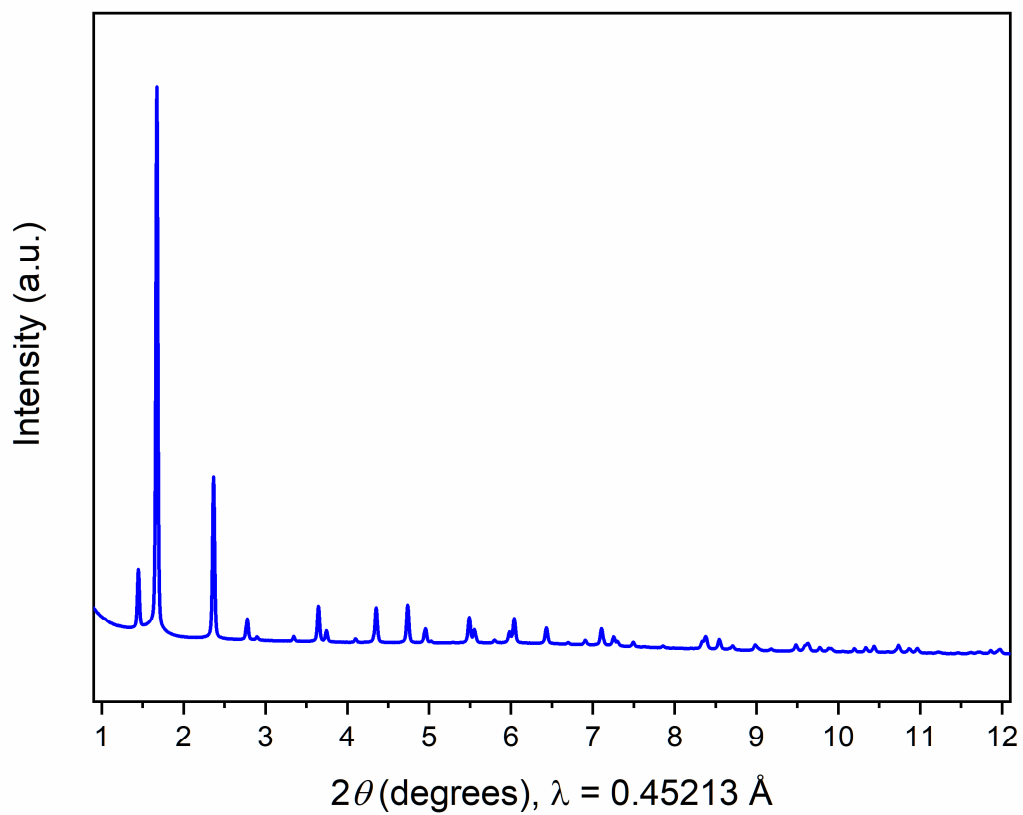
Fig. S65. Powder x-ray diffraction pattern of $FeZn_4(prv)_4(btdd)_3$ after catalytic cyclohexane oxidation.
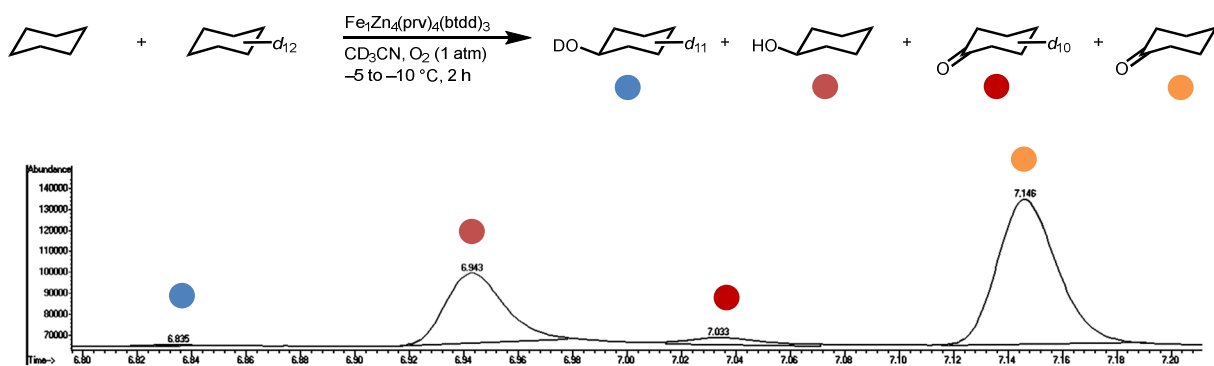
Fig. S66. Competition KIE experiment (upper) and representative GC-FID chromatogram with assigned product peaks (lower).
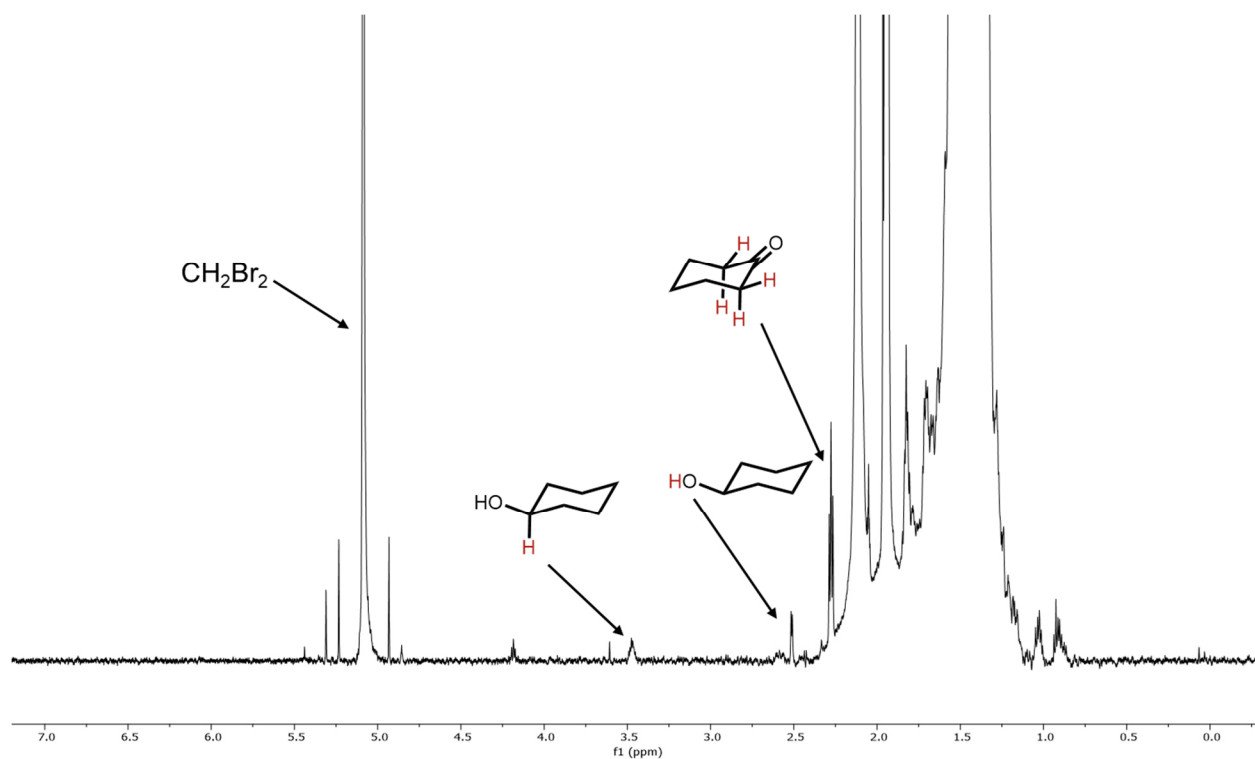
Fig. S67. Proton NMR spectrum (600 MHz, CD₃CN, 25 °C) of the solution resulting from the reaction of FeZn₄(prv)₄(btdd)₃ with O₂ and cyclohexane and cyclohexane-d_{12} (KIE experiment).
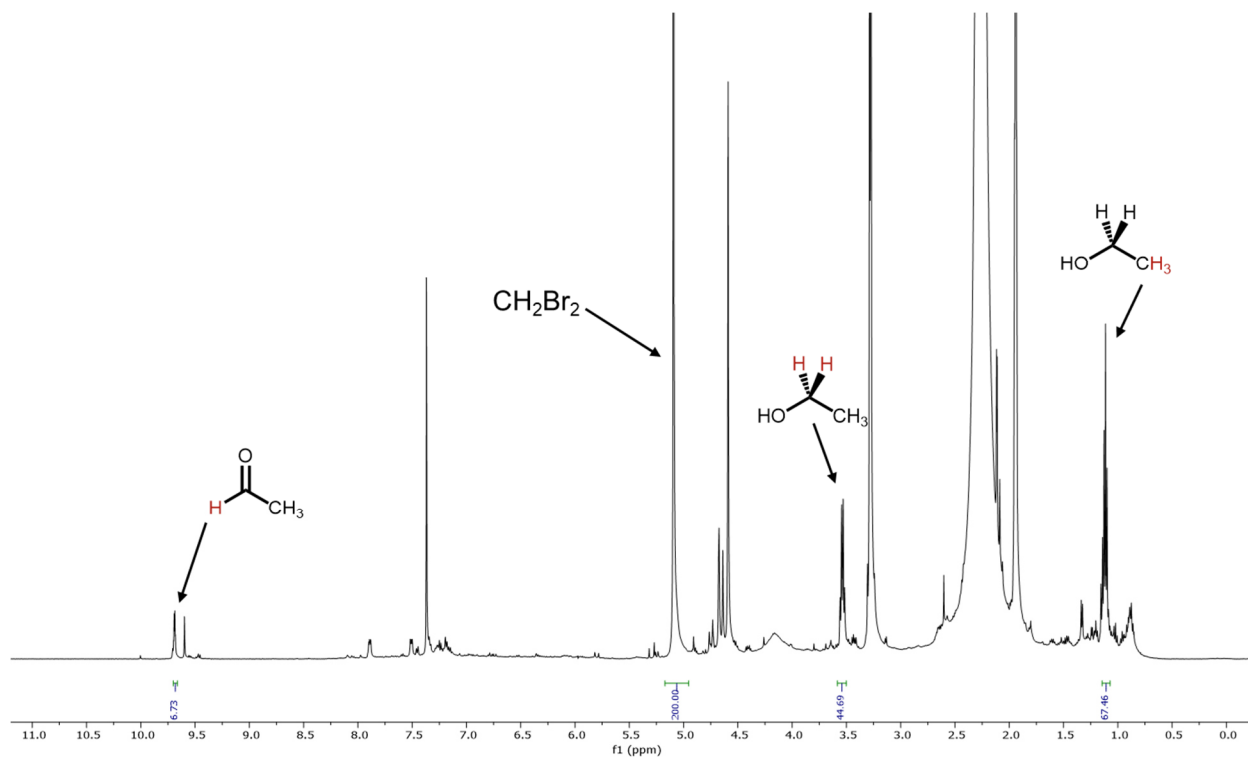
Fig. S68. Proton NMR spectrum (500 MHz, CD₃CN, 25 °C) of the solution resulting from the reaction of $Fe_{1.8}Zn_{3.2}(prv)_4(btdd)_3$ with O_2 and ethane.
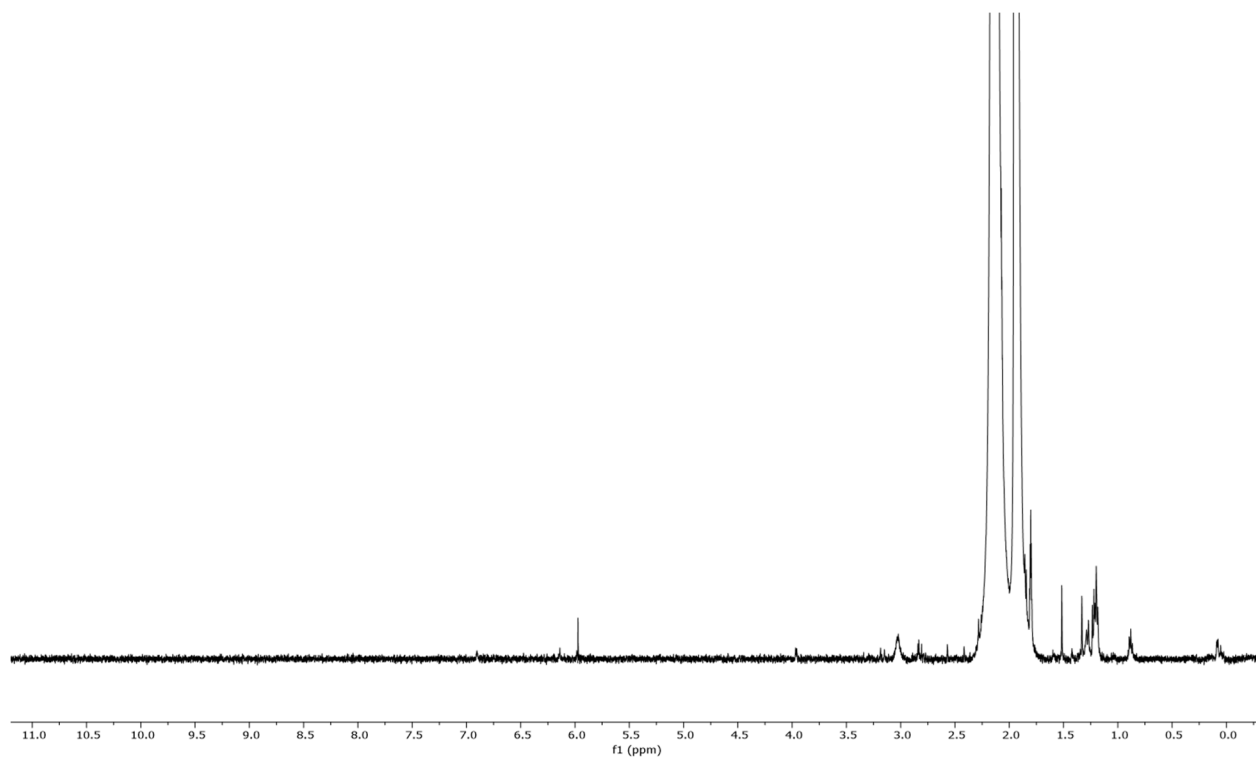
Fig. S69. Proton NMR spectrum (500 MHz, CD$_3$CN, 25 °C) of Fe$_{1.8}$Zn$_{3.2}$(prv)$_4$(btdd)$_3$ exposed to air and extracted with CD$_3$CN. No ethanol is present.
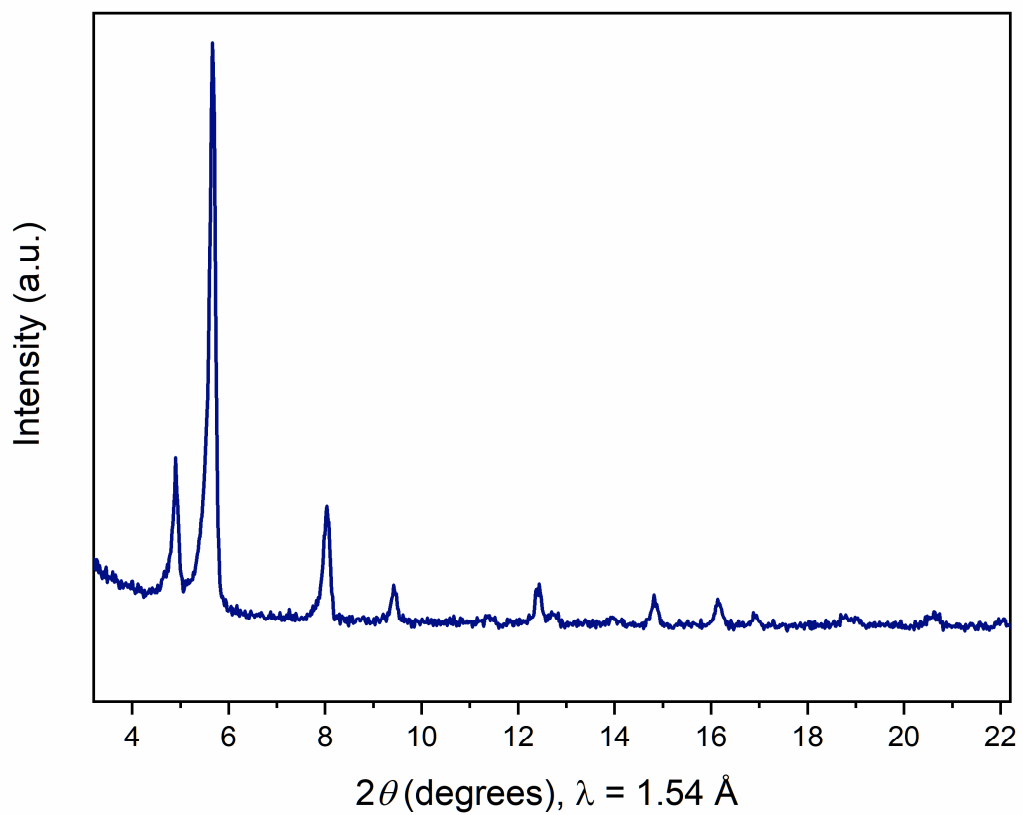
Fig. S70. Powder x-ray diffraction pattern of $Fe_{1.8}Zn_{3.2}(prv)_4(btdd)_3$ after ethane oxidation.
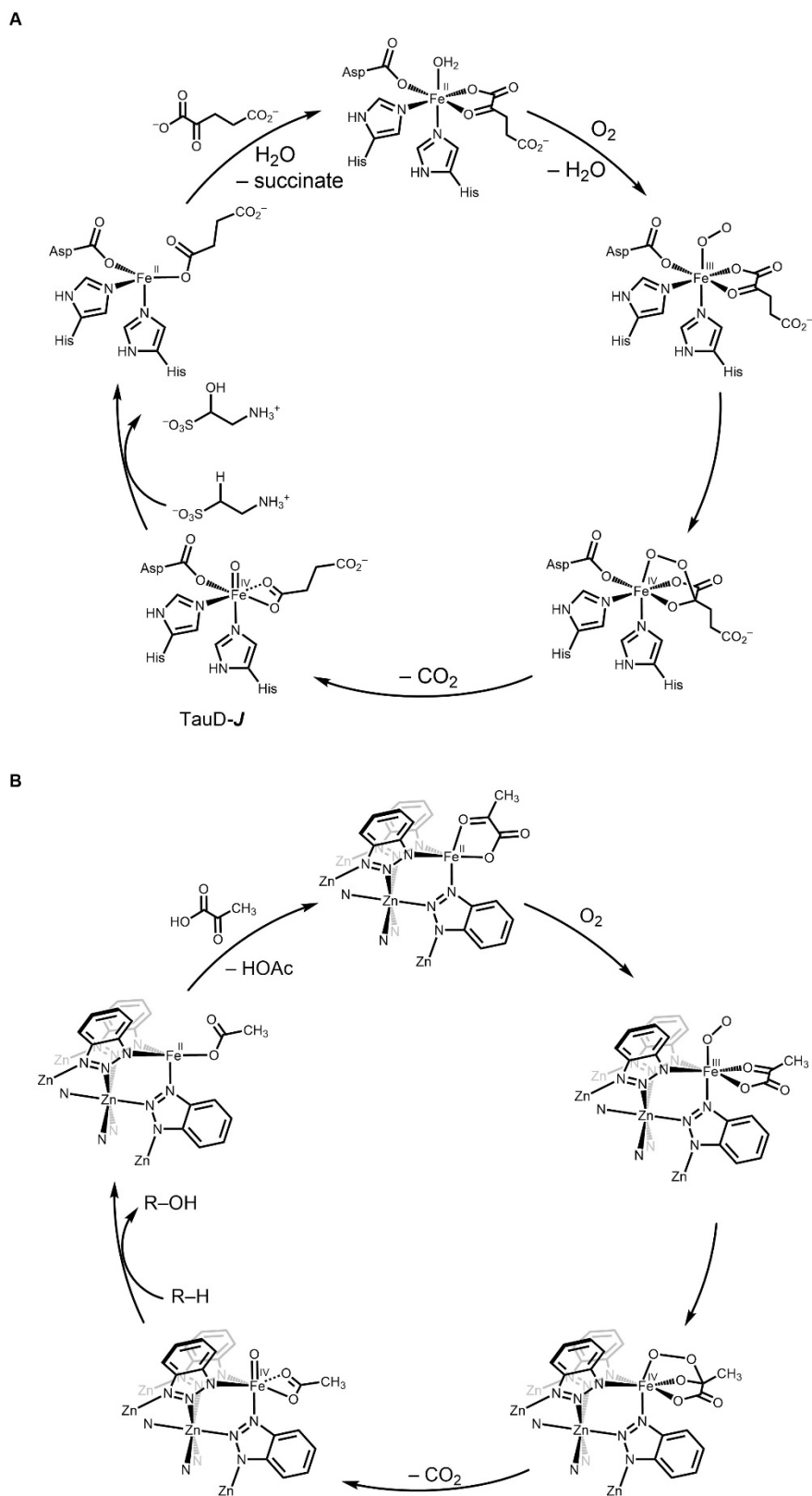
Fig. S71. (**A**) Catalytic cycle for taurine C–H hydroxylation by TauD. (**B**) Proposed catalytic cycle for C–H hydroxylation by $FeZn_4(prv)_4(btdd)_3$.

5. Supplementary tables

Table S1. Crystal data and structure refinement for $Zn_5Cl_4(btdd)_3$.

Empirical formula	$C_{36}H_{12}Cl_4N_{18}O_6Zn_5$
Formula weight, g/mol	1261.18
Temperature, K	100
Crystal system	cubic
Space group	*Fm-3m*
a, Å	30.9085(3)
b, Å	30.9085(3)
c, Å	30.9085(3)
α, °	90
β, °	90
γ, °	90
Volume, Å^3	29528.0(9)
Z	8
ρ_{calc}, g/cm^3	0.567
μ, /mm^{-1}	1.750
F(000)	4960.0
Crystal size, mm^3	$0.6 \times 0.6 \times 0.6$
Radiation	CuKα ($\lambda = 1.54184$ Å)
2θ range for data collection, °	8.09 to 157.082
Index ranges	$-35 \leq h \leq 10, -38 \leq k \leq 30, -33 \leq l \leq 29$
Reflections collected	15212
Independent reflections	1585 [$R_{int} = 0.0325$, $R_{sigma} = 0.0131$]
Data/restraints/parameters	1585/2/47
Goodness-of-fit on F^2	1.109
Final R indexes [I>=2σ (I)]	$R_1 = 0.0670$, wR$_2$ = 0.2007
Final R indexes [all data]	$R_1 = 0.0682$, wR$_2$ = 0.2024
Largest diff. peak/hole, e Å^{-3}	0.44/−1.0

Table S2. Crystal data and structure refinement for $Zn_5(prv)_4(btdd)_3$.

Empirical formula	$C_{48}H_{24}N_{18}O_{18}Zn_5$
Formula weight, g/mol	1467.58
Temperature, K	100
Crystal system	cubic
Space group	*Fm-3m*
a, Å	30.7107(2)
b, Å	30.7107(2)
c, Å	30.7107(2)
α, °	90
β, °	90
γ, °	90
Volume, Å^3	28964.7(6)
Z	8
ρ_{calc}, g/cm^3	0.673
μ, mm^{-1}	1.225
F(000)	5856.0
Crystal size, mm^3	$0.23 \times 0.23 \times 0.23$
Radiation	CuKα (λ = 1.54184 Å)
2θ range for data collection, °	5.756 to 157.026
Index ranges	$-33 \leq h \leq 26, -32 \leq k \leq 36, -33 \leq l \leq 35$
Reflections collected	19108
Independent reflections	1538 [R_{int} = 0.0300, R_{sigma} = 0.0151]
Data/restraints/parameters	1538/27/91
Goodness-of-fit on F^2	1.204
Final R indexes [I>=2σ (I)]	R_1 = 0.0542, wR_2 = 0.2036
Final R indexes [all data]	R_1 = 0.0572, wR_2 = 0.2111
Largest diff. peak/hole, e Å^{-3}	0.39/−0.55

Table S3. Mössbauer Spectral Parameters for Various Paramagnetic Fe(IV)=O Species, based on the data reported in Table 1 in reference *15*.

Index	Absorber [a]	S	δ [b], mm/s	ΔE_Q [c], mm/s	D [d], cm^{-1}	Ref
1	[Fe^{IV}=O(TMC)(MeCN)]$^{2+}$	1	0.17	+1.24	29(3)	87
2	[Fe^{IV}=O(N4Py)]$^{2+}$	1	−0.04	±0.93	22	88
3	[Fe^{IV}=O(OH$_2$)$_5$]$^{2+}$	2	0.38	−0.33	9.7(7)	89
4	[Fe^{IV}=O(TMG)$_3$(tren)]$^{2+}$	2	0.09	−0.29	5.0(5)	39
5	[Fe^{IV}=O(TMG)$_2$(dien)(MeCN)]$^{2+}$	2	0.08	+0.58	4.5(5)	90
6	[Fe^{IV}=O(TMG)$_2$(dien)(Cl)]$^{+}$	2	0.08	+0.41	4.0(5)	90
7	[Fe^{IV}=O(TMG)$_2$(dien)(N$_3$)]$^{+}$	2	0.12	−0.30	4.6(5)	90
8	[Fe^{IV}=O(H$_3$buea)]$^{-}$	2	0.02	+0.43	4.0(5)	91
9	[Fe^{IV}=O(tpa^{Ph})]$^{-}$	2	0.09	±0.51	4.3	14
10	[Fe^{IV}=O(TPA*)(MeCN)]$^{2+}$	1	0.01	±0.95		92
11	[(HO)(L)Fe^{IV}-O-Fe^{IV}(O)(L)]$^{3+}$ (L = TPA*)	1	−0.03	±0.92		92
12	[(TPA*)$_2$Fe^{IV}$_2$(μ-O)$_2$]$^{4+}$	1	−0.04	+2.09		93
13	[(TPA*)$_2$Fe^{III}Fe^{IV}(μ-O)$_2$]$^{3+}$	1	0.11	±0.44		93
14	[(HO)(L)Fe^{III}-O-Fe^{IV}(O)(L)]$^{2+}$ (L = TPA*)	2	0.09	−0.40		94
15	[(F)(L)Fe^{III}-O-Fe^{IV}(O)(L)]$^{2+}$ (L = TPA*)	2	0.10	+0.60		95
16	[(H$_2$O)(L)Fe^{III}-O-Fe^{IV}(O)(L)]$^{3+}$ (L = 6Me$_3$TPA)	2				96
17	[(H$_2$O)(L)Fe^{III}-O-Fe^{IV}(O)(L)]$^{3+}$ (L = 6MeTPA)	2	0.08	+0.5		97
18	[Fe^{IV}=O(TPA)(MeCN)]$^{2+}$	1	0.01	+0.92	28(2)	98
19	[Fe^{IV}=O(6MeTPA)(MeCN)]$^{2+}$	1				99
20	[Fe^{IV}=O(QBPA)(MeCN)]$^{2+}$	1				99
21	[Fe^{IV}=O(TQA)(MeCN)]$^{2+}$)	2	0.24	−1.05	17(1)	46
22	[Fe^{IV}=O(Me$_3$NTB)(MeCN)]$^{2+}$	1	0.02	+1.53	28(7)	100
23	Taurine dioxygenase (TauD-*J*)	2	0.30	−0.88	10.5	6
24	Prolyl 4-hydroxylase	2	0.30	−0.82	15.5	101
25	Halogenase CytC3	2	0.30	−1.09	8.1	102
26	Halogenase CytC3	2	0.22	−0.70	8.1	102
27	Halogenase SyrB2	2	0.30	±1.09		103
28	Halogenase SyrB2	2	0.23	±0.76		103
29	Tyrosine hydroxylase	2	0.25	−1.27	12.5	104
30	FeZn$_4$(prv)$_4$(btdd)$_3$ 300 mbar O$_2$ 150 K	2	0.27	−0.59		*this work*
31	FeZn$_4$(moba)$_4$(btdd)$_3$ 200 mbar O$_2$ dosed at 100 K, then held at 200 K for 2 h	2	0.29	−0.60	12.7	*this work*
32	Fe^{IV}=O(Me$_3$TACN)((OSiPh$_2$)$_2$O)	2	0.22	−0.23	13.2	17
33	[Fe^{IV}=O (H$_3$buea)]$^{-}$	2	0.04	±0.50	4.7	105
34	[Fe^{IV}=O(poat)]$^{-}$	2	0.11	+0.27	5.1(3)	33

[a] See table S4 below for ligand abbreviations. [b] The isomer shifts, δ, are given relative to α-iron foil. [c] If the sign of the quadrupole splitting, ΔE_Q, is given as ±, only its magnitude is reported in the literature. [d] Zero-field splitting parameter D determined by EPR or applied magnetic field Mössbauer spectroscopy.

Table S4. Ligand Abbreviations Used in table S3.

Index	Definition of Ligand Abbreviations
1.	tmc = 1,4,8,11-tetramethyl-1,4,8,11-tetraazacyclotetradecane
2.	N4Py see Figure 3 in reference 88
4.	TMG_3tren = 1,1,1-tris{2-[N(2)-(1,1,3,3-tetramethylguanidino)]ethyl}amine
5, 6, 7.	TMG_2dien ligand see Figure 1 in reference 90
8, 33.	H_3buea = tris(*tert*-butylureayethylene)aminato
9.	tpa^{Ph} = tris(5-arykpyrrol-2-ylmethyl)amine, in tpa^{Ph} phenyl replaces the Ar found in Scheme 1 in reference 14
10, 11, 14.	TPA* = tris(2-pyridylmethyl)amine
12, 13.	TPA* see Scheme 1 in reference 93 where 2b is tris(5-ethyl-2-pyridylmethyl)amine
15.	L = TPA* = tris(3.5-dimethyl-4-methoxylpyridyl-2-methyl)amine
16.	L = $6Me_3$TPA = N-(6-tris(methyl)-2-pyridylmethyl)-N,N-bis(2-pyridylmethyl)amine
17.	L = 6MeTPA = N-(6-methyl-2-pyridylmethyl)-N,N-bis(2-pyridylmethyl)amine
18.	TPA = tris(2-pyridylmethyl)amine
22	Me_3NTB = tris((N-methylbenzimidazol-2-yl)methylamine)
30.	Hprv = pyruvic acid, H_2btdd = bis(1H-1,2,3-triazolo [4,5-b],[4′,5′-i])dibenzo[1,4]dioxin
31.	Hmoba = 3,3-dimethyl-2-oxobutanoic acid, H_2btdd = bis(1H-1,2,3-triazolo [4,5-b],[4′,5′-i])dibenzo[1,4]dioxin
32.	Me_3TACN = 1,4,7-trimethyl-1,4,7-triazacyclononane
34.	poat = $C_{42}H_{45}N_4O_3P_3$ = a tripodal ligand containing three phosphinic amido groups

Table S5. The 5 K Mössbauer spectral fit parameters for desolvated $FeZn_4Cl_4(btdd)_3$ and partially-solvated $FeZn_4(prv)_4(btdd)_3$.[a]

Sample/	δ,[b] mm/s	ΔE_Q, mm/s	Γ, mm/s	Area, %	Total Area, ($\%\varepsilon$) (mm/s)	Spin State, Oxidation State, Coord. Number
$FeZn_4Cl_4(btdd)_3$ desolvated	1.053(9)	2.52(2)	0.59(1)	17(3)	3.80(2)	HS, Fe(II), 5
	0.907(4)	1.20(2)	0.59(1)	40(1)	-	HS, Fe(II), 4
	0.967(6)	1.77(2)	0.59(1)	33(1)	-	HS, Fe(II), 4
	0.20(3)	0.58(6)	0.59(1)	10(1)	-	Fe(III), 4 or 5
Wt. Ave.	0.957(4)	1.66(2)	0.59(1)	-	-	HS, Fe(II)
$FeZn_4(prv)_4(btdd)_3$ partially-solvated	1.080(2)	2.882(5)	0.463(5)	30.6(7)	4.42(2)	HS, Fe(II), 5
	1.080(2)	2.494(3)	0.463(5)	36(2)	-	HS, Fe(II), 5
	1.080(2)	2.105(3)	0.463(5)	30.6(7)	-	HS, Fe(II), 5
	0.10(5)	0.5(1)	0.463(5)	2.8(9)	-	Fe(IV) or Fe(III), 4
Wt. Ave.	1.080(2)	2.494(5)	0.463(5)	-	-	HS, Fe(II)
$FeZn_4(prv)_4(btdd)_3$ desolvated	1.061(1)	2.567(1)	0.315(2)	84.2(8)	5.59(1)	HS, Fe(II), 5
	1.128(5)	2.06(1)	0.315(2)	9.4(5)	-	HS, Fe(II), 6
	1.307(9)	2.80(2)	0.315(2)	6.4(3)	-	HS, Fe(II), 6

[a]The statistical uncertainties are given in parentheses. The absence of an uncertainty indicates that the parameter was fixed to the value given. The actual uncertainties may be two to three times larger.
[b]The isomer shifts are referred to α-iron foil at 295 K.

Table S6. Mössbauer spectral fit parameters determined from fits to the 5 K spectra obtained for O$_2$ dosed FeZn$_4$(prv)$_4$(btdd)$_3$.[a]

	δ,[b] mm/s	ΔE_Q, mm/s	Γ, mm/s	Area, %	Total Area, (%ε)(mm/s)	Spin State, Oxidation State, Coord. Number
Desolvated	1.061(1)	2.567(1)	0.315(2)	84.2(8)	4.79(5)	HS, Fe(II), 5
	1.128(5)	2.06(1)	0.315(2)	9.4(5)	-	HS, Fe(II), 6
	1.307(9)	2.80(2)	0.315(2)	6.4(3)	-	HS, Fe(II), 6
Dosed with 300 mbar O$_2$ at 100 K	1.060(1)	2.622(2)	0.315(3)	65(1)	5.02(5)	HS, Fe(II), 5
	1.13	2.12	0.315(3)	9.8(5)	-	HS, Fe(II), 6
	1.27	2.72	0.315(3)	4.9(2)	-	HS, Fe(II), 6
	0.260(4)	0.572(8)	0.315(3)	16.7(2)	-	HS, Fe(IV), 5 or 6
	0.69(1)	1.23(3)	0.315(3)	3.5(2)	-	HS Fe(III), 6
Dosed with 300 mbar O$_2$ at 125 K	1.061(1)	2.597(2)	0.305(3)	61(1)	5.20(5)	HS, Fe(II), 5
	1.13	2.12	0.305(3)	12.5(4)	-	HS, Fe(II), 6
	1.27	2.72	0.305(3)	6.3(2)	-	HS, Fe(II), 6
	0.262(3)	0.583(5)	0.305(3)	18.9(2)	-	HS, Fe(IV), 5 or 6
	0.69	1.23	0.305(3)	1.0	-	HS Fe(III), 6
Dosed with 300 mbar O$_2$ at 150 K	1.060(1)	2.601(2)	0.298(3)	59(1)	5.16(5)	HS, Fe(II), 5
	1.13	2.12	0.298(3)	13.8(4)	-	HS, Fe(II), 6
	1.27	2.72	0.298(3)	6.9(2)	-	HS, Fe(II), 6
	0.271(2)	0.591(5)	0.298(3)	20.0(2)	-	HS, Fe(IV), 5 or 6
Dosed with 300 mbar O$_2$ at 163 K	1.060(1)	2.604(1)	0.300(2)	60.5(5)	5.38(5)	HS, Fe(II), 5
	1.13	2.11(6)	0.300(2)	12.3(3)	-	HS, Fe(II), 6
	1.27	2.76(1)	0.300(2)	6.1(2)	-	HS, Fe(II), 6
	0.269(2)	0.597(4)	0.300(2)	21.1(1)	-	HS, Fe(IV), 5 or 6
Warmed to 250 K	1.054(1)	2.618(5)	0.308(4)	66(3)	5.12(5)	HS, Fe(II), 5
	1.03(2)	2.38(3)	0.308(4)	15(2)	-	HS, Fe(II), 6
	1.26(5)	2.8(1)	0.308(4)	4.7(5)	-	HS, Fe(II), 6
	0.27(1)	0.61(1)	0.308(4)	9.7(3)	-	HS, Fe(IV), 5 or 6
	0.70(1)	0.98(2)	0.308(4)	4.5(3)	-	HS Fe(III), 6
Warmed to 298 K	1.059(1)	2.571(2)	0.321(4)	87(2)	4.69(5)	HS, Fe(II), 5
	1.128	2.06	0.321(4)	4.3(9)	-	HS, Fe(II), 6
	1.35(2)	2.87(4)	0.321(4)	4.6(4)	-	HS, Fe(II), 6

[a]The statistical uncertainties are given in parentheses. The absence of an uncertainty indicates that the parameter was fixed to the value given. The actual uncertainties may be two to three times larger. [b]The isomer shifts are referred to α-iron foil at 295 K.

98

Table S7. Mössbauer spectral fit parameters determined from fits to the 5 K spectra obtained for O_2-dosed $FeZn_4(prv)_4(btdd)_3$.[a]

	δ,[b] mm/s	ΔE_Q, mm/s	Γ, mm/s	Area, %	Total Area, ($\%\varepsilon$) (mm/s)	Spin State, Oxidation State, Coord. No.
Dosed with 300 mbar O_2 at 163 K	1.058(1)	2.613(2)	0.289(3)	54(1)	5.68(3)	HS, Fe(II), 5
	1.155(6)	2.15(1)	0.289(3)	15.7(7)	-	HS, Fe(II), 6
	1.24(1)	2.77(1)	0.289(3)	7.8(3)	-	HS, Fe(II), 6
	1.03(4)	2.05(8)	0.289(3)	2.7(2)	-	HS, Fe(II), 5
	0.259(3)	0.617(6)	0.289(3)	19.9(2)	-	HS, Fe(IV), 5 or 6
Dosed with 600 mbar O_2 at 150 K	1.055(1)	2.621(2)	0.286(2)	51(1)	5.73(2)	HS, Fe(II), 5
	1.157(3)	2.163(7)	0.286(2)	16.9(4)	-	HS, Fe(II), 6
	1.229(6)	2.77(1)	0.286(2)	8.4(2)	-	HS, Fe(II), 6
	0.98(2)	1.93(3)	0.286(2)	3.3(1)	-	HS, Fe(II), 5
	0.248(2)	0.634(4)	0.286(2)	20.6(1)	-	HS, Fe(IV), 5 or 6

[a]The statistical uncertainties are given in parentheses. The actual uncertainties may be two to three times larger. [b]The isomer shifts are referred to α-iron foil at 295 K.

Table S8. Mössbauer spectral fit parameters determined from fits to the 5 K spectrum obtained for FeZn$_4$(prv)$_4$(btdd)$_3$ *ex situ* dosed with 200 mbar O$_2$ at 163 K.[a]

Sample	δ,[b] mm/s	ΔE_Q, mm/s	Γ, mm/s	Area, %	Total Area, (%ε) (mm/s)	Spin State, Oxidation State, Coord. Number
Ex situ dosed at 163 K with 200 mbar O$_2$	1.055(3)	2.671(9)	0.301(9)	43(3)	4.20(5)	HS, Fe(II), 5
	1.17(1)	2.16(3)	0.301(9)	17(1)	-	HS, Fe(II), 6
	1.28(3)	3.00(5)	0.301(9)	8.3(7)	-	HS, Fe(II), 6
	0.256(5)	0.63(1)	0.301(9)	32.2(6)	-	HS, Fe(IV), 5 or 6

[a]The statistical uncertainties are given in parentheses. The absence of an uncertainty indicates that the parameter was fixed to the value given. The actual uncertainties may be two to three times larger. [b]The isomer shifts are referred to α-iron foil at 295 K.

Table S9. Comparison of experimental Mössbauer parameters determined for the Fe(IV)=O species generated upon dosing $FeZn_4(prv)_4(btdd)_3$ with 300 mbar O_2 at 100 K and calculated Mössbauer parameters from DFT for six- and five-coordinate $S = 2$ Fe(IV)=O species in $Fe(O)(\kappa^2\text{-}OAc)Zn_4(prv)_3(bta)_6$, and $Fe(O)(\kappa^1\text{-}OAc)Zn_4(prv)_3(bta)_6$, respectively (see section 3).

	Experiment (5 K)	Calculated	
	Fe(IV)=O site	Six-coordinate Fe(IV)=O site	five-coordinate Fe(IV)=O site
δ (mm/s)	0.260(4)	0.253	0.144
$|\Delta E_Q|$ (mm/s)	0.572(8)	0.978	1.421
η	n.d.	0.128	0.537

Table S10. Zero-field Mössbauer spectral fit parameters[a] for pristine $FeZn_4(moba)_4(btdd)_3$ before and after O_2 dosing under the indicated conditions.

Sample	δ,[b] mm/s	ΔE_Q, mm/s	Γ, mm/s	Area, %	Texture[c]	Total Area, ($\%\varepsilon$)(mm/s)	Spin State, Oxidation State, Coord. Number
Desolvated $FeZn_4(moba)_4(btdd)_3$ at 5 K	1.059(1)	2.586(1)	0.341(3)	86(1)	1.105(1)	5.35(2)	HS, Fe(II), 5
	1.41(1)	2.76(2)	0.341(3)	8.3(7)	-	-	HS, Fe(II), 6
	1.52(2)	2.11(3)	0.341(3)	6.1(4)	-	-	HS, Fe(II), 6
Dosed with 100 mbar O_2 at 100 K, warmed to 200 K and held for 2 h, then cooled to 5 K for data collection	1.03(1)	2.59(2)	0.360(4)	16(2)	0.91(1)	5.27(3)	HS, Fe(II), 5
	1.31(3)	3.16(6)	0.360(4)	6.0(5)	-	-	HS, Fe(II), 6
	1.14(5)	2.85(5)	0.360(4)	8.9(9)	-	-	HS, Fe(II), 6
	0.294(2)	0.592(3)	0.360(4)	59.0(5)	-	-	HS, Fe(IV), 5 or 6
	0.45(2)	1.49(3)	0.360(4)	9.5(4)	-	-	HS, Fe(III), 6
Dosed with 200 mbar O_2 at 100 K, warmed to 200 K and held for 2 h, then cooled to 5 K for data collection	1.016(3)	2.611(7)	0.368(1)	13.5(8)	0.90(1)	5.22(1)	HS, Fe(II), 5
	1.273(7)	3.11(1)	0.368(1)	6.1(2)	-	-	HS, Fe(II), 6
	1.14(1)	2.84(1)	0.368(1)	7.6(3)	-	-	HS, Fe(II), 6
	0.292(1)	0.603(1)	0.368(1)	61.7(1)	-	-	HS, Fe(IV), 5 or 6
	0.445(4)	1.470(8)	0.368(1)	11.0(2)	-	-	HS, Fe(III), 6
Sample after dosing with 200 mbar as described above; data collected at 1.7 K	1.016(3)	2.611(7)	0.46(1)	14(6)	0.87(3)	3.63(5)	HS, Fe(II), 5
	1.273(7)	3.11(1)	0.46(1)	7(2)	-	-	HS, Fe(II), 6
	1.14(1)	2.84(1)	0.46(1)	8(2)	-	-	HS, Fe(II), 6
	0.292(1)	0.603(1)	0.46(1)	59(1)	-	-	HS, Fe(IV), 5 or 6
	0.445(4)	1.470(8)	0.46(1)	12(1)	-	-	HS, Fe(III), 6

[a]The statistical uncertainties are given in parentheses. The actual uncertainties may be two to three times larger.
[b]The isomer shifts are referred to α-iron foil at 295 K. [c]Texture is defined as the ratio of the left line area to the right line area of all doublets.

Table S11. Comparison of experimental Mössbauer parameters for the Fe(IV)=O species generated upon dosing $FeZn_4(moba)_4(btdd)_3$ with O_2 with calculated Mössbauer parameters obtained from DFT for $S = 1$ and $S = 2$ Fe(IV)=O species in $Fe(O)(\kappa^2\text{-OPiv})Zn_4(prv)_3(bta)_6$ (see section 3). Experimental dosing conditions are as described in table S10.

	Experiment (5 K)	Calculated	
	Fe(IV)=O site	$S = 2$ Fe(IV)=O site	$S = 1$ Fe(IV)=O site
δ (mm/s)	0.292(1)	0.265	0.160
$\|\Delta E_Q\|$ (mm/s)	0.603(1)	0.948	0.993
η	n.d.	0.494	0.885

Table S12. Spin Hamiltonian parameters modeled for the high-spin iron(II) sites in $FeZn_4(moba)_4(btdd)_3$. The values for A_{xx} and A_{yy} were constrained to be equal because allowing them to refine freely did not improve the fit. All parameters that were fixed for this model are italicized below, while all parameters allowed to refine freely are displayed in bold typeface. The linewidth is a fixed parameter that was chosen as a reasonable value, and so it is presented in normal typeface and without any uncertainty.

Subspectrum	$\delta, \Delta E_Q, \Gamma$ (mm s^{-1})	η	D (cm^{-1})	E/D	$A_{xx}/(g_N\mu_N)$, $A_{yy}/(g_N\mu_N)$, $A_{zz}/(g_N\mu_N)$ (T)
$S = 2$ iron(II)	*1.050(11), 2.57(8),* 0.40	**0.130(3)**	**−8.7(4)**	**0.22(2)**	**−24.3(1.2), −24.3(1.2), −3.46(5)**

104

Table S13. Spin Hamiltonian parameters corresponding to the optimized model of the VTVH Mössbauer spectra for O_2-dosed $FeZn_4(moba)_4(btdd)_3$ in the case of $S = 2$ Fe(IV)=O sites. The spin Hamiltonian parameters corresponding to the high-spin iron(II) subspectrum were taken from the model to the variable-field Mössbauer spectra for $FeZn_4(moba)_4(btdd)_3$ and were set as fixed values. All parameters that were fixed for this model are italicized, while all parameters allowed to refine freely are displayed in bold typeface. Linewidths are reported without uncertainties because they were not fit parameters. The areas were optimized separately in an iterative process as described in Section 2.12.3. The hyperfine parameters for the subspectrum corresponding to the iron(III) species first were fit separately and used as fixed parameters for all models, as described in Section 2.12.3.

Subspectrum	$\delta, \Delta E_Q, \Gamma$ (mm s^{-1})	η	Area (%)	D (cm^{-1})	E/D	$A_{xx}/(g_N\mu_N)$, $A_{yy}/(g_N\mu_N)$, $A_{zz}/(g_N\mu_N)$ (T)
$S = 2$ iron(II)	*1.05(11), 2.57(8), 0.40*	*0.13*	**21.2(4)**	*−8.7(4)*	*0.22(2)*	*−24.3(1.2), −24.3(1.2), −3.46(5)*
$S = 5/2$ iron(III)	*0.440(4), 1.47(4), 0.40*	*0.00*	**14.0(3)**	*0.00*	*0.00*	*−20.0(3), −22.0(3), −22.4(1.1)*
$S_{tot} = 0$ coupled Fe(IV)=O	*0.300(3), −0.610(18), 0.50*	*0.00*	**27.9(6)**	*0.00*	*0.00*	n/a
$S = 2$ uncoupled Fe(IV)=O	*0.300(3), −0.610(18), 0.50*	*0.00*	**36.9(7)**	**12.7(6)**	*0.00*	**−14.0(2), −14.0(2), −21.2(1.1)**

Table S14. Spin Hamiltonian parameters corresponding to the optimized model of the VTVH Mössbauer spectra for O_2-dosed $FeZn_4(moba)_4(btdd)_3$ in the case of $S = 1$ Fe(IV)=O sites. The spin Hamiltonian parameters corresponding to the high-spin iron(II) subspectrum were taken from the model to the variable-field Mössbauer spectra for $FeZn_4(moba)_4(btdd)_3$ and were set as fixed values. All parameters that were fixed for this model are italicized, while all parameters allowed to refine freely are displayed in bold typeface. Linewidths are reported without uncertainties because they were not fit parameters. The areas were optimized separately in an iterative process as described in Section 2.12.3. The hyperfine parameters for the subspectrum corresponding to the iron(III) species first were fit separately and used as fixed parameters for all models, as described in Section 2.12.3.

Subspectrum	δ, ΔE_Q, Γ (mm s^{-1})	η	Area (%)	D (cm^{-1})	E/D	$A_{xx}/(g_N\mu_N)$, $A_{yy}/(g_N\mu_N)$, $A_{zz}/(g_N\mu_N)$ (T)
$S = 2$ iron(II)	*1.05(11), 2.57(8), 0.40*	*0.130(3)*	**21.5(4)**	*−8.7(4)*	*0.22(2)*	*−24.3(1.2), −24.3(1.2), −3.46(5)*
$S = 5/2$ iron(III)	*0.440(4), 1.47(4), 0.40*	*0.00*	**14.8(3)**	*0.00*	*0.00*	*−20.0(3), −22.0(3), −22.4(1.1)*
$S_{tot} = 0$ coupled Fe(IV)=O	*0.300(3), −0.610(18), 0.50*	*0.00*	**24.1(5)**	*0.00*	*0.00*	n/a
$S = 1$ uncoupled Fe(IV)=O	*0.300(3), −0.610(18), 0.50*	*0.00*	**39.6(8)**	**15.6(8)**	*0.00*	**−35.7(5), −35.7(5), −36.6(1.8)**

Table S15. All models considered for $S = 1$ and $S = 2$ Fe(IV)=O species (corresponding to the fraction of uncoupled Fe(IV)=O sites). All parameters that were fixed for a given model are italicized, while all parameters allowed to refine freely are displayed in bold typeface. The rhombicity parameter for model 12 went beyond the rhombic limit (0.333) if allowed to refine freely, and it was thus fixed at 0.33. The chosen optimized models for the $S = 1$ and $S = 2$ scenarios are highlighted in blue and were selected based on their minimal associated RSS values and minimal fit parameters (e.g., exclusion of E in model 5 versus inclusion in model 7).

#	Spin	Sign ΔE_Q	Ax/Rh	A_{zz}?	D (cm^{-1})	E/D	$A_{xx}/(g_N\mu_N)$ (T)	$A_{yy}/(g_N\mu_N)$ (T)	$A_{zz}/(g_N\mu_N)$ (T)	RSS
1	$S = 1$	+	Ax	Yes	**12.9(6)**	*0.00*	**–31.0(5)**	**–31.0(5)**	**–60(3)**	3.39072
2	$S = 1$	+	Ax	No	**13.5(7)**	*0.00*	**–31.1(5)**	**–31.1(5)**	*0.00*	3.95049
3	$S = 1$	+	Rh	Yes	**12.9(6)**	**0.050(5)**	**–22.6(3)**	**–45.2(7)**	**–50(2)**	2.92641
4	$S = 1$	+	Rh	No	**13.6(7)**	**0.180(18)**	**–28.2(4)**	**–33.2(5)**	*0.00*	3.59765
5	$S = 1$	–	Ax	Yes	**15.6(8)**	*0.00*	**–35.7(5)**	**–35.7(5)**	**–36.6(1.8)**	2.64058
6	$S = 1$	–	Ax	No	**13.7(7)**	*0.00*	**–32.5(5)**	**–32.5(5)**	*0.00*	3.20476
7	$S = 1$	–	Rh	Yes	**16.2(8)**	**0.150(15)**	**–35.6(5)**	**–35.8(5)**	**–36.5(1.8)**	2.58292
8	$S = 1$	–	Rh	No	**14.1(7)**	**0.170(17)**	**–31.4(5)**	**–32.2(5)**	*0.00*	3.06870
9	$S = 2$	+	Ax	Yes	**13.3(7)**	*0.00*	**–13.7(2)**	**–13.7(2)**	**–23.3(1.2)**	3.76991
10	$S = 2$	+	Ax	No	**3.91(2)**	*0.00*	**–10.78(16)**	**–10.78(16)**	*0.00*	4.04183
11	$S = 2$	+	Rh	Yes	**12.8(6)**	**0.030(3)**	**–10.29(15)**	**–15.9(2)**	**–25.9(1.3)**	3.12650
12	$S = 2$	+	Rh	No	**4.25(2)**	*0.33*	**–10.70(16)**	**–10.46(16)**	*0.00*	3.84001
13	$S = 2$	–	Ax	Yes	**12.7(6)**	*0.00*	**–14.0(2)**	**–14.0(2)**	**–21.2(1.1)**	2.94714
14	$S = 2$	–	Ax	No	**3.90(2)**	*0.00*	**–11.23(17)**	**–11.23(17)**	*0.00*	3.39641
15	$S = 2$	–	Rh	Yes	**14.1(7)**	**0.170(17)**	**–15.4(2)**	**–12.52(19)**	**–23.1(1.2)**	2.70452
16	$S = 2$	–	Rh	No	**4.89(2)**	**0.28(3)**	**–11.62(17)**	**–10.84(16)**	*0.00*	3.26178

Table S16. Mössbauer spectral fit parameters[a] for $FeZn_4(prv)_4(btdd)_3$ post cyclohexane and O_2 treatment. The quadrupole splitting reported below for the three doublet fit (see fig. S55) is the average of the three values for this fit.

FeZn₄(prv)₄(btdd)₃ post cyclohexane	T, K	δ or δ_o, mm/s[b]	m^c	$<\Delta E_Q>$, mm/s	σ, mm/s[d]	ΔE_Q fit or range, mm/s	Area, %
Three doublet fit	5	1.108(7)	-		-	1.78(2)	25
	5	1.114(3)	-	2.52(2)	-	2.521(6)	50
	5	1.147(7)	-		-	3.27(2)	25
Distribution fit	5	1.10(1)	0.0045(5)	2.5(1)	0.9(1)	0.0–4.5	-

[a]The statistical errors are given in parentheses. The distribution fit has been obtained by using the Le Caër and Dubois method where the linewidth of each of the 20 components was constrained to 0.28 mm/s and in the three doublet fit, the fitted linewidth was 0.64(2) mm/s (*86*). [b]The isomer shift values are given relative to α-iron foil measured at 290 K. [c]The linear correlation coefficient, m, is the unitless slope in $\delta_i = \delta_o + m(\Delta E_{Q,i})$. [d]The half-width at half-maximum of the distribution fit.

Table S17: DFT optimized structures and cartesian coordinates (Å).

FeZn₄(prv)₄(bta)₆
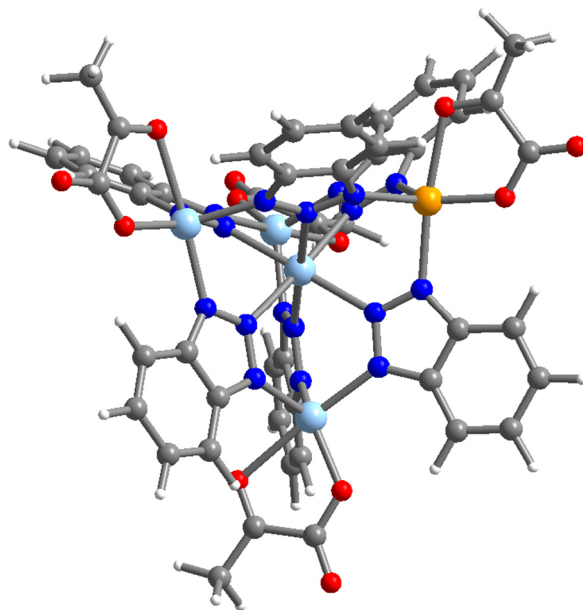
N	1.8478	-0.9255	1.3857
C	3.1629	-1.0794	1.7055
C	3.8486	-0.9914	2.9314
H	3.3235	-0.7659	3.8484
N	1.7359	-1.1142	0.0809
N	2.9073	-1.3864	-0.4777
C	3.8413	-1.3764	0.5077
C	5.2302	-1.6000	0.4805
H	5.7373	-1.8307	-0.4463
Fe	0.1015	-0.6089	2.6187
Zn	-0.1240	-0.9626	-1.0621
N	-1.2563	1.9684	-0.4093
C	-1.5807	2.8161	0.6028
C	-2.1952	4.0790	0.6108
H	-2.5220	4.5539	-0.3027
N	-0.7197	0.8855	0.1270
N	-0.6666	0.9749	1.4453
C	-1.1931	2.1821	1.7959
C	-1.3698	2.8086	3.0408
H	-1.0552	2.3368	3.9595
N	-0.9552	-2.2275	1.7724
N	2.1652	0.0386	-3.0728
C	2.5228	1.0310	-3.9306
C	3.6896	1.2509	-4.6812
H	4.5288	0.5727	-4.6329

N	0.9663	0.3250	-2.6007
N	0.5080	1.4568	-3.1095
C	1.4502	1.9393	-3.9639
C	1.4857	3.0792	-4.7842
H	0.6531	3.7650	-4.8355
N	-2.3755	0.4014	-2.8238
N	1.5746	-3.1551	-2.6401
N	-1.9936	-0.7325	-2.2672
N	-1.1957	-2.2628	0.4725
N	0.3593	-2.8312	-2.2242
C	1.5101	-4.4053	-3.1694
C	2.4886	-5.2477	-3.7241
H	3.5256	-4.9497	-3.7858
N	-0.5039	-3.8001	-2.4618
C	0.1699	-4.8191	-3.0599
C	-0.2543	-6.0794	-3.5176
H	-1.2887	-6.3817	-3.4286
N	-1.9558	-3.2944	0.1517
C	-2.2172	-3.9890	1.2901
C	-2.9331	-5.1744	1.5252
H	-3.4064	-5.7194	0.7207
C	-1.5752	-3.3013	2.3348
C	-1.6259	-3.7740	3.6563
H	-1.1179	-3.2613	4.4606
N	-2.7869	-1.7337	-2.6189
C	-3.7326	-1.2359	-3.4582
C	-4.7963	-1.8447	-4.1456
H	-4.9887	-2.9053	-4.0678
C	-3.4719	0.1405	-3.5868
C	-4.2727	0.9702	-4.3923
H	-4.0666	2.0281	-4.4752
C	5.2052	-1.2108	2.8925
H	5.7758	-1.1550	3.8112
C	5.8867	-1.5112	1.6847
H	6.9565	-1.6753	1.7179
C	3.7201	2.3782	-5.4671
H	4.6004	2.5896	-6.0604
C	2.6255	3.2762	-5.5268
H	2.6962	4.1410	-6.1741
C	-2.3752	4.6762	1.8359
H	-2.8465	5.6491	1.8905
C	-1.9576	4.0517	3.0372
H	-2.1113	4.5703	3.9746
C	-2.3335	-4.9323	3.8775
H	-2.3938	-5.3364	4.8799

C	-2.9794	-5.6252	2.8234
H	-3.5139	-6.5386	3.0506
C	2.0668	-6.4797	-4.1648
H	2.7869	-7.1640	-4.5954
C	0.7119	-6.8879	-4.0681
H	0.4371	-7.8687	-4.4345
C	-5.5701	-1.0279	-4.9356
H	-6.3984	-1.4531	-5.4880
C	-5.3144	0.3623	-5.0525
H	-5.9594	0.9576	-5.6862
C	0.4225	-0.3613	5.4821
O	-1.5944	-0.3629	4.2118
C	-1.1241	-0.3008	5.3363
O	1.0269	-0.4869	4.3490
O	0.9142	-0.2893	6.5903
C	-1.9553	-0.1684	6.5662
H	-3.0133	-0.1421	6.3157
H	-1.7355	-0.9977	7.2427
H	-1.6610	0.7339	7.1076
Zn	3.0673	-1.7517	-2.5412
O	4.9772	-2.1227	-2.7171
O	3.4256	-2.1252	-4.9088
C	5.5540	-2.3917	-3.8351
C	4.6007	-2.4002	-5.0688
O	6.7335	-2.6270	-4.0230
C	5.1827	-2.7441	-6.4014
H	6.0133	-2.0714	-6.6240
H	5.6191	-3.7447	-6.3596
H	4.4192	-2.6905	-7.1745
Zn	-1.3015	2.1819	-2.4562
O	-2.4480	3.4167	-3.4425
O	-0.2836	4.3741	-2.1824
C	-2.2293	4.6797	-3.5503
C	-0.9642	5.1809	-2.7895
O	-2.8894	5.4955	-4.1672
C	-0.6440	6.6390	-2.8461
H	-0.5060	6.9407	-3.8870
H	-1.4980	7.2164	-2.4861
H	0.2468	6.8560	-2.2609
Zn	-2.5039	-3.5954	-1.8125
O	-4.8023	-3.6021	-1.1358
O	-3.2112	-5.2991	-2.4646
C	-4.4222	-5.6837	-2.2644
C	-5.3049	-4.6505	-1.4992
O	-4.9301	-6.7394	-2.5956

C	-6.7341	-5.0000	-1.2432
H	-7.2375	-5.1951	-2.1925
H	-6.7861	-5.9384	-0.6872
H	-7.2306	-4.1988	-0.7003

Fe(O)(κ²-OAc)Zn₄(prv)₃(bta)₆
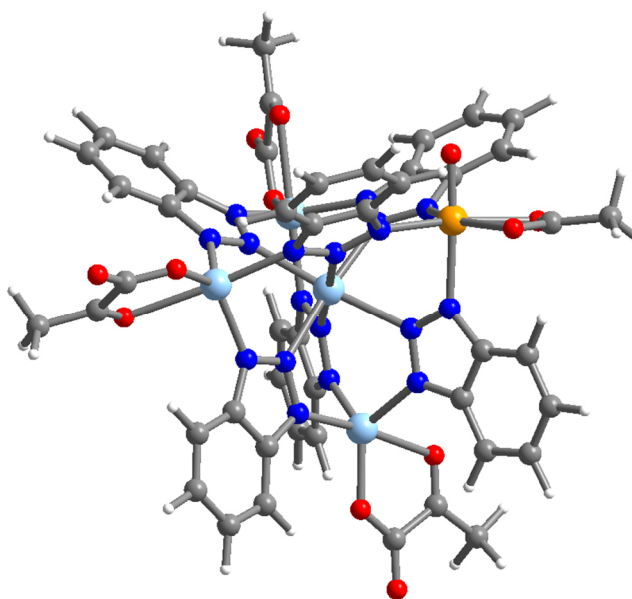
N	2.4758	-1.2502	2.5415
C	3.4477	-1.0607	3.4742
C	3.3969	-0.6586	4.8190
H	2.4564	-0.4365	5.3018
N	3.0552	-1.6292	1.4163
N	4.3657	-1.6985	1.5545
C	4.6677	-1.3446	2.8338
C	5.8955	-1.2395	3.5111
H	6.8271	-1.4568	3.0074
Fe	0.4256	-1.1106	2.8048
Zn	1.9666	-2.1542	-0.4477
N	0.5929	0.6045	-1.0406
C	0.2251	1.7750	-0.4613
C	-0.0153	3.0425	-1.0162
H	0.0669	3.2161	-2.0800
N	0.7383	-0.2916	-0.0838
N	0.4636	0.2166	1.1077
C	0.1519	1.5366	0.9244
C	-0.1405	2.5923	1.8079
H	-0.1289	2.4496	2.8752

N	-0.3567	-2.6531	1.5771
N	4.7577	-0.9550	-1.4153
C	5.3027	-0.0133	-2.2302
C	6.6219	0.4400	-2.4003
H	7.4409	0.0328	-1.8246
N	3.4490	-0.9599	-1.6289
N	3.1073	-0.0800	-2.5487
C	4.2401	0.5472	-2.9635
C	4.4497	1.5692	-3.9063
H	3.6221	1.9876	-4.4625
N	0.6877	-1.8079	-3.3340
N	4.5169	-4.0601	-0.3927
N	0.9366	-2.6678	-2.3581
N	0.3479	-3.2158	0.6183
N	3.2168	-4.0198	-0.6207
C	4.9175	-5.3545	-0.5064
C	6.1694	-5.9694	-0.3404
H	7.0448	-5.4022	-0.0594
N	2.7371	-5.2223	-0.8893
C	3.7729	-6.1023	-0.8356
C	3.8442	-7.4890	-1.0481
H	2.9721	-8.0648	-1.3203
N	-0.2130	-4.3392	0.2037
C	-1.3520	-4.5212	0.9221
C	-2.3395	-5.5188	0.8762
H	-2.2893	-6.3332	0.1673
C	-1.4417	-3.4408	1.8179
C	-2.5103	-3.3269	2.7229
H	-2.5725	-2.4925	3.4045
N	0.5879	-3.8943	-2.6941
C	0.0857	-3.8491	-3.9579
C	-0.4302	-4.8533	-4.7959
H	-0.4940	-5.8783	-4.4578
C	0.1554	-2.5058	-4.3717
C	-0.2710	-2.1139	-5.6517
H	-0.2003	-1.0876	-5.9835
C	4.6032	-0.5606	5.4719
H	4.6194	-0.2558	6.5107
C	5.8343	-0.8461	4.8272
H	6.7519	-0.7490	5.3935
C	6.8176	1.4436	-3.3197
H	7.8168	1.8286	-3.4793
C	5.7463	1.9978	-4.0661
H	5.9612	2.7850	-4.7774
C	-0.3230	4.0554	-0.1408

H	-0.5074	5.0525	-0.5195
C	-0.3771	3.8297	1.2557
H	-0.5940	4.6650	1.9093
C	-3.4648	-4.3157	2.6756
H	-4.3093	-4.2693	3.3514
C	-3.3849	-5.3952	1.7605
H	-4.1730	-6.1374	1.7588
C	6.2249	-7.3287	-0.5372
H	7.1679	-7.8461	-0.4164
C	5.0768	-8.0785	-0.8964
H	5.1787	-9.1452	-1.0494
C	-0.8510	-4.4540	-6.0426
H	-1.2571	-5.1891	-6.7257
C	-0.7677	-3.1033	-6.4672
H	-1.1052	-2.8495	-7.4641
O	0.2580	0.5463	4.1574
O	-1.5178	-0.3918	3.3163
C	-1.0028	0.4327	4.1238
C	-1.8731	1.2458	5.0391
H	-2.1558	0.6188	5.8883
H	-1.3376	2.1153	5.4146
H	-2.7858	1.5454	4.5260
O	0.4839	-2.1465	4.0447
Zn	0.7193	-5.4480	-1.2530
Zn	1.0481	0.1790	-3.0106
Zn	5.5595	-2.2967	-0.0864
O	7.3201	-2.1450	0.7497
O	7.1145	-3.0006	-1.7818
O	1.2261	1.5642	-4.3834
O	-1.1902	0.6912	-3.6259
O	0.6737	-7.3293	0.2277
O	-0.1459	-6.8698	-2.2795
C	0.0975	-8.2439	-0.3342
C	-0.3889	-8.0387	-1.8010
C	-1.1666	1.5540	-4.4858
C	0.2127	2.1000	-4.9669
C	8.4209	-2.4167	0.1427
C	8.2404	-2.9041	-1.3270
O	9.5521	-2.3372	0.5857
O	0.2205	2.9643	-5.8242
O	-0.9390	-8.9701	-2.3595
C	-0.1633	-9.5632	0.3145
H	0.2834	-10.3593	-0.2853
H	0.2293	-9.5735	1.3287
H	-1.2372	-9.7634	0.3122

C	9.4675	-3.2360	-2.1110
H	9.2026	-3.5642	-3.1135
H	10.1228	-2.3629	-2.1481
H	10.0376	-4.0063	-1.5868
C	-2.4007	2.1209	-5.1059
H	-2.4208	3.2022	-4.9525
H	-2.3627	1.9793	-6.1881
H	-3.2880	1.6542	-4.6843

Fe(O)(κ^1-OAc)Zn$_4$(prv)$_3$(bta)$_6$
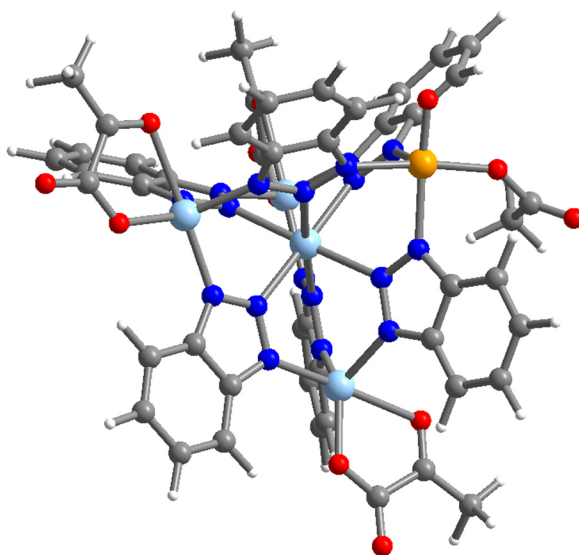
Zn	24.2871	7.0136	7.0818
Zn	22.5373	9.1569	9.3110
Zn	26.3756	4.7014	8.8466
Zn	26.2860	8.9057	4.7884
Fe	21.7801	4.9705	5.1397
N	24.4255	9.1960	7.0818
N	24.0158	4.7845	7.0844
N	26.4864	6.8531	6.8699
N	24.0669	7.0028	4.9025
N	24.5075	6.9501	9.2628
N	22.0988	7.0646	7.2924
N	23.8215	9.9766	7.9620
N	24.7765	3.9743	7.7891
N	27.2486	6.0850	7.6244
N	27.2150	7.6489	6.1087
N	24.7544	7.7618	4.0661
N	23.8741	7.7605	10.0920

N	25.1684	9.8970	6.2475
N	23.0821	4.1084	6.4381
N	21.4989	7.7407	8.2502
N	21.2633	6.2263	6.7056
N	25.2607	6.0827	9.9177
N	23.2150	6.2343	4.2574
C	24.1865	11.2574	7.6991
C	24.3234	2.7049	7.6139
C	28.5443	6.3899	7.3576
C	28.5227	7.4010	6.3781
C	24.3276	7.4829	2.8057
C	24.2209	7.4115	11.3579
C	25.0561	11.2074	6.5920
C	23.2337	2.7849	6.7290
C	20.2104	7.3210	8.3207
C	20.0502	6.3424	7.3212
C	25.1177	6.3300	11.2453
C	23.3394	6.4888	2.9277
O	27.7004	3.0887	7.6737
O	27.6658	7.9513	3.0812
O	20.9167	10.7263	8.5296
O	18.3368	6.6625	4.1945
C	23.8627	12.4733	8.3205
C	24.7459	1.4802	8.1513
C	29.7515	5.9061	7.8846
C	29.7083	7.9685	5.8870
C	24.6785	8.0109	1.5540
C	23.8385	7.9247	12.6085
C	25.6336	12.3694	6.0541
C	22.5320	1.6380	6.3274
C	19.1575	7.6820	9.1749
C	18.8207	5.6939	7.1251
C	25.6788	5.7156	12.3769
C	22.6688	5.9698	1.8104
C	24.4337	13.6057	7.7893
C	24.0491	0.3621	7.7576
C	24.0136	7.5020	0.4629
C	24.3921	7.3141	13.7096
C	25.3049	13.5542	6.6706
C	22.9611	0.4411	6.8529
C	17.9612	7.0337	8.9801
C	17.7955	6.0578	7.9653
C	25.2989	6.2276	13.5956
C	23.0254	6.4924	0.5888
C	20.4019	11.2413	9.5052

C	28.3590	2.4849	8.5002
C	28.2392	8.8641	2.5149
C	19.5459	6.6765	4.1706
O	27.3239	3.7521	10.2548
O	27.1436	10.4395	3.9489
O	21.8242	9.9473	10.9380
C	28.1761	2.8198	10.0113
C	27.9829	10.3282	2.9814
C	20.8838	10.8250	10.9271
C	29.3450	1.4259	8.1393
C	29.1866	8.6543	1.3829
C	19.3185	12.2612	9.4116
C	20.3397	7.9496	3.9735
O	28.8360	2.1891	10.8159
O	28.5808	11.2221	2.4120
O	20.3452	11.3465	11.8857
H	23.2065	12.5126	9.1780
H	25.5678	1.4250	8.8501
H	29.7691	5.1464	8.6529
H	29.6939	8.7591	5.1508
H	25.4236	8.7868	1.4568
H	23.1413	8.7481	12.6806
H	26.3004	12.3134	5.2051
H	21.7122	1.7009	5.6283
H	19.2908	8.4159	9.9570
H	18.6782	4.9794	6.3288
H	26.3682	4.8886	12.2760
H	21.9128	5.2061	1.9222
H	24.2180	14.5678	8.2354
H	24.3343	-0.6067	8.1457
H	24.2451	7.8815	-0.5237
H	24.1302	7.6680	14.6982
H	25.7238	14.4795	6.2976
H	22.4543	-0.4720	6.5699
H	17.1179	7.2721	9.6148
H	16.8259	5.5940	7.8440
H	25.7001	5.7909	14.5009
H	22.5375	6.1301	-0.3063
H	29.0787	0.4947	8.6435
H	29.3780	1.2892	7.0611
H	30.3283	1.6980	8.5286
H	28.8378	9.2130	0.5118
H	30.1565	9.0867	1.6373
H	29.2796	7.5954	1.1543
H	19.6237	13.1662	9.9407

H	18.4344	11.8971	9.9396
H	19.0862	12.4757	8.3712
H	21.0658	8.0836	4.7753
H	19.6610	8.7979	3.9472
H	20.8939	7.8961	3.0356
C	30.8860	7.4841	6.4063
C	30.9074	6.4657	7.3929
H	31.8266	7.8942	6.0635
H	31.8637	6.1305	7.7723
O	20.2463	5.5480	4.2587
O	21.9458	3.6897	4.1501

Fe(moba)Zn$_4$(prv)$_3$(bta)$_6$
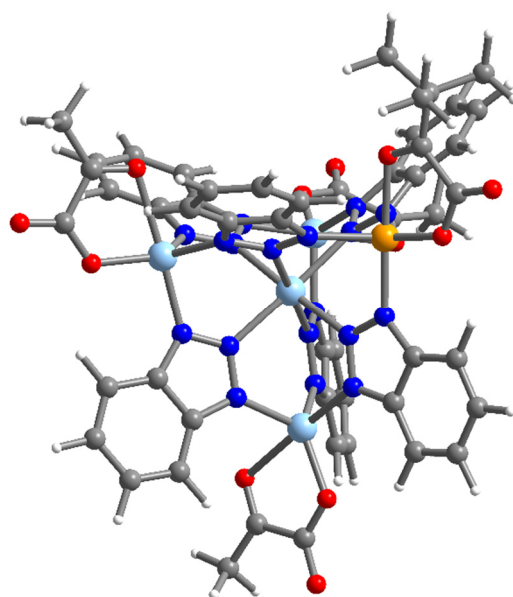
N	1.8866	-0.9386	1.3887
C	3.2086	-1.0951	1.7081
C	3.8887	-1.0288	2.9391
H	3.3521	-0.8219	3.8643
N	1.7711	-1.1047	0.0696
N	2.9557	-1.3636	-0.4947
C	3.8932	-1.3683	0.4957
C	5.2843	-1.5860	0.4638
H	5.7932	-1.7969	-0.4767
Fe	0.1876	-0.6121	2.5620
Zn	-0.0812	-0.9529	-1.0476
N	-1.1899	1.9523	-0.3834
C	-1.4421	2.8155	0.6443
C	-2.0430	4.0864	0.6781
H	-2.4195	4.5614	-0.2263

N	-0.6237	0.8593	0.1269
N	-0.4890	0.9631	1.4494
C	-0.9863	2.1815	1.8256
C	-1.0835	2.8099	3.0795
H	-0.7090	2.3341	3.9839
N	-0.8231	-2.1990	1.7686
N	2.1490	0.0425	-3.0581
C	2.4627	1.0200	-3.9580
C	3.6075	1.2426	-4.7444
H	4.4694	0.5799	-4.6931
N	0.9417	0.3094	-2.5665
N	0.4407	1.4197	-3.1064
C	1.3561	1.9041	-3.9963
C	1.3383	3.0210	-4.8508
H	0.4764	3.6838	-4.9033
N	-2.3908	0.4105	-2.7075
N	1.6175	-3.0926	-2.6083
N	-1.9606	-0.7329	-2.1807
N	-1.0819	-2.2486	0.4621
N	0.3890	-2.7717	-2.1990
C	1.5674	-4.3505	-3.1344
C	2.5617	-5.1835	-3.6790
H	3.6024	-4.8679	-3.7354
N	-0.4701	-3.7590	-2.4392
C	0.2203	-4.7798	-3.0285
C	-0.1902	-6.0502	-3.4756
H	-1.2303	-6.3628	-3.3833
N	-1.8549	-3.2931	0.1673
C	-2.1069	-3.9709	1.3249
C	-2.8319	-5.1471	1.5877
H	-3.3182	-5.7067	0.7900
C	-1.4449	-3.2643	2.3593
C	-1.4842	-3.7064	3.6930
H	-0.9528	-3.1789	4.4837
N	-2.7618	-1.7464	-2.5162
C	-3.7601	-1.2487	-3.3024
C	-4.8502	-1.8652	-3.9431
H	-5.0222	-2.9379	-3.8693
C	-3.5231	0.1435	-3.4235
C	-4.3719	0.9778	-4.1754
H	-4.1753	2.0471	-4.2531
C	5.2563	-1.2438	2.8965
H	5.8295	-1.2037	3.8235
C	5.9418	-1.5175	1.6805
H	7.0200	-1.6789	1.7119

C	3.5860	2.3530	-5.5712
H	4.4513	2.5690	-6.1983
C	2.4640	3.2233	-5.6313
H	2.4968	4.0744	-6.3120
C	-2.1472	4.6914	1.9198
H	-2.6091	5.6760	1.9976
C	-1.6661	4.0666	3.1016
H	-1.7620	4.5945	4.0507
C	-2.2087	-4.8606	3.9437
H	-2.2641	-5.2468	4.9618
C	-2.8720	-5.5700	2.9064
H	-3.4173	-6.4796	3.1591
C	2.1507	-6.4322	-4.1145
H	2.8853	-7.1167	-4.5401
C	0.7967	-6.8562	-4.0182
H	0.5335	-7.8514	-4.3780
C	-5.6788	-1.0390	-4.6838
H	-6.5356	-1.4700	-5.2027
C	-5.4456	0.3595	-4.7943
H	-6.1343	0.9590	-5.3903
C	0.3252	-0.3949	5.4151
O	-1.5186	-0.3423	3.9243
C	-1.2004	-0.3133	5.1210
O	1.0203	-0.5331	4.3148
O	0.7756	-0.3297	6.5534
C	-2.2336	-0.2009	6.2206
Zn	3.0784	-1.6909	-2.5285
O	4.9868	-2.0395	-2.7358
O	3.3188	-2.0856	-4.8839
C	5.5087	-2.3354	-3.8859
C	4.4992	-2.3689	-5.0772
O	6.6898	-2.5792	-4.1236
C	5.0327	-2.7445	-6.4214
H	5.8452	-2.0564	-6.6977
H	5.5045	-3.7366	-6.3628
H	4.2346	-2.7336	-7.1709
Zn	-1.3122	2.1544	-2.3986
O	-2.4482	3.4349	-3.3354
O	-0.1589	4.2245	-2.1003
C	-2.1460	4.6951	-3.3977
C	-0.8236	5.0902	-2.6663
O	-2.7819	5.5831	-3.9610
C	-0.4248	6.5294	-2.6930
H	-0.3328	6.8636	-3.7370
H	-1.2346	7.1407	-2.2677

H	0.5118	6.6816	-2.1469
Zn	-2.4280	-3.5872	-1.7576
O	-4.6714	-3.5583	-0.9637
O	-3.1454	-5.2842	-2.4053
C	-4.3614	-5.6498	-2.1398
C	-5.1941	-4.6122	-1.3214
O	-4.9052	-6.7054	-2.4573
C	-6.6114	-4.9623	-1.0052
H	-7.1583	-5.1485	-1.9416
H	-6.6397	-5.9186	-0.4624
H	-7.0873	-4.1649	-0.4251
C	-3.6398	-0.1830	5.6084
H	-3.7720	0.6729	4.9333
H	-3.8334	-1.0963	5.0296
H	-4.3875	-0.1141	6.4109
C	-1.9724	1.1118	6.9978
H	-2.7168	1.2020	7.8023
H	-0.9694	1.1177	7.4392
H	-2.0817	1.9856	6.3388
C	-2.0825	-1.4127	7.1708
H	-2.8308	-1.3276	7.9719
H	-2.2686	-2.3557	6.6363
H	-1.0825	-1.4434	7.6176

$S = 2$ Fe(O)(κ^2-OPiv)Zn$_4$(prv)$_3$(bta)$_6$
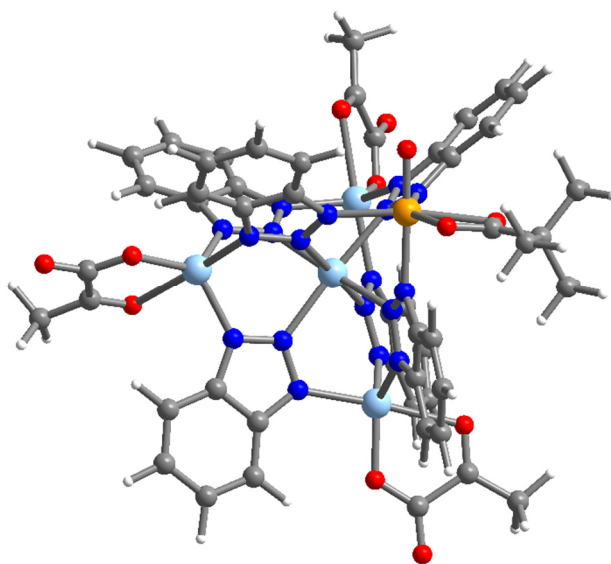
N	2.0428	0.0000	0.0000
C	2.8773	0.7567	0.7764

C	2.6261	1.7018	1.7865
H	1.6091	1.9323	2.0986
N	2.7934	-0.7439	-0.8132
N	4.0864	-0.5092	-0.6115
C	4.1967	0.4334	0.3724
C	5.3218	1.0440	0.9567
H	6.3282	0.7887	0.6251
Fe	0.0000	0.0000	0.0000
Zn	2.0275	-2.3607	-2.1013
N	0.3743	-0.6714	-4.1028
C	-0.0671	0.6068	-4.2634
C	-0.3174	1.3520	-5.4295
H	-0.1843	0.9160	-6.4190
N	0.5061	-0.9033	-2.8009
N	0.1439	0.1613	-2.0822
C	-0.2030	1.1589	-2.9637
C	-0.5604	2.5127	-2.8028
H	-0.6208	2.9597	-1.8152
N	-0.2314	-2.0756	-0.0134
N	4.6301	-1.2931	-3.5082
C	5.1140	-0.8557	-4.7069
C	6.3476	-0.2880	-5.0749
H	7.1375	-0.1164	-4.3452
N	3.3787	-1.7166	-3.7047
N	3.0212	-1.5863	-4.9780
C	4.0768	-1.0459	-5.6553
C	4.2330	-0.6876	-7.0078
H	3.4195	-0.8336	-7.7183
N	0.9624	-3.8274	-4.6844
N	4.8388	-3.3996	-1.0893
N	1.2795	-3.9705	-3.3960
N	0.5868	-2.9310	-0.6099
N	3.5636	-3.7272	-1.2869
C	5.4777	-4.4905	-0.5743
C	6.8072	-4.6949	-0.1632
H	7.5459	-3.8968	-0.2106
N	3.3331	-4.9890	-0.9299
C	4.5074	-5.5191	-0.4785
C	4.8398	-6.7997	-0.0008
H	4.1011	-7.5976	0.0493
N	0.2866	-4.1896	-0.2876
C	-0.7816	-4.1589	0.5612
C	-1.5081	-5.1876	1.1877
H	-1.2714	-6.2368	1.0175
C	-1.1117	-2.7941	0.7497

C	-2.1632	-2.4046	1.5980
H	-2.4030	-1.3546	1.7393
N	1.1079	-5.2264	-2.9965
C	0.6586	-5.9485	-4.0659
C	0.3202	-7.3083	-4.1993
H	0.3886	-7.9845	-3.3472
C	0.5673	-5.0459	-5.1556
C	0.1447	-5.4718	-6.4276
H	0.0886	-4.7828	-7.2691
C	3.7401	2.2940	2.3601
H	3.6012	3.0301	3.1527
C	5.0634	1.9734	1.9510
H	5.8988	2.4768	2.4388
C	6.4934	0.0622	-6.4068
H	7.4298	0.5108	-6.7401
C	5.4547	-0.1372	-7.3576
H	5.6284	0.1608	-8.3920
C	-0.6958	2.6711	-5.2520
H	-0.8918	3.2961	-6.1235
C	-0.8049	3.2407	-3.9563
H	-1.0762	4.2933	-3.8677
C	-2.8627	-3.4242	2.2214
H	-3.6875	-3.1728	2.8890
C	-2.5465	-4.7944	2.0147
H	-3.1419	-5.5540	2.5223
C	7.1211	-5.9549	0.3171
H	8.1384	-6.1617	0.6502
C	6.1542	-6.9942	0.3886
H	6.4612	-7.9705	0.7645
C	-0.1001	-7.7133	-5.4553
H	-0.3754	-8.7564	-5.6140
C	-0.1835	-6.8116	-6.5519
H	-0.5144	-7.1918	-7.5189
O	-1.0476	1.7527	-0.0173
O	-2.2802	-0.0313	-0.3597
C	-2.2049	1.2198	-0.2259
C	-3.4558	2.0948	-0.3074
O	-0.0629	-0.0069	1.6404
Zn	1.4319	-5.7001	-0.9961
Zn	1.0347	-1.9911	-5.5008
Zn	5.4984	-1.5767	-1.7037
O	7.1262	-0.7068	-1.0708
O	7.2198	-2.7406	-2.8710
O	1.1345	-1.5099	-7.3949
O	-1.1941	-2.2496	-6.2144

O	1.7298	-6.3761	1.2643
O	0.9380	-7.5884	-1.0343
C	1.3944	-7.5570	1.3349
C	0.9491	-8.3124	0.0423
C	-1.2413	-1.9241	-7.3997
C	0.0662	-1.4835	-8.1310
C	8.2970	-1.0595	-1.5048
C	8.2864	-2.2193	-2.5509
O	9.3828	-0.5863	-1.1774
O	-0.0136	-1.1500	-9.3113
O	0.6563	-9.5020	0.1397
C	1.3960	-8.3242	2.6164
H	2.0340	-9.2138	2.5099
H	1.7329	-7.6927	3.4450
H	0.3858	-8.7169	2.8062
C	9.6005	-2.6502	-3.1152
H	9.4663	-3.4707	-3.8275
H	10.0915	-1.7895	-3.5936
H	10.2719	-2.9427	-2.2944
C	-2.5073	-1.9286	-8.1917
H	-2.6763	-0.9280	-8.6157
H	-2.3898	-2.5929	-9.0610
H	-3.3524	-2.2424	-7.5703
C	-4.4283	1.6039	0.7845
H	-4.6617	0.5407	0.6445
H	-3.9971	1.7371	1.7873
H	-5.3632	2.1808	0.7336
C	-4.0827	1.8802	-1.7001
H	-3.3938	2.1931	-2.4975
H	-4.3312	0.8226	-1.8551
H	-5.0028	2.4766	-1.7867
C	-3.1192	3.5750	-0.0919
H	-4.0444	4.1694	-0.1097
H	-2.6208	3.7370	0.8728
H	-2.4583	3.9563	-0.8816

_S_ = 1 Fe(O)(κ²-OPiv)Zn₄(prv)₃(bta)₆
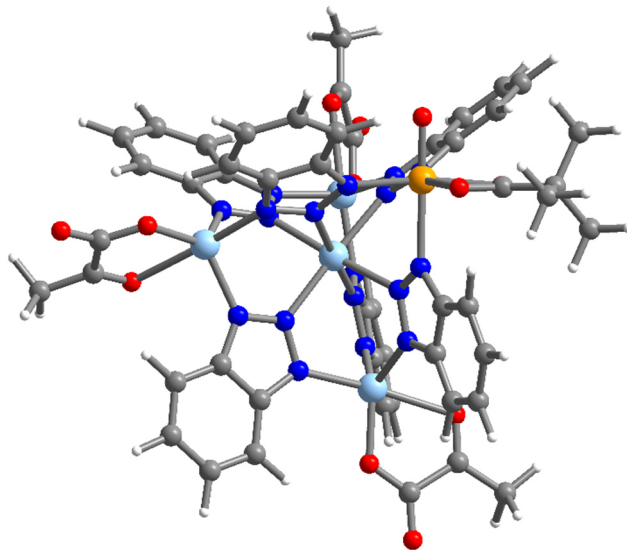
N	1.9506	0.0000	0.0000
C	2.7417	0.8440	0.7351
C	2.4365	1.8539	1.6638
H	1.4042	2.0878	1.9150
N	2.7406	-0.7727	-0.7419
N	4.0216	-0.4803	-0.5325
C	4.0784	0.5290	0.3876
C	5.1702	1.2073	0.9616
H	6.1924	0.9478	0.6863
Fe	0.0000	0.0000	0.0000
Zn	2.0618	-2.2909	-2.1469
N	0.5100	-0.6278	-4.2448
C	-0.0111	0.6166	-4.4271
C	-0.2942	1.3335	-5.6034
H	-0.1202	0.8988	-6.5871
N	0.6287	-0.8320	-2.9329
N	0.1936	0.2135	-2.2331
C	-0.2023	1.1714	-3.1344
C	-0.6466	2.5013	-2.9938
H	-0.7137	2.9667	-2.0151
N	-0.2548	-1.9135	-0.1033
N	4.7696	-1.3081	-3.3731
C	5.3412	-0.8889	-4.5392
C	6.6153	-0.3683	-4.8303
H	7.3650	-0.2256	-4.0535
N	3.5184	-1.6849	-3.6470
N	3.2425	-1.5414	-4.9391
C	4.3571	-1.0412	-5.5495

C	4.6098	-0.6922	-6.8898
H	3.8374	-0.8124	-7.6494
N	1.1533	-3.7638	-4.7799
N	4.7460	-3.3987	-0.9224
N	1.3512	-3.8985	-3.4674
N	0.5436	-2.7993	-0.6883
N	3.4868	-3.7048	-1.2223
C	5.3056	-4.4810	-0.3057
C	6.5876	-4.6996	0.2296
H	7.3505	-3.9233	0.2123
N	3.1880	-4.9434	-0.8339
C	4.3017	-5.4805	-0.2542
C	4.5533	-6.7448	0.3081
H	3.7891	-7.5199	0.3297
N	0.1128	-4.0378	-0.4726
C	-1.0164	-3.9678	0.2918
C	-1.8646	-4.9703	0.7947
H	-1.6927	-6.0228	0.5731
C	-1.2568	-2.5963	0.5441
C	-2.3369	-2.1734	1.3376
H	-2.5023	-1.1177	1.5340
N	1.1332	-5.1501	-3.0759
C	0.7748	-5.8771	-4.1754
C	0.4345	-7.2344	-4.3276
H	0.4144	-7.9029	-3.4670
C	0.7918	-4.9829	-5.2755
C	0.4832	-5.4164	-6.5775
H	0.5131	-4.7352	-7.4266
C	3.5175	2.5173	2.2212
H	3.3369	3.3105	2.9474
C	4.8602	2.1987	1.8776
H	5.6689	2.7555	2.3523
C	6.8555	-0.0262	-6.1506
H	7.8269	0.3861	-6.4257
C	5.8706	-0.1890	-7.1636
H	6.1186	0.0999	-8.1854
C	-0.7639	2.6254	-5.4447
H	-0.9894	3.2274	-6.3254
C	-0.9256	3.2005	-4.1568
H	-1.2607	4.2359	-4.0838
C	-3.1590	-3.1695	1.8384
H	-4.0112	-2.8922	2.4595
C	-2.9328	-4.5456	1.5663
H	-3.6223	-5.2839	1.9769
C	6.8216	-5.9439	0.7904

H	7.7995	-6.1607	1.2210
C	5.8221	-6.9537	0.8219
H	6.0660	-7.9186	1.2673
C	0.1267	-7.6467	-5.6136
H	-0.1444	-8.6883	-5.7884
C	0.1551	-6.7544	-6.7206
H	-0.0902	-7.1401	-7.7107
O	-0.6312	2.1797	0.0504
O	-1.9798	0.4673	-0.2374
C	-1.8174	1.7364	-0.0788
C	-3.0446	2.6390	-0.0316
O	-0.0889	-0.0077	1.6269
Zn	1.2815	-5.6010	-1.0565
Zn	1.2879	-1.9257	-5.5931
Zn	5.4882	-1.5898	-1.5032
O	7.0864	-0.7399	-0.7748
O	7.2643	-2.8196	-2.5169
O	1.5350	-1.4782	-7.4814
O	-0.8802	-2.2078	-6.4813
O	1.3232	-6.2084	1.2363
O	0.6916	-7.4613	-1.0902
C	0.9078	-7.3636	1.3112
C	0.5444	-8.1403	0.0056
C	-0.8288	-1.9150	-7.6747
C	0.5333	-1.4836	-8.3056
C	8.2769	-1.1244	-1.1184
C	8.3161	-2.3142	-2.1296
O	9.3469	-0.6579	-0.7339
O	0.5513	-1.1885	-9.4986
O	0.1604	-9.3027	0.1126
C	0.7348	-8.0790	2.6106
H	1.3290	-9.0046	2.6003
H	1.0216	-7.4349	3.4483
H	-0.3100	-8.4100	2.7072
C	9.6584	-2.7905	-2.5804
H	9.5583	-3.6312	-3.2746
H	10.2022	-1.9562	-3.0483
H	10.2609	-3.0686	-1.7032
C	-2.0234	-1.9508	-8.5704
H	-2.1682	-0.9596	-9.0250
H	-1.8252	-2.6275	-9.4149
H	-2.9144	-2.2639	-8.0163
C	-3.7930	2.3032	1.2774
H	-4.1099	1.2521	1.2851
H	-3.1569	2.4824	2.1559

H	-4.6866	2.9381	1.3639
C	-3.9413	2.3194	-1.2431
H	-3.4203	2.5274	-2.1881
H	-4.2371	1.2630	-1.2421
H	-4.8476	2.9409	-1.2033
C	-2.6277	4.1150	-0.0373
H	-3.5219	4.7492	0.0479
H	-1.9560	4.3454	0.7995
H	-2.1095	4.3835	-0.9681

Data S1. Crystallographic Information File for $Zn_5Cl_4(btdd)_3$.

Data S2. Crystallographic Information File for $Zn_5(prv)_4(btdd)_3$.